Gravitational-wave radiation from merging binary black holes and Supernovae

I. Kamaretsos

Submitted for the degree of Doctor of Philosophy
School of Physics and Astronomy
Cardiff University
October 2012

Declaration of authorship

- Declaration:
  This work has not previously been accepted in substance for any degree and is not concurrently submitted in candidature for any degree.

  Signed: ..... (candidate) Date: .....

- Statement 1:
  This thesis is being submitted in partial fulfillment of the requirements for the degree of Doctor of Philosophy (PhD).

  Signed: ..... (candidate) Date: .....

- Statement 2:
  This thesis is the result of my own independent work/investigation, except where otherwise stated. Other sources are acknowledged by explicit references.

  Signed: ..... (candidate) Date: .....

- Statement 3
  I hereby give consent for my thesis, if accepted, to be available for photocopying and for inter-library loan, and for the title and summary to be made available to outside organisations.

  Signed: ..... (candidate) Date: .....

Summary of thesis

This thesis is conceptually divided into two parts. The first and main part concerns the generation of gravitational radiation that is emitted from merging black-hole binary systems using Numerical Relativity methods. The second part presents the methodology of the search for gravitational-wave bursts that are emitted in core-collapse Supernovae.

My approach to Numerical Relativity is to utilise the late-time gravitational radiation of merging binary black holes to extract key astrophysical parameters from such systems via standard parameter estimation techniques. I begin with an introductory chapter that outlines the standard theories of stationary and perturbed black holes. In addition, up-to-date techniques in performing binary black hole simulations, the current and near-future status of the global network of gravitational-wave detectors, as well as the most promising gravitational-wave sources. I conclude the chapter with elements on parameter estimation techniques, such as Bayesian analysis and the Fisher information matrix. In Chapter 2, I discuss detection issues and parameter estimation results from the late-time radiation of colliding non-spinning black holes in quasi-circular orbits, and propose a practical test of General Relativity, as well as of the nature of the merged compact object. Chapter 3 involves similar parameter extraction calculations, but involves a more realistic approach, whereby the effect of the various angular parameters on parameter estimation is considered, placing an emphasis on the actual science benefit from measuring the gravitational radiation from perturbed intermediate and supermassive black holes. In Chapter 4 we present the results of an extensive Numerical Relativity study of merging spinning black hole binaries and argue that the mass ratio and individual spins of a non-precessing progenitor binary can be measured solely by observing the late-time radiation.

Chapter 5 presents the methodology in carrying out searches for gravitational-wave bursts (GWB) from core-collapse Supernovae with a dedicated for GWB searches pipeline (X-Pipeline) and presents the sensitivity performance of X-Pipeline in detecting GWBs associated with certain Supernova candidates during the two most recent LIGO-Virgo-GEO Science Runs.

Contents

List of Figures

List of Tables

Acknowledgements

I'm grateful to Bangalore Sathyaprakash for his supervision and exceptional advice throughout my three years of PhD studies in Cardiff. For a very fruitful and pleasant co-operation and sharing of ideas and knowledge. For his effort in teaching me to stand out as a researcher and develop good habits. Tolerating my inquisitive and disputing nature led to a special - most amusing for me! - type of interaction and was also an impressive skill of his that deserves an extra acknowledgment. Lastly, for being understanding, and helpful in providing financial support. Thanks for everything, Sathya!

I'm thankful to Patrick Sutton for accepting me as a student and providing attentive supervision and a healthy and most pleasing collaboration. For 'squashing' bugs by my side while carrying out the search for gravitational waves from core-collapse supernovae and sharing his knowledge and enthusiasm on burst search techniques and signal processing. Playing pool with him is surely an unforgettable experience and I would never dare question his 'Tom Jones' karaoke skills!

Mark Hannam, to whom I owe my initiation on numerical simulations of binary black holes. Always there to assist with the numerous issues I encountered during my work, and impossible to find in a less than a good mood!

To my fellow research students of the gravitational waves group in Cardiff (Go team Cardiff!) for excellent working conditions and all the help I received everytime I would ask for it. To my dear office-mates Ian Harry, Laura Nuttall, Duncan Macleod, Thomas Dent, David McKechan, Thomas Adams and Patricia Schmidt for all the fun we had in the office and especially to Ian for getting me acquainted with the ..Welsh culture by dragging me to the pub! Mark Edwards, discussing with you on anything that has to do with computer systems security was always delightful. It was also nice having around Jeroen Meidam.

I could say many things about Valeriu Predoi, but he is basically a 'crazy' Romanian that I could totally relate to and a good friend and colleague. A person I definitely admire him for his ability to ..survive, ..only to drink more beer. For the endless lonely nights we spent drinking together and all the experiences and thoughts we shared in this crazy city.

Our postdoc dream team, John Veitch, Gareth Jones, James Clark, Mike Pürrer, Frank Ohme, Erin MacDonald and especially Chris Messenger and Thomas Dent, all of whom have definitely enhanced my PhD experience.

It has been fun and educative admitting undergraduate students every Summer. Kiersten Ruisard, Sebastian Khan, Scotty Coughlin, Hannah Evans and David Schinkel are lovely people with whom I had quite a pleasant interaction.

Several things would not have been possible without the help of the computing

support team, especially of Richard Frewin, Ian Harry, Duncan Macleod, Mark Edwards and Rodney Smith.

It was my privilege to collaborate externally with Sascha Husa, Alessandra Buonanno, Thomas Dent, Jolien Creighton, Luciano Rezzolla, Vitor Cardoso and Chris Van De Broeck, and for productive discussions on various aspects of black hole simulations and parameter estimation. While performing GWB searches from Supernovae, it was a pleasure to collaborate with Pete Kalmus, Amber Stuver, Lex Corpuz and Kevin Loew.

I wish to thank my dear examiners Stephen Fairhurst and Luc Blanchet who are taking the time to carefully read through this thesis!

I also acknowledge administrative staff of the School of Physics and Astronomy, Louise Winter, Nicola Hunt, Helen James, Philip Treadgold, Glesni Lloyd and especially Walter Gear, for a much friendly support and understanding.

To my friends in Greece, *Χρύσα*, *Ευαγγελία*, *Γιώργο Λιόλιο*, *Πέτρο*, *Θανάση* and *Γιώργο Καλίκα* for all their kind words during my adventure in 'foreign lands'.

To my brother *Βαγγέλης* and my parents *Θωμάς* and *Ελένη*, who have always believed in me (and have been funding me!) ..I dedicate this thesis to them.

Authored papers and collaborative work summary

Large sections of this Thesis include collaborative work, that has been either published, or is in preparation. The author holds either leading authorship or most significant contribution.

1. Chapter 2: "Black-hole hair loss: Learning about binary progenitors from ringdown signals", Ioannis Kamaretsos, Mark Hannam, Sascha Husa and B.S. Sathyaprakash, Phys. Rev. D 85, 024018.

   This chapter presents detection and parameter estimation results of the gravitational radiation emitted by a perturbed Kerr black hole (ringdown radiation) that ensues from the merger of a *non-spinning* binary black-hole progenitor. We preview the feasibility of measuring the progenitor mass ratio in several near-future and planned detectors, such as Advanced LIGO, Einstein Telescope and the Laser Interferometer Space Antenna. If General Relativity is correct, our signal model can also be used to implement a test on the nature of the compact object.

2. Chapter 3: "From black holes to their progenitors: A full population study in measuring black hole binary parameters from ringdown signals", Ioannis Kamaretsos, Journal of Physics: Conference Series, 363, 012047.

   A necessary extension to the previous chapter, which takes into account the effect of all the signal model's angular parameters on the parameter estimation, and discusses the impact of measuring this type of gravitational-wave signals, on astrophysical issues relating to the formation and existence of intermediate-mass and supermassive black holes.

3. Chapter 4: "Is black-hole ringdown a memory of its progenitor?", Ioannis Kamaretsos, Mark Hannam and B.S. Sathyaprakash, Physical Review Letters 109, 141102 (2012).

   Complementary in concept to Chapter 2. By performing an extensive Numerical Relativity study of binary systems with *spinning* black-hole components, we suggest the feasibility of measuring the mass ratio in *non-precessing* systems, as well as the individual spin components of the progenitor, solely by measuring the ringdown radiation of the final black hole. The title is chosen so as to denote the contradiction with the commonly accepted view

that the late-time radiation from merging binaries is independent of the progenitor properties.

Also published in several Science magazines. In New Scientist as: "Space-time ripples record black hole crashes", 19 August 2012, magazine issue 2878.

4. A long version of Chapter 4 is in preparation and is not included in this Thesis: To be submitted to Phys. Rev. D. It supports Chapter 4's conclusions and discusses in more detail parameter estimation results from merging *spinning* black-hole binaries of a large range of masses, in the Einstein Telescope and Advanced LIGO detectors. We also argue on the trustworthiness of our Numerical Relativity waveforms and signal model.

5. Chapter 5: For the LIGO and Virgo Scientific Collaboration (LVC). Currently in review process within LVC. This chapter presents the first externally-triggered search for gravitational-wave bursts from core-collapse Supernovae, as well as describes the methodology. The author has generated the analytical waveforms and conditioned all waveforms used in the search, as well as contribute in the development of the relevant pipeline, so as to perform the actual analysis for the three Supernova triggers that were selected, using data from the S5 and S6 LIGO-Virgo-GEO Science Runs.

6. The last section has been removed from this Thesis and will be documented as a separate LIGO technical report. It presents the sensitivity performance of X-Pipeline in detecting gravitational-wave bursts associated with X-Ray outbursts of six highly energetic low-mass X-Ray binaries situated in our Galaxy. It makes use of data from the LIGO S5 Science Run.

Conventions

I will follow the standard convention of using latin indices to denote spatial vectors (x=1, y=2, z=3) and greek indices to denote space-time vectors (t=0, x=1, y=2, z=3) and follow the Einstein summation convention for four-dimensional and spatial quantities,

$$a^{\mu}b_{\mu} = \sum_{\mu=0}^{3} a^{\mu}b_{\mu}. \tag{1}$$

Unless stated otherwise I always use the assumption that $c = G = 1$. Also, I use the negative metric signature of $-+++$.

To simplify partial differentials we set:

$$\partial_{\mu} = \frac{\partial}{\partial x^{\mu}} \tag{2}$$

The D'Alembert operator is denoted as:

$$\Box = g^{\mu\nu}\partial_{\mu}\partial_{\nu}, \tag{3}$$

which in flat spacetime becomes

$$\Box = -\frac{\partial}{\partial t^2} + \frac{\partial}{\partial x^2} + \frac{\partial}{\partial y^2} + \frac{\partial}{\partial z^2} = -\frac{\partial}{\partial t^2} + \nabla^2 \tag{4}$$

The Cristoffel symbol is given by:

$$\Gamma^{\rho}_{\mu\nu} = \frac{1}{2}g^{\rho\sigma}\left(\partial_{\mu}g_{\sigma\nu} + \partial_{\nu}g_{\sigma\mu} - \partial_{\sigma}g_{\mu\nu}\right) \tag{5}$$

The Riemann tensor is defined as:

$$R^{\mu}_{\nu\rho\sigma} = \partial_{\rho}\Gamma^{\mu}_{\nu\sigma} - \partial_{\sigma}\Gamma^{\mu}_{\nu\rho} + \Gamma^{\mu}_{\alpha\rho}\Gamma^{\alpha}_{\nu\sigma} - \Gamma^{\mu}_{\alpha\sigma}\Gamma^{\alpha}_{\nu\rho} \tag{6}$$

The Ricci tensor is:

$$R_{\mu\nu} = g^{\alpha\beta}R_{\alpha\mu\beta\nu} = R^{\alpha}_{\mu\alpha\nu} \text{ or } g^{\alpha\beta}R_{\mu\alpha\nu\beta} = R_{\mu\alpha\nu}{}^{\alpha} \tag{7}$$

while the Ricci scalar is:

$$R = g^{\mu\nu}R_{\mu\nu}, \tag{8}$$

where $g^{\mu\nu}$ denotes the metric tensor of four-dimensional spacetime.

Chapter 1

Introduction

My major motivation for performing numerical simulations of merging binary black holes is for the accurate calculation of the gravitational waveform that is emitted in the process, and for the largest possible parameter space. This will make the detection and accurate parameter estimation of such systems more likely in the era of second generation interferometric gravitational-wave detectors. By correlating these waveforms -via the so-called matched-filtering technique- with the observational data from the global network of detectors, we will be able to extract bottom-line astrophysical information on the existence, formation and growth of black holes, and test General Relativity (GR) in the regime of very strong fields.

1.1 Short treatment on black holes

One of the most astonishing residuals of gravitational collapse events, such as the core collapse of a massive star is the formation of a black hole (BH) [9]. Imagine two observers that keep time measurements: One is sitting on the surface of the collapsing stellar core, the other observing the collapse from far away. At some point the first observer approaches the gravitational radius, which, assuming the collapse is completely spherically symmetric, has a value of $2M$. Assuming that the freely falling observer and his watch are not affected by tidal forces, he will not measure anything unusual. On the other hand, the latter observer will measure the light pulses sent by the freely falling observer to arrive less frequently in time, while they will also redshift, thus becoming dimmer. Eventually the first observer will tend to appear standing still on the gravitational radius, while disappearing. As for the rest of the star, it will gradually become fainter, an effect which will appear to begin from the center of the stellar disc and spread towards the limb [10].

In the case of a collapsing body leading to a BH, properties such as its composition, asymmetries in its distribution of mass and electric charge, or the distribution of magnetic field energy, do not influence the properties of the resulting stationary black hole. This conclusion follows qualitatively from an analysis of the behavior of small perturbations in the course of the formation of the final BH. The BH is characterised by an event horizon (EH) which differentiates it from all other theoretical descriptions of objects, in the context of standard thermodynamics, electromagnetism and GR [11, 12].

1.1.1 Black hole no-hair conjecture

A black hole, if left alone, will eventually reach a stationary state. If it was initially disturbed by a collection of particles and fields in its exterior not in equilibrium, the whole system will immediately begin to re-arrange itself, with accompanying electromagnetic and gravitational radiation towards infinity, as well as into the black hole horizon. As the collection of particles and fields that surrounded the black hole had finite energy densities, then, without any compensation for the radiated or absorbed energy, it is expected that these processes settle down, leaving the black hole in a stationary Kerr state.

Wheeler conjectured that in its evolution to the stationary state, an isolated black hole expels through radiation all the characteristics that radiation can remove. He came to this conclusion by summarizing the results of a large number of papers devoted to the final state of a black hole [13]. Since for a spin-s massless boson field the radiation is connected with changing the multipole moment of the system, Wheeler conjectured that a stationary black hole resulting from a collapse of neutral matter which interacts only gravitationally (s = 2) is described by a metric having only two free parameters: the mass ($\ell = 0$) and the angular momentum ($\ell = 1$). This conclusion was also reached in [14, 15].

If the collapsing matter was also electrically charged, the stationary metric that finally ensues is therefore described by fixing the three parameters: mass (M), spin (J) and total electric charge (Q) as measured by a distant observer. Actually, what made Wheeler insist on these quantities, was the fact that they could be measured by distant observers by applying an analog to Gauss's flux theorem. As for the presence of a, non-monopole, magnetic field around the black hole, it is not possible, as was proved in [16, 17]. These arguments show that Wheeler's conjecture is equivalent to the following impressive proposition: That regardless of the specific details of the collapse or the structure and properties of the collapsing body, the resulting stationary black hole is described by an exterior geometry

specified by the parameters M, J, and Q. This is what Wheeler expressed as: "Black holes have no hair" in [13].

Kerr uniqueness theorem

Stationary BHs are solutions of non-linear equations with specific assumptions on the topology and causal structure of spacetime. One might expect a greater diversity of BH solutions, as well as a more complicated structure. However, the reverse is observed: the class of possible solutions describing the final stationary configuration is quite restricted, allowing for a complete description of these objects. The physical reason is that the gravitational field is universal and acts on any matter possessing mass-energy. For physical fields to be in equilibrium around a BH, certain conditions should hold that are equivalent to eliminating all degrees of freedom of the fields that are capable of propagating. Consequently, the general picture is considerably simplified. The uniqueness theorem summarised in this section gives support for this conclusion.

The Kerr solution is probably the only empty stationary BH solution, as indicated by a theorem from Carter [18]. The assumptions he made were:

- The space is stationary, axisymmetric and regularly predictable,
- $T_{\mu\nu} = 0$ holds everywhere,
- The past horizon intersects the future event horizon in a compact connected two-dimensional surface.

His main conclusion was that all solutions fall into disjoint classes, which are parametrised by the mass and angular momentum as measured at infinity.

Astrophysical black holes

In this thesis I have not treated charged non-rotating/rotating BHs, as in any realistic situation, the electric charge of a BH is negligible. To a good approximation, the ratio of the charge Q to mass M of a BH cannot exceed 10^{-8} C/kg [19]. On the other hand, there is ample evidence from electromagnetic (EM) observations that astrophysical BHs do possess considerable spin angular momentum. Specifically, estimates from considering the continuum spectra of accretion disks [20], measurements of quasi-periodic oscillations of X-rays from low mass X-ray binaries [21], or Fe Ka line profiles [22] indicate that a significant fraction of BHs are rapidly spinning, with a/M values up to at least 0.5, although a few could

have spins a/M as low as 0.1 or as high as $\sim$0.99. A possible drawback of these results is that they do not involve isolated binary black hole (BBH) systems, but low-mass or high-mass X-ray binaries where material is accreting around the BH, hence increasing its angular momentum.

Similar results seem to hold for supermassive BHs that power the outflows in Active Galactic Nuclei (AGN) galaxies [23], with the exception that the spin range extends to lower values. These moderately to highly spinning supermassive BHs might later become part of a compact binary system, e.g. in a galaxy merger scenario.

An educated guess on the spin values of stellar-mass BHs not interacting with accretion tori can be made via core-collapse simulations. In a series of numerical simulations with varying pre-supernova models [24], most of the nascent BH spins were between $a = J/M^2 \simeq 0.2$ and $a \simeq 0.6$, while they appear to be limited at values below $a \simeq 0.9$, due to the likely appearance of non-axisymmetric rotational instabilities. However, their finding requires confirmation by three-dimensional simulations.

1.1.2 Different notions of black hole horizon

Event and apparent horizons

The event horizon is that 2+1 dimensional subset of spacetime where outgoing light rays neither reach the future null infinity $\mathcal{J}$ nor the BH center (singularity). More precisely, it is the boundary of causal past of future null infinity [11, 19]. The event horizon happens to be a gauge-invariant entity, therefore containing important geometric information on the BH spacetime.

An orientable compact spacelike two-dimensional surface in $\mathcal{D}^+(\mathcal{J})$ is an outer trapped surface if the convergence - also called expansion in this case - of orthogonal outgoing null geodesics is non-positive. The outer boundary $\partial\mathcal{G}_1(\tau)$ of a connected component $\mathcal{G}_1(\tau)$ of the trapped surface is called an apparent horizon. Its existence implies the presence of an event horizon, either coinciding with it, or situated on the outside. Each component of $\partial\mathcal{G}(\tau)$ is a two-dimensional surface such that the outgoing null rays have zero expansion. Two inspiraling BHs that merge would have their event horizons merge, but if their apparent horizons existed, they would not necessarily join up immediately. A third apparent horizon, of the merger event, would temporarily be formed [11].

For a BH in a stationary state, the apparent and event horizons actually coincide. Before reaching this state though, the apparent horizon can evolve extremely

rapidly, even discontinuously, unlike the event horizon which always evolves in a continuous manner. This kind of behaviour had been predicted to occur in binary black hole collisions [11] and has been observed in numerical simulations of binary black holes, see also Section 1.4.5. This depends on the distribution of matter-energy around the surface, in which case the outgoing null rays will start to converge therefore displacing the surface of zero expansion outwards.

The intersection of the event horizon with a constant time spatial hypersurface, Σ_t, that is the spatial 'snapshot' of the horizon at the instant of time associated with Σ is a closed, two-dimensional surface. Assuming that $T_{ab}k^a k^b \geq 0$ for all null vectors k^a, its proper surface area, $\mathcal{A}$ obeys the interesting relation that it can never decrease in sequential time-slices [25],

$$\delta\mathcal{A} \geq 0. \tag{1.1}$$

The irreducible, or minimum mass of a BH is defined as [26, 27, 28],

$$M_{irr} \equiv \left(\frac{\mathcal{A}}{16\pi}\right)^{1/2}, \tag{1.2}$$

which implies an upper bound to the energy of the gravitational radiation emitted when a BH coalesces with another [25]. For the case of equal mass Schwarzchild BHs it is easy to show that this bound is equal to $(1-\sqrt{2}/2)M_{tot}$.

Dynamical and isolated horizons

The dynamical and isolated horizons are also locally defined, nonetheless they provide more insight on the evolution of a BH than the AH. The dynamical horizon is directly defined from the AH: consider a sequence of AHs lying on hypersurfaces, between Σ_t and $\Sigma_{t+\Delta t}$. The resulting worldtube, i.e. the union of these surfaces, may not be continuous since the AH can move discontinuously from time-slice to time-slice. If we exclude non-continuous sections of the worldtube and in the case where the BH is accreting matter or radiation enlarging its horizon, each time slice of this worldtube is simply called a dynamical horizon [29, 30].

The isolated horizon [31, 32, 33] is quite similar to a dynamical horizon and in the case where there is no matter or radiation falling into the BH, these two surfaces are identical.

The dynamical horizon framework, therefore, combines advantages from all the different notions of BH horizons. It provides information on the BH thermodynamical and physical properties and their evolution, such as the relation of its

surface area, mass and angular momentum with the flux of matter and radiation across its surface. In numerical simulations, it aids in visualizing the notion of a BH and its evolution in a binary BH coalescence scenario, as we shall see in Section 1.4.

1.2 Quasinormal modes of black holes

The following account on perturbation theory and quasinormal modes of black holes is not intended to be comprehensive, but to prepare the reader for Chapters 2, 3 and 4 by providing a minimum theoretical background.

1.2.1 Overview of BH quasinormal modes

Quasinormal modes (QNMs) of BH spacetimes are characteristic modes of perturbations of BHs that naturally result in wave solutions of the linearly perturbed spacetime that satisfy an outgoing boundary condition at infinity and an ingoing boundary condition at the horizon. They are the characteristic, resonant modes of oscillations of BHs whose superposition or collective effect is often termed the *ringdown* gravitational-wave (GW) radiation. Each mode of oscillation is exponentially decaying over time and is represented by an amplitude term, $A_{\ell mn}$ and a complex characteristic frequency $\omega_{\ell mn} = \omega^R_{\ell mn} - i\,\omega^I_{\ell mn}$, where ℓ, m, n are indices we use to denote different modes; ℓ and m are multipolar indexes of the angular eigenfunctions of the QNM, while an increasing overtone number n denotes an increasing decay rate of the QNM.

The real and imaginary parts of the complex frequency of mode (ℓ, m, n) are its oscillation frequency, $\omega_{\ell mn} = 2\pi f_{\ell mn}$ and damping time, $\tau_{\ell mn}$ respectively and depend only on the BH's mass, M and magnitude of spin momentum, $|\vec{S}|$. Not surprisingly, the QNM frequencies scale with the inverse of the BH mass, while the QNM damping times are proportional to the mass, while their dependence on the spin is less prominent. For instance, for a BH with $M = 10^7 M_\odot$ and dimensionless spin, $|\vec{S}|/M^2 = 0.7$ the $(2, 2, 0)$ mode - which is prominently excited in BBH mergers - has a frequency $f_{220} \simeq 1.73\,\mathrm{mHz}$ and damping time $\tau_{220} \simeq 606\,\mathrm{s}$. We will expand on the properties of QNM radiation in BBH mergers in Chapters 2, 3 and 4.

The main difference between QNM problems and other prototypical physical problems involving small oscillations, such as the vibrating string with fixed ends, is that the system is now dissipative; the waves can escape either to infinity or

into the BH. For this reason an expansion in normal modes is not possible [34, 35]. This also justifies the prefix "quasi-". There is a discrete infinity of QNMs, defined as eigenfunctions satisfying the above boundary conditions. The corresponding eigenfrequencies have a real and imaginary part.

1.2.2 Brief history of BH QNMs

The history of BH perturbation theory extends back for more than five decades, when Regge and Wheeler analyzed a special class of gravitational perturbations of the Schwarzschild geometry [36]. In 1970, Zerilli extended the Regge-Wheeler analysis to more general perturbations of a Schwarzschild BH, thereby showing that the perturbation equations are reduced to a pair of Schrodinger-like equations [37]. In the same year, QNMs were first discovered numerically, in the scattering of gravitational wavepackets by a Schwarzschild BH, where the late-time waveform is composed of damped sinusoids [38]. Chandrasekhar and Detweiler [39] compute numerically some of the more weakly damped mode frequencies. Since then, QNMs have been thoroughly studied in a wide range of spacetimes, and in the context of a few alternative metric theories of gravity, such as Brans-Dicke, Chern-Simons, theories that include Gauss-Bonnet terms [40], as well as Bekenstein's Tensor-Vector-Scalar theory [41].

1.2.3 Perturbative analysis of Kerr black holes

Near-stationary BHs

The terrain of a BH in equilibrium is indeed more thoroughly explored and more straightforward to deal with. It is a physically acceptable end state of any BH which is left unperturbed for some time, due to gravitational radiation damping out its external field vibrations.

Following Chandrasekhar (1983) [12] the perturbed metric of a Kerr BH can be written in the general axisymmetric form:

$$ds^2 = -\mathrm{e}^{2\nu}dt^2 + \mathrm{e}^{2\psi}(d\phi - q_1 dt - q_2 dr - q_3 d\theta)^2 + \mathrm{e}^{2\mu_2}dr^2 + \mathrm{e}^{2\mu_3}d\theta^2. \tag{1.3}$$

It is assumed that when the metric is perturbed by some external cause, there are two different kinds of perturbation:

- Either q_1, q_2 and q_3 are perturbed to first order,
- or $\delta\nu$, $\delta\psi$, $\delta\mu_2$ and $\delta\mu_3$ are introduced.

Looking at equation Eq. (1.3), it is easy to see that these two cases are differentiated, as the first, affecting the $dtd\phi$ components, induces dragging of inertial frames, whereas the second is independent of the sign of ϕ and therefore does not induce rotation. The first kind of perturbations are referred to as 'axial' and the second, as 'polar'. In the literature the different perturbations are often referred to as odd-parity and even-parity, respectively and they are encountered in many different approaches to linearised BH perturbations as we shall see. The reason for this nomenclature is that the first set transforms as $(-1)^{\ell}$ under space inversion. The second set, on the other hand, transforms as $(-1)^{\ell+1}$. Strictly speaking, this means that the first kind of perturbations are of alternating odd/even parity for even/odd multipoles ℓ.

Linearized perturbations of Kerr BH

As explained towards the end of Section 1.1.1, we will be working with the more astrophysically plausible BHs corresponding to the Kerr solution, rather than with Schwarzchild or Reissner-Nordstrom BHs. For treatises on QNMs in Schwarzchild and Reissner-Nordstrom spacetimes see [42] and [43, 44], respectively. In the usual approach to BH perturbation, we consider a metric which is expanded to higher perturbative-order terms,

$$\tilde{g}_{\mu\nu} = g_{\mu\nu} + h^{(1)}_{\mu\nu} + h^{(2)}_{\mu\nu} + h^{(3)}_{\mu\nu} \ldots , \tag{1.4}$$

where superscripts ($i = 1, 2, 3, ..$) denote the perturbative order and $g_{\mu\nu}$ is a background stationary metric, which depends on the problem in question, it could be for instance, a Schwarzschild or a Kerr metric. If only the first order terms are retained in all calculations the approach is called linearised perturbation.

By expanding the perturbed metric tensor in tensorial spherical harmonics, we have the harmonics behaving differently under the angular transformations $\theta \to \pi - \theta$ and $\phi \to \pi + \phi$. The separated equations split into two sets: the axial or odd (Regge-Wheeler) and the polar or even (Zerilli), belonging to parities $(-1)^{(l+1)}$ and $(-1)^{l}$ respectively. Regge and Wheeler reduced the equations describing the axial perturbations to a single Schroedinger-like equation with the potential $V^{(l)}_{s}$,

$$\frac{d^2\Psi^{(l)}_s}{dr^2_*} + \left(\omega^2 - V^{(l)}_s\right)\Psi^{(l)}_s = 0\,, \tag{1.5}$$

$$V^{(l)}_{s=2} = \left(1 - \frac{2M}{r}\right)\left[\frac{l(l+1)}{r^2} - \frac{6M}{r^3}\right], \tag{1.6}$$

where $r_* = r + 2M\,\ln(r/2M-1)$ and s denotes the spin of the field which is set to $s=2$ for gravitational-type perturbations. Note that the tortoise coordinate, $r_* \to -\infty$ at the horizon (i.e. as $r \to r_+$), and to $r_* \to +\infty$ at spatial infinity.

Only much later a formulation for polar-type perturbations was produced [37] and remarkably a similar Schroedinger-like equation is satisfied, but with the potential

$$V^{(l)}_{s=2} = 2(r-2M)\frac{9M^3 + 3\lambda^2 M r^2 + \lambda^2\,(1+\lambda)\,r^3 + 9M^2\lambda\,r}{r^4\,(\lambda\,r+3M)^2}, \tag{1.7}$$

with $\lambda = (1/2)(l+1)(l-2)$. Equations 1.5 and 1.7 imply that the curvature of a pointlike mass is manifested as a potential barrier which extends throughout spacetime. This is reminiscent of the quantum mechanics problem of the scattering of a particle's wavefunction by a potential barrier. Consequently, the response of a black hole to polar and axial perturbations can be studied by investigating the manner in which a gravitational wave incident on the black hole is transmitted, absorbed and reflected on this barrier.

For first-order perturbations in the metric, the Regge-Wheeler-Zerilli formalism, involves separating angular variables with tensor harmonics of indices (ℓ, m). The equations decouple to the even (or polar) part with parity $(-1)^\ell$ under a transformation $(\theta,\phi) \to (\pi-\theta, \pi+\phi)$ and the odd (or axial) part with parity $(-1)^{\ell+1}$. The Zerilli equation is given by

$$\begin{aligned} \left[-\frac{\partial^2}{\partial t^2} + \frac{\partial^2}{\partial r_*^2} - V_Z(r)\right]\psi^{(1)}_{\ell m}(t,r) = 0\,, \\ V_Z(r) = \left(1-\frac{2}{r}\right)\frac{2\lambda^2(\lambda+1)r^3 + 6\lambda^2 r^2 + 18\lambda r + 18}{r^3(\lambda r+3)^2}\,. \end{aligned} \tag{1.8}$$

Quasi-normal modes

For most spacetimes of interest the potential $V \to 0$ as $r_* \to -\infty$, and in this limit solutions to the wave equation (1.5) behave as $\Psi \sim e^{-i\omega(t\pm r_*)}$. Classically nothing should leave the horizon: only ingoing modes (corresponding to a plus sign) should be present, and therefore

$$\Psi \sim e^{-i\omega(t+r_*)}\,, \quad r_* \to -\infty \;\; (r \to r_+)\,. \tag{1.9}$$

For asymptotically flat spacetimes, the metric at spatial infinity tends to the

Minkowski metric. We discard unphysical waves by requiring

$$\Psi \sim e^{-i\omega(t-r_*)}, \quad r \to \infty\,, \tag{1.10}$$

A different mathematical and physical approach in producing an analytical solution of QNMs emitted from a perturbed black hole concerns the case of a point particle of mass $m \ll M$ falling into the BH, instead of a GW packet scattering. The resulting gravitational waveform satisfies the inhomogeneous form of wave equation Eq. 1.5,

$$\frac{d^2\Psi_s^{(l)}}{dr_*^2} + \left(\omega^2 - V_s^{(l)}\right)\Psi_s^{(l)} = K(\omega, r)\,, \tag{1.11}$$

where $K(\omega, r)$ is a quantity related to the initial data. The solution can be found by applying a standard Green's function approach [45]. Applying the standard procedure, we take two independent solutions of the homogeneous equation, at the horizon and at infinity,

$$\lim_{r_*\to-\infty} \Psi_1 \sim e^{-i\omega r_*}\,, \tag{1.12}$$

$$\lim_{r_*\to+\infty} \Psi_2 \sim a_1(\omega)e^{-i\omega r_*} + a_2(\omega)e^{i\omega r_*}\,, \tag{1.13}$$

the general solution can be expressed via the Wronskian of the two solutions as [46]:

$$\Psi(t, r) = \frac{1}{2\pi}\int_{-\infty+ic}^{\infty+ic} \Psi(\omega\,, r)e^{-i\omega t}d\omega\,. \tag{1.14}$$

and leads to an equation that describes the QNM contribution to the wave function for an observer far from the BH [34],

$$\Psi(t, r) = -\mathrm{Re}\left[\sum_n A_n(K)e^{-i\omega_n(t-r_*)}\right]\,, \tag{1.15}$$

where the sum is over all points of the complex frequency, ω, plane for which the amplitude of ingoing waves, a_1, is zero, in Eq. 1.13, that is, where we have outgoing radiation, which by definition, must be the QNM contribution.

Computing QNM frequencies

There appears to be no general method for computing the frequencies of QNMs, instead a number of different approaches. In essence, one must solve the eigenvalue problem represented by the wave equation, with boundary conditions specified at

the horizon and at infinity. Exact analytical solutions to the wave equation are not to be found, except in very few spacetime backgrounds, e.g. where the potential appearing in the wave equation reduces to the Pöschl-Teller potential [47], which allows for an analytical calculation of the QNM frequencies of Schwarzschild, Reissner-Nordstrom, and slowly rotating Kerr black holes [48]. For asymptotically flat spacetimes, a number of computational approaches have been developed, such as the WKB approximation, its variant for highly-damped modes, the monodromy technique, see [35] for an introduction, and the continued fraction method [46]. This last method is quite accurate in computing the QNM complex frequencies, even of high overtones, and has been used by the authors of [49], whose results we make use of in later Chapters.

Additional ringdown epoch oscillations in GR context

It may be the case that the abovementioned QNMs classes of oscillations do not make up the entire spectrum of oscillations during the ringdown phase. For instance, the existence of a "horizon mode" (HM) has been proposed, which is characterized by properties of the Kerr horizon and is excited by gravitational perturbations during a BBH merger. These perturbations produce a set of exponentially-decaying modes with frequencies $m\,\Omega_{HM}$, where m is the azimuthal quantum number of the gravitational radiation of a co-rotating particle located on the horizon [50]. Evidence of this horizon mode oscillation, whose frequencies and decay times are generally lower/shorter than of the QNM spectrum, was found in a particular equal-mass non-spinning BBH simulation [50]. I was not convinced on the prospect of significant excitation of this mode during BBH mergers and have therefore ignored it in this work. I consider the subject of interest though and worthy of future investigation.

Higher perturbative-order QNMs in binary BH mergers are distinct sets of QNM modes that arise by considering higher-order perturbations in the metric and can also be subject to detection in near-future observations [51]. Specifically, second order QNM frequencies are found to be roughly twice the first order ones, while the excited GW amplitude is up to about 10% that of the first order, for binary BH mergers [51, 52]. Detections of second order QNMs could be used as a more stringent test of the no-hair theorem.

1.3 Numerical Relativity

Determining the dynamical evolution of a physical system governed by Einstein's equations of GR is in general not easy. Although several analytical solutions exist for relatively simple systems under the proper assumptions, this cannot be done for the evolution of more complicated systems, such as two orbiting generic-spins Kerr BHs [53, 28]. Hence the task of solving Einstein's field equations needs to be performed numerically.

After more than 4 decades from the first numerical investigations on the evolution of binary black hole systems, and especially after the breakthrough in 2005, where long enough simulations to extract physical quantities became possible [54, 55, 56], the numerical relativity (NR) community is now able to contribute accurate inspiral through merger and ringdown waveforms for a significant subset of initial configurations that will aid the detection of GWs from such systems, as well as the extraction of their key astrophysical parameters. At the same time, NR should provide the necessary waveforms for performing tests of GR on those systems which are in the so-called strong field regime and decide on the nature of the compact objects that are involved [57, 58, 59, 60].

1.3.1 3 plus 1 formulation of General Relativity

In order to perform this numerical integration we first have to recast Einstein's four-dimensional field equations into a suitable form. The 3+1 decomposition, as it is called, was first devised to study the initial value problem in GR [61, 62]. Also, to address problems related to dynamic spacetimes, as well as to provide a Hamiltonian formulation of GR with possible implications in constructing a theory of quantum gravity [63]. For a historical approach and reasoning of this formulation see also Chapter 21 in [28]. But the necessity of solving Einstein's equations numerically has triggered a more modern approach with slight modifications [64, 30].

Space parametrised by time

The basic abstraction is the slicing of the spacetime manifold into spacelike hypersurfaces, Σ_t, parametrised by a universal time variable, where the three-dimensional geometry in each hypersurface is treated upon. For this structure of hypersurfaces to be well defined one needs not only to define an appropriate metric in each hypersurface, but also to impose perpendicular infinitesimal connection vectors between adjacent slices. These can be used to infer the proper distance between any two points in space and time. More specifically, the defined spatial metric

gives the distance between any two points on a given hypersurface Σ_t,

$$g_{ij}^{(3)}(t,x,y,z)dx^i dx^j, \tag{1.16}$$

while the variation of this metric in time is also needed, that is, knowing the spatial metric in the next slice,

$$g_{ij}^{(3)}(t+dt,x,y,z)dx^i dx^j. \tag{1.17}$$

The connection vectors can be defined via the lapse of proper time between adjacent hypersurfaces, Σ_t and Σ_{t+dt}. Given any two points, (t,x^i) and $(t+dt,x'^i)$ the norm, N, is what measures the proper time lapse, and is a function of the form $N(t,x^i)$. Equipped with these quantities we can compute the proper interval between any two points in space and time. In the usual four-dimensional approach, the proper interval between two points in spacetime, (t,x^i) and $(t,x^i)+dx^m$, is

$$ds^2 = g_{bc}^{(4)}dx^b dx^c. \tag{1.18}$$

To calculate the same proper interval in the 3+1 decomposition, two infinitesimally close points in space and time can be connected with $dx^i + N^i(t,x^i)dt$, while the proper time interval is $N(t,x^i)dt$. The form of the proper interval in flat four-dimensional spacetime can be used to deduce a suitable expression. This should be the square of proper distance within a hypersurface, minus the square of proper time between the hypersurfaces where the endpoints lie,

$$ds^2 = g_{ij}^{(3)}(dx^i + N^i dt)(dx^j + N^j dt) - (N\,dt)^2. \tag{1.19}$$

1.4 The bifunctional adaptive mesh code for binary black hole evolution

The bifunctional adaptive mesh (BAM) code was initially developed by Bernd Brügmann [65, 66] focusing on binary black hole simulations. Traditionally the domain of numerical computation was taken to be a fixed, single rectangular grid. BAM uses multiple nested levels with varying grid resolution some of which are comoving with the BHs ("moving boxes" and "moving puncture" paradigm), where "puncture" refers to an analytical representation of the singularities inside the BHs [30], which is also used in numerical simulations to refer to the position of the BH. The novel concept is the monitoring of the numerical errors, and wherever

or whenever the error becomes too large, an additional finer grid is introduced. Similarly, if the error is small enough, the grids are adjusted or even removed altogether. Since the error is a dynamic quantity, the whole structure of levels of nested grids is dynamically changing. This technique is what is referred as "adaptive mess" [67, 65].

1.4.1 Arnowitt-Deser-Misner mass

In the context of GR, there is no such notion as local definition-measurement of quantities such as the 4-momentum, angular momentum or charge. For to obtain a value for any observable quantity one has to define a coordinate system that encloses the space under consideration. Defining any local coordinate system would have the issue that it is as valid as any other local coordinate system. Each would yield a different result depending for instance on the surrounding mass-energy distribution which was not considered. The solution to this is to choose a frame that is asymptotically flat. For astrophysical purposes, this takes place where the enclosing mass of a region divided by its characteristic dimension is much smaller than one.

A useful measure of the mass-energy of a system is provided by the Arnowitt-Deser-Misner (ADM) mass. It measures the total mass-energy of a gravitating, isolated system within a spatial hypersurface at infinity, that encloses the system. Let x^1, x^2, x^3 be spatial asymptotical and euclidean coordinates in a hypersurface Σ. The total energy can be defined as [19],

$$E = \frac{1}{16\pi} \lim_{r\to\infty} \int \left(\frac{\partial h_{ij}}{\partial x^i} - \frac{\partial h_{ii}}{\partial x^j} \right) N^j dA \,. \tag{1.20}$$

$$\tag{1.21}$$

The value of the ADM mass at infinity is computed by expressing it as a volume integral and integrating over the available grid [68]. The ADM mass at infinity is

$$M^{\infty}_{ADM} = -\frac{1}{2\pi} \int \nabla^2 \phi \, dV \,, \tag{1.22}$$

where ϕ is an expression of the gravitational potential of the punctures.

Another example is the Schwarzschild spacetime in Painl*evé*-Gullstrand coordinates. All the above expressions yield an ADM mass of zero in these coordinates. The reason for this is that the shift in Painl*evé*-Gullstrand coordinates does not fall off sufficiently fast. If nothing else, this result shows that we must be careful

to check that the metric satisfies the correct asymptotic conditions in the adopted coordinate frame. It also motivates a search for other mass definitions, such as the Bondi-Sachs mass [69] and the Komar mass [70], which have not been used in this work and I will therefore not discuss them here.

Other BH mass concepts used in BAM

There are other definitions of mass, used extensively in numerical simulations and specifically applied to BH systems. The so-called apparent horizon mass is analogous to the irreducible mass of a Schwarzchild BH but is calculated from the area of the apparent horizon, $\mathcal{A}_{AH}$, instead of using the event horizon,

$$M_{AH} = \sqrt{\frac{\mathcal{A}_{AH}}{16\,\pi}}. \tag{1.23}$$

For a nonspinning puncture, the ADM mass has been found to agree numerically with the apparent horizon mass. For spinning punctures, it agrees with the following expression [66],

$$M^2 = (M_{AH})^2 + \frac{S^2}{4\,(M_{AH})^2}\,, \tag{1.24}$$

which is a slight modification of the Christodoulou formula for a non-charged BH [26], where in place of the irreducible mass lies the apparent horizon mass.

1.4.2 Initial data for BBH simulations

In BAM the puncture initial data are generated by means of a pseudo-spectral elliptic solver [71], and are evolved with an algorithm based on the approach in [55]. The user supplies a range of initial separations, a range of inspiral orbits, the binary mass ratio and the BHs's angular momenta. These are used to produce a list of low-eccentricity initial data sets. The punctures are initially placed on the y-axis at a distance ratio from $(x\,,\,y\,,\,z) = (0\,,\,0\,,\,0)$ equal to the specified mass ratio. Concerning the BH masses, they are not provided by the user, but estimated indirectly, by computing their ADM masses, see [72] for details. The initial BH momenta are p_x and p_y, with $p_z = 0$ to numerical precision. The first two components are the perpendicular - to the BH separation vector - and radial - in the direction of BH separation - respectively. The p_y momentum component is what accounts for the small initial radial motion of the BHs.

In using the BAM code our main approach is to produce initial momenta

such that we get a low eccentricity inspiral of the order $10^{-2} - 10^{-3}$. This is because BH binary inspirals are expected to have low eccentricities by the time they enter the sensitivity band of ground-based detectors [73]. See Section 1.6 for status and properties of various detectors. In puncture simulations the simplest and fastest way of doing this is by estimating the momenta using the formalism of Post-Newtonian (PN) evolution [74, 75, 76, 77], or the effective one-body approach (EOB) [78, 79]. Specifically, to consider a conservative 'adiabatic' PN model without radiation reaction, that does not inspiral, and to calculate the appropriate momenta consistent with quasi-circular orbits for a given list of puncture separations [66, 80, 81].

Unlike Newtonian dynamics, eccentricity is hard to define in the two-body problem in GR, therefore approximate eccentricity estimates are performed. The method applied in BAM utilises the extracted gravitational waveform [81, 82]. If the phase and frequency of the Ψ_4 Newman-Penrose scalar is ϕ_{GW} and ω_{GW}, while ϕ_{GW}^{fit} and ω_{GW}^{fit} are fits to the EOB/PN 'non-eccentric' evolution frequency and phase over several orbital periods, the following eccentricity estimates are performed,

$$e_\phi = \frac{\phi_{GW}(t) - \phi_{GW}^{fit}(t)}{4}\,, \tag{1.25}$$

$$e_\omega = \frac{\omega_{GW}(t) - \omega_{GW}^{fit}(t)}{2\,\omega_{GW}^{fit}(t)}\,. \tag{1.26}$$

One advantage of using the extracted GWs and not the actual orbital data for eccentricity estimates, is that it is not subject to gauge dependencies, see also Section 1.4.3. To reduce the eccentricity in BBH simulations a simple procedure is to integrate the post-Newtonian equations of motion through hundreds of orbits, and use the BHs' momenta values at the desired separation, that is, where the numerical simulation starts [80]. More recently, a more efficient iterative procedure has been in use, which can quickly lower the eccentricity to values below 10^{-3} [82]. It performs a EOB/PN orbital evolution for a few steps, in each step varying the EOB/PN initial momenta, until the binary exhibits eccentricity oscillations that agree with those in a numerical relativity evolution of the same system. This process is then repeated, with the new numerical simulation having initial momenta that were adjusted from the last EOB/PN evolution to yield lower eccentricity [82].

1.4.3 Gravitational waveform extraction

Gravitational radiation is a characteristic feature of vacuum GR, that represents a physical quantity. Far from the source, where gravitational radiation is weak and can conveniently be described in the context of linearised GR [28], the GW information is contained in the term h_{ab},

$$g_{ab} = \eta_{ab} + h_{ab}\,, \quad |h_{ab}| \ll 1\,, \tag{1.27}$$

that is, a perturbation on a Minkowski spacetime background. Using the trace-reverse of h_{ab},

$$\bar{h}_{ab} \equiv h_{ab} - \frac{1}{2}\,\eta_{ab}\,h_d{}^d\,, \tag{1.28}$$

and imposing the convenient Lorentz gauge condition,

$$\nabla_a \bar{h}^{ab} = 0\,, \tag{1.29}$$

we give a physical meaning to the perturbed part of the metric, which satisfies a vacuum wave solution of Einstein's linearised equations [28, 19, 83],

$$\Box\,\bar{h}_{ab} \equiv \nabla^d \nabla_d\,\bar{h}_{ab} = 0\,. \tag{1.30}$$

The background metric, as well as the linear perturbation are not gauge-independent quantities. An infinitesimal coordinate transformation $x^{\mu'} \leftarrow x^\mu + \xi^\mu$ with $\xi^\mu \ll 1$ yields a new tensor field that describes the exact same physical situation. One solution might be to agree on a choice of gauge, but many authors have adopted the gauge-invariant Moncrief formalism [84].

We can expand the metric perturbations h_{ab} in multipoles that are classified according to their properties under parity transformation, as was done for BH perturbations in Section 1.2.3. In the same way, odd (or axial) multipoles are those that transform as $(-1)^{l+1}$ under the transformation $(\theta,\,\varphi) \to (\pi-\theta,\,\pi+\varphi)$, while even (or polar) are those multipoles that transform as $(-1)^l$. As a result, the metric perturbations in the TT gauge can be separated as [85, 86, 30],

$$h^{+,\times} = \sum_{\ell=2}^{\infty} \sum_{m=-\ell}^{\ell} \left[\left(h^{+,\times}_{\ell m}\right)^{(\mathrm{O})} + \left(h^{+,\times}_{\ell m}\right)^{(\mathrm{E})} \right]\,. \tag{1.31}$$

For spatial infinity, the two polarisations can be combined, separately for the

odd and even parity parts. For the odd part we get [30]

$$h^{+\,(\mathrm{O})} - i\,h^{\times\,(\mathrm{O})} = \frac{-i}{r}\sum_{\ell=2}^{\infty}\sqrt{\frac{(l+2)!}{(l-2)!}}\,P_{\ell m}(t,r)\,Y^{-2}_{\ell m}(\theta,\phi)\,, \tag{1.32}$$

where $Y^{-2}_{\ell m}$ are the spin $s=-2$ weighted spherical harmonics and $P_{\ell m}(t,r)$ is computed from the odd-parity, gauge-invariant Moncrief function explained in [84]. For the even part we get [30],

$$h^{+\,(\mathrm{E})} - i\,h^{\times\,(\mathrm{E})} = \frac{1}{r}\sum_{\ell=2}^{\infty}\sqrt{\frac{(l+2)!}{(l-2)!}}\,R_{\ell m}(t,r)\,Y^{-2}_{\ell m}(\theta,\phi)\,, \tag{1.33}$$

where $R_{\ell m}(t,r)$ is the even-parity, gauge-invariant Moncrief function [84]. Using the identities that spherical harmonics obey,

$$Y^{s}_{\ell m}(\pi-\theta,\,\pi+\phi) = (-1)^{\ell}\,Y^{s}_{\ell m}(\theta,\,\phi), \quad Y^{s}_{\ell m}(\theta,\,\phi) = (-1)^{m}(Y^{s}_{\ell m})^{*}(\theta,\,\phi) \tag{1.34}$$

we can separate the two polarisations of the metric perturbation and derive expressions for the radiated energy and momentum in linearized gravity similar to Eqs. 1.53-1.55, but in terms of the Moncrief functions.

Conventions within the numerical relativity community

It has been agreed to use $h_+ - ih_\times$ as the extracted quantity in NR, to describe the gravitational waveform [87]. It can be decomposed into modes, $H_{\ell m}$, using the spin weighted spherical harmonics:

$$h_+ - ih_\times = \frac{M}{r}\sum_{\ell=2}^{\infty}\sum_{m=-\ell}^{\ell} H_{\ell m}(t)\,Y^{-2}_{\ell m}(\iota,\phi)\,. \tag{1.35}$$

The expansion parameters H_{lm} are complex functions of the retarded time $t-r$ and, if we fix r to be the radius of the sphere at which we extract waves, then H_{lm} are functions of t only.

The explicit expression for the spin-s weighted spherical harmonics, Y^{-s}_{lm}, in terms of the Wigner d-functions is

$$Y^{-s}_{lm} = (-1)^{s}\sqrt{\frac{2\ell+1}{4\pi}}d^{\ell}_{m,s}(\iota)e^{im\phi}, \tag{1.36}$$

where

$$d^{\ell}_{m,s}(\iota) = \sum_{k=k_1}^{k_2} \frac{(-1)^k[(\ell+m)!(\ell-m)!(\ell+s)!(\ell-s)!]^{1/2}}{(\ell+m-k)!(\ell-s-k)!k!(k+s-m)!} \times \left(\cos\left(\frac{\iota}{2}\right)\right)^{2\ell+m-s-2k} \left(\sin\left(\frac{\iota}{2}\right)\right)^{2k+s-m}, \quad (1.37)$$

with $k_1 = \max(0, m-s)$ and $k_2 = \min(\ell+m, \ell-s)$.

For reference, I provide some of the most important spin-2 weighted spherical harmonics, that have also been used extensively in this thesis,

$$Y^{-2}_{22} = \sqrt{\frac{5}{64\pi}}(1+\cos\iota)^2\, e^{2i\phi}, \quad (1.38)$$

$$Y^{-2}_{2-2} = \sqrt{\frac{5}{64\pi}}(1-\cos\iota)^2\, e^{-2i\phi}, \quad (1.39)$$

$$Y^{-2}_{21} = \sqrt{\frac{5}{16\pi}}\sin\iota\,(1+\cos\iota)\, e^{i\phi}, \quad (1.40)$$

$$Y^{-2}_{2-1} = \sqrt{\frac{5}{16\pi}}\sin\iota\,(1-\cos\iota)\, e^{-i\phi}, \quad (1.41)$$

$$Y^{-2}_{20} = \sqrt{\frac{15}{32\pi}}\sin^2\iota, \quad (1.42)$$

$$Y^{-2}_{33} = -\sqrt{\frac{21}{2\pi}}\cos^5\frac{\iota}{2}\sin\frac{\iota}{2}\, e^{3i\phi}, \quad (1.43)$$

$$Y^{-2}_{3-3} = \sqrt{\frac{21}{2\pi}}\cos^5\frac{\iota}{2}\sin\frac{\iota}{2}\, e^{-3i\phi}, \quad (1.44)$$

$$Y^{-2}_{44} = \sqrt{\frac{63}{\pi}}\cos^6\frac{\iota}{2}\sin^2\frac{\iota}{2}\, e^{4i\phi}. \quad (1.45)$$

The Newman-Penrose formalism

A common way of dealing with problems in GR is to consider the Einstein equations in a suitably chosen, that reflects maybe the symmetry of the region, local coordinate system. Another approach is to define a set of four linearly-independent vector fields in which a set of quantities is described and then one applies the equations that they obey.

The "trace-free" part of the Riemann tensor is called the Weyl tensor,

$$C_{abcd} = R_{abcd} - \frac{1}{2}(g_{ac}R_{bd} - g_{ad}R_{bc} - g_{bc}R_{ad} + g_{bd}R_{ac}) + \frac{1}{6}(g_{ac}g_{bd} - g_{ad}g_{bc})R\,. \quad (1.46)$$

It is identical to the Riemann tensor in vacuum, satisfies the same symmetry properties as the Riemann tensor and is invariant under conformal transforma-

tions, which makes it vanish for any conformally flat metric.

The Riemann tensor has 20 independent components, 10 contained in its trace, the Ricci scalar, and the other 10 in the Weyl tensor. In the Newman-Penrose formalism the Weyl tensor's independent components are expressed in terms of five complex scalar quantities, $\Psi_0, ..., \Psi_4$. They are the representation of the Weyl tensor in a suitably chosen null tetrad [88, 12].

For numerical relativity purposes, the frame of choice is the so-called quasi-Kinnersley frame, where the Ψ_1 and Ψ_3 scalars vanish. The null tetrad of choice is composed by the real radially outgoing and ingoing vectors, l^a and k^a, a complex vector orthogonal to the previous two, m^a and its complex conjugate, $\bar{m}^a$. That is, they satisfy the following null requirements and the orthogonal conditions:

$$l \cdot l = k \cdot k = m \cdot m = \bar{m} \cdot \bar{m} = 0\,, \tag{1.47}$$

$$l \cdot m = l \cdot \bar{m} = k \cdot m = k \cdot \bar{m} = 0\,, \tag{1.48}$$

while the only non-vanishing inner products are,

$$l \cdot k = 1 \text{ and } m \cdot \bar{m} = -1\,. \tag{1.49}$$

The Weyl scalar Ψ_4 is then defined in this frame as,

$$\Psi_4 = -C_{abcd} k^a \bar{m}^b k^c \bar{m}^d\,. \tag{1.50}$$

The Weyl tensor can be very well replaced by the Riemann tensor in this definition. Note that in this treatment, only the Ψ_4 scalar is considered, which represents a measure of outgoing gravitational radiation. The Ψ_0 scalar is interpreted as ingoing gravitational waves, while Ψ_2 as longitudinal parts of the gravitational field, related to the mass and angular momentum in the spacetime [30].

Contracting the Weyl or Riemann tensor with such a tetrad yields [30],

$$\Psi_4 = \ddot{h}_+ - i\,\ddot{h}_\times\,. \tag{1.51}$$

1.4.4 Numerical calculation of Ψ_4 and physical quantities

The numerical simulations employ the 3+1 formalism which means that quantities, such as the Riemann tensor (in terms of which the Ψ_4 scalar is written) need to be broken down to their three-dimensional spatial counterpart and defined in every time-slice. This is achieved by the Gauss-Codazzi and the Mainardi equations which relate the space-time projections of the four-dimensional Riemann tensor

to the ADM variables and its three-dimensional counterpart, see [30, 66]. Defining the projection operator, $\perp$, as [62],

$$\perp S_{\alpha\beta} := (\delta^{\mu}{}_{\alpha} + \hat{n}^{\mu}\hat{n}_{\alpha})(\delta^{\nu}{}_{\beta} + \hat{n}^{\nu}\hat{n}_{\beta})S_{\mu\nu}\,,$$

where $S_{\alpha\beta}$ is some arbitrary tensor and $\hat{n}^{\alpha}$ the timelike unit normal vector of the time-slice. It is then possible to express Ψ_4 exclusively in terms of the ADM variables [66],

$$\Psi_4 = -\frac{1}{4}\left(R_{abcd}v^a v^c - 2\perp R_{\alpha bcd}\hat{n}^{\alpha}v^c + \perp R_{\alpha b\gamma d}\hat{n}^{\alpha}\hat{n}^{\gamma}\right)(u^b - iw^b)(u^d - iw^d)\,,$$

where,

$$u^i = [-y,\, x,\, 0], \quad v^i = [x,\, y,\, z]\,,$$
$$w^i = g^{ia}\epsilon_{abc}\,u^a v^b\,.$$

One then obtains the contributions of the individual modes ℓ, m by projecting Ψ_4 onto the spin weight -2 spherical harmonics $Y^{-2}_{\ell m}$,

$$A_{\ell m} = \langle Y^{-2}_{\ell m}, \Psi_4\rangle = \int_0^{2\pi}\int_0^{\pi} \Psi_4\,(Y^{-2}_{\ell m})^*\,\sin\theta d\theta d\phi\,. \tag{1.52}$$

In the BAM code the above integrand is evaluated, at every time step, on a Cartesian coordinate grid and interpolated onto a sphere of a certain grid spacing of (θ, ϕ) values and a radius of choice, called the extraction radius. The interpolation utilises fifth-order polynomials, while the subsequent integration over the sphere is performed using the fourth-order Simpson method [66].

Other quantities of interest in BBH simulations is the total amount of energy radiated, as well as the radiated momentum and angular momentum. These are computed in BAM via the Ψ_4 scalar by the following expressions, which I provide

for reference [89],

$$\frac{dE}{dt} = \lim_{r\to\infty}\left[\frac{r^2}{16\pi}\int_\Omega \left|\int_{-\infty}^{t}\Psi_4\, d\tilde{t}\right|^2 d\Omega\right], \tag{1.53}$$

$$\frac{dP_i}{dt} = -\lim_{r\to\infty}\left[\frac{r^2}{16\pi}\int_\Omega \ell_i \left|\int_{-\infty}^{t}\Psi_4\, d\tilde{t}\right|^2 d\Omega\right], \tag{1.54}$$

$$\frac{dJ_z}{dt} = -\lim_{r\to\infty}\left\{\frac{r^2}{16\pi}\mathrm{Re}\left[\int_\Omega\left(\partial_\phi\int_{-\infty}^{t}\Psi_4\, d\tilde{t}\right)\left(\int_{-\infty}^{t}\int_{-\infty}^{\hat{t}}\Psi_4^*\, d\tilde{t}\, d\hat{t}\right)d\Omega\right]\right\}, \tag{1.55}$$

where

$$\ell_i = (-\sin\theta\cos\phi,\ -\sin\theta\sin\phi,\ -\cos\phi)\,. \tag{1.56}$$

Using Eq. 1.52 we can rewrite the expression for the luminosity, Eq. 1.53, as a sum over all modes by expanding onto the spherical harmonics,

$$\frac{dE}{dt} = \lim_{r\to\infty}\left[\frac{r^2}{16\pi}\left|\int_{-\infty}^{t}\sum_{l,m}A_{\ell m}d\tilde{t}\right|^2\right], \tag{1.57}$$

which allows us to calculate the radiated luminosity from each individual mode ℓ, m. More details on how we calculate the radiated energies, as well as other physical quantities for each mode, are presented in Chapters 2 and 4.

1.4.5 Numerical calculation of the apparent horizon

As mentioned in section 1.1.2, BHs are characterized and mostly described by their horizons. It is clear then, that numerical simulations of black hole binaries would not be complete without the ability to locate BH horizons in numerically generated spacetimes. In this section I outline how the apparent horizon is probed numerically in the BAM code. The apparent horizon finder routine follows mainly the route of Gundlach [90] and Alcubierre [91]. The program calculates the apparent horizon as a height function around a center. This height function can either be given by values $h(\theta,\phi)$ at discrete values for θ and ϕ, or by expansion into spherical harmonics:

$$h(\theta,\phi) = \sqrt{4\pi}\sum_{l=0}^{l_{max}}\sum_{m=-l}^{l}a_{lm}Y_{lm}(\theta,\phi). \tag{1.58}$$

In [91] the overall factor $\sqrt{4\pi}$ is explained as then a_{00} is the average coordinate radius, a_{10} is its average displacement in the z-direction and so on. The spherical harmonics are the usual, defined as

$$Y_l^m(\theta,\phi) = \sqrt{\frac{(2l+1)(l-m)!}{4\pi(l+m)!}} P_l^m(\cos\theta) e^{im\phi}\,, \tag{1.59}$$

which in the program and in [90] are split into real and imaginary parts via

$$e^{im\phi} = \cos(m\phi) + i\sin(m\phi)\,. \tag{1.60}$$

The spherical harmonics are then written as the sine and cosine part of the exponential representation i.e. $Y = Y_c + iY_s$. Moreover, for $m = 0$ the phase vanishes and Y_l^0 will be real.

The shape of the apparent horizon is governed by the expansion of a congruence of null rays which is,

$$\Theta = \nabla_i n^i + K_{ij} n^i n^j - \mathrm{tr}K, \tag{1.61}$$

where ∇_i is the covariant derivative determined by the 3-metric γ_{ij}, n^i is the (space-like) outward normal on the horizon surface and K_{ij} is the extrinsic curvature. The AH then satisfies $\Theta = 0$. In [91] it was found that by parametrising the surface as a level set,

$$F(x^i) = 0, \tag{1.62}$$

Θ can be rewritten in terms of F and its derivatives as,

$$\Theta = \left(\gamma^{ij} - \frac{\nabla^i F\, \nabla^j F}{|\nabla F|^2}\right)\left(\frac{\nabla_i \nabla_j F}{|\nabla F|} - K_{ij}\right)\,, \tag{1.63}$$

as in this parametrisation the unit normal vector, n^i, is simply the quantity,

$$\frac{\nabla^i F}{|\nabla F|} = n^i.$$

The apparent horizon is defined by the requirement that it is the outermost 2-surface with $\Theta = 0$ everywhere on that surface. Although the AH is defined locally and is relatively easy to compute, it is often not the best tool to give insight into the evolution of a system of BHs. Unlike event horizons, they can move discontinuously from one spatial time-slice Σ_t to another, even in relatively simple binary BH simulations. Also, under a conformal transformation the AH can change location, while the EH remains invariant. However, they are very

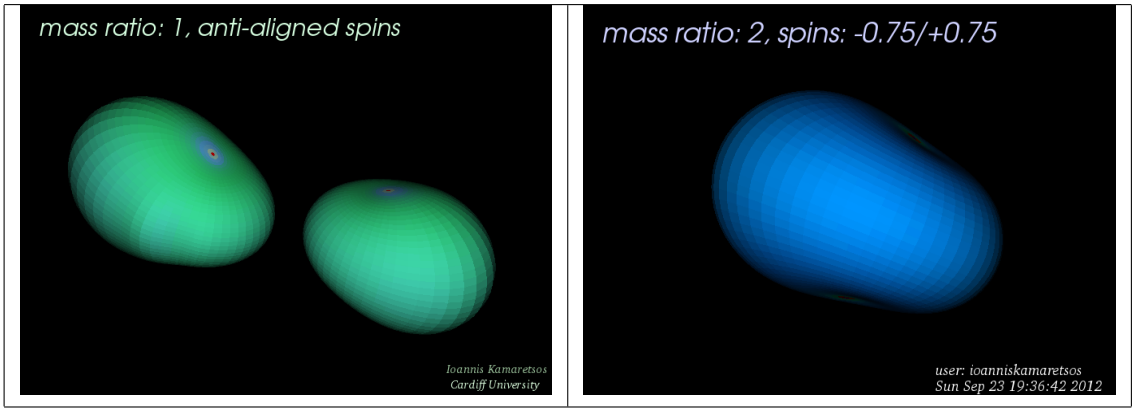

Figure 1.1: Screenshots from animations showing the evolution of apparent horizons in coalescing BH binaries [1, 2]. *Left* panel shows the last moments before the individual, yet highly non-spherical apparent horizons merge, while *right* panel depicts a highly deformed common apparent horizon, shortly after it is formed.

useful for visualization purposes and Science outreach, Fig. 1.1, see also [2, 1].

1.4.6 Convergence testing and credibility of the results

I briefly explain how to use the concepts of convergence testing for checking the accuracy of a numerical simulation. Initially, convergence tests serve as a code validation method, and help in dealing with coding errors, bugs, or even typos. The next step though involves making a statement on the trustworthiness and accuracy of the results. In cases where the problem admits an analytical solution, direct comparison would provide hints on the validity of the results. In our case, one can only rely upon the numerical solution itself.

Let us denote a choice of grid spacing by h and the numerical solution of a field at a point (t, x) on that grid, by $\Phi(t, x)$. If an analytical value is not known, assume that there exists a true value of this field and Taylor expand around it.

$$\Phi_h(t, x) = \Phi_{true}(t, x) + hE_1 + h^2 E_2 + h^3 E_3 + \mathcal{O}(h^4), \tag{1.64}$$

where the coefficients E_i are error terms that do not depend on the grid spacing.

In the so-called three-level convergence test, we use three different grid resolutions, for which we compare the numerical solutions. For the two finest resolutions the rescaled errors should be closer to each other than for the two coarsest ones. Let N be the number of gridpoints in the coarsest resolution grid, and for simplicity choose the higher ones with $2N$ and $4N$ gridpoints, respectively. Assume that the gridspacing on a grid of n gridpoints is then given by $h = 1/N$ and that the field under investigation, Φ, is second order accurate, that is the numerical error

scales with h^2,

$$\Phi_N = \Phi_o + h^2 E_1 + h^3 E_3 + \mathcal{O}(h^4), \tag{1.65}$$

Redoing the same simulation with the higher resolutions yields,

$$\begin{aligned} \Phi_{2N} &= \Phi_o + \frac{1}{4} h^2 E_1 + \frac{1}{8} h^3 E_3 + \mathcal{O}(h^4), \\ \Phi_{4N} &= \Phi_o + \frac{1}{16} h^2 E_1 + \frac{1}{64} h^3 E_3 + \mathcal{O}(h^4). \end{aligned} \tag{1.66}$$

Interestingly enough, knowing the analytical solution or the true value is not needed, which makes this procedure self-consistent. It is easy to show this, along with the convergent behaviour of Φ, by subtracting Eqs. (1.66)

$$\Phi_{2N} - \Phi_{4N} = \left(\frac{1}{2^2} - \frac{1}{4^2} \right) h^2 E_1 + \left(\frac{1}{2^3} - \frac{1}{4^3} \right) h^3 E_3 + \mathcal{O}(h^4), \tag{1.67}$$

as higher resolution pairs of solutions will have continuously smaller error coefficients. This also shows one down-side of the three-level convergence test, as it would be more prudent to have four different resolutions, so as to obtain three pairs of differences whose convergence we can test. If a clear convergence rate is observed, it is then possible to employ the Richardson extrapolation formalism to remove the error term of the next order, therefore producing a yet more accurate estimate of the true result, and to also calculate an uncertainty estimate [92].

1.5 Promising sources of gravitational radiation

1.5.1 Compact Binary Coalescence

The inspiral and coalescence of binary compact objects, such as BH-BH, neutron star-neutron star (NS-NS), BH-NS, and white dwarf (WD) binaries are some of the most promising candidate events for GW detection in current and near-future ground-based interferometers. See also Section 1.6.

Supermassive black-hole binaries

The existence of BHs with a mass higher than $10^5 M_\odot$ is strongly implied by the mass - velocity dispersion in the galactic bulge of low-luminosity galaxies, as well as in a number of galaxies which contain active galactic nuclei [93, 94]. Astronomical observations in the infrared, X-ray and gamma-ray part of the spectrum have given ample evidence of Supermassive black holes (SMBHs) dwelling at the centers of

most galaxies. They range widely in mass, from $10^5 M_\odot$ to about $10^9 M_\odot$, yet their mass distribution at various epochs of the Universe is hard to determine from EM observations alone [95, 96, 97, 98, 99]. Gravitational-wave observations will provide additional clues on their spatial and mass distribution. Considering that in the earlier epochs of the universe, the formation and evolution of galaxies were tightly correlated with their central massive BH's evolution [100], will help discriminate among the different scenarios of galaxy formation and growth.

Several studies have been realized in the field of predicting the coalescence rates of SMBHs at various stages of the Universe [101, 102, 103, 104, 105, 106, 107, 108], yet the actual rates remain highly uncertain.

Intermediate mass black-hole compact binaries

The existence of intermediate-mass black holes (IMBHs) ($\sim$200 - $\sim 10^5 M_\odot$) remains to this date ambiguous, as is their mass distribution. Colliding globular clusters in closely interacting galaxies is a mechanism thought to obtain a compact binary IMBH system [109, 110]. In younger galaxies, it is possible that a binary IMBH is formed inside young dense stellar clusters, especially when the fraction of binary stars is sufficiently high [111].

Estimates of IMBH-IMBH coalescence rates can be found in [7, 111, 110, 112]. A relatively optimistic rate is $R_{opt} = 0.007$ Gyr^{-1} per globular cluster (GC^{-1}), where it is assumed that 10% of star clusters are sufficiently massive and have a sufficient stellar binary fraction to form an IMBH-IMBH binary once in their lifetime, taken at 13.8 Gyr. The maximum possible rate would come from assuming that all of the star clusters satisfied the above conditions. The corresponding rate value would then be $R_{max} = 0.07$ GC^{-1} Gyr^{-1}. If the number of relatively luminous galaxies within a distance of 1 Gpc is approximately 5.3×10^7, [113] and the number of young dense stellar clusters per such galaxy is of the order of 100, then the aforementioned optimistic estimate gives an astrophysical rate of 0.037 events per year, while the maximum rate would be 0.37 events per year.

Another IMBH formation mechanism which has not been taken into account in the above estimate is the prospect of mergers of stellar mass BHs inside globular clusters which can aid the growth of IMBHs in this type of environment. Significant populations of non-escaping stellar BHs can exist within globular clusters which can mass-segregate to the core of the cluster [114].

Stellar mass black hole binaries

BHs in the $\sim$5 to $\sim$20 $M_\odot$ mass range are thought to exist throughout most of the galaxies, being the final product of stars that had a mass of more than $\sim$15 $M_\odot$ in the beginning of their main sequence. The following mechanisms are considered plausible for the existence of binaries. The first scenario is the evolution of an isolated binary. Lacking observations of coalescing BH binaries makes it quite hard to estimate the actual coalescence rate of these sources, but a plausible event rate is anywhere between 0.01 and 30 per Myr per Milky Way-equivalent galaxy [115]. The second scenario, involves dynamical interactions in dense stellar environments (e.g. globular clusters and dense clusters in the bulges of galaxies) that tighten the black-hole binary before coalescence is driven by radiation reaction. An interesting case of this type is argued in [116], where stellar-mass black holes residing close to supermassive BHs in galactic nuclei are thought to aggregate into steep density cusps. Resulting parabolic and hyperbolic encounters cause loss of energy via GWs and eventually lead to a significant number of tight BH-BH binaries. The BH binaries that form in this manner should have eccentricities as high as $\sim$0.9 as they enter the LIGO band, hence making them distinguishable. Depending on the initial stellar mass function of stars in galactic nuclei, as well as the actual detection distance of Advanced LIGO, the expected observation rate of such events could be between $\sim$1 to $\sim 10^3$ per year in Advanced LIGO. The most probable astrophysical rates, as well as expected observation rates in various detectors are summarised in Table 1.1.

The recent identification of two stellar mass BH X-ray binaries with BH mass around $10-20\,M_\odot$ inside the M22 globular cluster [114] shows that populations of stellar mass BHs do exist within globular clusters, that is, ejection of black holes is not as efficient as predicted by most models [117]. It is also argued in [114] that M22 may contain a total population of $\sim 5-100$ stellar mass black holes. This raises the possibility of the formation of stellar mass BH binaries that may have been segregated near the center of the cluster. This follows earlier evidence, of a $\sim 10\,M_\odot$ BH accreting matter in RZ 2109, a globular cluster in elliptical galaxy NGC 4472 [118].

Intermediate and Extreme mass ratio inspirals

It is quite plausible that stellar mass compact objects could be captured around intermediate-mass or supermassive BHs in dense cluster environments or in the centres of galaxies [119], constituting what is termed an intermediate, or extreme

	NS-NS	NS-BH	BBH (field)	BBH (in clusters)
$\mathcal{R}_{\rm MW}$, yr^{-1}	10^{-6}-5×10^{-4}	$\leq 10^{-7}$-10^{-4}	$\leq 10^{-7}$-10^{-5}	$\sim 10^{-6}$-10^{-5}
$\mathcal{D}_{\rm iLIGO}$	20 Mpc	43 Mpc	100 Mpc	100 Mpc
$\mathcal{R}_{\rm iLIGO}$, yr^{-1}	3×10^{-4} - 0.3	$\leq 4\times10^{-4}$ - 0.6	$\leq 4\times10^{-3}$ - 0.6	$\sim$ 0.04 - 0.6
$\mathcal{D}_{\rm aLIGO}$	300 Mpc	650 Mpc	$z\simeq 0.4$	$z\simeq 0.4$
$\mathcal{R}_{\rm aLIGO}$, yr^{-1}	1 - $\sim$800?	$\leq$ 1 - $\sim$1500?	$\leq$ 30 - $\sim$4000?	$\leq$ 300 - $\sim$4000?
$\mathcal{D}_{\rm ET}$	$z\simeq 2.9$	$z\simeq 3.5$	$z\simeq 4$	$z\simeq 10$
$\mathcal{R}_{\rm ET}$, yr^{-1}	$\geq 10^4$?	$\leq$ 10? - $\geq 10^4$?	$\leq$ 30 - $\geq 10^5$?	$\leq$ 300 - $\geq 10^5$?

Table 1.1: Probable upper and lower bounds of stellar-mass compact binary coalescence event rates in Milky Way (MW), as well as expected observation rates, $\mathcal{R}$, in various detectors. Second and third rows give the distance reach, $\mathcal{D}$, and expected observation rates for each type of source in a iLIGO-like detector. The following rows show the corresponding values for $\mathcal{R}$ and $\mathcal{D}$ in the 2^{nd} and 3^{rd} generation detectors, Advanced LIGO and Einstein Telescope. For a comprehensive list of proposed mechanisms in deriving astrophysical rates see [7].

mass ratio binary, depending on whether the ratio of masses is between 10^2-10^4, or higher than 10^4 respectively. Both types could serve as excellent sources in ground- and space-based detectors.

However, no satisfactory solution exists to date on the problem of intermediate mass ratio inspirals, that is, of accurately extracting a waveform at a separation between a few tens to a few gravitational radii. It could be treated in terms of a hybrid scheme of post-Newtonian approximations and perturbation theory [120]. Concerning the detection rates of such sources, the upper limit is considered to be around 10 events per year for Advanced LIGO [120].

On the other hand, the extreme mass ratio case has been tackled with more success by a careful treatment of radiation reaction and BH perturbation theory [121]. The corresponding event rate is estimated to be of the order of a few $\times 10^2$ Gyr^{-1} per massive black hole [122].

Compact binaries composed of black holes, neutron stars and white dwarfs

A few pulsars which are members of a binary NS system have been discovered. This small sample allows to extrapolate to obtain an estimate of the actual number of such systems. A second method is based on population-synthesis codes, in which some of the unknown model parameters are constrained by observations and others by theoretical considerations. Observations of similar types of objects, such as low-, intermediate- and high-mass X-ray binaries provide indirect evidence on the correctness of the assumptions. Unfortunately, the only type of compact

binary source for which actual observational constraints can be placed, is NS/NS systems since some of those binaries involve at least one pulsar member, allowing direct observation [123, 124].

1.5.2 Continuous waves

Continuous gravitational waves have a fairly monotonous and well-defined frequency, as well as amplitude and can be produced by a variety of sources. It can actually be one of the previous categories, for instance a binary system of compact objects orbiting each other far from their coalescence epoch, or a neutron star or white dwarf swiftly rotating about its axis with an irregularity on it. This general class of sources does not involve catastrophic events and are comparatively weak gravitational waves since they evolve over longer periods of time.

1.5.3 Burst-like gravitational waves

It is believed that many short-lived EM transient events of cataclysmic nature, such as Supernovae, Gamma-Ray Bursts (GRBs) and X-Ray Flashes (XRFs) produce an accompanying (short-lived) gravitational-wave burst, and that these GW sources can be concurrently observed through different 'messengers', such as gamma rays, X-rays, optical, radio, and/or neutrino emission [125, 126].

Core-collapse supernovae

It is believed that core-collapse Supernovae, with their multitude of asymmetric and violent processes, will have a significant gravitational-wave signature [6, 127]. Modelling these processes and the associated GWBs is a difficult task, but will give insight into the actual mechanisms that are excited in Supernova explosions. Some models do not even exhibit an explosion, most models though agree that a significant amount of energy, of the order of $10^{-7} M_{\odot} c^2$, is typically radiated in GWs [127]. There is a high uncertainty on the exact form of the signal and its dependence on initial conditions, but most models predict a GWB duration of about 100 msec to 2-3 secs, while the GW energy is mostly emitted in the 100 Hz to 800 Hz frequency range. For more details on the generation and detection of GWs from core-collapse Supernovae, see Chapter 5.

Gamma-Ray Bursts and other EM transients

GRBs are most likely associated with some kind of catastrophic event that involves stellar-mass objects. They are classified as 'short-hard' and 'long-soft' according to the duration and frequency range of the prompt gamma-ray outburst. The two types are thought to originate from different cataclysmic processes taking place in cosmological distances [128]. Long GRBs are considered to be emitted from 'anomalous' type Ib/c core-collapse Supernovae [129]. Short GRBs are believed to be produced during the merger of either two neutron stars or a neutron star and a stellar mass black hole [128, 130].

Transients in X-rays could occur in low/high-mass X-ray binary systems or could be cosmological in origin and thus of entirely different nature. The latter are termed XRFs and are the analogue of long GRBs, but with lower luminosities and a softer spectrum [131]. It is unclear whether they are associated with Supernovae, or they are intrinsically weak events or typical long GRBs viewed off-axis.

A low/high-mass X-ray binary (L/H MXB) is a binary system whose more/less massive component is either a black hole or a neutron star. The donor, is either a main sequence star, an evolved red giant star, or a supergiant that fills its Roche lobe and therefore transfers mass to the compact member. Several persistently powerful, galactic LMXB X-ray sources, such as Sco X-1, could be detectable in advanced LIGO [132], as the accreting matter induces oscillations and/or non-axisymmetric deformations in the compact object. The author of this thesis has performed the only known GWB search from a set of galactic LMXBs with data acquired from initial LIGO during the S5 Science Run. It is not included in this thesis, but as a separate LIGO technical document.

1.5.4 Other types of sources

Parabolic encounters of compact objects

An additional possibility of GW bursts exists, the kind that are produced during unbound, or loosely bound orbits between compact objects. They are very well approximated by parabolic trajectories and can involve any type and mass range of compact objects.

In [133] they study encounters of stellar mass BHs inside globular clusters and provide an estimate of at least one detection per year for Advanced LIGO for reasonably optimistic cases. While not very promising in terms of estimating large number of parameters of the involving components, the systematic detection of GWs from these encounters could constrain the stellar BH mass function in dense

clusters, as well as test assumptions on dense cluster models, such as the velocity distribution and mass segregation.

Inspiraling stellar mass compact objects in highly eccentric orbits around massive BHs in the centres of galaxies is believed to be commonplace and could generate detectable bursts of gravitational radiation at each periapsis passage. The detection rate of such sources could be at least one per year in a LISA-like spaced-based detector [134].

A special class of close encounters are head-on collisions of compact objects. They are thought though to be more infrequent than parabolic encounters, while their GW emission should in general be less powerful [133].

Primordial stochastic gravitational waves and cosmic strings

Stochastic gravitational radiation are relic GWs from the early evolution of the universe that arise from a large number of random, independent events that combine to create a continuous and roughly isotropic gravitational wave background. One of the most exciting recent predictions is the GW signature of early-Universe cosmic strings. Networks of unstable cosmic strings could produce powerful GW bursts that could be detected by interferometric GW detectors such as LIGO, Virgo, and LISA [135]. What is more exciting is that these GW bursts might be accompanied by EM transients in all parts of the spectrum [136].

Astrophysical gravitational wave background

In addition to the cosmological background, an astrophysical contribution may exist as a result of the superposition of a large number of unresolved sources, consisting of any of the above-mentioned types [137].

1.6 Global effort in detecting gravitational waves

Gravitational waves (GWs) are predicted to exist within the theory of GR, but despite numerous efforts of detection in the last four decades, they have not been observed directly. Yet, very few physicists doubt their existence, as GR has been very successful in explaining gravity; locally, in the solar system, in astronomy and astrophysics, and in the evolution of the entire Universe starting with the Big Bang. Most importantly, there exists considerable indirect evidence of GWs in measurements of the periapsis precession and orbital decay in compact NS-NS, NS-WD and WD-WD binary systems [138, 139, 140, 141].

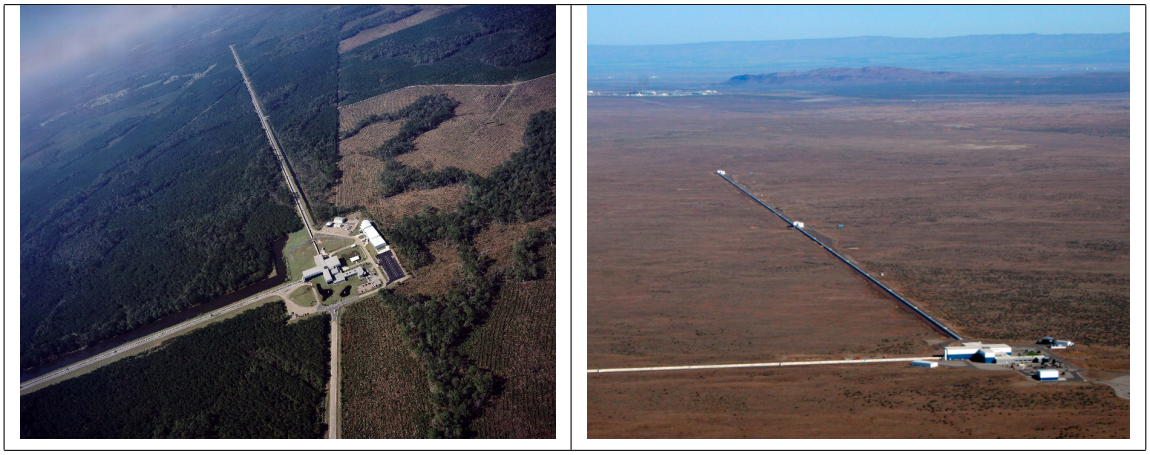

Figure 1.2: Aerial views of the LIGO detectors, which are spaced almost 10 msec of light travel time. Left panel is a picture of the Livingston detector, while right panel shows the Hanford detector.

1.6.1 Ground-based interferometric detectors

The LIGO Science Runs

The initial LIGO (iLIGO) project in U.S. comprised basically of two 4 km arm detectors, one in Hanford, Washington (LHO or H1) and one in Livingston, Louisiana (LLO or L1). A half length, 2 km, interferometer was also contained inside the same vacuum system at Hanford (also known as H2). A smaller scale detector, the Caltech 40-meter prototype interferometer, was one of the first interferometric detectors, but has served mostly as a test bed for new optical configurations and control systems.

The first Science Run, S1, took place in 2002, followed by Science Runs, S2, S3 and S4 in the years 2003 to 2005. Starting in November 2005, the observatories completed their definitive Science Run, S5 in the initial LIGO configuration in October 2007, Table 1.2. Taking into account duty cycle, maintenance, and tuning breaks more than a year of total coincident data was collected. An additional data run commenced in 2009, with the so-called Enhanced LIGO detectors, reaching completion in 2010. There are various analysis groups within the LIGO Scientific Collaboration undertaking the search for chirp signals from binary inspirals, periodic signals from neutron stars, burst signals from Supernovae Chapter 5, Gamma Ray Bursts and X-Ray Flashes, as well as from a probable stochastic background. The data analysis pipelines utilize a variety of sophisticated signal-extraction techniques: matched filtering using templates, time-frequency analysis and correlations between the datastreams, always taking into account the auxiliary and environmental data channels. The examination of the available data is

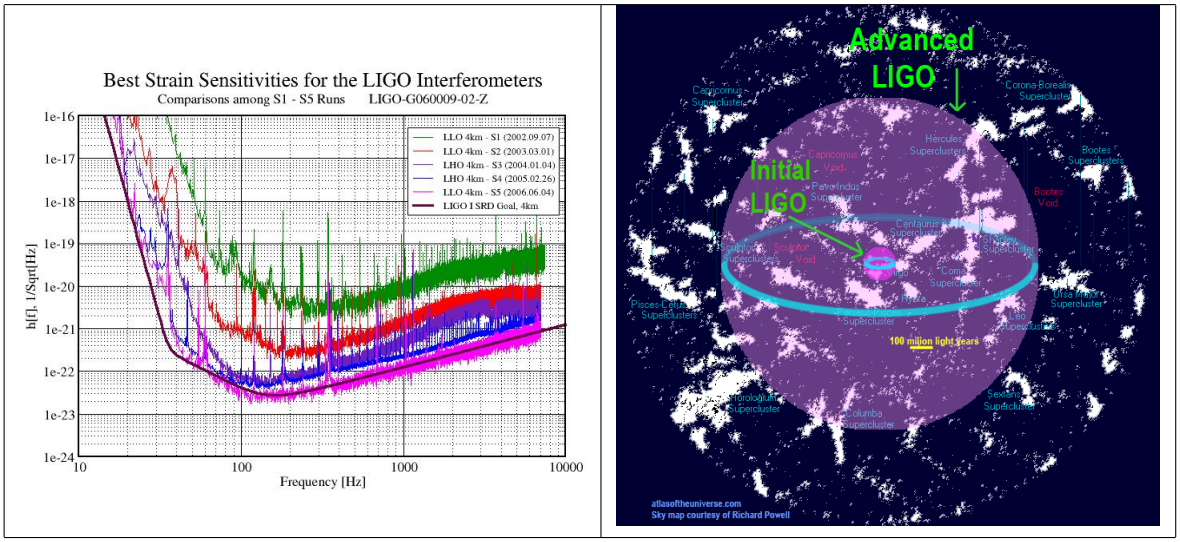

Figure 1.3: Left panel depicts the continuously improving sensitivity of the iLIGO detectors throughout the various Science Runs. The design sensitivity was achieved in 2007. Right panel shows the dramatic increase in detection horizon and volume from iLIGO to aLIGO.

ongoing, but thus far no plausible GW event has been discovered, instead they have been used to establish tighter upper limits on the gravitational-wave flux from the abovementioned types of sources [142, 143, 144, 145, 146].

Advanced LIGO

Advanced LIGO (aLIGO) is a major hardware and software upgrade of all three initial LIGO interferometers, involving enhancements in the detectors' readout, control systems, optical cavities and seismic isolation components. They should commence taking science-worthy data around 2015-2016. Innovative technologies include "light-squeezing" [147], where quantum-mechanically squeezed laser light is injected into the output port to gain sensitivity in a broad frequency range. The upgrade will improve sensitivity and hence the horizon of detection by almost an order of magnitude compared to iLIGO, thus reaching to almost a Gpc for stellar-mass BH binaries, Table 1.1, see also Fig. 1.3. Depending on the actual, near-Universe rates of various GW sources this should make GW detections anything from being achievable, to a common occurrence. Results on detection and astrophysical science we can achieve with Advanced LIGO, for BBH systems at various distances and configurations, are presented in Chapters 2 and 3.

GEO 600 and GEO-HF

GEO 600 is a 600 m arm detector situated near Hannover, Germany. It took science-worthy data during S1 and S3. Although its sensitivity was $\sim$ 2 orders of magnitude worse than the LIGO detectors, it had a very high duty cycle of $\sim$ 98%. Following upgrades, GEO 600 operated throughout the whole of S4. It did not join S5 at the start of the LIGO run, but from 21 January 2006 was in a night-and-weekend data-taking mode, shifting into full-time data taking mode during the period 1 May to 16 October 2006. GEO 600 continued operating in Astrowatch mode between November 2007 and July 2009 ('A5' and 'A6' runs) immediately after which upgrades began, see also Table 1.2. These focus of the upgrades is on increasing the sensitivity at frequencies greater than a few hundred Hz, a project by the name GEO-HF. Since 2010 GEO has been implementing squeezed-light techniques which have improved its sensitivity for a broad range of frequencies, especially above 700 Hz [147].

Virgo

Virgo is a 3 km arm detector in Cascina, Italy, that joined the LIGO and GEO 600 S5 run with 10 Weekend Science Runs (WSRs) starting in late 2006 until March 2007. Full-time data taking, under the title of Virgo Science Run 1 (VSR1), began on 18 May 2007, and concluded at the end of S5 on October 1st 2007, Table 1.2, thus making possible a joint LIGO-Virgo run during this period. During VSR1, the science-mode duty factor was around 81% and by the end of the run maximum neutron star binary inspiral range was frequently up to about 4.5 Mpc. Another joint data collection periods took place, with the LIGO S6/VSR2 and VSR3 Virgo Science Runs, Table 1.2. There is also provision to enhance this detector, under the name AdvVirgo, which will apply similar upgrades to those for aLIGO and over a similar timescale.

Japanese interferometric detectors

Tama 300 was the first interferometric detector, in 2001, that commenced taking data with sufficient sensitivity and stability that would enable a potential detection of gravitational waves from the galactic centre, while a confident detection of a 1.4 $M_{\odot}$ - 1.4 $M_{\odot}$ binary neutron star coalescence within 10 kpc was possible [148]. TAMA 300 operated in coincidence with the LIGO and GEO 600 detectors during LIGO S1, S2 and S3. Since then, there have not been any more coincident runs, as the focus has shifted to the Cryogenic Laser Interferometer Observatory (CLIO)

Science Run	Start Date	End Date
LIGO - S5	4 November 2005	1 October 2007
Virgo - VSR1	18 May 2007	1 October 2007
GEO 600 - S5	1 May 2006	16 October 2006
H2 & GEO - A5	early 2008	early 2009
GEO 600 - A5	November 2007	July 2009
LIGO - S6	7 July 2009	20 October 2010
Virgo - VSR2	7 July 2009	11 January 2010
Virgo - VSR3	11 August 2010	20 October 2010
GEO-HF - A6	early 2010	late 2011

Table 1.2: Timeline of LIGO, Virgo and GEO epochs of science-worthy data. 'A5' and 'A6' denote the so-called astrowatch periods.

prototype detector, which serves as a testbed for the second-generation Japanese detector called Large-scale Cryogenic Gravitational-Wave Telescope (LCGT), recently renamed KAGRA [149].

KAGRA is a 3-km arm instrument currently under construction in the Kamioka mine and planned to perform coincident observations with the rest of the second generation detectors around the globe, from around 2018. There are two main distinct features in the KAGRA configuration not to be encountered in the rest of the second generation detectors. Firstly, the entire detector is constructed underground, where seismic noise and gravity gradient noise is lower compared to the surface. This allows for improved sensitivity in the $\sim 5 - 50$ Hz frequency range. Secondly, the cryogenic operation of the interferometer, which involves cooling of all test masses down to 20 K, significantly reduces mirror and suspension thermal noise, as well as the thermal lensing effect, which is a very big issue for the room-temperature advanced detectors. Characteristically, increasing the mirrors' temperature from 20 K to 23 K the inspiral range of a simulated neutron-star binary with the full-power operation decreases from 250 Mpc to 230 Mpc [149].

Einstein Telescope

Design studies are under way concerning a third-generation, underground GW-detector called the Einstein GW Telescope (ET) [150]. This is a European Commission funded study with working groups looking into various aspects of the design including the site location and characteristics, suspensions technologies; detector topology and geometry (e.g. an equilateral triangle configuration); the

science benefit from such an observatory [151, 152]. It is quite possible that some of the knowledge gained from building the KAGRA detector will be proved useful in dealing with technical aspects of the ET installation and operation. However, this project goes far beyond the advanced detector network and concerns detector sensitivities a factor of ten better in amplitude, featuring a lowest point at approximately $2{\cdot}10^{-25}$ $\mathrm{Hz}^{-1/2}$, while operating at sensitivities below 10^{-23} $\mathrm{Hz}^{-1/2}$ in the range $\sim$3 Hz to 10 kHz [153]. Three slightly different configurations of the detector are planned whose potential sensitivity curves are presented in [154]. The proposed topology is triangular, in which each arm-cavity is used twice to form three coplanar detectors with a 60-degree opening angle; this is approximately equivalent to three individual Michelson interferometers, rotated with respect to one another, and not only provides the possibility of generating a null-stream, but also of measuring both GW polarisations [155]. Parameter estimation results for stellar-mass and IMBH BBH systems in ET are described in Chapters 2, 3 and 4.

Indian initiative

The operation of an advanced interferometric gravitational-wave detector is planned in India, called LIGO-India, under an international collaboration with LIGO [156]. It is a 4-km arm instrument for which parts from the Advanced LIGO Hanford detector will be supplied. Regular operation and science runs should start from around 2019. Apart from the obvious benefit of increasing the total coverage time of the global detector network, it offers a very significant improvement in establishing the sky location of GW sources, and in the case of a binary inspiral, a better estimation of the luminosity distance, orbital inclination and the system's mass parameters [157, 158].

1.6.2 Space-based detectors

Laser Interferometer Space Antenna

One of the biggest questions in modern astronomy is the creation of galaxies and the role of their central black holes in their formation and evolution. GWs from such inspiraling and merging systems can provide crucial information to tackle these questions [159], see also Chapter 2. To probe more massive systems, such as supermassive BH binaries in the centers of galaxies ($\mathrm{M}_{tot} \gtrsim 10^6 M_\odot$), requires a spaced-based detector, which will have a much longer baseline and will not be affected by Earth's seismic and gravity gradient noise at low frequencies. The once planned, NASA-ESA joint effort, LISA (Laser Interferometer Space Antenna)

detector would be sensitive to waves in the frequency band between 0.05 mHz to 100 mHz. It would measure GWs via laser interferometry, to monitor the fluctuations in the relative distances between three spacecraft, arranged in an equilateral triangle with $5 \cdot 10^6$ km arms, and placed in an Earth-like heliocentric orbit, trailing the Earth at 20°. Such a mission could even possibly discover cosmological sources originating in the very early phase of the Big Bang, and speculative astrophysical objects, such as cosmic strings [136, 135] as well as low-frequency ($\simeq 5$ mHz) and low-mass ($\simeq 5\, M_\odot$) nearby sources such as white dwarf binaries [160]. The Galactic population of white dwarf binaries and AM CVn (white dwarf system with white dwarf donor or helium-core star donor) objects will actually be the dominant source in frequencies above 0.1 mHz and below $\simeq 3$ mHz, where these binaries will produce a confusion-limited signal [4, 160], see also beginning of Chapter 3.

Next Gravitational Wave Observatory

After the probable cancellation of LISA was announced, ESA started revising the mission concept and initiated a European-led LISA variant. The Next Gravitational Wave Observatory (NGO), also known as European LISA (eLISA) might be the first mission to survey the low-frequency GW band, from 0.1 mHz to 1 Hz, probing all types of objects that would be detectable by LISA [161]. It is very similar to LISA in that it consists of three spacecraft orbiting the Sun in a triangular configuration, but the arm-length is 10^6 km, while there are only two measurement arms and not three; one of the three spacecraft serves as the "mother" and defines the apex of a "V", while the other two, simpler spacecraft, are positioned at the ends of the V-shaped formation. It will be less sensitive than LISA with the lowest point of its sensitivity curve reaching about an order of magnitude higher than LISA, see Fig. 3.1 of Chapter 3. NGO will probably be launched later than 2022.

1.6.3 Other ongoing efforts in detecting gravitational waves

Resonant bar detectors

The earliest attempts to detect GWs involved resonant bar detectors, with Joseph Weber beginning their development in the 1960s [162, 163]. Since then, several institutions around the globe have been operating their own bar detectors, such as ALLEGRO in the U.S., AURIGA in Italy and NIOBE in Australia. They are typically large metal cylinders cooled to a few °K and supposed to be sensitive to

GWs in narrow frequency bands, typically of a few tens of Hz around the resonant frequency of the bar, which is in the order of kHz [164]. Some recent resonant detectors, such as GRAVITON (Brazil) and MiniGRAIL (Netherlands) have a spherical shape, providing omnidirectional sensitivity [165].

1.7 Parameter estimation from perturbed BHs

1.7.1 Fisher matrix analysis

Once we have a high level of confidence that a certain data stream contains a signal, a rough estimate of its parameter values can be obtained by the template parameters that yielded the maximum SNR. However, a long-established method used to provide oneself with the parameters' error bounds is through the Fisher matrix formalism.

The signal can be viewed as a finite or infinite-dimensional quantity in a n-dimensional space of parameters characterising a type of source [166]. Of course, any other waveform that is characterised by the same set of parameters, or a subset of them, can be represented in this same space. The noise can be viewed as a quantity with number of elements equal to the number of samples of the given detector output, that for each sample displaces the signal out of the original signal space [166]. We can define the power spectral density weighted scalar product of two waveforms, specifically the partial derivatives with respect to the parameters, p_a and p_b, of the Fourier transformed waveforms: $\tilde{h}_{,p_a}$ [167, 166, 168],

$$g_{ab} = \langle h_{,p_a}, h_{,p_b} \rangle = \int_0^\infty \frac{2\ df}{S_h(f)} \left[\tilde{h}_{,p_a} \tilde{h}^*_{,p_b} + \tilde{h}^*_{,p_a} \tilde{h}_{,p_b} \right]. \tag{1.68}$$

The scaled up by the square of the SNR (ρ^2), product is called the Fisher matrix. Assuming the signal is buried in background noise that is stationary and gaussian, one can apply the Fisher matrix formalism to get a proper statistical estimate of the influence of the noise [166]. The way we do it is the following: If the signals' true parameters are denoted by p^a and the measured parameters (plus the random noise effects) are denoted p'^a, then we can get the probability density function of the deviation, p^a - $p'^a = \Delta p^a$, denoting the inverse of the Fisher matrix, which is called the covariance matrix, by C_{ab} [167, 166],

$$P(\Delta p^a) d^n \Delta p = \frac{d^n \Delta p}{\sqrt{(2\pi)^n C}} e^{-\frac{1}{2} C^{-1}_{ab} \Delta p^a \Delta p^b} \tag{1.69}$$

where C is the determinant of the covariance matrix. As I have mentioned earlier, the Fisher matrix, Γ_{ab}, is equal to C_{ab}^{-1} which is equal to $\rho^2 \langle h_{,p_a}, h_{,p_b} \rangle$ usually denoted $\rho^2 g_{ab}$. Thus the above expression can be written,

$$P(\Delta p^a) d^n \Delta p = \frac{\rho^n \sqrt{g} d^n \Delta p}{(2\pi)^{n/2}} e^{-\frac{1}{2}\rho^2 g_{ab} \Delta p^a \Delta p^b} \tag{1.70}$$

where g is the determinant of g_{ab}. Therefore, at a given SNR, the probability of finding the measured parameters inside a volume V_p of the parameter space, that is, the parameter value error 'box', is just the integral of $P(\Delta p^a) d^n \Delta p$ over that volume [166].

Caveats of the Fisher matrix analysis

Apart from the obvious disadvantage that the Fisher matrix can be singular or ill-conditioned, one main caveat is that the SNR of an event has to be sufficiently high for this method to be internally consistent [169, 170]. If the opposite is true, this formalism may give an underestimate of the errors. This is explained in detail in [169].

Another disadvantage is limited control over any prior information on the system. One way it could be achieved though, is by imposing some restriction on Δp^a of Eq. 1.69. Equivalently, by multiplying Eq. 1.69 by some suitable exponential function of the parameters.

1.7.2 Bayesian inference

The origins of the Bayesian approach to probability theory date back over three hundred years, to mathematical physicists, such as Bayes, Laplace, and the Bernoulli brothers, and was developed as yet another tool for reasoning in situations where it is not possible to argue with certainty. In the past few decades Bayesian inference techniques have been applied with success in many areas in astronomy. They constitute, what is believed, a very sensible and accurate way of estimating the parameters. It has not been used in searching for signals [171], although there has been a proposed method on verifying detection for inspiral signals [172]. In this approach, the notion of probability should be intuitively thought of as representing a degree of belief, a state of knowledge, about something given the available information.

The mathematical description of the term probability is restricted by demand-

ing to be a real number between zero and one, as well as satisfy:

$$Pr(X|I) + Pr(\bar{X}|I) = 1\,, \tag{1.71}$$

$$Pr(X, Y|I) = Pr(X|Y, I) \times Pr(Y|I)\,, \tag{1.72}$$

where X and Y are the propositions made, $\bar{X}$ denotes that X is false, comma is the conjuction 'and', while the vertical bar means that anything to the right of it is taken as being true. This is the same as in conventional statistics, with the exception that the notion of probability is not confined to being related to frequency distributions of certain propositions.

The most important for our purposes relationships, can be derived from Eqs. 1.72, the first of which is called *Bayes' theorem*,

$$Pr(X|Y, I) = \frac{Pr(Y|X, I) \times Pr(X|I)}{Pr(Y|I)}\,, \tag{1.73}$$

$$Pr(X|I) = Pr(X, Y|I) + Pr(X, \bar{Y}|I)\,. \tag{1.74}$$

They are powerful due to the fact that they 'flip' the propositions around the conditioning symbol, that is $Pr(X|Y, I)$ is related to $Pr(Y|X, I)$.

For our purposes, I change the notation of joint probability from Pr to P, which now denotes a probability density function. Also, in a N-dimensional parameter space, I denote the parameters by $\vec{\theta} = (\theta_1, \theta_2, .. \theta_N)$ and rearrange the terms in the Bayes theorem Eq. (1.73) as [171],

$$\begin{gathered} P(d\,|\,\vec{\theta}, I) \times P(\vec{\theta}\,|\,I) = P(d\,|\,I) \times P(\vec{\theta}\,|\,d, I)\,, \\ Likelihood \times Prior\ information = Evidence \times Posterior\ estimate\,, \\ \mathcal{L}(\vec{\theta}) \;\times\; \pi(\vec{\theta})\, d\vec{\theta} \;=\; Z \;\times\; p(\vec{\theta})\, d\vec{\theta}\,, \end{gathered} \tag{1.75}$$

where d denotes the acquired data which modulates our prior belief into posterior distributions.

When describing these quantities in terms of certain hypotheses, I use a slightly different notation. $P(H_j|d, I)$ denotes the *posterior probability* of model, or hypothesis H_j given the data, $\pi(H_j|I)$ is the *prior probability* of hypothesis H_j, while $P(d|H_j, I)$ is the *marginal likelihood*, or more commonly *evidence*, for model H_j, and can be written as

$$P(d|H_j, I) = L(H_j) = \int\int ... \int \pi(\vec{\theta}|H_j, I)\, p(d|\vec{\theta}, H_j, I)\, d\vec{\theta}\,, \tag{1.76}$$

where $\pi(\vec{\theta}|H_j, I)$ is the prior probability density for the parameters $\vec{\theta}$ given the model H_j and $p(d|\vec{\theta}, H_j, I)$ is the *likelihood*, which provides a measure of the fit of the data to the model. Both, the prior and posterior probability densities are normalised to 1, that is,

$$\int\int ... \int \pi(\vec{\theta}|H_j, I)\, d\vec{\theta} \;=\; \int\int ... \int P(\vec{\theta}\,|\,d, I)\, d\vec{\theta} = 1\,, \tag{1.77}$$

For the noise model in this case, there are no free parameters since the noise profile is known, and the evidence is given for Gaussian noise by,

$$P(d|H_{\rm N}, I) = \prod_{k=1}^{N} \left(2\pi\sigma_k^2\right)^{-1} \exp\left(-\frac{\left|\tilde{d}_k\right|^2}{2\sigma_k^2}\right), \tag{1.78}$$

For the signal model however, the evaluation requires integration over the prior domain (denoted $\mathbf{\Theta}$) of all parameters, codified in a vector $\vec{\theta}$ and is given by

$$\begin{aligned} P(d|H_S, I) \;&=\; \int_{\mathbf{\Theta}} d\vec{\theta}\, p(\vec{\theta}|H_S, I) \prod_{k=1}^{N} \left(2\pi\sigma_k^2\right)^{-1} \\ &\times\; \exp\left(-\frac{\left|\tilde{h}_k(\vec{\theta}) - \tilde{d}_k\right|^2}{2\sigma_k^2}\right). \end{aligned} \tag{1.79}$$

The integral in Eq. (1.79) becomes rapidly unfeasible, with increasing number of parameters, to integrate with the exhaustive method. To avoid this problem, we can make use of a probabilistic algorithm called Nested Sampling, which I briefly describe in the next section.

1.7.3 How Nested Sampling works

Nested Sampling concerns a collection of modern numerical techniques via which the computation of multi-dimensional integrals is more computationally efficient compared to the usual discrete summation of the integrand. Looking at Eq. (1.75) it is evident that the likelihood and the prior are the input quantities, while the evidence and the posterior distributions are the outputs of this procedure, with the evidence Eq. (1.76) being the prime quantity, while the posterior estimation comes as a by-product. The first is useful in performing model selection, while the latter for parameter estimation, which is what we will be concerned with.

The first main idea is sorting the $\vec{\theta}$ parameters according to their likelihood

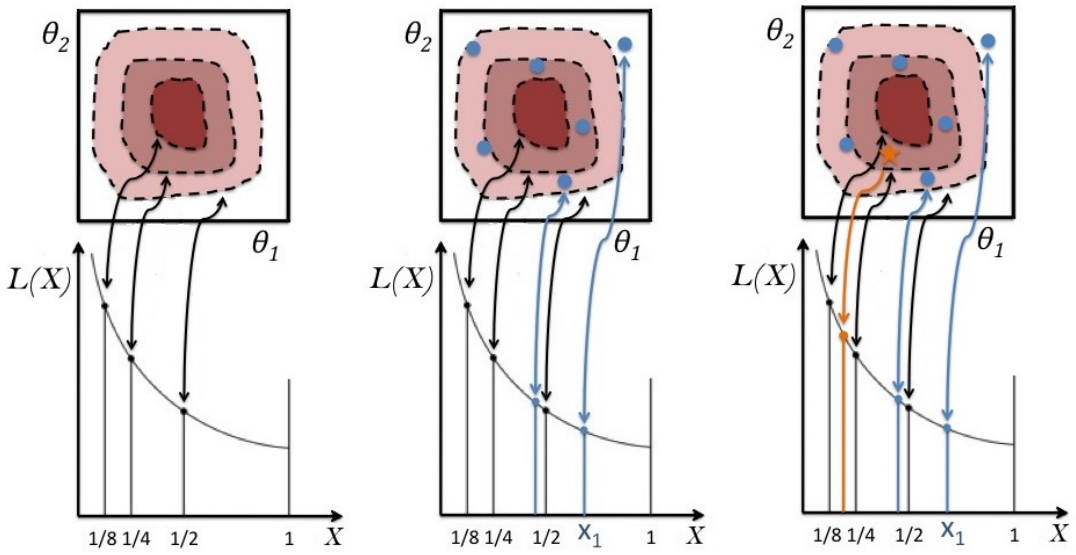

Figure 1.4: All panels depict various likelihood contours in the $\vec{\theta}$ parameter space (which is here assumed to be two-dimensional), along with the corresponding values in the cumulative prior function X.

values and then construct a cumulative function of the volume prior such that it covers all likelihood values greater than λ,

$$X(\lambda) = \int_{\mathcal{L}(\theta)>\lambda} \pi(\vec{\theta})\, d\vec{\theta}\,.$$

The above function is decreasing for increasing λ, taking values from 1 to 0 due to the normalisation condition Eq. (1.77), see also leftmost panel of Fig. 1.4.

This function is also invertible, hence the inverse function, $L(X) = L(X(\lambda))$ gives the likelihood contour value such that the enclosed volume prior is X, Fig. 1.4. I give an example by taking a number of uniformly distributed points from a two-dimensional prior distribution $\vec{\theta} = (\theta_1, \theta_2)$. Let us pick $n = 6$ points, shown as blue circular disks in the middle panel of Fig. 1.4. As seen in this plot, each point in the parameter space $\vec{\theta}$ is associated with a X-value, namely the percentage of volume that would be enclosed in contour $L(\vec{\theta})$. In our example, there exists a corresponding sequence of 6 X-values, $x_1, x_2, .. x_6$. Let x_1 denote the largest X-value, that is the rightmost point in the middle panel of Fig. 1.4. That point is associated with a likelihood contour line, as every other point. The next step in the Nested Sampling process replaces x_1 with a point chosen randomly (with uniform distribution) in the $[0, x_1]$ range (orange star in rightmost panel of Fig. 1.4). Let x_2 now denote the largest X-value in the sequence. This procedure is repeated, with every iteration resulting in a prior volume shrinkage by a factor of roughly

$e^{1/n}$.

Chapter 2

Black-hole hair loss: learning about binary progenitors from ringdown signals

Perturbed Kerr black holes emit gravitational radiation, which (for the practical purposes of gravitational-wave astronomy) consists of a superposition of damped sinusoids termed quasi-normal modes. The frequencies and time-constants of the modes depend only on the mass and spin of the black hole — a consequence of the *no-hair* theorem. It has been proposed that a measurement of two or more quasi-normal modes could be used to confirm that the source is a black hole and to test if general relativity continues to hold in ultra-strong gravitational fields. In this paper we propose a practical approach to testing general relativity with quasi-normal modes. We will also argue that the relative amplitudes of the various quasi-normal modes encode important information about the origin of the perturbation that caused them. This helps in inferring the nature of the perturbation from an observation of the emitted quasi-normal modes. In particular, we will show that the relative amplitudes of the different quasi-normal modes emitted in the process of the merger of a pair of nonspinning black holes can be used to measure the component masses of the progenitor binary.

2.1 Introduction

The black hole no-hair theorem states that a charged, stationary and axially symmetric black hole with an event horizon of spherical topology can be described by the Kerr-Newman geometry [173, 174], where it is characterized by just three quantities – its mass, spin and electric charge [175, 176, 18, 177, 178].

Astrophysical black holes are believed not to have any charge and so are described by the Kerr geometry [173], characterized by just their mass and spin angular momentum. An important consequence of the no-hair theorem concerns the behaviour of Kerr black holes when subjected to an external perturbation. There is strong evidence that black holes are stable against such perturbations [38, 36, 179, 180, 181, 182, 183] (see, however, Ref. [184]). Perturbed black holes regain their axisymmetric configuration by emitting gravitational radiation. The radiation observed by a detector takes the form

$$h(t) = \sum_{\ell,m,n} A_{\ell mn} e^{-t/\tau_{\ell mn}} \cos\left(\omega_{\ell mn} t + \phi_{\ell mn}\right), \tag{2.1}$$

and it consists of a superposition of quasi-normal modes (QNMs) with characteristic mode frequencies $\omega_{\ell mn}$ and time-constants $\tau_{\ell mn}$. Here $\ell = 2, \ldots,$ and $m = -\ell, \ldots, \ell$, are the spheroidal harmonic indices and n is an index corresponding to the overtones of each mode. The amplitudes $A_{\ell mn}$ depend on the relative orientation of the detector and the black hole as well as the nature of the perturbing agent and $\phi_{\ell mn}$ are constants defining the initial phase of the various modes[1]. One of the goals of this paper is to determine the amplitudes of the most significant modes excited during the merger of a pair of black holes.

The mode frequencies and time-constants of a black hole of mass M are given by the general expressions

$$\omega_{\ell mn} = \frac{F_{\ell mn}(j)}{M}, \quad \tau_{\ell mn} = M G_{\ell mn}(j) \tag{2.2}$$

where $F_{\ell mn}(j)$ and $G_{\ell mn}(j)$ are functions of the dimensionless black hole spin magnitude, $j = a/M$. All mode frequencies and time-constants then depend only on the mass M and the spin magnitude j of the black hole and no other parameter – a consequence of the no-hair theorem. Several authors have noted that this aspect of the no-hair theorem could be used to test if massive compact objects at galactic cores are actually rotating black holes described by the Kerr metric of general relativity [185, 49, 186]; alternatively, it could be used as a strong field test of general relativity itself [185].

The key idea behind the proposed tests is the following: If one can reliably decompose the observed gravitational radiation from a ringing black hole into a superposition of different modes, then the frequencies and time-constants of each of the modes could be used to infer the mass and spin of the black hole. If the

[1]For a recent review on black hole quasi-normal modes see Ref. [35]

object is truly a black hole, then the masses and spins obtained from the different modes should all be consistent within the measurement errors. Inconsistencies in the values of the masses and spins inferred from different modes would be an indication of the failure of general relativity or that the radiation was emitted from an object that is not a black hole. If a merging binary does not lead to a black hole then the post-merger, ringdown phase may not result in a superposition of QNMs that can be characterized by just two parameters. Such signatures could be inferred by a model-independent analysis of the data, e.g., a time-frequency transform, or by assessing the posterior probability for alternative models.

In this paper we estimate the relative amplitudes $A_{\ell mn}$ of the various modes by fitting a superposition of QNMs to the radiation emitted by a merging black-hole binary obtained from numerical-relativity simulations. These simulations involve the 'simple' case of *initially non-spinning* black holes in quasi-circular orbits and different mass ratios of the binary, in the range 1:1 to 1:11. Analytical fits of the amplitudes so obtained are extrapolated to mass ratios of up to 25, so as to study a variety of different systems. The validity of our extrapolation can only be confirmed by future numerical simulations of binary black holes with such large mass ratios.

From the analytical fits we construct a model waveform and calculate the signal-to-noise ratios (SNRs) in different modes during the merger of supermassive black-hole binaries of total mass in the range $\sim 10^6$-$10^8\,M_\odot$ observed with the Laser Interferometer Space Antenna (LISA)[2] [187] and of intermediate-mass black-hole binaries of total mass in the range $\sim$ 100-$10^3\,M_\odot$ observed with the Einstein Telescope (ET) [188] and advanced configuration of the Laser Interferometer Gravitational-Wave Observatory (aLIGO) [189, 190, 191, 192]. The response of a gravitational-wave detector is, of course, not separately sensitive to the different modes but to only their superposition. However, it should be possible to measure the relative strengths of the different modes by fitting a generic model to the observed data. We will pursue this latter approach in a forthcoming publication and restrict ourselves to a theoretical study of the relative importance of different modes.

We find that over most of the parameter space explored, the modes with indices $(\ell, m, n) = (2, 2, 0), (3, 3, 0), (2, 1, 0)$ and $(4, 4, 0)$ have SNRs for the ringdown phase larger than 500 in LISA provided the source is within a red-shift of $z = 1$ and

[2]Recently, the National Aeronautics and Space Administration in the United States opted out of the LISA mission. However, European Space Agency is pursuing an alternative that is similar in scope to LISA and we believe studying what science LISA could deliver is still very relevant.

larger than 50 in ET provided the source is within a distance of 1 Gpc. For aLIGO, the SNRs in $(2, 2, 0)$ and $(3, 3, 0)$ modes are larger than 10 in a significant region of the parameter space. However, other sub-dominant modes will not be visible in aLIGO when the source is at a distance of 1 Gpc or greater. In all cases black hole ringdown signals that result from equal-mass binaries can have far larger SNRs. The distance reach of LISA and ET to ringdown signals is large enough that one can expect a few events per year with quite a large ($\gtrsim 100$) SNR [193, 110]. One can, therefore, expect that future observations of black hole mergers will provide an excellent opportunity to test GR using several different QNMs.

We will present a specific implementation of the test of the no-hair theorem and discuss a *minimal* and a *maximal* set of parameters that could be used to carry out such a test. The *chief* result of this paper is that the relative amplitudes of the modes depend on the mass ratio q of the progenitor binary and that by measuring the relative amplitudes, in addition to the frequency and time-constant, it should be possible to measure the component masses of the binary that led to the QNMs.

The rest of this paper is organized as follows. Section 2.2 is devoted to a discussion of the numerical relativity simulations used in this work, focusing on their accuracy, so as to give an idea of how reliable are our estimates of the relative amplitudes of different modes. The waveform model used in this study is given in Section 2.3, stating the conventions and assumptions made in constructing the model. Section 2.4 constructs the amplitudes of the various modes in the ringdown signal using numerical simulations of Section 2.2. Section 2.4 also deals with different options for identifying the ringdown phase, the method that was actually followed, the connection between the mode amplitudes and the mass ratio of the binary from which the black hole results and how this information was included in the signal model. In Section 2.5, we discuss the detectability of the various modes with aLIGO, ET and LISA, and possible astrophysical information we can glean from such observations. Sections 2.6 and 2.7 present the results from a covariance matrix analysis of how well we are able to measure the parameters of the ringing black hole and the progenitor binary. In Section 2.8, we propose a practical test of the no-hair theorem, making several remarks on which modes and parameters we could use for such a test. We make concluding remarks and outlook for further work in Section 2.9. We use a system of units in which the Newton's constant and the speed of light are both set to unity, $c = G = 1$.

2.2 Numerical simulations of merger and ringdown signals

In this section, we shall briefly discuss how the numerical simulations were performed. We used the BAM code [66, 194]. The code starts with black-hole-binary puncture initial data [72, 195] generated using a pseudo-spectral elliptic solver [71], and evolves them with the χ-variant of the moving-puncture [55, 56, 196] version of the BSSN [197, 64] formulation of the 3+1 Einstein evolution equations. We estimate initial momenta for low-eccentricity inspiral using the post-Newtonian methods outlined in [80, 81]. Spatial finite-difference derivatives are sixth-order accurate in the bulk [194], Kreiss-Oliger dissipation terms converge at fifth order and a fourth-order Runge-Kutta algorithm is used for the time evolution. Time interpolation in the Berger-Oliger-like adaptive mesh refinement algorithm converges at second order accuracy. In the limit of infinite resolution the code is thus expected to converge with second order accuracy. However, in the regime of currently feasible simulations, the spatial finite differencing error dominates by far. Artificial dissipation has no measurable effect on the phase accuracy of the waves. For well-resolved simulations we thus find sixth-order accuracy, as expected.

The gravitational waves emitted by the binary are calculated from the Newman-Penrose scalar Ψ_4, extracted at a distance $D_{\rm L}$ from the source. The details of our implementation of this procedure are given in Ref. [66]. Here we recall those details that are important to this paper. The quantity $D_{\rm L}\Psi_4$ is decomposed into spin-weighted spherical harmonics, and related to the GW strain as

$$
\begin{aligned}
D_{\rm L}\Psi_4 &= D_{\rm L}(\ddot{h}_+ - i\ddot{h}_\times) && (2.3)\\
&= \sum_{\ell,m} \Psi_{4,\ell m}\, {}_{-2}Y^{\ell m}(\iota,\phi). && (2.4)
\end{aligned}
$$

To calculate the radiated power, or luminosity, we require $\dot{h}$, which can be obtained by one time-integration of the spherical-harmonic coefficients $\Psi_{4,\ell m}$. In principle we need to fix only one constant of integration to obtain $\dot{h}$ from Ψ_4, but in practice the integration is contaminated by numerical noise, see e.g., [198, 199, 200]. As part of our analysis of the data, we produced both h and $\dot{h}$, by (a) fixing the integration constants to ensure that h oscillates around zero, and rings down to zero, (b) removing low-and high-frequency noise via FFTs, and (c) removing further spurious noise effects by subtracting low-order polynomial fits through the strain.

We use results from simulations of non-spinning binaries with mass ratios $q = \{1, 2, 3, 4\}$ that were previously presented in Refs. [201, 81] and an additional simulation of a $q = 11$ binary that was carried out as a part of this study.

Detailed error analyses for the first four simulations were presented in Refs. [201, 81], although those works focused on the inspiral phase, while here we focus on the ringdown phase. We find that for the $q = \{1, 2, 3, 4\}$-simulations, the error in the amplitude of the ringdown signal is dominated by the error due to wave extraction at a finite distance from the source. The wave extraction was performed at $R_{\rm ex} = 70M$ for the data used in this paper. Waves were extracted at larger radii ($80M$ and $90M$), but the numerical resolution was lower at these radii and numerical errors began to dominate the uncertainty of the ringdown waveform in the subdominant modes. We also found that the *ratios* of the waveform luminosities were remarkably robust with respect to the wave-extraction radius, and for these the errors are even lower; a similar effect was found in Ref. [202], where the amplitude ratios between harmonics also played a major role in the study.

The new $q = 11$ simulation included only two orbits of inspiral before merger, and was produced primarily to calculate the ringdown signal. The sizes of the mesh-refinement levels were varied to optimize both memory usage and numerical accuracy of the wave extraction, which was now performed at $R_{\rm ex} = 100\,M$. Three simulations were performed to validate the accuracy of the results; the resolutions at the wave extraction sphere were $\{0.533, 0.427, 0.356\}/M$, and the finest resolution at each black hole aims to capture the inspiral GW phase with high accuracy; our focus was on the accuracy of the ringdown. Here the amplitude accuracy of all the modes we consider in this paper was within 0.5%, and this uncertainty was dominated by the error due to extraction at a finite distance from the source.

The spin of the final black hole is 0.25 ± 0.01, and $(0.3 \pm 0.01)\%$ of the energy of the system is radiated during the last two orbits and merger and ringdown. The final black hole recoils by $55 \pm 5\,{\rm km/s}$. The large uncertainty in the recoil is due mostly to having the waveform from only a small number of orbits before merger, which makes it difficult to remove the oscillatory inspiral recoil from the results, as was done in Ref. [81]. Our results for this system are consistent with previous simulations of $q = 10$ binaries [203, 204, 205].

2.3 Antenna response to a ringdown signal

Quasi-normal modes are transients that live for a very short duration in the detector band: In the case of intermediate-mass black holes that could be observed in ET, the time constant is at best about 60 ms (for a BH of mass $10^3\,M_\odot$ and spin $j = 0.7$), while for supermassive black holes that could be observed in LISA the longest time constant is about 100 min (for a BH of mass $10^8\,M_\odot$ and spin $j = 0.7$) (see Table 2.4). Consequently, it is not necessary to consider the motion of LISA or ET during the observation of a quasi-normal mode, at least not in the current evaluation of what science one might extract from their observation.

Let us consider the response of an interferometric detector to a ringdown signal. We assume that the radiation is incident from a direction $(\theta,\,\varphi)$ with respect to, say, a geo-centric coordinate system. Let $(\mathbf{e}^R_x,\,\mathbf{e}^R_y,\,\mathbf{e}^R_z)$ be a set of orthonormal vectors representing a coordinate frame in which the ringdown modes take the transverse-traceless form; that is, the metric perturbation h_{ij} due to the ringdown modes can be written in this frame as

$$h^{ij} = h_+\, e^{ij}_+ + h_\times\, e^{ij}_\times \tag{2.5}$$

where h_+ and $h_\times$ are the plus and cross polarizations, whose explicit expressions for a ringdown signal will be given below, and $\mathbf{e}_{+,\times}$ are the polarization tensors given by

$$\mathbf{e}_+ = \mathbf{e}^R_x \otimes \mathbf{e}^R_x - \mathbf{e}^R_y \otimes \mathbf{e}^R_y, \tag{2.6}$$

$$\mathbf{e}_\times = \mathbf{e}^R_x \otimes \mathbf{e}^R_y + \mathbf{e}^R_y \otimes \mathbf{e}^R_x. \tag{2.7}$$

The response $h^A(t)$ of an interferometer, labelled by A, can be written as:

$$h^A(t) = F^A_+(\theta,\varphi,\psi)\,h_+(t) + F^A_\times(\theta,\varphi,\psi)\,h_\times(t). \tag{2.8}$$

Here ψ is the polarization angle,

$$\cos\psi = \mathbf{e}_\theta \cdot \mathbf{e}^R_x, \tag{2.9}$$

and $F^A_{+,\times}(\theta,\varphi,\psi)$ are the antenna pattern functions of the detector given by,

$$F^A_+ = \mathbf{D}^A_{ij}\mathbf{e}^{ij}_+, \quad F^A_\times = \mathbf{D}^A_{ij}\mathbf{e}^{ij}_\times, \tag{2.10}$$

where $\mathbf{D}^A$ is the detector tensor. If $\mathbf{e}^A_{1,2}$ are unit vectors (not necessarily orthogonal

to each other) along the two arms of an interferometer, then the detector tensor is given by

$$\mathbf{D}^A = \mathbf{e}_1^A \otimes \mathbf{e}_1^A - \mathbf{e}_2^A \otimes \mathbf{e}_2^A. \tag{2.11}$$

For our purposes it is most useful to express the radiation from a source in the source frame, in terms of its expansion in spin-weighted spherical harmonics of weight -2, namely ${}_{-2}Y^{\ell m}$:

$$h_+ - ih_\times = \sum_{\ell=2}^{\infty} \sum_{m=-\ell}^{\ell} h^{\ell m}\, {}_{-2}Y^{\ell m}(\iota,\, \phi). \tag{2.12}$$

Here, $(\iota,\, \phi)$ refer to the co-latitude and the azimuth angle at which the radiation is emitted from the source; ι is also the angle between the line-of-sight and the orbital (spin) angular momentum of the binary (black hole). The complex coefficients $h^{\ell m}$ in the expansion are referred to as ℓm modes. Explicit expressions for the first few modes in the post-Newtonian approximation for the inspiral phase of a binary's evolution can be found in [206, 76, 207, 208, 77, 209, 210, 211, 212, 74, 75]. It is useful to write the modes explicitly in terms of their real and imaginary parts

$$h^{\ell m} = A_{\ell m} e^{-i\Phi_{\ell m}} = h_+^{\ell m} - ih_\times^{\ell m}. \tag{2.13}$$

This helps in extracting the amplitude and phase of each mode in terms of its plus and cross modes obtained in numerical simulations:

$$A_{\ell m} = \sqrt{(h_+^{\ell m})^2 + (h_\times^{\ell m})^2}, \quad \Phi_{\ell m} = \tan^{-1}\left[-\frac{h_\times^{\ell m}}{h_+^{\ell m}}\right]. \tag{2.14}$$

Noting that ${}_{-2}Y^{\ell m}(\iota,\, \phi) = {}_{-2}Y^{\ell m}(\iota,\, 0)\, e^{im\phi}$, we can rearrange the sums in Eq. (2.12) using Eq. (2.14) to get [198]

$$h_+ = \sum_{\ell,m>0} A_{\ell m}\, Y_+^{\ell m}\, \cos(\Phi_{\ell m} - m\phi), \tag{2.15}$$

$$h_\times = -\sum_{\ell,m>0} A_{\ell m} Y_\times^{\ell m}\, \sin(\Phi_{\ell m} - m\phi), \tag{2.16}$$

where we have dropped the "memory-effect" $m = 0$ terms, for which the amplitude is low (see, e.g., a recent numerical study [213]). Note that while these modes are non-oscillatory during inspiral, they do exhibit ringdown, which has been studied in some detail with numerical codes in axial symmetry, where they are the only non-zero modes (see, e.g., [214]). In the above expressions, the angular functions

$Y^{\ell m}_{+,\times}(\iota)$ are the following combinations of the spin-weighted spherical harmonics:

$$\begin{aligned} Y^{\ell m}_{+}(\iota) &\equiv {}_{-2}Y^{\ell m}(\iota,0) + (-1)^{\ell}\,{}_{-2}Y^{\ell -m}(\iota,0), \\ Y^{\ell m}_{\times}(\iota) &\equiv {}_{-2}Y^{\ell m}(\iota,0) - (-1)^{\ell}\,{}_{-2}Y^{\ell -m}(\iota,0). \end{aligned} \tag{2.17}$$

For the inspiral phase of a binary when the two compact bodies are widely separated, post-Newtonian (PN) approximation gives the amplitudes $A_{\ell m}(t)$ and phases $\Phi_{\ell m}(t)$ as expansions in v/c, where v is the velocity of the bodies (see, e.g., [206]). Numerical relativity simulations can be used to extract them when the PN approximation breaks down. In the case of perturbed black holes, which a binary will result in, black hole perturbation theory predicts that the modes are damped sinusoids with their amplitudes and phases given by:

$$A_{\ell m} = \frac{\alpha_{\ell m}\, M}{D_{\rm L}}\, e^{-t/\tau_{\ell m}}, \quad \Phi_{\ell m}(t) = \omega_{\ell m}\, t, \tag{2.18}$$

where M is the mass of the black hole and $D_{\rm L}$ is its luminosity distance from Earth. Time-constants $\tau_{\ell m}$ and frequencies $\omega_{\ell m}$ can be computed from black hole perturbation theory (see, e.g., Ref. [49] for a recent comprehensive listing of frequencies and time-constants). However, the amplitudes $\alpha_{\ell m}$ depend on the nature of the perturbation and are not analytically accessible in the case of black holes that form from the coalescence of a binary. We shall "measure" them later in this paper using results of our numerical simulations.

Using the above equations, the output of the numerical simulations for the plus and cross polarizations corresponds to the following expressions:

$$\begin{aligned} h_{+}(t) &= \sum_{\ell,m>0} \frac{\alpha_{\ell m}\, M}{D_{\rm L}}\, Y^{\ell m}_{+}(\iota)\, e^{-t/\tau_{\ell m}}\, \cos\left(\omega_{\ell m} t - m\phi\right), \\ h_{\times}(t) &= \sum_{\ell,m>0} \frac{\alpha_{\ell m}\, M}{D_{\rm L}}\, Y^{\ell m}_{\times}(\iota)\, e^{-t/\tau_{\ell m}}\, \sin\left(\omega_{\ell m} t - m\phi\right). \end{aligned} \tag{2.19}$$

We have dropped the overtone index n from all the relevant quantities (amplitudes, frequencies and time-constants) of quasi-normal modes, as we are assuming that higher (i.e., $n > 0$) overtones, quickly become negligible in amplitude, compared to the fundamental $n = 0$ overtone. Only the fundamental $n = 0$ overtone of the various modes is considered in this paper.

The amplitudes $A_{\ell m}$ of the various modes depend on the nature of the perturbation. For ringdowns resulting from the merger of two non-spinning black holes, $A_{\ell m}$

depend on the mass M of the final black hole and mass ratio $q = m_1/m_2\,(q \geq 1)$ of the progenitor binary.

In the next section we will estimate the amplitude of dominant modes by fitting the late time signal from a numerical relativity simulation to a superposition of ringdown modes. For binaries with non-spinning black holes considered in this paper we find that modes with $(\ell, m) = (2,2), (2,1), (3,3)$ and $(4,4)$ are the ones that are excited with amplitudes large enough to be interesting. For these modes, the angular functions $Y^{\ell m}_{+,\times}(\iota)$ are given by

$$\begin{aligned} Y^{22}_{+}(\iota) &= \sqrt{\frac{5}{4\pi}}\,\frac{(1+\cos^2\iota)}{2}, \\ Y^{22}_{\times}(\iota) &= \sqrt{\frac{5}{4\pi}}\,\cos\iota, \end{aligned} \tag{2.20}$$

$$\begin{aligned} Y^{21}_{+}(\iota) &= \sqrt{\frac{5}{4\pi}}\,\sin\iota, \\ Y^{21}_{\times}(\iota) &= \sqrt{\frac{5}{4\pi}}\,\cos\iota\,\sin\iota, \end{aligned} \tag{2.21}$$

$$\begin{aligned} Y^{33}_{+}(\iota) &= -\sqrt{\frac{21}{8\pi}}\,\frac{(1+\cos^2\iota)}{2}\,\sin\iota, \\ Y^{33}_{\times}(\iota) &= -\sqrt{\frac{21}{8\pi}}\,\cos\iota\sin\iota, \end{aligned} \tag{2.22}$$

$$\begin{aligned} Y^{44}_{+}(\iota) &= \sqrt{\frac{63}{16\pi}}\,\frac{(1+\cos^2\iota)}{2}\,\sin^2\iota, \\ Y^{44}_{\times}(\iota) &= \sqrt{\frac{63}{16\pi}}\cos\iota\sin^2\iota. \end{aligned} \tag{2.23}$$

In the case of binaries comprising of black holes with generic spins, the relative amplitudes of the various modes will also depend on the magnitude and direction of the spin vectors of the progenitor black holes. A detailed study of the dependence of the relative amplitudes of the various modes on the initial spin configurations and mass ratio of the progenitor binary is necessary to assess how accurately one might be able to use quasi-normal modes to measure a progenitor binary's parameters. For this, a more exhaustive set of simulations covering the full parameter space of binary black holes is required and will be taken up in the future.

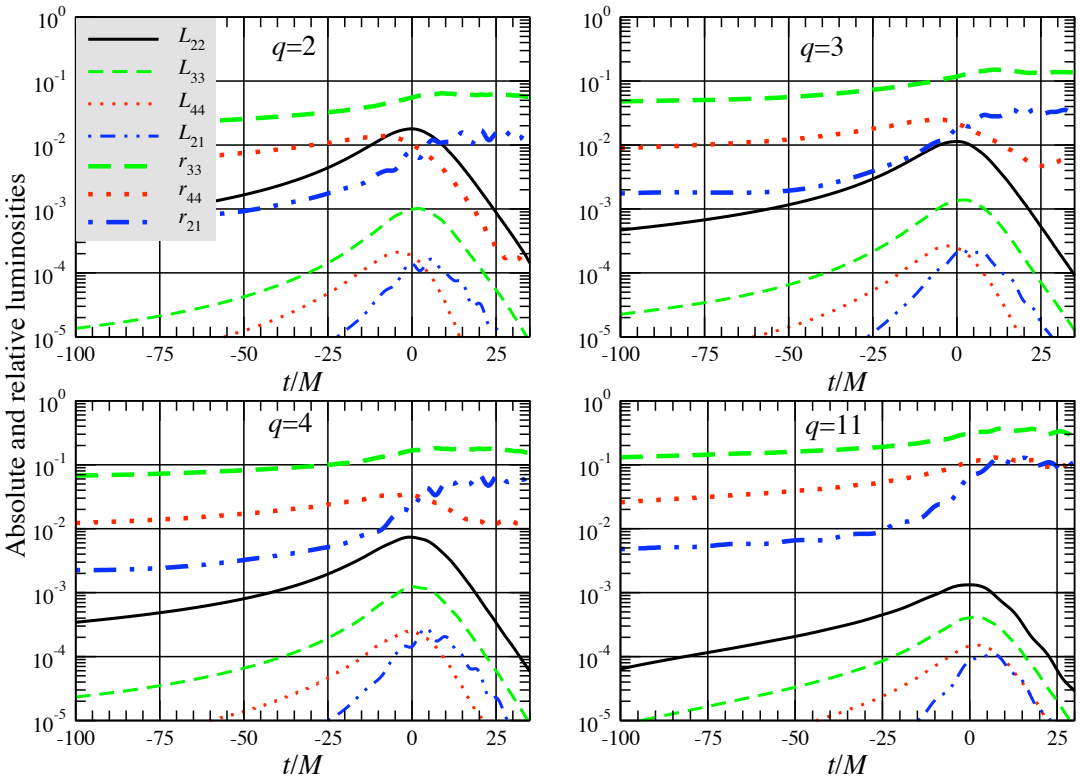

Figure 2.1: This plot shows the relative luminosities, or radiated power, in modes $(2,2)$, $(3,3)$, $(4,4)$, and $(2,1)$. L_{lm} represent the luminosities (in units $c = G = 1$ in which luminosity is dimensionless) and r_{lm} denote the ratios $r_{lm} = L_{lm}/L_{22}$. The different panels correspond to systems with different mass ratios as indicated in the panel. Note that as the mass ratio increases, the luminosity in each mode decreases but the amplitudes of all higher-order modes relative to the $(2,2)$-mode increase. We have omitted — both in the figure and in this work — the next most dominant modes, $(5,5)$, $(3,2)$, $(4,3)$, $(6,6)$ and $(5,4)$ as they are generally less than one percent as luminous as the $(2,2)$ mode. (see, however, Pan et al [3]).

We conclude this section by noting that using the expression for the two polarizations in Eq. (2.19) the detector response given in Eq. (2.8) can be written as:

$$h^A(t) = \sum_{\ell,m>0} B^A_{\ell m} e^{-t/\tau_{\ell m}} \cos\left(\omega_{\ell m} t + \gamma^A_{\ell m}\right), \tag{2.24}$$

where the superscript A is an index denoting the detector in question (which is relevant when we have a network of detectors), $B_{\ell m}$ ($\gamma_{\ell m}$) is the following combination of the amplitudes $A_{\ell m}$ (respectively, phases $m\phi$), antenna pattern functions

F_+^A and $F_\times^A$ and the inclination angle ι :

$$B_{\ell m} = \frac{\alpha_{\ell m} M}{D_{\rm L}} \sqrt{\left(F_+^A\, Y_+^{\ell m}\right)^2 + \left(F_\times^A\, Y_\times^{\ell m}\right)^2}, \tag{2.25}$$

$$\gamma_{\ell m} = \phi_{\ell m} + m\,\phi + \tan^{-1}\left[\frac{F_\times^A\, Y_\times^{\ell m}}{F_+^A\, Y_+^{\ell m}}\right]. \tag{2.26}$$

Note that, for the sake of clarity, we have dropped the index A on $B_{\ell m}$ and $\gamma_{\ell m}$. Here, $\phi_{\ell m}$ are arbitrary constant phases of each quasi-normal mode [3] The effective amplitudes $B_{\ell m}$ are proportional to the intrinsic amplitudes $\alpha_{\ell m}$ of the modes and vary inversely with the luminosity distance. Their magnitude also depends on the various angles (θ, φ, ψ, ι) describing the position of the source on the sky and its orientation relative to the detector through the antenna pattern functions F_+ and $F_\times$ and spherical harmonic functions $Y_+^{\ell m}$ and $Y_\times^{\ell m}$. The constant phases $\gamma_{\ell m}$ also depend on the angles and the fiducial azimuth angle ϕ.

The above form of the response is more helpful in understanding which, or which combination, of the parameters can be measured and how many detectors are required in solving the inverse problem, namely to fully reconstruct the incident gravitational wave and the parameters of the source that emitted the radiation. We shall use the above form of the waveform to compute the signal-to-noise ratios and the covariance matrix.

2.4 Amplitudes of modes excited during the ringdown phase of a black hole binary

In this section we will use numerical simulations to evaluate the amplitude of the various modes excited as a function of the mass ratio q. We will examine how the amplitude of the dominant 22-mode varies as a function of q. Of particular interest would be the growth of 21-, 33- and 44-modes relative to the 22-mode as the binary system becomes more asymmetric. We will provide simple analytical fits to the amplitudes of all the different modes and discuss how the inclination angle of the black hole's final spin will affect the amplitude of the ringdown signal. Our analysis is complementary to previous studies of the mode structure of unequal-mass nonspinning binaries, for example [198, 216].

[3] Specifically, the $\ell = m$ modes have a nearly consistent rotational phasing, while the $\ell \neq m$ modes seem to have somewhat distinct associated dynamics, with differentiated amplitude and phasing relationships during the merger process.[215]

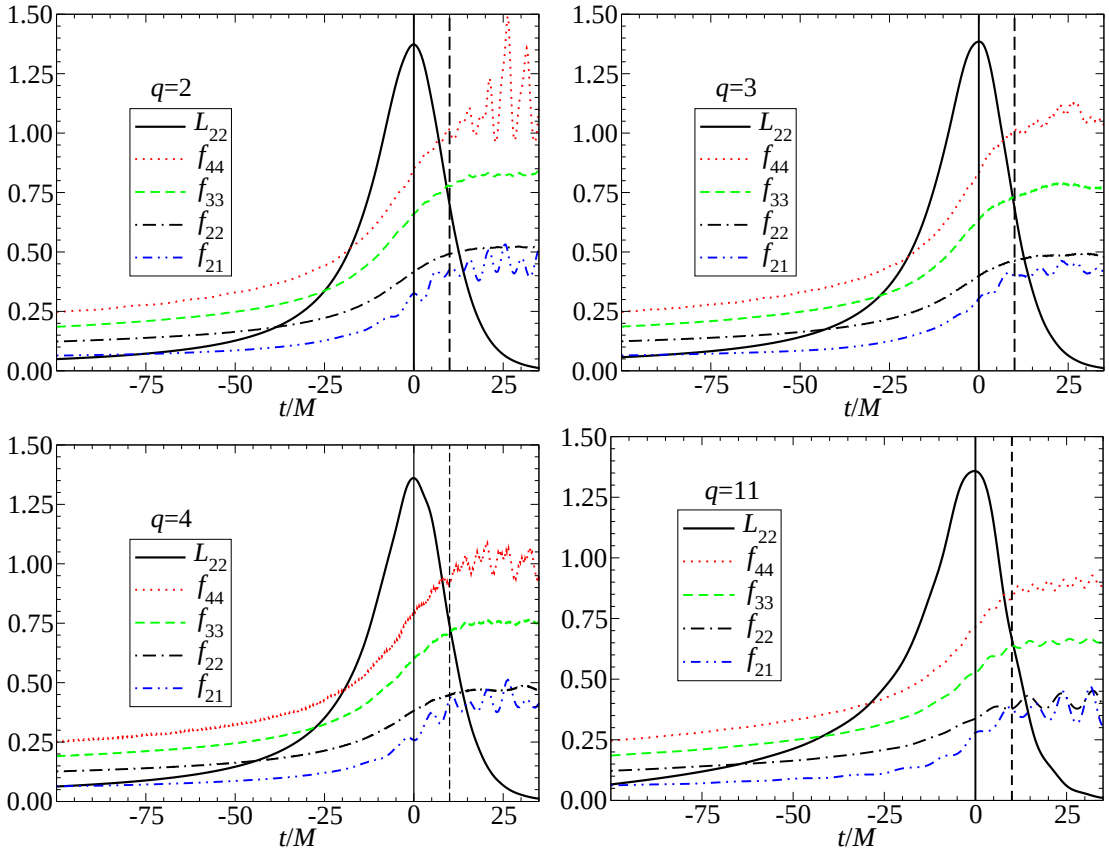

Figure 2.2: Evolution of the first few dimensionless mode frequencies $f_{\ell m} = M\omega_{\ell m}$ as a function of the dimensionless time t/M, for different values of the mass ratio q of the progenitor binary. Also shown in arbitrary units is the luminosity in the 22 mode. All mode frequencies, especially f_{22} and f_{33}, stop evolving and stabilise soon after the binary merges to form a single black hole. The waveform is assumed to contain a superposition of only quasi-normal modes a duration $10M$ after the luminosity in 22 mode reaches its peak.

2.4.1 Evolution of the luminosity

An important question that arises in the study of QNMs excited during the merger of a black hole binary is the determination of the most dominant modes in the infinite mode sum in Eq. (2.1) for this particular kind of perturber. This analysis is necessary to construct a good model of the waveform to use in the analysis.

Figure 2.1 plots the luminosity in gravitational waves, $L_{\ell m} = D_{\rm L}^2 \left[(\dot{h}_+^{\ell m})^2 + (\dot{h}_\times^{\ell m})^2\right]$, in the first four most dominant modes as a function of the dimensionless time t/M, where M is the initial total mass of the binary. The luminosities are plotted for four values of the mass ratio $q = 2, 3, 4$ and 11. We have left out the plot corresponding to the equal mass case $q = 1$, as in this case the modes with odd values of m are not excited and hence not as interesting as when the masses are unequal. The luminosity peaks just before the two black holes collide but different modes peak at different times. The 21- and 33-modes peak after the 22-mode reaches its maximum. However, the 44-mode shows the opposite behaviour. For a more thorough investigation on the different multipolar contributions to the total radiated energy, see Ref. [215].

Although the 33-mode is absent when $q = 1$, it is already more dominant than the 44-mode when $q = 2$ and remains the most dominant after the 22-mode, throughout the inspiral and merger phase and for all mass ratios (except, of course, when $q = 1$). The 44-mode remains more dominant than the 21-mode for the most part, but the trend reverses after merger. This is because the 21-mode reaches its peak luminosity a little after the 44-mode. For $q = 2$, when the 22-mode reaches its peak, the luminosity in the 33-mode is an order-of-magnitude smaller than the dominant 22-mode; luminosities in 21- and 44-modes are 50 times smaller than the 22-mode.

In addition to the luminosities, we have also plotted their ratios $r_{\ell m} = L_{\ell m}/L_{22}$ with respect to the 22-mode. It is clear that for more symmetric systems (i.e. $q \gtrsim 1$) higher modes are hardly excited. For instance, when $q = 2$ the luminosity of the 21- and 44-modes remains below $\sim$ few percent of the 22-mode, while the 33-mode is always less than $\sim 5\%$ of the 22-mode. As the mass ratio increases the higher order modes are excited with greater amplitudes. The different mode amplitudes become comparable to the 22-mode and to one another as the mass ratio increases. In the next two sub-sections we will give a more quantitative evaluation of the relative mode amplitudes in the ringdown part of the signal.

2.4.2 Identifying the ringdown phase

An important task of our study is the identification of the point when the signal is purely a superposition of various quasi-normal modes. This is necessary in order that the proposed tests of general relativity are not corrupted due to the presence of extraneous signals. By assuming that the ringdown phase occurs sooner than it actually does, we are in danger of corrupting the waveform. Equally, by identifying the ringdown phase to be much later than it actually is, we will significantly weaken the tests since the signal amplitude falls off exponentially from the beginning of the ringdown phase. A proper identification of the beginning of the ringdown phase is needed to correctly extract the amplitude of the quasi-normal modes and to compute the signal-to-noise ratio and other quantities.

To this end, we shall use the evolution of the frequency of the various modes $h_{\ell m}$. As a binary evolves, the frequency of each mode $h_{\ell m}$ increases, the rate of increase itself being greater as the two black holes get closer. When the two black holes merge, a common horizon forms and the frequency of each mode stabilizes, finally reaching the quasi-normal mode value as predicted by black hole perturbation theory. We shall identify the beginning of the ringdown phase to be (approximately) the epoch when the frequency of the various modes begin to stabilize.

We can compute the frequency of each mode from the evolution of its phase given by the second of the equations in Eq. (2.14). Once the phase is known it is straightforward to write down the (dimensionless) frequency $f_{\ell m} = M\,\omega_{\ell m} = \mathrm{d}\Phi_{\ell m}(t)/\mathrm{d}(t/M)$. The ringdown phase can be assumed to begin when $f_{\ell m}$ computed from our numerical simulations are close to those obtained from black hole perturbation theory. We will first take a look at the predictions from black hole perturbation theory and then compare those predictions to the results obtained from our numerical simulations and plotted in Fig. 2.2.

There has been a lot of work on the computation of the frequencies and time-constants of various modes of a perturbed Kerr black hole. Berti et al [49] have found simple fits, as a function of the spin parameter j, to the dimensionless mode frequencies[4] $f_{\ell m} = M\,\omega_{\ell m}$ and quality factors $2\,Q_{\ell m} = \tau_{\ell m}\,\omega_{\ell m}$. The fitting functions for the 22, 21, 33 and 44 modes are given by [49]

$$\begin{aligned} f_{22} &= 1.5251 - 1.1568(1-j)^{0.1292}, \\ Q_{22} &= 0.7000 + 1.4187(1-j)^{-0.4990}, \end{aligned} \tag{2.27}$$

[4]Note that we only consider here, the least damped $n = 0$ overtone for each mode and have therefore dropped the overtone index from mode frequencies, quality factors and time-constants.

Table 2.1: Dimensionless frequencies $f_{\ell m}$ for various modes for different values of the black hole spin j that results from the merger of a binary of mass ratio q. We assume that the ringdown phase begins when the frequencies of various modes stop increasing and stabilize to a constant value. For each mode frequency, the column labelled "Fit" gives the values computed using Eqs. (2.27)-(2.30) and that labelled "NR" shows values at the "beginning" of the ringdown mode, a duration $10M$ after the gravitational wave luminosity in the 22 mode reaches its peak (dashed vertical line in Fig. 2.2).

q	j	f_{22}		f_{21}		f_{33}		f_{44}	
		Fit	NR	Fit	NR	Fit	NR	Fit	NR
1	0.69	0.53	0.51	0.46	–	0.84	–	1.14	1.08
2	0.62	0.50	0.49	0.44	0.42	0.80	0.78	1.09	1.05
3	0.54	0.48	0.47	0.43	0.41	0.76	0.74	1.03	1.01
4	0.47	0.46	0.45	0.42	0.43	0.73	0.72	0.99	0.97
11	0.25	0.41	0.39	0.39	0.41	0.66	0.64	0.89	0.85

$$\begin{aligned} f_{21} &= 0.6000 - 0.2339(1-j)^{0.4175}, \\ Q_{21} &= -0.3000 + 2.3561(1-j)^{-0.2277}, \end{aligned} \tag{2.28}$$

$$\begin{aligned} f_{33} &= 1.8956 - 1.3043(1-j)^{0.1818}, \\ Q_{33} &= 0.9000 + 2.3430(1-j)^{-0.4810}, \end{aligned} \tag{2.29}$$

$$\begin{aligned} f_{44} &= 2.3000 - 1.5056(1-j)^{0.2244}, \\ Q_{44} &= 1.1929 + 3.1191(1-j)^{-0.4825}. \end{aligned} \tag{2.30}$$

These fits are quite robust and they differ from the actual values obtained for the frequencies and quality factors by no more than 3% [49]. Table 2.1 lists frequencies f_{22}, f_{21}, f_{33} and f_{44}, for several different values of the spin parameter j. The chosen values of j correspond to the final spins of black holes that result in our numerical simulations of binaries with different mass ratios q. Values in columns labelled "Fit" are those obtained using Eqs. (2.27)-(2.30) and those in columns labelled "NR" are those obtained from our numerical relativity simulations as follows.

Figure 2.2 plots the frequencies $f_{\ell m}$ for the 22, 21, 33, and 44 modes as (black) dot-dashed, (blue) dot-dot-dashed, (green) dashed and (red) dotted curves. As expected, the frequency of each mode increases, quite rapidly towards the end, but stabilizes to a constant value – the quasi-normal mode frequency of the final

Table 2.2: For different mass ratios (column 1), we list the final spin j of the black hole (column 2), amplitudes of different modes at three different epochs: (i) when the 22 mode reaches its peak luminosity (top panel), an epoch $10M$ (middle panel) and $15M$ after the 22 mode reaches its peak luminosity. We list the absolute value of the amplitude for the 22 mode and the ratio of amplitudes of the rest of the modes to the 22 mode. The beginning of ringdown, taken as the point when the instantaneous frequency of each mode begins to stabilize, is typically found to be $\sim$ 1-2 cycles after the peak luminosity. For concreteness we take the beginning of the ringdown mode to be $10M$ after the peak luminosity.

q	j	At peak luminosity			
		α_{22}	α_{33}/α_{22}	α_{44}/α_{22}	α_{21}/α_{22}
1	0.69	0.365	0.000	0.052	0.000
2	0.62	0.321	0.149	0.050	0.114
3	0.54	0.266	0.216	0.070	0.178
4	0.47	0.225	0.259	0.087	0.203
11	0.25	0.100	0.349	0.156	0.312
		At $10M$ after peak			
		α_{22}	α_{33}/α_{22}	α_{44}/α_{22}	α_{21}/α_{22}
1	0.69	0.217	0.000	0.043	0.000
2	0.62	0.194	0.161	0.030	0.121
3	0.54	0.158	0.247	0.052	0.195
4	0.47	0.140	0.267	0.069	0.234
11	0.25	0.063	0.377	0.154	0.407
		At $15M$ after peak			
		α_{22}	α_{33}/α_{22}	α_{44}/α_{22}	α_{21}/α_{22}
1	0.69	0.152	0.000	0.038	0.000
2	0.62	0.132	0.156	0.020	0.135
3	0.54	0.108	0.244	0.044	0.212
4	0.47	0.095	0.264	0.057	0.262
11	0.25	0.048	0.347	0.137	0.478

black hole. The plots also show the (arbitrarily scaled) luminosity in the 22-mode as a (black) solid curve. The epoch at which the luminosity reaches its peak (indicated by a solid vertical line) has been set to be $t/M = 0$. We see that the onset of the ringdown phase occurs significantly after the luminosity reaches its peak. For simplicity, we have chosen the beginning of the ringdown phase to be a duration $t = 10\,M$ after the system reaches its peak luminosity, indicated by a dashed vertical line in Fig. 2.2. In reality for the $\ell = m$ modes, it is $4M$-$5M$ earlier than for the (2, 1) mode. The luminosity curves, Fig. 2.1, exhibit a similar behaviour. See also [215].

Most modes seem to stabilize at the onset of the ringdown phase. For $q \lesssim 4$

the frequency of 22 and 33 modes stabilize, but it is less so with 21 and 44 modes. In our $q = 11$ simulations all mode frequencies seem to oscillate around a mean value, 22 and 21 more than 33 and 44. From Fig. 2.1, we see that after reaching the peak luminosity the amplitudes of 21 and 33 modes relative to the 22 mode (thick lines) are constant. This justifies why we might fit a q-dependent function to the relative amplitudes of various modes (see Sec. 2.4.3 and Fig. 2.3) that is valid throughout the ringdown phase. The same cannot be said about the 44 mode.

Under columns labelled "NR", Table 2.1 gives frequencies f_{22}, f_{21}, f_{33} and f_{44} at the onset of the ringdown mode (i.e., an epoch $t = 10M$ after the luminosity of the 22 mode reaches its peak) obtained from our numerical relativity simulations. Modes with odd ℓ or m are not excited when a binary comprising a pair of equal mass black holes merges, which is the reason why these entries are missing from the Table. The mode frequencies at $10M$ after peak luminosity agree with the fits obtained from black hole perturbation theory to within 5%. Hence we believe that our method is quite robust in identifying the ringdown phase.

2.4.3 Relative amplitudes in the ringdown phase

Our goal here is to estimate the amplitudes of the various modes in the ringdown phase. The transition from the inspiral to the ringdown phase is very smooth and it is not easy to pick a unique instant after which the transition occurs. Amplitudes of the various modes in the ringdown phase are given in Table 2.2 at three different epochs:

- at the epoch when the luminosity of the 22 mode reaches its peak,
- a duration $10M$ after the 22 mode reaches its peak luminosity, and
- a duration $15M$ after the 22 mode reaches its peak luminosity.

The Table lists the *absolute* amplitude α_{22} of the 22 mode and *relative* amplitudes $\alpha_{\ell m}/\alpha_{22}$ of the rest of the modes. These amplitudes are plotted in Fig. 2.3.

First let us note that although, as expected, the absolute amplitude of the 22 mode depends on the epoch that we identify as the start of the ringdown phase, the amplitudes of the sub-dominant modes relative to the 22 mode are not too sensitive to that identification. This is especially true for the 33 and 44 modes whose peak luminosity is at the same epoch as that of the 22 mode [thin (green) dashed and (red) dotted curves in Fig. 2.1], but less so for the 21 mode [thick (blue) dot-dot-dashed curve in Fig. 2.1, bottom right panel of Fig. 2.3], whose

peak luminosity occurs significantly after that of the 22 mode. As mentioned before, for concreteness we shall take the starting point of the ringdown mode as an epoch $10M$ after the 22 mode reaches its peak luminosity (the dashed vertical line in Fig. 2.2). All discussions in the remainder of this paper are based on this identification. A duration of $10M$ corresponds to between 1 and 2 gravitational-wave cycles of the merger signal.

As the mass ratio of the progenitor binary increases, the amplitude of the 22 mode rapidly decreases but the sub-dominant modes approach each other in power (see Fig. 2.1) and their amplitudes increase (cf. Table 2.2 and Fig. 2.3). For a mass ratio of $q = 4$, the 33 and 21 modes have amplitudes 1/4 that of 22 while at $q = 11$ they are 40% of the 22 mode. Of course, the overall luminosity decreases as the mass ratio increases and one expects no radiation in the limit $q \to \infty$. Indeed, the emitted energy during the 'merger' phase goes roughly as the square of the symmetric mass ratio $\nu = m_1 m_2/M^2$ of the progenitor binary [198].

Let us note that the values in Table 2.2 do not all refer to the same final black hole spin. All our black holes are initially non-spinning and the final spin is simply the residual angular momentum of the progenitor binary. The final spin, therefore, depends on the mass ratio, and is greatest when the two black holes are of the same mass. In principle, it should be possible, but in practice very difficult, to produce numerical data for different mass ratios all with the same final spin. To do so we require an accurate mapping between the mass ratio and initial black-hole spins, and the spin of the final black hole. For example, configurations that lead to a nonspinning Schwarzschild black hole are suggested in Ref. [217] and more generic cases are considered in Refs. [218, 219, 220, 221]. However, fine-tuning the spin of the final black hole requires that the component black holes are also spinning, and in this paper we consider only binaries with non-spinning components.

2.4.4 Fitting functions for relative amplitudes

For the purpose of computing the signal-to-noise ratio and the covariance matrix it is convenient to have analytical expressions for the relative amplitudes of the various modes. Our fits are meant to capture the dependence of the amplitudes on the mass ratio in the range we have considered in this paper. They are not meant to explore the complex dynamics of a ringing black hole and are not necessarily valid outside the region we have explored.

We have seen that the amplitudes inferred from the simulations depend on how we identify the beginning of the ringdown phase. As mentioned before, in our calculations we have assumed that the ringdown phase begins an epoch $10M$

after the 22 mode reaches its peak luminosity. We find that the amplitude of the 22 mode at this epoch as a function of the mass ratio can be fitted by

$$\alpha_{22}(q) = 0.25\, e^{-q/7.5}. \tag{2.31}$$

The solid curve in the top left panel in Fig. 2.3 shows that this is a good fit to the data points (filled squares). Dot-dot-dashed and dotted lines in the same panel show the fits that describe $\alpha_{22}(q)$ at the peak of the luminosity and $15M$ after the peak, respectively. In all cases, the data is pretty well approximated by an exponentially falling function.

The relative amplitudes of the sub-dominant 21, 33 and 44 modes are well fitted by the following functions

$$\alpha_{21}(q) = 0.13\, \alpha_{22}(q)\, (q-1)^{1/2}, \tag{2.32}$$

$$\alpha_{33}(q) = 0.18\, \alpha_{22}(q)\, (q-1)^{1/3}, \tag{2.33}$$

$$\alpha_{44}(q) = 0.024\, \alpha_{22}(q)\, q^{3/4}. \tag{2.34}$$

They are plotted as solid curves in the relevant panels of Fig. 2.3. The fits are motivated by the fact that when $q = 1$ only modes with even values of ℓ and m are excited, while those with odd ℓ or m are absent. Note that the relative amplitudes grow as a binary becomes more asymmetric and so higher order modes should be more easily detectable if the mass ratio is large. In absolute terms, of course, all modes are exponentially damped as a function of q.

In this work we estimated the relative amplitudes of different modes at a single epoch. It might be more reliable to estimate their average over a small duration, for instance between $10M$-$15M$. This could diminish any 'numerical noise' present and extract more accurate fits but we did not explore this alternative approach in this work.

2.5 Visibility of ringdown modes

In this section we will study the signal-to-noise ratio (SNR) obtained by various detectors for the ringdown phase of the coalescence of a black hole binary. We will begin by defining the matched filter SNR, followed by the noise power spectral densities of aLIGO, AdvVirgo, ET and LISA and the choice of signal parameters used in the study. We will then discuss the visibility of the different modes, focusing on the distance reach of the various detectors.

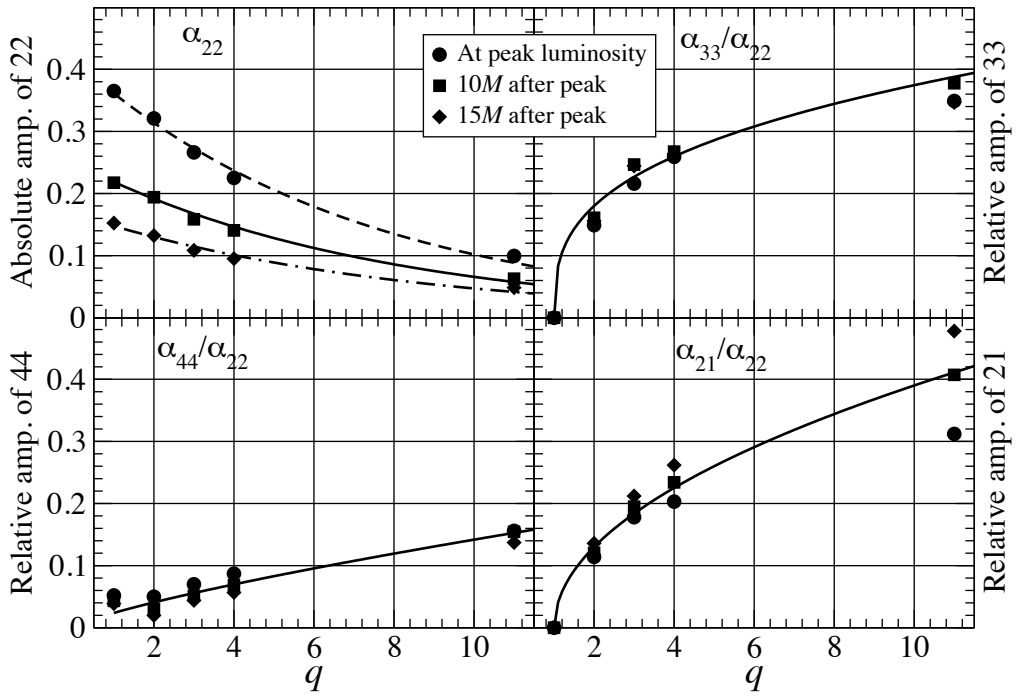

Figure 2.3: This plot shows the amplitudes as a function of the mass ratio for different modes at the peak of the luminosity of the 22 mode (circles), an epoch $10M$ and $15M$ after the peak (respectively, squares and triangles). We have plotted the *absolute* amplitude α_{22} of the 22 mode and ratio of the sub-dominant mode amplitudes $\alpha_{\ell m}/\alpha_{22}$ relative to 22 (cf. Table 2.2). The solid lines are the best fits [cf. Eqs. (3.5)-(3.8)] to the amplitudes at $10M$ after the peak luminosity.

2.5.1 Matched filter SNR

The matched filter SNR ρ obtained while searching for a signal of known shape buried in Gaussian background is given by (see, e.g., [222])

$$\rho^2 = 4 \int_0^\infty \frac{|H(f)|^2}{S_h(f)} \mathrm{d}f \tag{2.35}$$

where $S_h(f)$ is the detector noise power spectral density and $H(f)$ is the Fourier transform of the signal assumed (in this work) to be a superposition of the 22, 21 and 33 modes. In the time-domain our waveform is given by Eq. (3.1) where the sum is over $(\ell, m) = (2,2), (2,1), (3,3)$ and we have ignored all higher order modes including the $(4,4)$ mode. The coefficients $\alpha_{\ell m}$ required to compute the waveform are assumed to be as in Eqs. (3.5)-(3.6).

The ringdown signal is a superposition of different modes and its visibility depends not only on the relative amplitudes but also on the relative *phases* of the

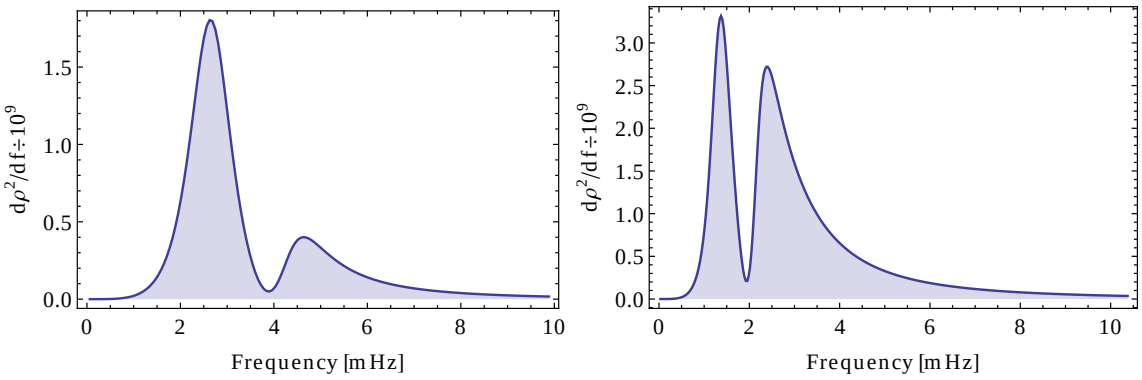

Figure 2.4: The signal-to-noise ratio integrand for LISA for a quasi-normal mode signal that is composed of 22, 21 and 33 modes — the three most dominant ones. The source is assumed to be at a red-shift of $z = 1$ and the various angles are as in Table 2.3. The left panel corresponds to a black hole of mass $M = 5 \times 10^6\, M_\odot$ and the right panel to a black hole of mass $M = 10^7\, M_\odot$. In both cases the mass ratio of the progenitor binary is taken to be $q = 10$.

different modes. To this end, it is useful to define the SNR of a mode as

$$\rho^2_{\ell m} = 4 \int_0^\infty \frac{|H_{\ell m}(f)|^2}{S_h(f)} \mathrm{d}f, \tag{2.36}$$

with the caveat that the total SNR ρ^2 is *not* the quadrature sum of $\rho^2_{\ell m}$ since there are also interference terms that can be negative.

2.5.2 Sensitivity curves

In our study, we will consider the performance of three detectors: the aLIGO ET and LISA. A fit to the aLIGO noise spectral density tuned to detect binary neutron stars is[5]

$$\begin{aligned} S_h(f) &= 10^{-49} \Big[10^{16-4\,(f-7.9)^2} + 0.08\, x^{-4.69} \\ &+ 123.35\, \frac{1 - 0.23\, x^2 + 0.0764\, x^4}{1 + 0.17\, x^2} \Big] \mathrm{Hz}^{-1} \end{aligned} \tag{2.37}$$

where $x = f/215\,\mathrm{Hz}$. In the case of ET we consider the sensitivity curve designated ET-B [223] whose noise power spectral density is given by $S_h(f) =$

[5]The fit was provided by C. Capano, Syracuse University.

$10^{-50} h_n(f)^2\,\mathrm{Hz}^{-1}$

$$\begin{aligned} h_n(f) &= 2.39\times10^{-27}\,x^{-15.64} + 0.349\,x^{-2.145} \\ &+ 1.76\,x^{-0.12} + 0.409\,x^{1.10}, \end{aligned} \tag{2.38}$$

where $x = f/100\,\mathrm{Hz}$. We take LISA noise spectral density to be the one that was used by the LISA Parameter Estimation Taskforce in Ref. [224], which also corresponds to the noise curve from the second round of the Mock LISA Data Challenge [225, 226].

2.5.3 Choice of various parameters

The SNR depends on a number of source parameters as well as the location of the source on the sky. We have limited our investigations to studying the SNR and covariance matrix as a function of the black hole's (observed) mass M and the mass ratio q of the progenitor binary, for fixed values of the distance to the black hole and various angles. In the case of LISA the black hole is assumed to be at a red-shift of $z = 1$ which corresponds (in our cosmological model) to a luminosity distance of $D_\mathrm{L} \simeq 6.73\,\mathrm{Gpc}$. In the case of aLIGO and ET we set $D_\mathrm{L} = 1\,\mathrm{Gpc}$. In all cases the angles are fixed to be $\theta = \psi = \iota = \varphi = \pi/3$. For a statistical analysis of the effect of these angular parameters on the detectability of a ringdown signal see Chapter 3.

The black hole mass is varied over the range $[100,\, 10^3] M_\odot$ in the case of aLIGO, $[10,\, 10^3]\, M_\odot$ in the case of ET and $[3\times10^6,\, 10^8]\, M_\odot$ in the case of LISA. These choices are dictated by the frequency sensitivity of the instruments which further dictates the range of black hole masses whose ringdown radiation they are most sensitive to.

Our choice of parameters is summarized in Table 2.3. We reiterate that our masses are *observed masses* which means that the intrinsic mass of the black hole is smaller by a factor $1 + z \simeq 1.2$, for aLIGO and ET and by a factor of $1 + z = 2$ in the case of LISA. Although the signal visibility simply scales as the inverse of the distance, the fact that the mass is blue-shifted means that we cannot easily scale our results to another (say, a greater) distance for the same intrinsic masses. Such a scaling will be valid if at the same time the intrinsic masses are also scaled up/down by the appropriate red-shift factor.

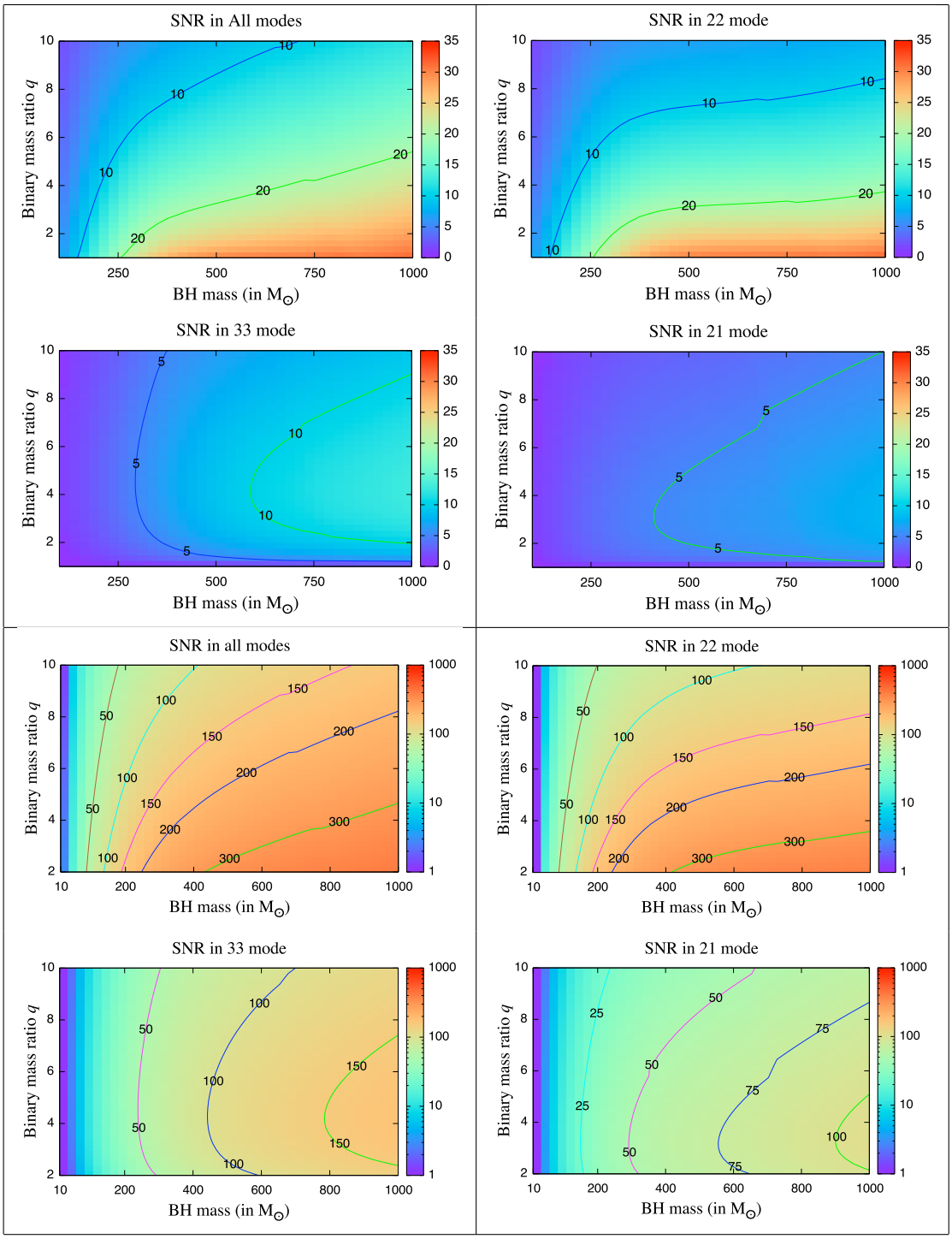

Figure 2.5: Signal-to-noise ratio (SNR) in Advanced LIGO (top set of four panels) and Einstein Telescope (bottom set of four panels) as a function of the black hole's mass M and progenitor binary's mass ratio q for different modes. Most of the contribution to the SNR comes from the 22 mode but other modes too have significant contributions, 33 being more important than 21. The source is assumed to be at a distance of 1 Gpc and various angles are as in Table 2.3.

Table 2.3: This Table lists the values of the various parameters used in our study. In all cases the angles are all set to $\theta = \varphi = \psi = \iota = \phi = \pi/3$.

Detector	$D_{\rm L}$/Gpc	$M/M_\odot$	q
aLIGO	1.00	$[100,\, 10^3]$	2-10
ET	1.00	$[10,\, 10^3]$	2-10
LISA	6.73	$[3\times10^6,\, 10^8]$	2-25

2.5.4 Visibility of different modes

It is instructive to plot the SNR integrand $\mathrm{d}\rho^2/\mathrm{d}f = |H(f)|^2/S_h(f)$ as it depicts how the different modes become important for systems with different masses. Fig. 2.4 plots this quantity for two systems as seen in LISA. The left panel corresponds to a black hole of total mass $M = 5\times10^6\,M_\odot$ and the right panel to $M = 10^7\,M_\odot$. The mass ratio q is $q = 10$ in both cases and the angles are as in Table 2.3.

The various mode frequencies $F_{\ell m} = \omega_{\ell m}/(2\pi)$ of the two systems are $F_{22} \simeq 2.74\,\mathrm{mHz}$, $F_{21} \simeq 2.54\,\mathrm{mHz}$ and $F_{33} \simeq 4.26\,\mathrm{mHz}$ for the lighter black hole and $F_{22} \simeq 1.37\,\mathrm{mHz}$, $F_{21} \simeq 1.27\,\mathrm{mHz}$ and $F_{33} \simeq 2.13\,\mathrm{mHz}$ for the heavier black hole. Let us first note that the 22 mode of the lighter black hole and 33 mode of the heavier black hole are close to the region where LISA has best sensitivity. This will be relevant in the discussion that follows.

The intrinsic amplitudes of the 21 and 33 modes are a little more than a third of the 22 mode for $q = 10$. However, since the SNR integrand depends on the signal power weighted down by the noise power, for a given black hole mass the SNR integrand could be as large as, or even dominated by, modes different from the 22 mode. This does not happen for the 21 mode since the frequencies of the 22 and 21 modes are very close to each other and so the 21 mode is always far smaller than the 22 mode. For a black hole mass of $10^7\,M_\odot$ the 33 mode is as strong as the 22 mode and for masses even larger, the 33 mode overwhelms the 22 mode. The total SNR for the $5\times10^6\,M_\odot$ black hole is $\rho = 1670$, with the different modes contributing $\rho_{22} = 1500$, $\rho_{21} = 625$, and $\rho_{33} = 950$. The SNR is clearly dominated by the 22 mode.

In the case of the heavier black hole, the total SNR is $\rho = 2520$, with the different modes contributing $\rho_{22} = 1940$, $\rho_{21} = 920$, $\rho_{33} = 1860$. In this case, the 33 mode is as strong as the 22 mode but the 21 mode, as expected, is sub-dominant.

2.5.5 Exploring black hole demographics with ET and LISA

Figures 2.5 and 2.6 plot the SNR in the ringdown signal (plots titled "SNR in all modes") and contribution from the 22, 21 and 33 modes (plots titled accordingly) as a function of the black hole mass M and mass ratio q of the progenitor binary for aLIGO, ET and LISA; M and q are varied over the range as in Table 2.3. Most of the contribution to the SNR comes from the 22 mode followed by 33 and 21. Let us recall that SNRs from different modes do not add in quadrature.

In the case of aLIGO, the 22 and 33 modes will be visible in a significant fraction of the parameter space explored provided the source is within a distance of 1 Gpc. The 21 mode will not be visible in aLIGO at this distance except perhaps for the heaviest systems explored.

In the case of ET, assuming a SNR threshold of 10 for detection, the signal is visible to a red-shift of $z \sim 0.8$ in most of the parameter space explored. Black holes of total mass $M > 400 M_{\odot}$ that form from the coalescence of binaries whose mass ratio is less than 4 will be visible at red-shifts $z \sim$ 2-3.5

In the case of LISA, ringdowns produce a very large SNR. Even assuming an SNR threshold of 40, LISA should see the formation of supermassive black holes in the range $[10^6, 10^8]\, M_{\odot}$ up to a red-shift of at least $z \sim 6$ but if the progenitor black holes have mass ratio $q < 10$ they should be visible from the earliest moments of their formation in the Universe.

Our results unambiguously demonstrate that ET and LISA can together probe black hole demographics, ET exploring the lower end of the mass spectrum of seed black holes and LISA the higher end of that spectrum. The two detectors together cover a large mass range from $\sim 10^2\, M_{\odot}$, all the way to $\sim 10^8\, M_{\odot}$. (Although out of the range of masses explored, note that ET could observe heavier black holes of mass $10^4\, M_{\odot}$ and LISA could explore lighter black holes of mass $10^5\, M_{\odot}$.) The distance reach will be different depending on the mass ratio of the progenitor binary and the total mass of the black hole. Even so, LISA and ET will make it possible to explore the formation of black holes and trace their merger histories and possibly help understand the role of black holes as seeds of galaxies and large scale structure in the Universe.

2.6 What can a ringdown signal measure?

By measuring the ringdown signal and resolving it into different modes, we should be able to learn a great deal about the merger dynamics and test general relativity. For instance, by determining the total mass of the binary from the inspiral phase

and comparing it to the mass of the black hole obtained from the ringdown phase we can measure, quite precisely, how much mass is converted into radiation in the process of merger. LISA can typically measure the total mass of a binary from its inspiral phase to a fraction of a percent. We shall see in this section that the ringdown modes can determine a black hole's mass to a percent or tenth of a percent depending on the mass ratio. Therefore, the inspiral and ringdown phases together can shed light on how much mass is lost in the process of merger and how that depends on the mass ratio of the binary and, not probed in this study but expected to depend on, the spin magnitudes and orientations of progenitor black holes.

When black holes merge, some of the orbital angular momentum goes into the final black hole. Therefore, the final black hole will spin in a direction different from either of the progenitor black holes. Independent measurements of the orbital angular momentum from the inspiral phase and black hole spin from the ringdown phase, could unravel the spin-orbit dynamics of black hole merger. While this is an exciting possibility, in this paper we have focussed only on binaries with non-spinning components. For such systems, the relative amplitudes of the different modes depend on only the mass ratio of the progenitor binary. For binaries with spinning black holes it is hard to guess how many more parameters might be required to characterize the relative amplitudes and hence their measurability. We will address this question in a forthcoming publication. We shall show in this section that one can exploit this fact to determine the mass ratio of the progenitor binary from the measurement of the ringdown mode alone. Consistency of the mass ratios from the inspiral and ringdown phases could offer further tests of general relativity.

In this section we will explore what measurements might be possible by using ringdown signals alone and what we might learn by combining the information obtained from the inspiral phase of the signal with that obtained from the ringdown phase. To this end, we shall assume that the signals are loud and compute the covariance matrix to get an estimate of the measurement uncertainties in the various parameters of a ringdown signal $h^A(t)$. The covariance matrix C^A_{km} is the inverse of the Fisher matrix F^A_{km} given by [227, 170, 228],

$$F^A_{km} = \left\langle \frac{\partial h^A}{\partial \lambda^k}, \frac{\partial h^A}{\partial \lambda^m} \right\rangle, \quad \lambda^k = \{M, j, q, \ldots\}, \tag{2.39}$$

where for any two functions $g(t)$ and $h(t)$ the angular bracket $\langle g, h\rangle$ denotes their

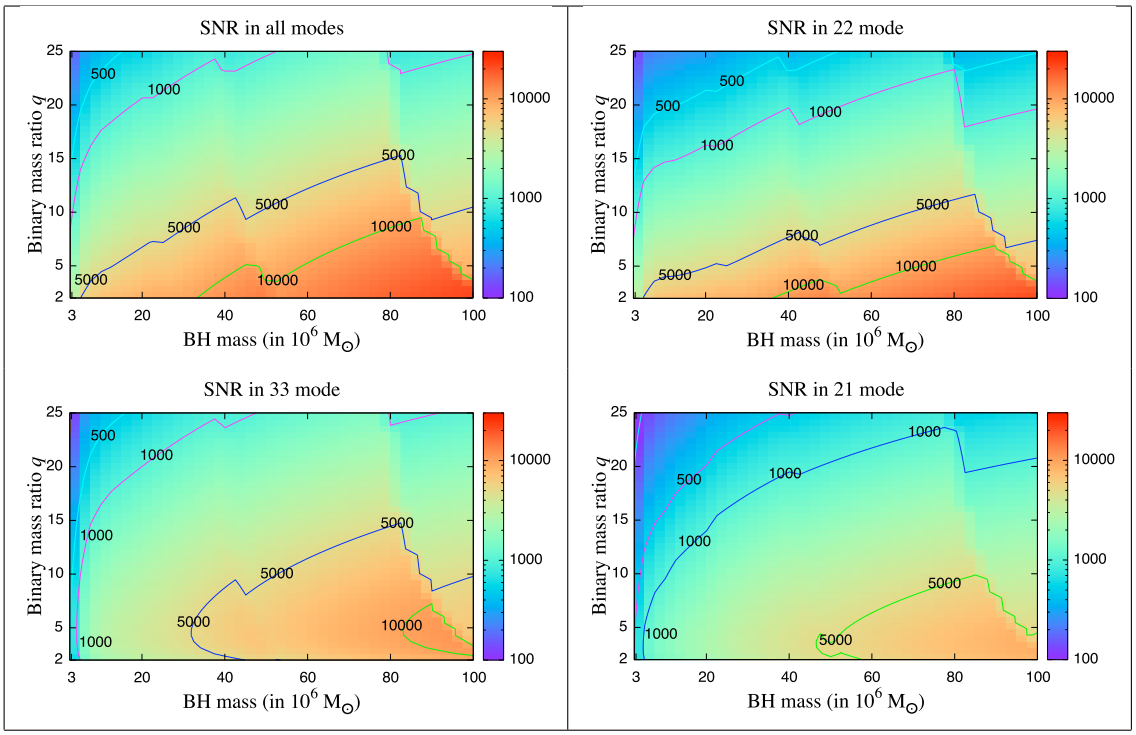

Figure 2.6: Same as Fig. 2.5 but for LISA and the source is assumed to be at a red-shift of $z = 1$. Also, the mass ratio is allowed to vary over a larger range from 2 to 25 instead of 2 to 10. The 'steps' that can be seen around $40 \times 10^6 M_\odot$ and $80 \times 10^6 M_\odot$ are mostly due to the LISA noise curve.

scalar product defined by

$$\langle g,\, h\rangle = 4\,\Re\int_0^\infty G(f)\,H^*(f)\frac{\mathrm{d}f}{S_h(f)}. \tag{2.40}$$

Here, as before, A is an index denoting the detector in question, $S_h(f)$ is the one-sided noise power spectral density of the detector, $G(f)$ and $H(f)$ are the Fourier transforms of the time-domain functions $g(t)$ and $h(t)$, respectively, and a $*$ denotes the complex conjugate of the quantity in question. The above integrals are often performed numerically and it is essential then to appropriately choose the lower and upper limits in the integral so that outside this limit the integral has negligible contribution. Note that the detector noise power spectral density rises steeply outside a certain frequency range often assuring the convergence of these integrals. If a network of detectors is used to estimate the parameters then the Fisher matrix for the network is simply the sum of the Fisher matrices for the individual detectors:

$$F_{km} = \sum_A F^A_{km}, \tag{2.41}$$

where the sum is over all the detectors in the network.

2.6.1 The full parameter set

In the case of a binary consisting of non-spinning black holes on a quasi-circular orbit, the effective amplitudes $B_{\ell m}$ in Eq. (3.1) of the quasi-normal modes of the final black hole, depend on a set of eight parameters[6] (M, j, q, $D_{\rm L}$, θ, φ, ψ, ι) : the mass M and spin magnitude j of the black hole, the mass ratio q of the progenitor binary, the position vector ($D_{\rm L}$, θ, φ) of the black hole with respect to Earth, the polarization angle ψ and the inclination ι of the black hole's spin angular momentum with respect to the line-of-sight. The phases $\gamma_{\ell m}$ are given by Eq. (2.26) and they depend on the angles (θ, φ, ψ, ι, ϕ, $\phi_{\ell m}$), where (ι, ϕ) are the spherical polar coordinates giving the direction in which the black hole quasi-normal mode is emitted in a frame fixed to the black hole and $\phi_{\ell m}$ are the initial phases of different quasi-normal modes. Thus, if we consider a superposition of three quasi-normal modes then there will be 12 parameters, including ϕ_{22}, ϕ_{33} and ϕ_{21}. The amplitudes $B_{\ell m}$ depend on eight of these parameters (exceptions are ϕ, ϕ_{22}, ϕ_{33} and ϕ_{21}) and phases $\gamma_{\ell m}$ also depend on a (different) set of eight

[6]Recall that the final spin of the black hole is determined by the mass ratio of the progenitor binary and so it is not necessary to treat both q and j as independent. However, such a treatment allows us to check if the final black hole spin is consistent with the mass ratio as predicted by numerical relativity simulations, which would indeed be another test of general relativity.

parameters (exceptions are $D_{\rm L}$, M, q, and j).

2.6.2 Measurements with a network of detectors

Measuring all the parameters of a ringdown signal will require simultaneous observation of the signal in two or more detectors. Let us first take a look at the configurations of LISA, ET and advanced ground-based detectors.

ET and LISA both have a triangular topology and consist of three V-shaped interferometers, with an opening angle of 60 degrees, rotated relative to each other by 120 degrees. The three interferometers are completely equivalent, in terms of sensitivity, to two L-shaped interferometers [229], with arms that are only three-quarters in length of the arms in the triangle. Thus, for the purpose of detection and measurement, we can consider ET and LISA to be a network of two collocated detectors. At least three advanced ground-based detectors (two LIGO detectors and Virgo) would be operating by 2015, with the possibility of the Japanese Large Cryogenic Gravitational Telescope joining the network soon after. Thus, there will be a global network of ground-based detectors that will be operating for a number of years from around 2015.

Of all the parameters, the direction to the source (θ, φ) is the most critical and difficult to measure from the ringdown modes alone. However, since the ringdown modes we study are preceded by the inspiral phase of a binary coalescence, we can expect the direction to the source to have been measured to some degree of accuracy. In the case of LISA, the inspiral phase of supermassive black holes could last for several months to years in the detector band. The modulation of the signal caused by LISA's motion relative to the source over the observation period will be good enough to measure the sky position (see, for instance, Ref. [230]). ET, together with a network of other detectors, advanced or 3rd generation detectors present at the time, should be able to triangulate the source. This is also true with the network of advanced detectors. Thus, we shall assume that the parameters (θ, φ) are known, leaving 10 parameters to be measured from the ringdown phase. However, for very massive systems (depending on the detector in question), only the ringdown phase might be visible and for such systems it will not be possible to infer the location of the source without a network of detectors. Such events will not be very useful for testing GR.

As expected, the relative contributions of the inspiral and ringdown phases depend on the total mass of the system: For lighter masses the ringdown phase makes little impact on parameter estimation; for heavier systems just the opposite is true. For systems with intermediate masses the contributions could be roughly

equal. Such systems will be golden binaries with the best ability to test GR.

A single detector can measure the mass M and spin j of the black hole by simply inverting the QNM frequencies and damping times. Additionally, each detector in a network would also measure three independent amplitudes B^A_{22}, B^A_{21} and B^A_{33} and three independent phases γ^A_{22}, γ^A_{21} and γ^A_{33} — a set of 12 additional measurements from two detectors. Of course, the amplitudes and phases (as well as the time-constants and mode frequencies) are all expressed in terms of the 10 physical parameters and will not treated as independent. The counting argument given here shows that a set of two or more detectors allows enough measurements to fully reconstruct the ringdown signal.

Therefore, one can, in principle, measure all the ten parameters of a QNM composed of three modes, using a network of two or more detectors. We have not, however, explored the problem in its full generality as the Fisher matrix that includes both intrinsic and extrinsic parameters happens to be highly ill-conditioned. In such cases, the Fisher matrix is not the right approach for computing the errors incurred. We will, in the near future, investigate this problem by other means, for instance using Bayesian inference. For now, our goal is to see how well a subset of interesting parameters can be measured if, as mentioned earlier, we know some of the parameters from the inspiral phase.

For the sake of simplicity, we shall assume that the phase of the different quasi-normal modes at the beginning of the ringdown are all the same and equal to zero: $\phi_{22} = \phi_{21} = \phi_{33} = 0$. In this work, we have dropped them from further consideration so that we can focus our effort on the main goal of the paper, which is to show that one can infer the mass ratio of the progenitor binary by measuring two or more quasi-normal mode amplitudes. We shall, therefore, assume that the ringdown signal depends on the parameters (M, j, q, $D_{\rm L}$, ι, ψ, ϕ), seven parameters in all. A single detector can measure the mass and spin of the black hole from the different mode frequencies and damping times, as well as three amplitudes and three phases. Consequently, in the case of a simplified signal model, where we have dropped the constant phases and the location of the black hole from the list of parameters, we do not need a network of detectors to resolve the signal parameters.

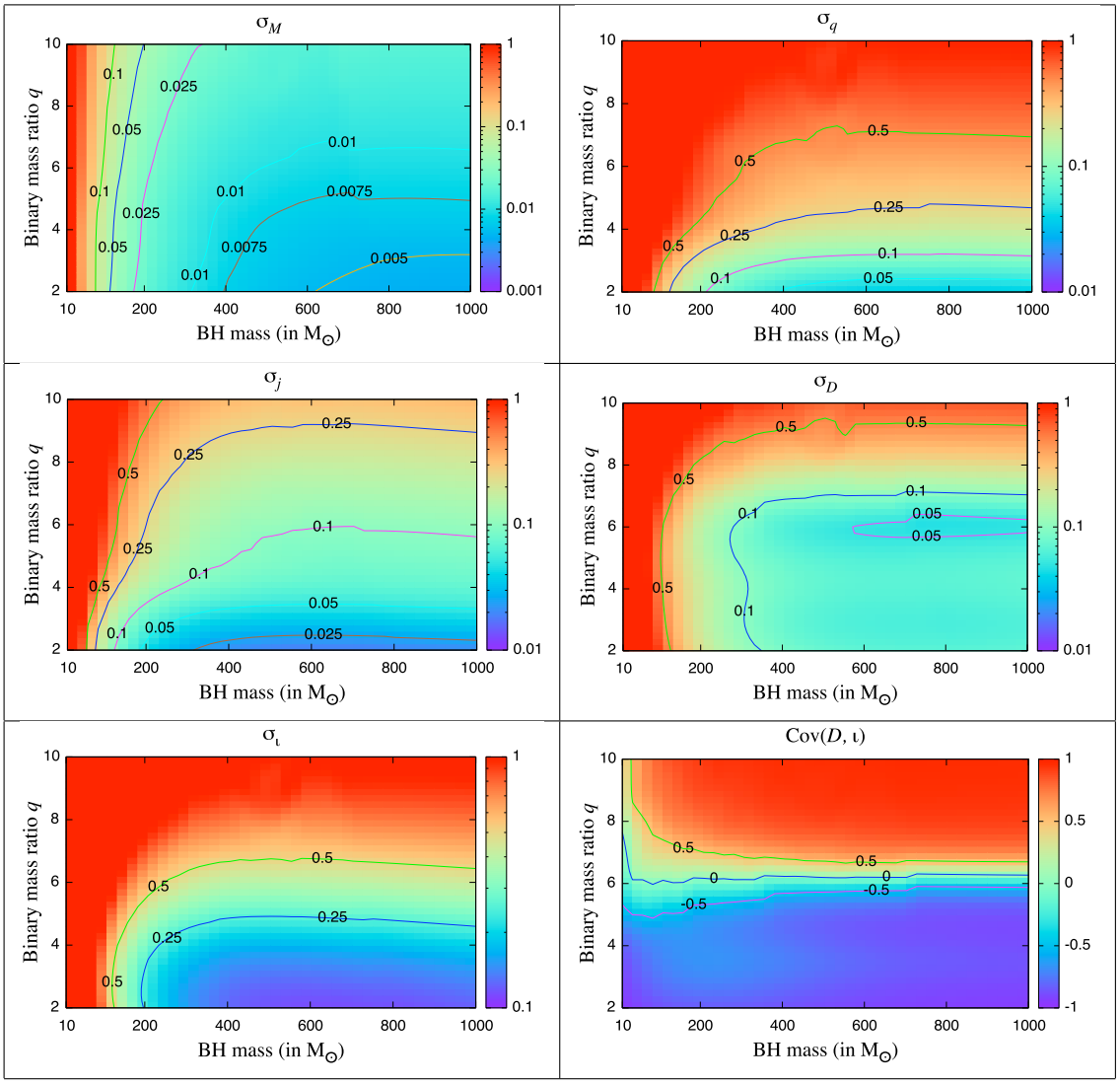

Figure 2.7: Dimensionless fractional errors σ_k/λ_k in various parameters as a function of the black hole mass and progenitor binary's mass ratio. The black hole is assumed to form at a luminosity distance of $D_{\rm L} = 1\,{\rm Gpc}$ and the various angles are assumed to be as in Table 2.3. The bottom right panel plots the correlation coefficient between the luminosity distance and the orientation ι of the black hole's spin with respect to the line-of-sight. The general trend for the errors is to increase with increasing mass ratio and decreasing mass, except for $D_{\rm L}$ for which there appears to be an 'island' around $q = 6$. We have used the ET-B sensitivity curve in computing the covariance matrix.

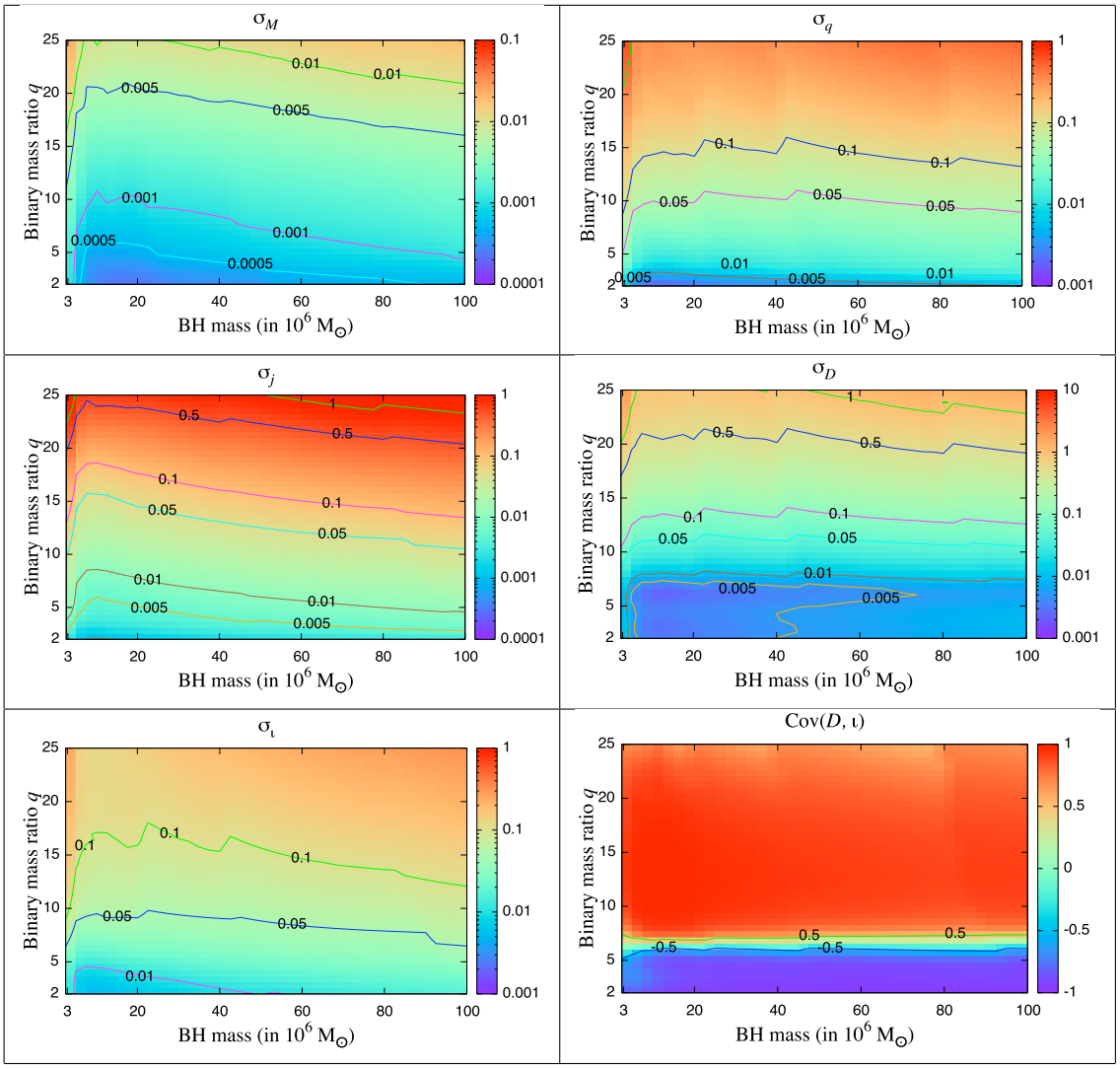

Figure 2.8: As in Fig. 2.7 but for supermassive black holes observed in LISA at a red-shift of $z = 1$. Note also that the mass ratio q in this case is allowed to vary from 2 to 25.

2.7 Understanding mass loss, spin re-orientation and mass ratio from ringdown signals

We have computed the covariance matrix C_{km} [cf. Eq. (2.39)] of ringdown signals as a function of the black hole mass M and the mass ratio q of the progenitor binary. In computing the covariance matrix, we used, as described in the previous section, a signal model with seven parameters: $\lambda^k = \{M,\, j,\, q,\, D_{\rm L},\, \iota,\, \psi,\, \phi\}$. The full covariance matrix contains 7 variances C_{kk} and 21 covariances $C_{mk} = C_{km}$, $k \neq m$. The full set of results is too large as our covariance matrix contains 28 independent elements at each point in the $(M,\, q)$ plane. To save space, we have chosen a subset of these for further discussion.

We will discuss the error in the estimation $\sigma_k = \sqrt{C_{kk}}$ of 5 of the 7 parameters, $\lambda^k = \{M,\, j,\, q,\, D_{\rm L},\, \iota\}$, and also include in our discussion the covariance between the luminosity distance $D_{\rm L}$ and the inclination ι of the black hole's spin axis with the line-of-sight. Also, it is instructive to deal with the *correlation coefficient* defined as $c_{km} \equiv C_{km}/(\sigma_k\, \sigma_m)$, instead of the covariances themselves. Correlation coefficients are bound to the range $[-1,\, 1]$ and capture how variation in one parameter might be offset by varying another. A correlation coefficient of 0 for a pair of parameters indicates that they are completely independent of each other and have "orthogonally" different effects on the waveform. For instance, the amplitude A and phase φ of a simple sinusoid function $s(t) = A\, \sin[\omega\,(t - t_0) + \varphi]$ will have a correlation coefficient of 0, while the phase and time offset t_0 are perfectly anti-correlated and so have a correlation coefficient of -1 : A change in the phase cannot be mimicked by a change in the amplitude but it is completely replicated by a change in the time offset. Consequently, the amplitude is completely independent of the phase and time offset, while only one of phase or time offset can be considered to be an independent parameter[7]. When covariances are close to ± 1, the parameters concerned will have large uncertainties and this, as we shall see below, is a major source of error for the parameters[8] $(D_{\rm L},\, \iota)$.

Figures 2.7 and 2.8 plot fractional errors (i.e. $\sigma_{\lambda_k}/\lambda_k$) incurred in the measurement of the parameters $(M,\, q,\, j,\, D_{\rm L})$ and the absolute error in the parameter $\cos\iota$. We have also plotted the correlation coefficient $c_{D_{\rm L}\iota}$, labelled in the figure as ${\rm Cov}(D, \iota)$. Figure 2.7 corresponds to ET's observation of stellar and intermediate mass black holes in the range $[10,\, 1000]\, M_\odot$ and the mass ratio q of the progen-

[7] In fact, the Fisher matrix for the parameter set $(A,\, \varphi,\, t_0)$ will, as can easily be verified, be singular.

[8] This important point was noted recently by Nissanke et al [231].

itor binary in the range [2, 10]. Figure 2.8 corresponds to LISA's observation of supermassive black holes of mass M in the range $[3 \times 10^6,\ 10^8]\, M_\odot$ and mass ratio q in the range $[2, 25]$. In the case of aLIGO, in most of the parameter space and for all parameters (except the total mass), the fractional errors are larger than 50% and so they are not shown. Advanced LIGO will determine the total mass of an intermediate mass black hole that forms from the merger of two nearly equal mass black holes within 1 Gpc to within a few percents and this could be very interesting for some of the tests of general relativity to be discussed below.

Let us recall that our results for mass ratios greater than 11 are based on the extrapolation of analytical fits to numerical simulations of binary black hole mergers that are only available up to a mass ratio of $q = 11$. In the next few sections we will discuss our results in the context of the science questions they can address.

2.7.1 Mass ratio and component masses of the progenitor binary

A key result of our study is that one can measure the mass ratio of a progenitor binary by observing the ringdown signals emitted by the black hole that forms from the merger. While the different mode frequencies and time-constants all depend only on the mass of the black hole and its spin magnitude, their relative amplitudes depend on the mass ratio. As we have argued before, under certain circumstances it should be possible to measure the relative amplitudes of the different modes, thereby measure the mass ratio of the progenitor binary and hence deduce its component masses.

The top right panels of Figs. 2.7 and 2.8 show the fractional accuracy with which the mass ratio can be determined assuming that the signal is composed of three ringdown modes, namely (2,2), (3,3) and (2,1). ET will not measure the mass ratio very well in most of the parameter space. However, for equal mass mergers, ET should constrain the mass ratio to within 5%. Remarkably, LISA will be able to measure the mass ratio to better than 10% over 60% of the parameter space studied and black holes that result from the merger of equal mass black holes enable the determination of q to better than 1%.

Since the mass ratio of a binary is easily determined from the inspiral phase, its measurement also from the ringdown phase offers newer tests of general relativity.

2.7.2 Mass loss to gravitational radiation

In the process of inspiral and merger, a binary black hole emits a significant fraction (a few percent) of its mass as gravitational radiation. The total mass of a binary can be measured very accurately from the inspiral radiation it emits. Estimates[9] range from a fraction of a percent (for an equal mass binary black hole of total mass 200 $M_\odot$ at a distance of 1 Gpc) in the case of Einstein Telescope [232] to 50 parts per million (for an equal mass binary black hole of total mass $2 \times 10^6\, M_\odot$ at a distance of 3 Gpc) in the case of LISA [193]. For most binaries observed with ET and LISA, the total mass before merger can be measured with an error that is much smaller than the fraction of mass that is expected to be lost in gravitational radiation during merger.

What we see from the top left panels of Figs. 2.7 and 2.8 is that the mass of the final black hole that results from a merger can also be measured very accurately. ET cannot measure masses of stellar mass black holes very well but if intermediate mass black holes (and binaries composed of such black holes) exist, then ET will measure their masses to better than 1%, assuming the source is at 1 Gpc, over a significant range of the parameter space ($q \lesssim 6$ and $M > 400\, M_\odot$) we explored. A black hole that results from the merger of two black holes each of mass roughly about $500\, M_\odot$ could be measured to an accuracy of better than half-a-percent.

LISA is able to measure the mass of a supermassive black hole that it observes at a red-shift of $z = 1$ with an accuracy of better than 1% all over the parameter space that we explored. Masses of supermassive black holes that form from the merger of two roughly equal-mass ($q \lesssim 10$) black holes could be measured to an accuracy of 0.1%. This means that from the ringdown signal alone, we should be able to measure masses of supermassive black holes even at a red-shift of $z = 5$ to better than 1%.

It would, therefore, be very interesting to compare the observed mass loss with the predictions of analytical and numerical relativity and verify if the mass loss is in accord with their predictions. Such comparisons will put general relativity to new kinds of tests in the dissipative regime of the theory. Let us recall that the luminosity of a binary black hole, close to merger, could be as large as $10^{50}\,\mathrm{J\,s^{-1}}$,

[9]Note that most of the literature quotes error in the measurement of the chirp mass $\mathcal{M} \equiv M\,\nu^{3/5}$, where M is the total mass and ν is the symmetric mass ratio of the binary. To estimate the error in the total mass we have used the error propagation formula

$$\left(\frac{\sigma_M}{M}\right)^2 = \left(\frac{\sigma_{\mathcal{M}}}{\mathcal{M}}\right)^2 + \frac{9}{25}\left(\frac{\sigma_\nu}{\nu}\right)^2 - \frac{6}{5} c_{\mathcal{M},\nu} \left(\frac{\sigma_{\mathcal{M}}}{\mathcal{M}}\right)\left(\frac{\sigma_\nu}{\nu}\right).$$

where $c_{\mathcal{M},\nu}$ is the correlation coefficient of the parameters $\ln \mathcal{M}$ and $\ln \nu$.

which is arguably the largest luminosity any physical system could have. It would be very interesting to test the theory when the luminosity is as large as this.

These phenomenal accuracies with which masses can be measured raise the question if it is prudent to treat the mass of a binary to be constant in the course of its inspiral and merger. It might be possible to deduce the rate of mass loss by treating in our computation of the waveforms the mass of the system to be a function of time.

2.7.3 Exploring naked singularities

The magnitude and orientation of the spin of the final black hole that results from the merger of a black hole binary depend on a number of parameters of the progenitor binary: magnitudes and orientations of the spins of the two component black holes relative to the orbital angular momentum and the mass ratio of the progenitor binary. A spinning black hole binary has a rather large parameter space, six parameters more than a non-spinning system. Limited studies have been carried out in assessing how well one might be able to measure black hole spins from the inspiral phase of the merger of a black hole binary [233, 234]. Numerical relativity simulations of the merger of spinning black holes are still in their early stages. In the coming years we are likely to learn a great deal about spin dynamics of a binary before and after merger. While these are important problems to be addressed in the future, we recall that in this paper we have only studied binaries comprising of initially non-spinning black holes.

Figures 2.7 and 2.8, middle left panels, show how accurately one might be able to measure the spin magnitude j in ET and LISA, respectively. The accuracy here is not as good as in the case of the black hole mass. ET can deduce the final spin to within 10% over 40% of the parameter space and to better than 5% in 20% of the parameter space, for black holes that form within 1 Gpc. LISA, on the other hand, can measure spin magnitudes to better than 5% over 50% of the parameter space and to better than 1% over 20% of the parameter space for black holes that form within a red-shift of $z = 1$. Spins of black holes that form from the merger of nearly equal mass black holes can be measured to 0.5%. Thus, LISA should be able to reliably measure spin magnitudes that are only a few percent larger than 1. Measuring spin magnitudes to such a high accuracy will be useful in testing whether a merging binary results in a black hole or a naked singularity [185].

2.7.4 Spin orientations and the luminosity distance

The measurement accuracy of spin orientation, given by $\cos\iota$, is shown in the bottom left panels of Figs. 2.7 and 2.8. $\cos\iota$ can be measured to within 10% in about one-third of the parameter space in the case of ET and to better than 5% in about one-half of the parameter space in the case of LISA. The dynamics of spins before and after merger could be relevant in understanding the x-shaped radio galaxies [235].

The spin orientation of a black hole is very strongly correlated with the luminosity distance. We see from the bottom right panels that the correlation coefficient is close to either $+1$ or -1 in most of the parameter space. The transition from negative to positive correlation between $D_{\rm L}$ and $\cos\iota$ occurs when mass ratio $q \simeq 6$. The significance of this number is not clear to us at the moment. This correlation completely destroys the accuracy with which the luminosity distance can be measured. For instance, we see that in the case of ET $\sigma_{D_{\rm L}}/D_{\rm L}$ is in the range 5-10%, although the SNR in this region of the parameter space is ~ 300. The parameter $\cos\iota$ in this region is also determined rather poorly, at about 25%.

These numbers are better in the case of LISA: For 50% of the parameter space, LISA can measure the distance to within 10% but black holes that result from the merger of roughly equal mass systems might allow the luminosity distance to be determined to 1% or less. Using the inspiral phase alone, but with the help of subdominant signal harmonics, luminosity distance can be measured to a fraction of a percent in the case of LISA. Thus, it would be very interesting to see how similar are the distances obtained from these different phases of the merger dynamics.

2.8 Parametrization for testing the no-hair theorem

In this section we will consider a practical implementation of testing general relativity using quasi normal modes. To test general relativity with quasi-normal modes, it is *not* necessary to consider all the *physical* parameters but only those that are necessary to fully characterize the shape of the signal. The ringdown signal composed of a superposition of n quasi-normal modes can be written as

$$h(t) = \sum_{\ell,m} A_{\ell m} e^{-t/\tau_{\ell m}} \cos(\omega_{\ell m} t + \gamma_{\ell m}), \tag{2.42}$$

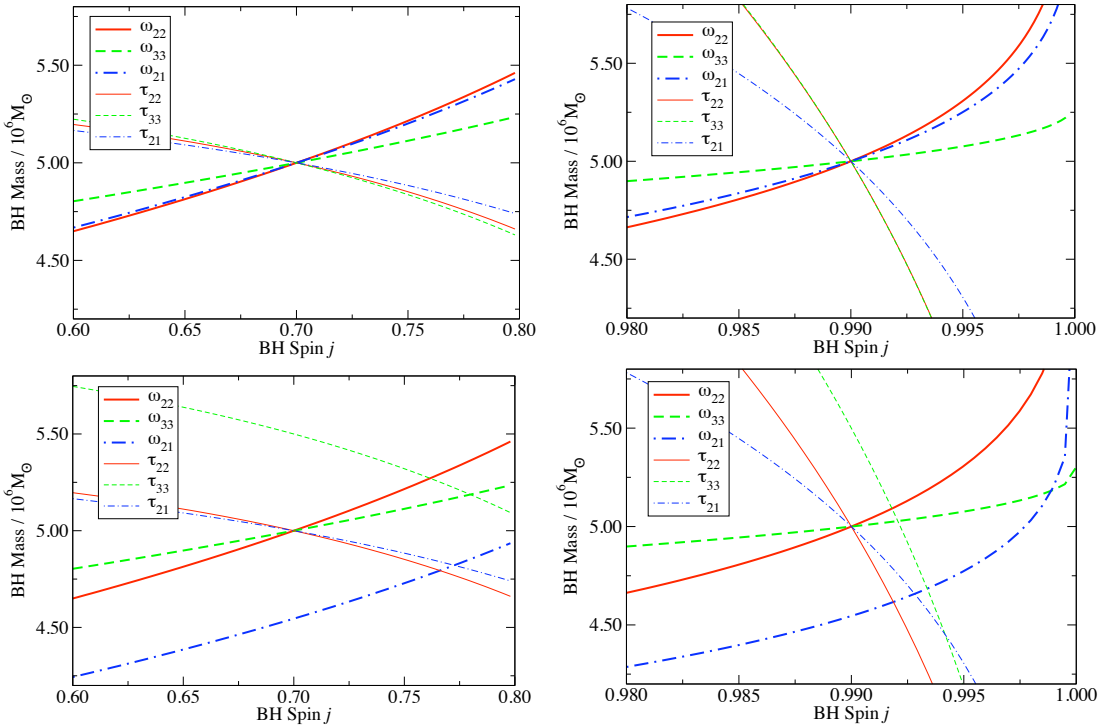

Figure 2.9: Curves of constant mode frequencies and time-constants in the $(M,\, j)$-plane obtained with Eqs. (2.43) for the (2,2) mode and similar equations for other modes. Top panels correspond to the case when all measured values are exactly as predicted by black hole perturbation theory. The bottom panels correspond to the case where the (3,3) and (2,1) mode frequencies and time constants differ from the GR value by 10% but the (2,2) frequency and time-constant are as in GR. An interesting thing to note is that for a large range of values of the black hole spin, the curves of constant τ_{22} and τ_{33} almost overlap, providing the opportunity for a more accurate test of the no-hair theorem. (see the text for details.)

where there are n each of the amplitudes $A_{\ell m}$, time-constants $\tau_{\ell m}$, frequencies $\omega_{\ell m}$ and phases $\gamma_{\ell m}$. The signal is, therefore, characterized by a set of $4n$ parameters in total.

2.8.1 Maximal set

The most exhaustive test of the no-hair theorem would be to treat all $4n$ parameters to be independent. Of the $4n$ parameters, only the $2n$ mode frequencies and time-constants would facilitate the test, the others should be retained in order to fully capture the covariances and variances in the $2n$ test parameters. The consistency among every mode frequency and time constant makes the test more stringent but the presence of a large number of parameters (when n is greater than 2) weakens the test. The reason for the latter is that a model with too many parameters will/should be penalized for its flexibility by any carefully formulated test. In a covariance matrix formulation of the test, this will be reflected by large variances in $\tau_{\ell m}$ and $\omega_{\ell m}$ (which are our test parameters) and in a Bayesian model selection a model with a larger number of parameters will suffer from having a large evidence.

How would the test work in practice? For each measured test parameter (and the associated error in its measurement), one could draw a curve (or a band including the error) in the $(M,\, j)$ plane, by using their expressions in general relativity in terms of the mass and spin of the black hole. If the curves/bands fail to intersect at a single point/region in the $(M,\, j)$ plane then that would invalidate general relativity or, alternatively, indicate that the object is not a black hole. The maximal set could be weak due to the large variances of the various parameters but strong because many different bands have to pass through the same region.

Let us illustrate how the test works with some examples. Let us suppose our signal model consists of a superposition of $(\ell,\, m) = (2,\, 2), (2,\, 1), (3,\, 3), (4,\, 4)$ modes. In this case the maximal set contains 16 parameters, of which 8 mode frequencies and time-constants are the test parameters. Let us denote by $\hat{\omega}_{\ell m}$ and $\hat{\tau}_{\ell m}$, the values of the mode frequencies and time-constants *measured* by projecting the data onto a superposition of quasi-normal modes as in Eq. (2.42). For each measured parameter, we can construct an equation in $(M,\, j)$ using the relation

between the parameter and $(M,\, j)$ given in Eqs. (2.27)-(2.30):

$$\begin{aligned}\hat{\omega}_{22} &= \frac{1}{M}\left[1.5251 - 1.1568(1-j)^{0.1292}\right], \\ \hat{\tau}_{22} &= \frac{2}{\omega_{22}}\left[0.7000 + 1.4187(1-j)^{-0.4990}\right],\end{aligned} \tag{2.43}$$

and similar equations for other modes. (Note that we have used $f_{22} = M\omega_{22}$ and $2\,Q_{\ell m} = \tau_{\ell m}\omega_{\ell m}$ in rewriting these equations as dimensionful quantities.) Measurement errors can be folded into the analysis by using

$$\begin{aligned}\hat{\omega}_{22} \pm \sigma_{\omega_{22}} &= \frac{1}{M}\left[1.5251 - 1.1568(1-j)^{0.1292}\right], \\ \hat{\tau}_{22} \pm \sigma_{\tau_{22}} &= \frac{2}{\omega_{22}}\left[0.7000 + 1.4187(1-j)^{-0.4990}\right],\end{aligned} \tag{2.44}$$

with similar equations for other modes.

For a $5\times10^6\,M_\odot$ black hole, the mode frequencies and time-constants for three different spin values $j = 0.1,\, 0.7,\, 0.9,\, 0.99$, are given in Table 2.4. If the ringdown

Table 2.4: The frequencies $F_{\ell m} = \omega_{\ell m}/(2\pi)$ (in mHz) and time-constants $\tau_{\ell m}$ (in s) of the first four dominant modes for a $5\times10^6 M_\odot$ black hole of different spin magnitudes j.

j	F_{22}	F_{21}	F_{33}	F_{44}	τ_{22}	τ_{21}	τ_{33}	τ_{44}
0.10	2.48	2.43	3.98	5.36	282	277	269	266
0.70	3.46	2.96	5.48	7.44	303	301	295	290
0.90	4.30	3.30	6.70	9.06	383	355	379	375
0.99	5.73	3.66	8.60	11.4	823	559	828	837

signal is consistent with the formation of a black hole with spin magnitude, say, $j = 0.7$ ($j = 0.99$) then the mode frequencies and time-constants would be precisely as in the 2nd (respectively, 4th) row of Table 2.4, modulo the errors in their measurement. Therefore, curves defined by $\omega_{\ell m}(M, j) = \hat{\omega}_{\ell m}$ and $\tau_{\ell m}(M, j) = \hat{\tau}_{\ell m}$ will all meet at a single point in the $(M,\, j)$ plane as in the upper two panels of Fig. 2.9, the point of intersection giving the mass and spin magnitude of the black hole. The left panel corresponds to the formation of a black hole of spin magnitude $j = 0.7$ and the right panel to $j = 0.99$, in both cases $M = 5\times10^6\,M_\odot$. If, however, one of the mode frequencies, say ω_{33} is different from the general relativistic value

by 10%, then the corresponding curves would fail to meet as shown in the lower two panels of Fig. 2.9.

If general relativity is true then some of the curves lie almost one on top of the other (e.g. $\omega_{22} = \text{const.}$ is almost identical to $\omega_{21} = \text{const.}$ in the $j = 0.7$ case and $\tau_{22} = \text{const.}$ is identical to $\tau_{33} = \text{const.}$ both in the $j = 0.7$ and $j = 0.99$ cases) but even a slight departure from general relativity will lead to big departures as demonstrated by the lower panels of the same figure. In any measurement the parameters are subject to statistical and systematic errors that must be folded into the analysis which will be taken up in a forthcoming study.

Do we need to treat all time-constants and mode frequencies to be independent in a test of the no-hair theorem? We shall argue below that it is not necessary to treat all $4n$ parameters to be independent; in fact, we shall see that the parametrization is not unique, offering a lot of flexibility in testing GR.

2.8.2 Minimal set

The minimal, or the simplest, model would consist of the smallest number of parameters needed to check the consistency between the modes as predicted by the no-hair theorem, yet large enough to capture all the variances and covariances between the parameters of interest. Since the mode frequencies and time-constants are all determined in GR by the mass M and spin magnitude j of the black hole, the smallest number of parameters required to test GR would be three: these could be any three time-constants or two time-constants and one mode frequency, and so on. It would then be necessary to express the other mode frequencies and time-constants in terms of *any two* of the three parameters that were taken to be independent. Two of the three independent parameters could be used to solve for (M, j). One could then see if the measured value of the third parameter is consistent with its predicted value based on the values of M and j. Let us note that without a prior knowledge of the amplitudes $A_{\ell m}$ and phases $\gamma_{\ell m}$ it will not be possible to measure the chosen time-constants and mode frequencies as they would induce covariances that cannot be neglected in estimating the errors incurred in their measurement. Thus, we (tentatively) conclude that the minimal set required for a signal model with n modes would be $2n + 3$. However, the three test parameters can be chosen in any way one wishes but choosing only three assures that the error in their measurement is the smallest. In this sense the minimal set could be a very stringent test of GR.

In reality, of course, the amplitudes of different modes are determined by the physical parameters $(M, j, q, D_{\rm L}, \theta, \varphi, \psi, \iota)$ (cf. the discussion at the beginning

of this section). We can assume the parameters (q, $D_{\rm L}$, θ, φ) to be known from the inspiral phase and (M, j) to be determined by the time-constants and/or mode frequencies of the ringdown signal. This leaves the two angles (ψ, ι). Thus, when n is greater than 2, it is not necessary to consider all mode amplitudes to be independent but just two of them. Thus the minimal set of parameters to be considered for testing the no-hair theorem is $n + 5$ (n phases, $\gamma_{\ell m}$, the 3 test parameters and the two angles ψ and ι).

2.9 Conclusions and future work

In this paper, we have explored what information can be extracted from a black hole's ringdown signal, wherein the perturbation is caused by the tidal deformation produced during the merger of two non-spinning black holes. To this end we used numerical simulations of the late inspiral and ringdown to estimate the relative amplitudes of the various modes excited. The simulations consisted of initially non-spinning black holes in quasi-circular orbits for several mass ratios, ranging from 1:1 to 1:11.

We find that several modes have large enough luminosity — or signal-to-noise ratio — to be detectable in LISA and ET. Specifically, in order of decreasing power, modes (2,2), (3,3), (2,1), (3,2), (4,4), (5,5), (4,3), (6,6), (5,4) and (4,2) for LISA and the first four to five modes for ET, have significant luminosities. Note that not all of these can necessarily be resolved, but it probably is the case for the first three (see below). In the analysis though, we decided to include only (2,2), (3,3) and (2,1), mainly because the available data were most accurate for those modes.

We argued that the ringdown signal depends on the mass ratio of the progenitor binary and that this can be measured, with an error that is estimated from a Fisher matrix analysis. We showed how the luminosities change with the mass ratio. Indeed, by constructing fits to the mode amplitudes in terms of the mass ratio, we were able to include this effect in the analysis and estimate the errors involved in the measurement of various parameters. An important issue was to determine the epoch when the ringdown phase starts, so as to evaluate the relative amplitudes at that point. This was taken to be the point where each mode's frequency stops having an upward trend. The epoch at which the peak luminosity is reached is slightly different for different modes, but the mode amplitudes were all measured at a time $10M$ after the peak luminosity of the 22 mode.

We computed the measurement errors of a number of other parameters for

ringdowns observed in LISA and ET. These include the black hole mass, its spin, luminosity distance and inclination angle and how these vary with the final BH mass and the binary mass ratio. If we do not consider initial BH spins, the inclination angle can be measured solely by observing the three most dominant modes of the ringdown waveform, assuming that these can be resolved.

Together, LISA and ET will be able to provide ample evidence for the distribution of supermassive, intermediate mass and stellar mass black holes, for a large part of the known Universe. For most of the parameter space, the reach of LISA for ringdowns is $z \sim 6$, while for ET at least $z \sim 0.8$. Also, by being able to measure the mass ratio, hints on the merger history and formation of black holes of a large range of masses could be inferred by studying ringdown signals.

A practical implementation for testing the no-hair theorem and deciding the nature of the compact object that results from the merger, was presented, illustrating several key components. We started by providing a general framework, which is based on the number of parameters necessary to apply the test. Specifically, using n modes, a generic test will use the $2n$ frequencies and time-constants. This test is implemented by plotting the $\omega_{\ell m}$ and $\tau_{\ell m}$ curves on the mass-spin plane of the final black hole, where all the curves should intersect inside the same region if the object is a black hole. A key point was that some of the curves are special, as they almost overlap and can be thus used to check for small deviations from general relativity.

Future work should extend the study to include numerical simulations of initially spinning black holes, as this corresponds to a more realistic scenario. Additionally, there is effort to produce more accurate numerical simulations so that less dominant modes could be studied when the mass ratio is large.

The current study has not investigated the question of decomposition of modes of a ringdown signal in real data. The SNRs of different modes, especially in the case of LISA, suggest that it should be possible to resolve the modes and carry out the proposed tests of general relativity. However, a more in-depth investigation needs to be done, for instance by using a Bayesian model selection to discriminate between different models. Given some prior information, the relative probability of two different multimode ringdown waveforms - injected in Gaussian and stationary noisy data - could be computed.

Finally, a Fisher matrix-based parameter estimation approach (such as the one presented in this work) may not be robust or accurate enough, especially when the parameter space is large and the signal-to-noise ratios are low [169]. For this reason, future studies should also involve parameter estimation in the context of

the afore mentioned Bayesian analysis, as well as a Bayesian approach to a test of the no-hair theorem. In the latter case the posterior joint probabilities of two different models, given the 'initial data', could be compared. The first hypothesis would be that the observed object is a black hole, while the second that either GR is incorrect or the merged object is not a black hole.

Chapter 3

From black holes to their progenitors: A full population study in measuring black hole binary parameters from ringdown signals

A perturbed black hole emits gravitational radiation, usually termed the ringdown signal, whose frequency and time-constant depends on the mass and spin of the black hole. I investigate the case of a binary black hole merger resulting from two initially non-spinning black holes of various mass ratios, in quasi-circular orbits. The observed ringdown signal will be determined, among other things, by the black hole's spin-axis orientation with respect to Earth, its sky position and polarization angle - parameters which can take any values in a particular observation. I have carried out a statistical analysis of the effect of these variables, focusing on detection and measurement of the multimode ringdown signals using the reformulated European LISA mission, Next Gravitational-Wave Observatory, NGO, the third generation ground-based observatory, Einstein Telescope and the advanced era detector, aLIGO. To the extent possible I have discussed the effect of these results on plausible event rates, as well as astrophysical implications concerning the formation and growth of supermassive and intermediate mass black holes.

3.1 Introduction

Astrophysical observations to date have provided sturdy evidence that black holes (BHs) may exist and play an important role in many physical processes [236, 237, 110]. With direct evidence still lacking, it is expected that observation of gravitational waves (GWs) from merged BHs will not only provide indisputable evidence for the existence of BHs, but also the ability to extract accurate information about the progenitor system and the BH.

The ringdown radiation consists of a superposition of, in principle, an infinite number of essentially damped sinusoids, termed quasi-normal modes. Their frequencies and time-constants depend only on the mass and spin of the BH – a consequence of the *no-hair* theorem [49]. In a recent work [58] we have argued that the amplitude terms of the various quasi-normal modes encode important information about the origin of the perturbation that caused them, such as the component masses of the progenitor binary. This allows performing parameter estimation on the system from the strong-field regime, as opposed to using the inspiral phase. However, in that study, as well as in previous studies of parameter estimation from ringdown signals [49, 186], only a small region of the parameter space was explored. In a realistic scenario, a BH ringdown signal can have any sky location and polarization. All the while, it could have originated from a BH with any spin-axis orientation with respect to Earth. These variables have a significant effect on the observed ringdown signal and a direct impact on the science we can achieve by observing GWs from merged BHs.

In the present study, I have investigated in detail how these angular parameters affect the detection and measurement of the ringdown signals. To this end, I have varied the angular parameters over their full range, thereby considering a large population of BH mergers. I have considered supermassive BHs (SMBHs of mass $\geq 10^6 M_\odot$) visible in NGO and intermediate mass BHs (IMBHs of mass $\sim 10^3 M_\odot$) observable in ET and aLIGO. I have computed the probability distribution functions of signal to noise ratios (SNR), as well as measurement errors of a chosen set of parameters, for a wide range of the BH mass and for mass ratios between 2 and 20. Finally, I translate these probabilities to proportions of observed events in NGO and ET that will yield parameter errors below certain thresholds and discuss how observations of ringdown signals could help in dealing with open questions on the existence and history of SMBHs and IMBHs.

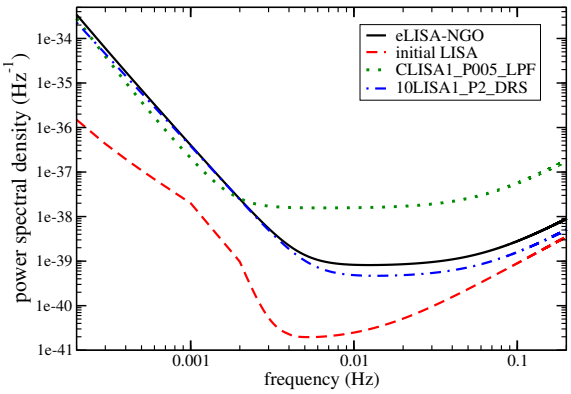

Figure 3.1: Noise power spectral densities for various proposed configurations of LISA-like space detectors. The dashed red line corresponds to the original LISA mission, while the rest of them refer to European designs of LISA. In all cases, the galactic binary white dwarf confusion noise [4, 5] is included, which has a negligible visible effect on the newer LISA curves though, due to their, almost two orders of magnitude worse sensitivity. Additionally, a low frequency cut-off - not shown - was induced at $5 \times 10^{-5} Hz$. In this study, I am using the latest arrangement for the European mission of LISA, labeled eLISA-NGO in this graph.

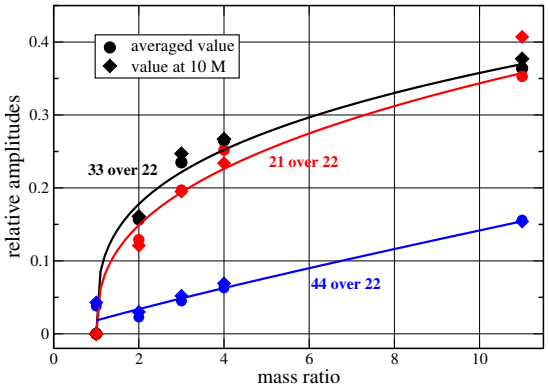

Figure 3.2: This plot shows the relative amplitudes of modes $(3,3)$, $(2,1)$ and $(4,4)$ over $(2,2)$ as a function of the mass ratio. The diamond points show the values that correspond to a time $10M$ after the peak luminosity of the 22 mode in the equal mass case (see also Fig. 2.3). Fits to these points were used in this previous work. On the other hand, the circle points, which are used in the present study, were computed by taking into account all the points in the waveform, in a time region starting at the peak luminosity of 22 and ending $30M$ later. The solid lines shown, constitute fits to these circle points, given by expressions (3.6)-(3.8).

3.2 Full population Analysis

I have closely followed the procedure of Ref. [58] for estimating the signal-to-noise ratios and measurement errors. In this Section I will discuss the signal model and the parameter space covered in this study.

In the generic case where we have a network of detectors, we write the response to a ringdown signal as:

$$h^a(t) = \sum_{\ell,m,n\geq 0} B^a_{\ell mn} e^{-t/\tau_{\ell mn}} \cos\left(\omega_{\ell mn} t + \gamma^a_{\ell mn}\right), \tag{3.1}$$

where the superscript a is an index denoting the detector in question and $\omega_{\ell mn}$, $\tau_{\ell mn}$ are the frequencies and time-constants of each mode, which are functions of the mass and spin magnitude of the BH. For further reference, see [35, 238]. In

this study I neglect modes with overtone index $n \geq 1$, thereby considering only the least damped modes. From now on, the n index (n=0) is omitted. The terms $B_{\ell m}$ and $\gamma_{\ell m}$ are the following combinations of the antenna pattern functions F^a_+, $F^a_\times$, amplitude factors $\alpha_{\ell m}$ and the angular functions $Y^{\ell m}_+(\iota)$, $Y^{\ell m}_\times(\iota)$:

$$B^a_{\ell m} = \frac{M\alpha_{\ell m}}{D_{\rm L}}\sqrt{\left(F^a_+\, Y^{\ell m}_+\right)^2 + \left(F^a_\times\, Y^{\ell m}_\times\right)^2}, \tag{3.2}$$

$$\gamma^a_{\ell m} = \phi_{\ell m} + m\,\phi + \tan^{-1}\left[\frac{F^a_\times\, Y^{\ell m}_\times}{F^a_+\, Y^{\ell m}_+}\right]. \tag{3.3}$$

Here, $\phi_{\ell m}$ are arbitrary constant phases of each mode. The effective amplitudes $B_{\ell m}$ vary inversely with the luminosity distance and proportionally to the intrinsic amplitudes $\alpha_{\ell m}$ of the modes, which are determined by the numerical simulations. The angular functions $Y^{\ell m}_{+,\times}(\iota)$ are the following combinations of the spin-weighted spherical harmonics [186]:

$$\begin{aligned} Y^{\ell m}_+(\iota) &\equiv {}_{-2}Y^{\ell m}(\iota,0) + (-1)^\ell\, {}_{-2}Y^{\ell -m}(\iota,0), \\ Y^{\ell m}_\times(\iota) &\equiv {}_{-2}Y^{\ell m}(\iota,0) - (-1)^\ell\, {}_{-2}Y^{\ell -m}(\iota,0). \end{aligned} \tag{3.4}$$

The antenna pattern functions are functions of the sky location coordinates, θ and ϕ and the polarization angle ψ, that is, $F^a_+(\theta,\varphi,\psi)$, $F^a_\times(\theta,\varphi,\psi)$. The spherical harmonics are angular functions of the inclination angle, ι and the azimuth angle ϕ. The first refers to the angle formed by the BH's spin angular momentum and the line-of-sight, while the latter is the azimuth angle defined in a non-rotating frame fixed to the BH.

3.2.1 Chosen waveform

The ringdown waveform used is of the form described by Eqs. (3.1)-(3.3). It is a signal comprised of four modes, with mode indices $(\ell, m, n) = (2,2,0), (3,3,0), (2,1,0), (4,4,0)$. Our choice is based on the ordering of the various modes according to power output, as determined from numerical simulations of non-spinning unequal mass binaries [58, 215, 49].

Numerical simulations of merging black-hole binaries were performed using the BAM code [66, 194], so as to obtain the amplitudes, $\alpha_{\ell m}$ of the various modes in Eq.(3.2), as well as their frequencies and time-constants (see also Table I of [58]). These simulations involve the case of *initially non-spinning* BHs in quasi-circular orbits and for different mass ratios of the binary. For the mass ratios, $q = \{1,2,3,4\}$ the simulation results were first presented in [198, 201, 81], while

an additional simulation of a $q = 11$ binary was carried out in [58].

The amplitude terms $\alpha_{\ell m}$ in Eq. 3.2, are given by the expressions:

$$\alpha_{22}(q) = 0.25\, e^{-q/7.5}, \tag{3.5}$$

$$\alpha_{33}(q) = 0.18\, \alpha_{22}(q)\, (q-1)^{0.32}, \tag{3.6}$$

$$\alpha_{21}(q) = 0.15\, \alpha_{22}(q)\, (q-1)^{0.38}, \tag{3.7}$$

$$\alpha_{44}(q) = 0.018\, \alpha_{22}(q)\, q^{0.89}. \tag{3.8}$$

These constitute fits, that were produced by fitting the merger-ringdown part of the numerical simulations data, taking into account all the different mass ratios for which these were performed. All points in a time region beginning at the peak luminosity of 22 and ending $30M$ later were considered, for each mass ratio. As opposed to the method that was applied in our previous work [58], where the relative amplitude values at $10M$ were used, this approach is expected to be more robust and to average out any numerical noise that might be present in this part of the waveform. Nevertheless, as can be seen from Fig. 3.2, these two methods do not give very different results. Note also that the above fitting functions, as well as the mode frequencies and time-constants, may be less accurate in the higher mass ratio values of around 20, where extrapolation has been performed.

3.2.2 The simulations

In Ref. [58] we had ignored the effect of the various angles $\{\theta, \varphi, \psi, \iota\}$ on the quasi-normal mode spectrum and their impact on the detection and measurement of ringdown signals. To assess this effect, the aforementioned analysis was repeated by varying the angular parameters $\{\theta, \varphi, \psi, \iota\}$. Specifically, six uniformly spaced values were chosen for these angles. This results in $6^4 = 1296$ distinct relative orientations between the detector and the BH and its spin axis. Additionally, a couple of simulations with eight uniformly spaced values were performed, that is $8^4 = 4096$ configurations, to allow the comparison. Hence, it was decided that six values in each parameter was acceptable in capturing the behaviour of the observable quantities.

The values in the polarization angle, ψ and the azimuth sky location angle, φ were linearly sampled in the ranges $[0, \pi]$ and $[0, 2\pi]$ respectively. Whereas, the values in the inclination angle ι and sky position, θ - which range from 0 to π - are deduced from the uniformly spaced values of $\cos(\iota)$ and $\cos(\theta)$ in the range $[-1, +1]$. Note that this excludes configurations of optimally oriented binaries,

that is of $\iota = 0$ and $\iota = \pi$.

3.2.3 The parameter space

The parameter set of the ringdown signal in the case of a non-spinning black hole binary, consists of the following nine parameters: $\{M,\, j,\, q,\, D_{\rm L},\, \theta,\, \varphi,\, \psi,\, \iota,\, \phi\}$. Namely, the mass M, the dimensionless Kerr parameter or spin magnitude, j of the BH, the mass ratio q of the progenitor binary, the sky location vector $(D_{\rm L},\, \theta,\, \varphi)$ of the BH with respect to Earth, the polarization angle ψ, the inclination angle ι and the BH azimuth angle ϕ. Note however, that in this case, the final spin of the BH is directly mapped to the mass ratio of the progenitor binary, therefore q and j are not treated as independent.

The above parameters are the standard ones, as they pertain to all of the modes. Additional parameters can be introduced, that are characteristic to each mode, such as an initial phase factor $\phi_{\ell m}$, see Eq. (3.3). Therefore, the total number of parameters can increase with the number of modes. We are considering a four mode signal, therefore we have a total of 13 parameters. One thing to note is that the $\ell = m$ modes have a nearly consistent rotational phasing, while the $\ell \neq m$ modes seem to have somewhat distinct associated dynamics, with differentiated amplitude and phasing during the merger process [215].

By virtue of the large number of parameters involved, it was unmanageable to treat the effect of all of them in this analysis. Thus, some of the above mentioned parameters had to be fixed. Specifically, the initial phase angles, $\phi_{\ell m0}$ in all the four modes considered, were chosen as zero. In addition, the luminosity distance is chosen to be 6.73 Gpc for NGO, and 1 Gpc for ET and aLIGO. Lastly, the BH azimuth angle, ϕ was given the value $\pi/3$. Note that this angle does not have an effect on the SNR, but of course needs to be considered in the waveform.

3.2.4 Choice of masses and mass ratios

The BH mass and the binary mass ratio constitute key parameters and the results depend quite strongly on them. The reasoning behind the choice of mass values is the following. First of all, the low and high mass end is limited by the sensitivity band of the detectors. The existence of BHs in the mass range $10^5 - 10^6 M_\odot$, is highly predicted by the mass - velocity dispersion in the galactic bulge of low-mass, low-luminosity galaxies, as well as in a number of galaxies which contain active galactic nuclei [93, 94]. The evidence for SMBHs ranging from $10^6 M_\odot$ to $10^9 M_\odot$, is quite abundant. They are thought to dwell at the centers of most galaxies. For various recent SMBHs mass estimation results and methods see for instance

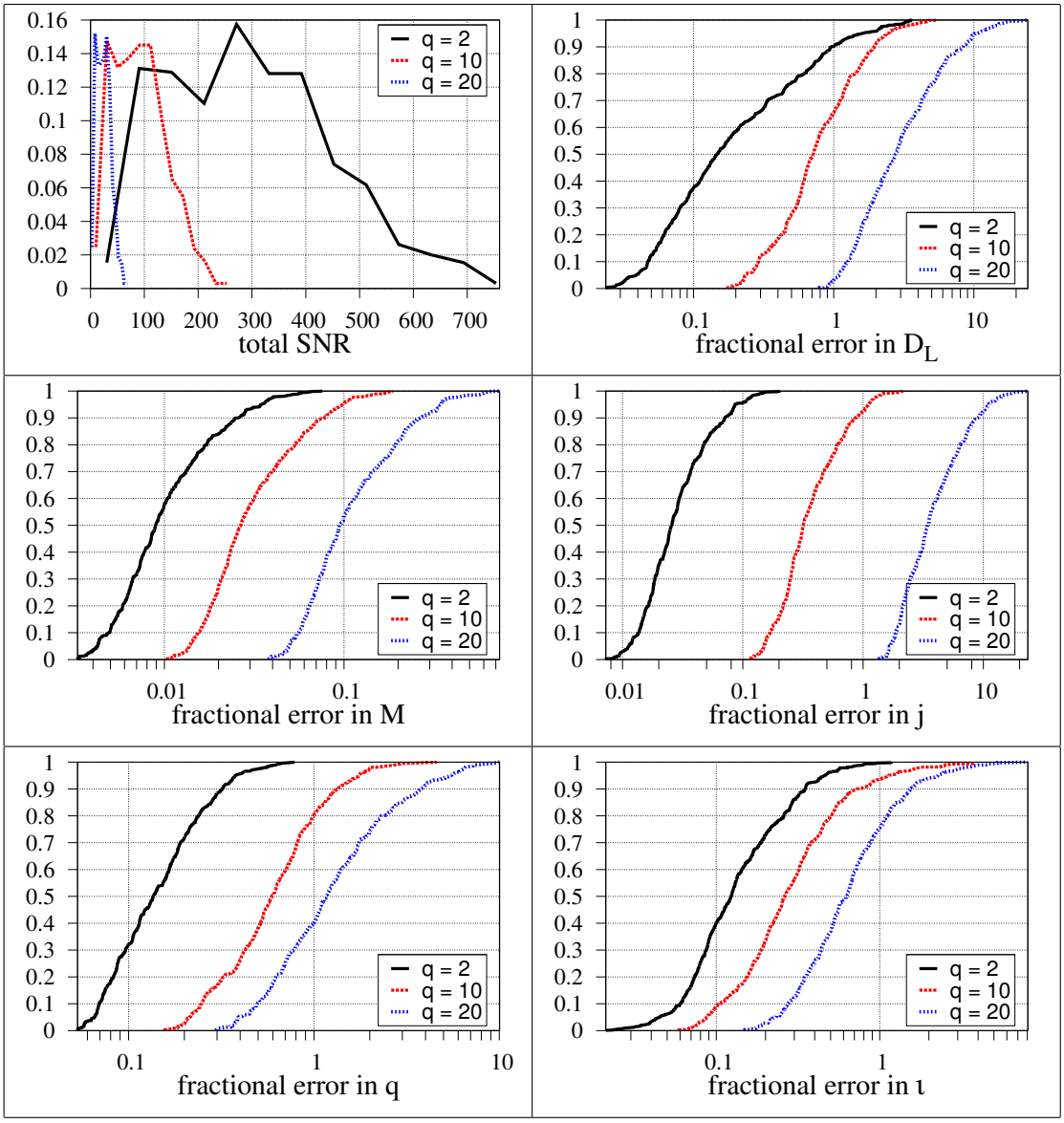

Figure 3.3: Frequency distributions for the total SNR and the measurement errors in NGO, for a $5\times10^6 M_\odot$ BH situated at a luminosity distance of 6.73 Gpc ($z \simeq 1$). The top left plot shows the probability to have a detector-BH configuration which will yield the SNR shown, while the rest of the plots concern cumulative frequency distributions for the measurement errors. In each graph, the comparison is shown among different mass ratios, q, specifically taking the values of 2, 10 and 20. For q=2 - black solid lines - the parameter estimation for the BH mass and spin is outstanding in all configurations. This effectiveness degrades considerably with increasing q. For q of around 10 it is still acceptable, while at q$\simeq$20, all parameters except the mass are very likely to have huge errors, of the order of 200%.

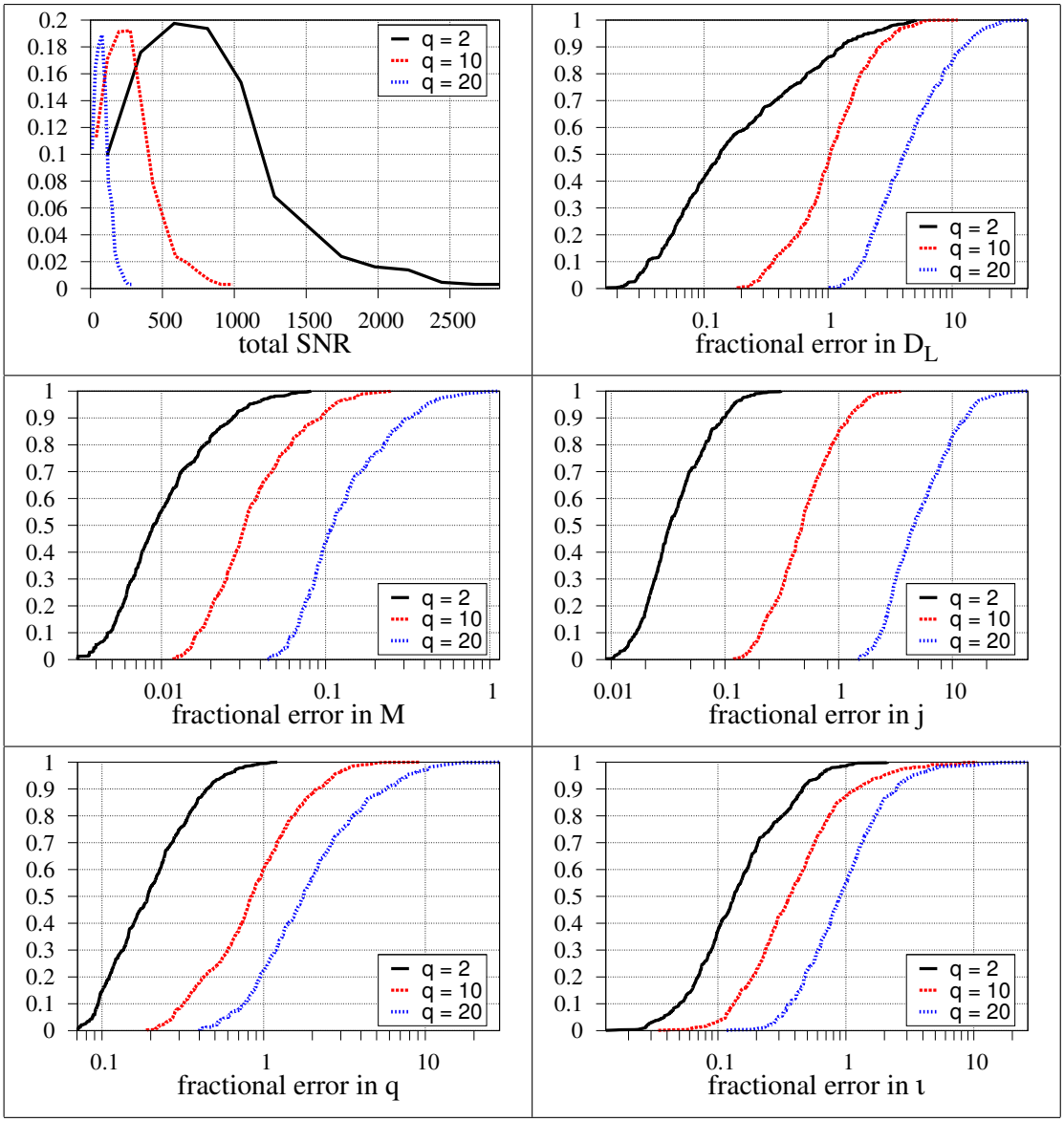

Figure 3.4: Same as in Fig. 3.3, but concerning a $25 \times 10^6 M_\odot$ BH. This figure concerns a BH 5 times more massive than that of Fig. 3.3, but some of the results are actually slightly worse, as the multimodal signal's power spectrum is shifted away from the lowest part of NGO's sensitivity curve.

[95, 96, 97, 98, 99]. The SNR in NGO is quite low for BH masses of less than about $5 \times 10^5 M_\odot$. I take the lower end of the mass range to be $5 \times 10^6 M_\odot$ and consider two other values of $25 \times 10^6 M_\odot$ and a $10^8 M_\odot$ BH, to cover the interesting range of masses potentially observable in NGO.

In the case of ET and aLIGO I have considered three IMBHs of mass $200 M_\odot$, $600 M_\odot$ and $1000 M_\odot$. It is believed that BHs in this range are situated in the centers of many globular clusters. However, their existence is being questioned, the evidence is thought to be strong but circumstantial [239, 94, 240, 111, 241].

Concerning the mass ratios, only unequal mass binaries are presented, except for one case in aLIGO. We do not consider the equal mass case as such systems are not as likely to occur in nature as slightly asymmetric ones. For NGO we examine the mass ratios of 2, 10 and 20, whilst lower mass ratios of 2, 5 and 10 are considered for ET. We, therefore, have in total, 9 different sets of simulations for each detector. Let me emphasize here that there is a possibility that massive BH binaries in the early universe ($z \leq 10$) will have a mass ratio significantly larger than one. For instance, in [242] it is suggested that low-redshift massive BH mergers occur predominantly with a mass ratio of 10 or higher.

3.3 Signal detectability and Parameter estimation

I will discuss the total signal to noise ratio, as well as the fractional errors in estimating the following 5 parameters: $\{M,\, j,\, q,\, D_{\rm L},\, \iota\}$. These errors are actually the quantities, $\sigma_\lambda = \sqrt{C_{\lambda\lambda}}$, which are computed from the covariance matrix, $C_{\ell m}$ [227, 170, 228, 167].

The results from all the distinct arrangements of the system (see Section 3.2.2) are presented via cumulative frequency distribution plots. That is to say, the different system configurations are classified according to the value they render in the error of the observable quantity in question. The proportion of a number of occurrences in a small width of values should, to a good approximation, equal the probability that a randomly placed observer will measure that quantity to take this range of values.

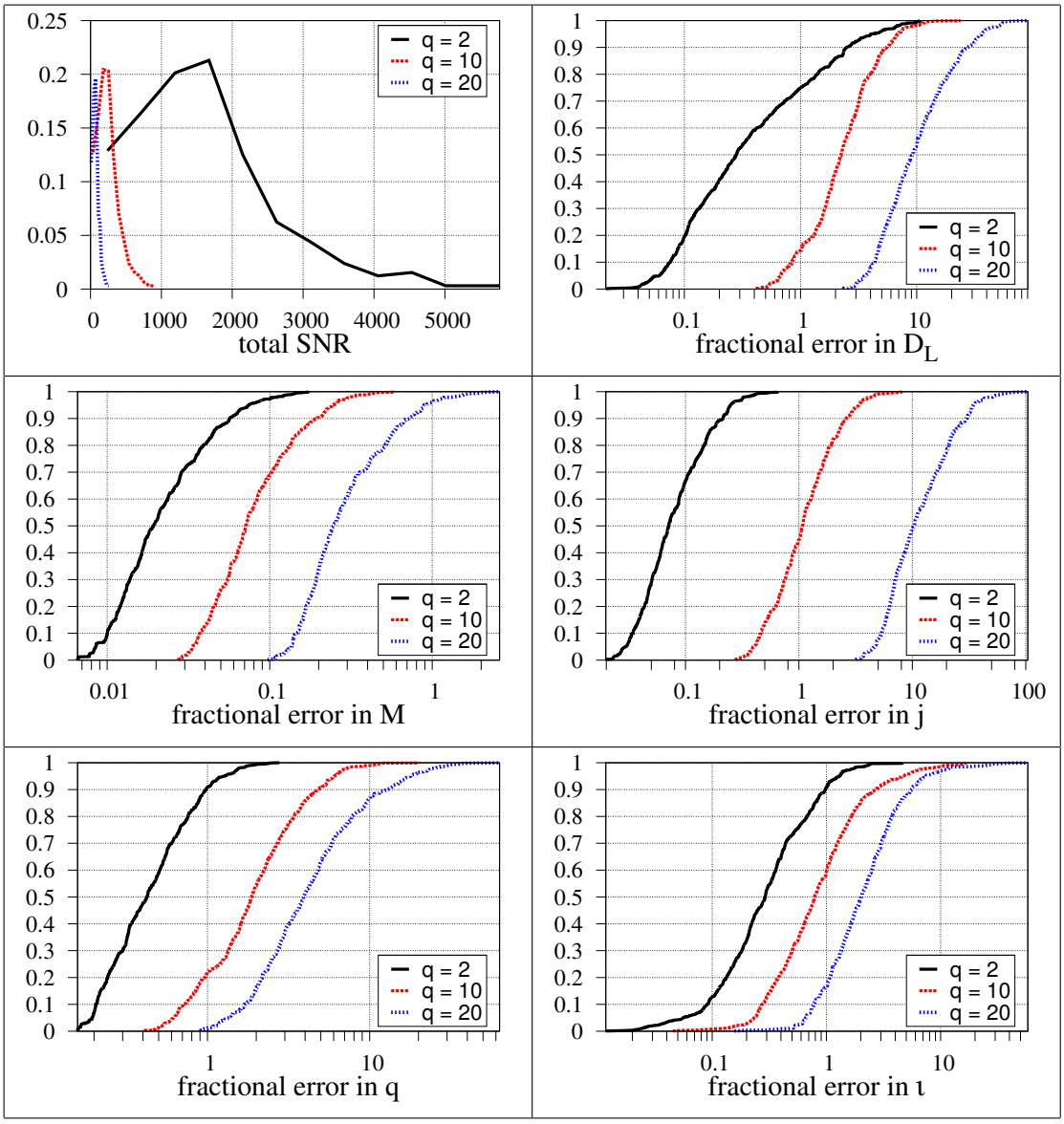

Figure 3.5: Same as in Figs. 3.3 and 3.4, but for a $10^8 M_\odot$ BH. The results slightly deteriorate with respect to the lower mass BH of Fig. 3.4.

3.3.1 NGO

The sensitivity curve[1] that we use is what is thought to be possible for NGO and it is contrasted with other LISA-like sensitivity curves in Fig. 3.1. It refers to a 4-link interferometer, comprised of one mother and two daughter spacecraft, having armlengths of $10^9 m$ and trailing a few degrees behind the Earth, in heliocentric orbit.

The main noise contributions are the acceleration noise, the shot noise, as well as some other measurement noise. These are respectively:

$$\begin{aligned} S_{acc,m}(f) &= 1.37 \times 10^{-32}(1 + \frac{10^{-4}}{f})f^{-4}\ m^2 Hz^{-1}, \\ S_{SN,m} &= 5.25 \times 10^{-23}\ m^2 Hz^{-1}, \\ S_{OMN,m} &= 6.28 \times 10^{-23}\ m^2 Hz^{-1}. \end{aligned}$$

The formula for the amplitude sensitivity curve is,

$$\sqrt{S_h(f)} = \sqrt{5}\frac{2}{\sqrt{3}}T(f)\frac{\sqrt{4S_{acc} + S_{SN} + S_{OMN}}}{L}\ Hz^{-1/2}, \tag{3.9}$$

while the transfer function is

$$T(f) = \sqrt{1 + \left(\frac{f}{0.41\left(\frac{c}{2L}\right)}\right)^2}.$$

with $L = 10^9 m$ and $c = 299,792,458$ metres per second.

3.3.2 Results for NGO

Our results for NGO are plotted in Figs. 3.3-3.5. For the $5 \times 10^6 M_\odot$, $25 \times 10^6 M_\odot$ and $10^8 M_\odot$ BHs the SNR curves (top left subplots of Figs. 3.3-3.5) peak at around 300, 600 and 1700 respectively. Relative frequency distributions were chosen for their plotting, as they portray clearly where the maximum occurs, as well as how they fall off. The higher mass ratio SNR curves have a similar outline. The fact that all of the curves resemble log-normal distributions, with steep risings and long tails, is mostly attributed to the fact that only a small fraction of the configurations, those close to the optimal orientation of the binary, will yield the highest SNRs.

Regarding the rest of the plots in Figs. 3.3-3.5, the general trend is that the mass and spin have comparable, low fractional errors, whilst the other group of

[1] see https://lisa-light.aei.mpg.de/bin/view/DetectorConfigurations

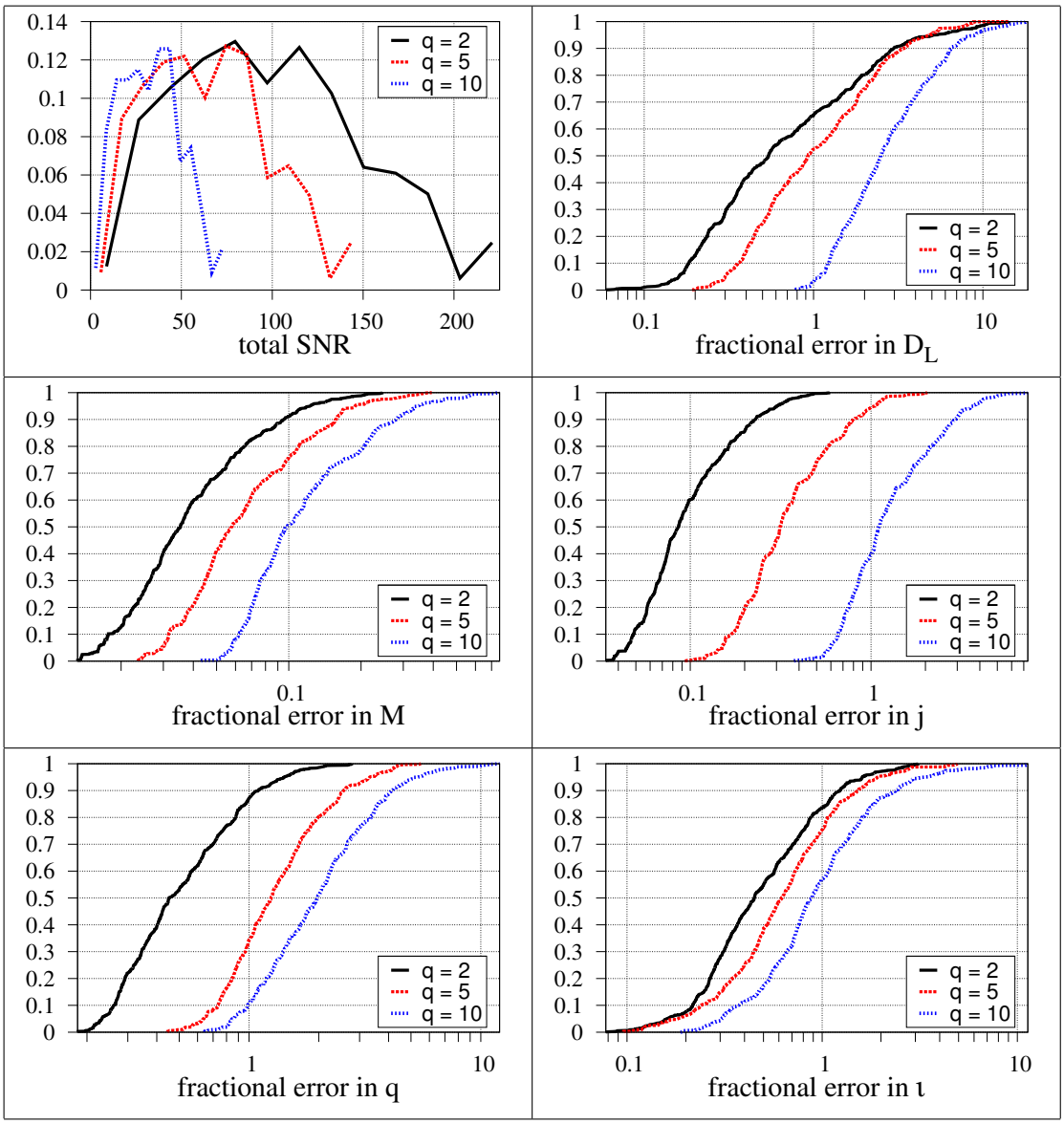

Figure 3.6: Similar graphs as those in Figs. 3.3 - 3.5, although for the ET detector, concerning a IMBH of $200M_{\odot}$. The luminosity distance of the BH is now picked closer, at 1 Gpc ($z \simeq 0.2$). Also, note that the progenitor mass ratios now take lower values, namely 2, 5 and 10.

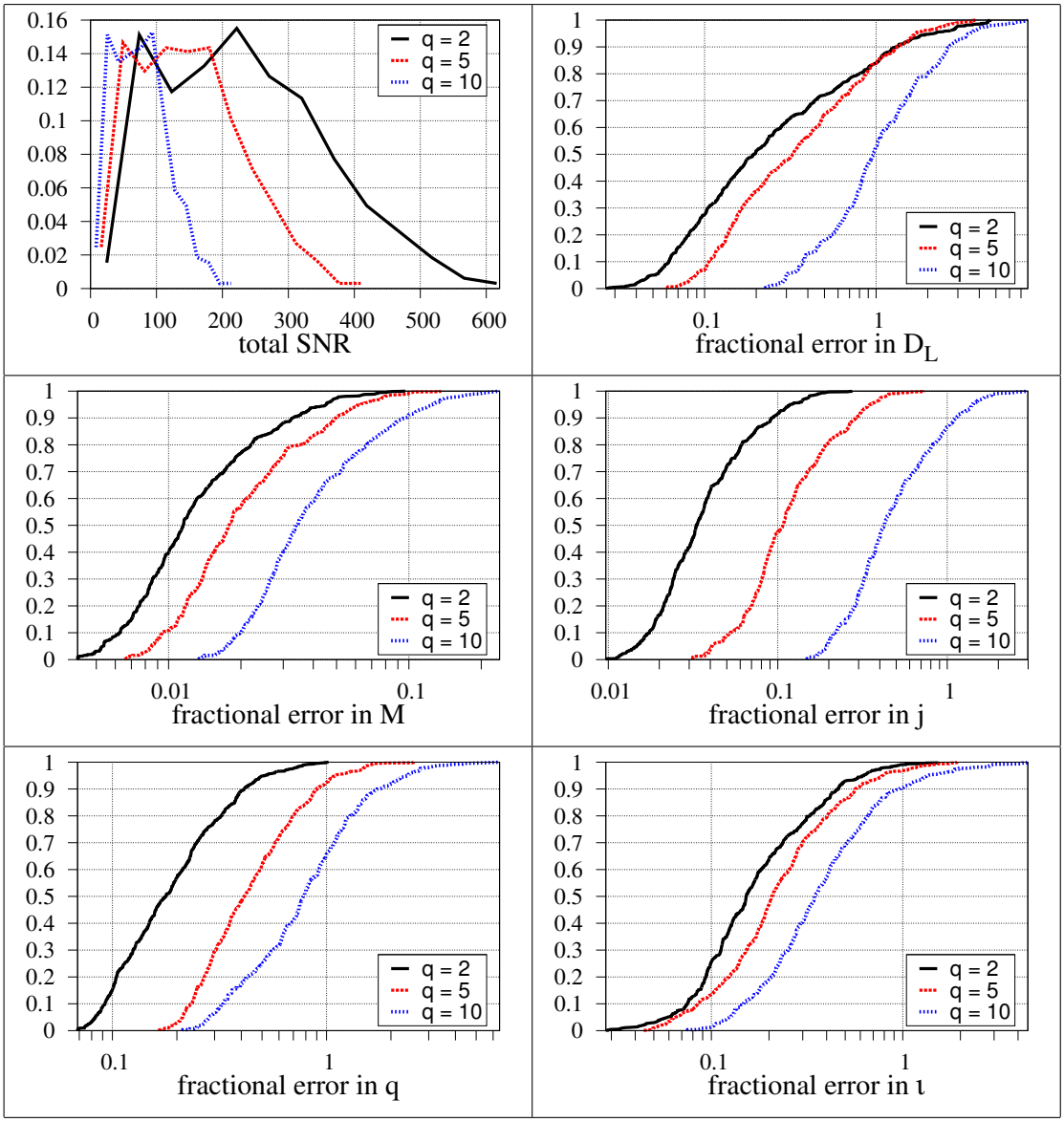

Figure 3.7: As in Fig. 3.6, but for a $600M_\odot$ black hole.

parameters, namely the luminosity distance, mass ratio and inclination angle, yield an order of magnitude higher error values. This is not surprising, considering that the mass and spin have a direct effect on the modes' frequencies, $\omega_{\ell mn}$ and time-constants, $\tau_{\ell mn}$, quantities that determine to first order the shape of the ringdown waveform.

Quoting a few numbers for a progenitor of mass ratio 2, the probability to get a binary merger event that will yield a mass error less than 1% is correspondingly 58%, 55% and 10%, as we go from the lower mass to the higher mass value. The lowest mass value actually gives the best results, whereas the signal's main power content takes place near the lowest sensitivity area of the NGO detector. The

spin magnitude exhibits a similar trend with the probabilities to fall below a 10% fractional error being 96%, 90% and 67% respectively.

For the second group of parameters, I again quote how likely it is to do better than 10%. For the luminosity distance, the values are 38%, 41% and 20%, corresponding to the BH masses $5 \times 10^6 M_\odot$, $25 \times 10^6 M_\odot$ and $10^8 M_\odot$. The mass ratio is harder to determine accurately, with the likelihoods being 32%, 15% and only 2% respectively. Lastly, there is a 40%, 37% and 13% likelihood of achieving an accuracy better than 10% in the inclination angle.

3.3.3 Einstein Telescope and Advanced LIGO

ET's very low sensitivity curve accounts for impressive results in the mass range $\sim 500 M_\odot$ to $\sim 1000 M_\odot$ and for mass ratios between 1 and 5. I consider the sensitivity curve designated ET-B [223], whose noise power spectral density is given by $S_h(f) = 10^{-50} h_n(f)^2\,\mathrm{Hz}^{-1}$, with:

$$\begin{aligned} h_n(f) &= 2.39 \times 10^{-27}\, x^{-15.64} + 0.349\, x^{-2.145} \\ &+ 1.76\, x^{-0.12} + 0.409\, x^{1.10}, \end{aligned} \tag{3.10}$$

where $x = f/100\,\mathrm{Hz}$.

As for advanced LIGO, the noise spectral density is [2]

$$\begin{aligned} S_h(f) &= 10^{-49} \Bigg[10^{16 - 4\,(f-7.9)^2} + 0.08\, x^{-4.69} \\ &+ 123.35\, \frac{1 - 0.23\, x^2 + 0.0764\, x^4}{1 + 0.17\, x^2} \Bigg]\, \mathrm{Hz}^{-1}, \end{aligned} \tag{3.11}$$

where $x = f/215\,\mathrm{Hz}$.

3.3.4 Results for ET and aLIGO

The results obtained for ET and advanced LIGO are plotted in Figs. 3.6-3.9. We fix the luminosity distance of the BH to be 1 Gpc. For the lowest mass considered (a $200 M_\odot$ BH) although the SNR could be pretty high (in the range 30-200), errors in the estimation of parameters are poor (see Fig. 3.6). $\{D_L, q, \iota\}$ have 50% probability to be measured to an accuracy of $\sim 50\%$, while errors on $\{M, j\}$ are

[2] This fit was provided by C. Capano, Syracuse University and is tuned for detecting binary neutron stars.

90% and 60% likely to be below 10%. For the higher mass ratios the results, as expected, are worse.

The results for $600M_\odot$ and $1000M_\odot$ BHs are shown in Figs. 3.7 and 3.8. The parameter estimation accuracies for these systems observed with ET is almost as good as that for a SMBH with NGO. Referring to the heaviest BH and mass ratio in the range 2-5, it is 100%-99% and 96%-53% likely to acquire errors below 10% for the BH mass and spin. For the $\{D_L, q, \iota\}$, the efficiencies are correspondingly 50%-15%, 23%-0% and 60%-17%. The results are similar for the $600M_\odot$ case (see Fig. 3.7).

Fig. 3.9 shows two examples for aLIGO: a BH resulting from an equal mass binary and one for which the mass ratio is 5. Most configurations give ringdown SNR values in the range 10 to 30, not large enough for a good estimation of parameters. This translates to a 30% likelihood for a fair measurement of 10% accuracy in the mass and mass ratio, while the luminosity distance, spin and inclination angles are all measured to accuracies far worse than 10%.

3.4 Astrophysical implications

3.4.1 Supermassive black holes

The presence of SMBHs in the centers of massive galaxies seems to be a well established fact. Detecting their gravitational wave signals can give additional clues on their spatial[3] and mass distribution, as well as help discriminate among the different scenarios of their formation and growth. This could be done, for instance, by measuring the BH mass function as a function of red-shift. Additionally, determining the mass ratios [58] of these early universe merger events will be an important piece of information in selecting out the current models on SMBH formation. Note that, in NGO, BHs of mass higher than $10^{7-8}M_\odot$ are visible almost entirely due to the ringdown signal that they emit rather than the inspiral signal.

Several studies have been realized in the field of predicting the coalescence rates of SMBHs [101, 102, 103, 104, 105, 106, 107, 108]. Let us admit an event rate of $\sim 10\ yr^{-1}$ at $z \simeq 1$, which ascertains a scenario of most efficient BH coalescence [243]. Then, assuming that the BH masses are both around $5\times10^6 M_\odot$, Figs. 3.3 and 3.4, there is a good chance that in 6 of the events, the BH mass will be measured more accurately than 1% and that in 9 of the events the BH

[3]Unless the inspiral phase is inside NGO's band, it will not be possible to determine the sky position of the signal. The only hope in this case would be the existence of an electromagnetic counterpart to the merger event.

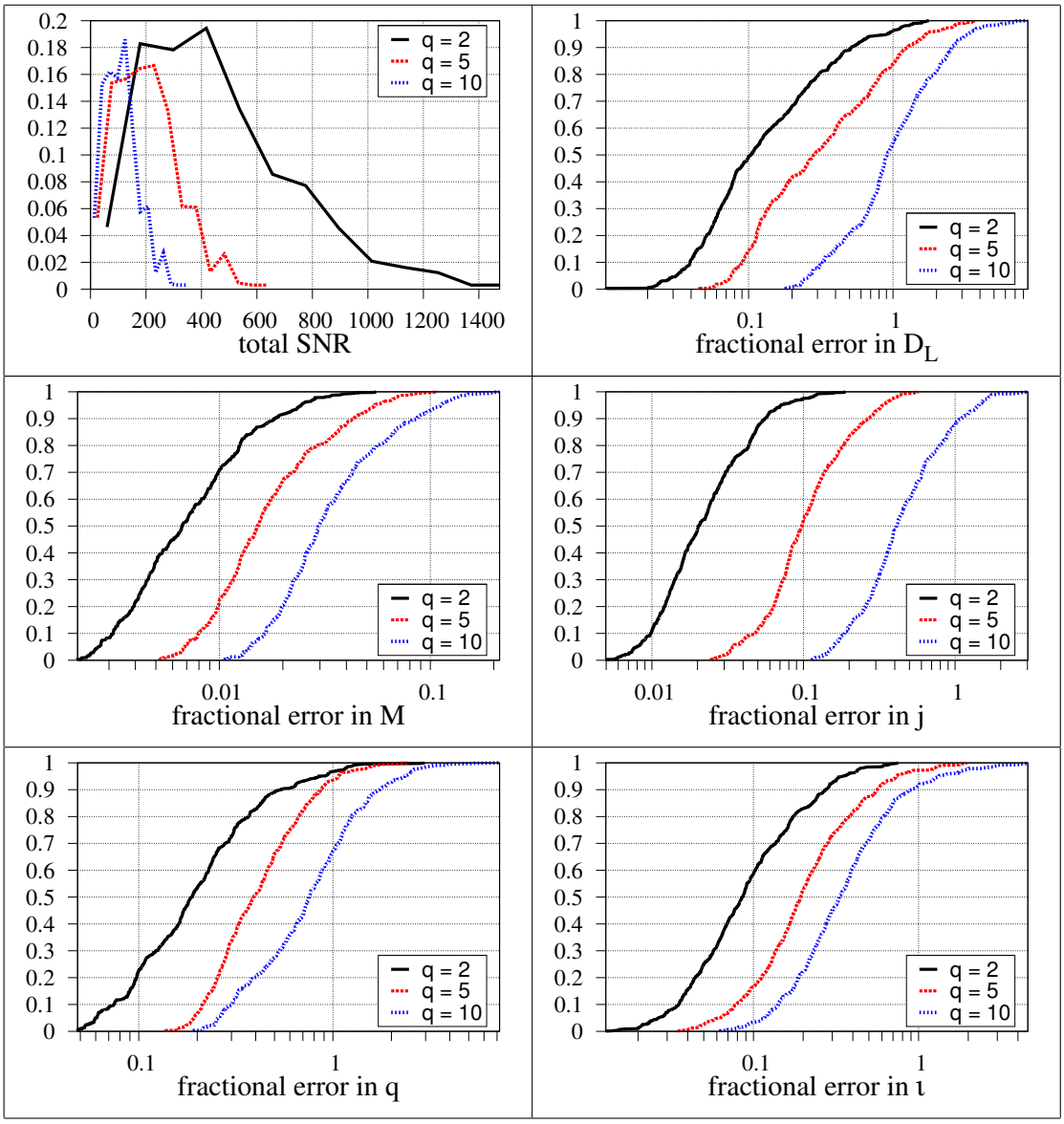

Figure 3.8: As in Figs. 3.6 and 3.7, but for a $1000M_\odot$ BH, a sweet spot in ET. The results are very encouraging for this size of BH and distance, with a very high probability to get errors lower than 10% in most of the parameters at mass ratios 2-5.

spin magnitude will have an accuracy better than 10%. As for the parameters $\{D_L, q, \iota\}$, in approximately 3-4 of the events they will feature errors lower than 10%, while in 7 of the events, the errors will lie below 30% for D_L and below 20% for q and ι.

Let me clarify that ringdown signals in NGO, will be detectable out to about $z \simeq 5$, but the distance of $z = 1$ was chosen to make the quote on the errors. If we take the distance at $z = 3$, an optimistic rate of merger events will be of the order of 100 [243]. If we assume that they all involve BHs of masses $\simeq$ 2-3 $\times 10^6 M_\odot$, then in around 90 of them the error[4] in the mass will be below 10% and in 60 of them the spin magnitude error will fall below the 10% threshold. For the rest of the parameters, about 50 of the observed events should yield measurements better than 50% accuracy. Although this looks poor at the outset, it should suffice for a statistical test of different models of BH formation and growth.

3.4.2 Intermediate-mass black holes

The existence of intermediate-mass black holes remains uncertain, as is their mass distribution. Colliding globular clusters in interacting galaxies could be a mechanism to obtain a compact binary IMBH system [109, 110]. Another possibility could be the formation of a binary IMBH inside a young dense stellar cluster, especially when the fraction of binary stars is adequately high [111].

Estimates of IMBH-IMBH coalescence rates can be found in [7, 111, 110, 112]. A relatively optimistic rate is $R_{opt} = 0.007\, GC^{-1}Gyr^{-1}$, where it has been assumed that 10% of star clusters are sufficiently massive and have a sufficient stellar binary fraction to form an IMBH-IMBH binary once in their lifetime, taken at 13.8 Gyr. The maximum possible rate would come from assuming that all of the star clusters satisfied the above conditions. The corresponding rate value is then $R_{max} = 0.07$ $GC^{-1}Gyr^{-1}$.

If the number of relatively luminous galaxies within a distance of 1 Gpc is approximately 5.3×10^7, [113] and the number of young dense stellar clusters per such galaxy is of the order of 100, then the optimistic estimate gives 0.037 events per year, while the maximum rate would be 0.37 events per year. An event within this distance will in some likelihood, involve IMBHs with masses between $\sim 6 \times 10^2 M_\odot$ and $\sim 10^3 M_\odot$ which means a relatively fair chance for errors to be low for several of the parameters using Einstein Telescope (see Figs. 3.7, 3.8).

[4]An additional simulation at $z = 3$, of a $5 \times 10^6 M_\odot$ BH, with a progenitor mass ratio of 2 was performed.

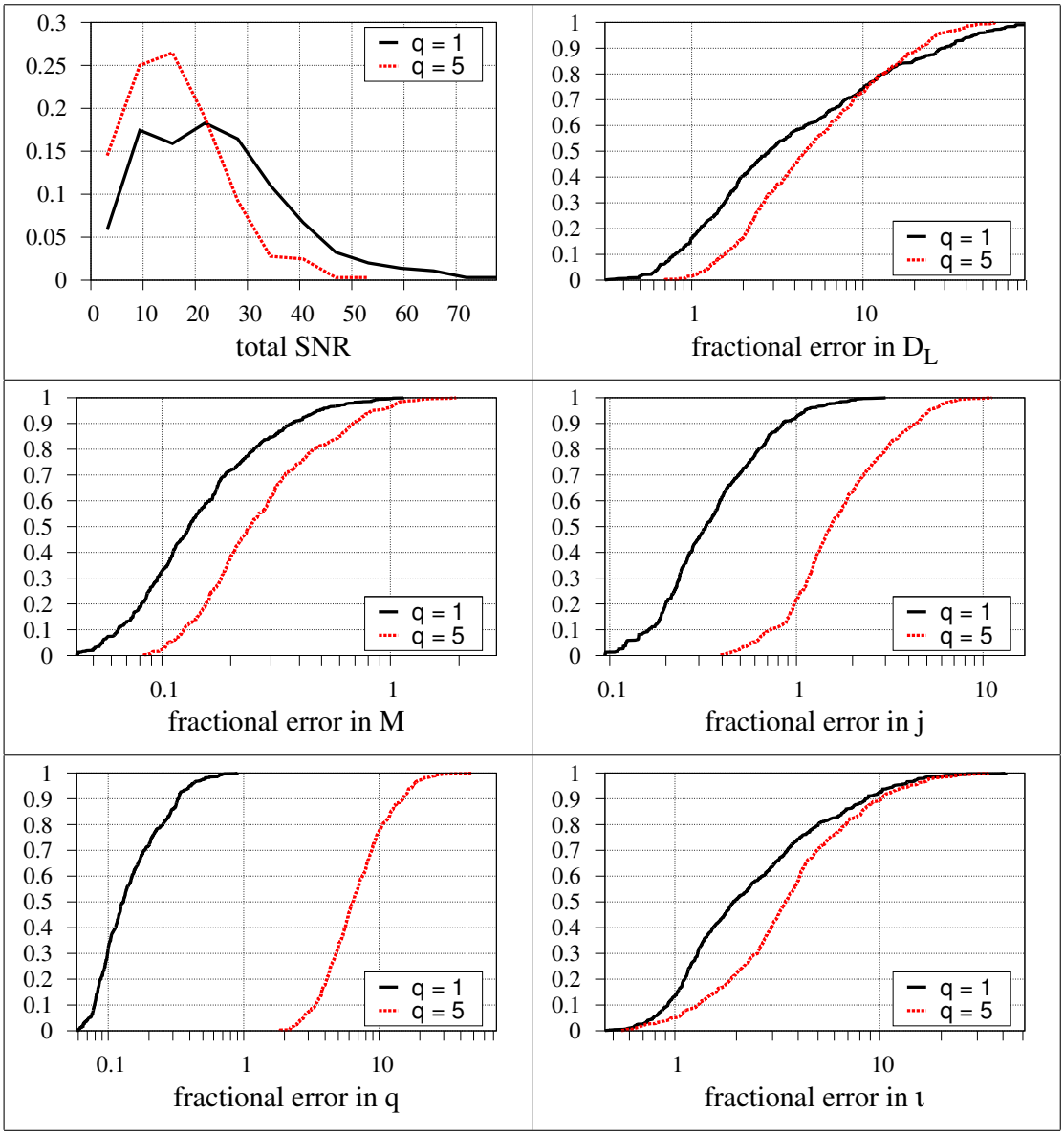

Figure 3.9: Frequency distributions involving the most optimistic scenario for advanced LIGO: a $1000M_{\odot}$ BH which is the merger of an equal mass binary, that is $q = 1$. The BH is again situated at 1 Gpc. A mass ratio of 5 is shown as well for contrasting.

3.5 Conclusions

The present study constitutes a sensible and realistic approach to the subject of parameter estimation from a multimodal ringdown signal, inasmuch as it is supposed to be emitted from a merged binary in a generic configuration. Parameters such as the inclination angle ι, along with the sky location θ and φ and the signal polarization ψ have an effect on the observed quasi-normal mode spectrum. Their impact on the detectability and parameter estimation has been assessed, by performing a large sample of Fisher-matrix analysis simulations, allowing for a simple statistical analysis of the results.

I am quoting frequency distributions for the errors at the representative distances of $z \simeq 1$ (6.73 Gpc) for supermassive BHs, in NGO, and of $z \simeq 0.2$ (1 Gpc) for intermediate-mass BHs, in the Einstein Telescope and advanced LIGO. An additional simulation was performed for a $5 \times 10^6 M_\odot$ BH at $z \simeq 3$. The results are quite satisfactory in determining the mass and spin, especially for the low mass ratios from 1 to ~ 5, where in typically 90% of the cases their errors fall below 10%. The effectiveness in measuring the luminosity distance, mass ratio and inclination angle is almost an order of magnitude worse.

The effects of these results on, as much as possible, realistic event rates in NGO and ET are discussed. The likelihood to have a waveform parameter measured to an accuracy of a certain threshold translates to the same proportion of observed events featuring error values below that threshold. As an example, if supermassive BHs within a luminosity distance of $z = 1$ coalesce at a rate of $\simeq 10$, then NGO could act as a SMBH dynamics probe, as almost all of these events will yield very low errors $1\% - 10\%$ in the BH mass and spin, while in half of the events the errors in the luminosity distance, mass ratio and inclination angle will be of the order of 20%.

Chapter 4

Is black-hole ringdown a memory of its progenitor?

We have performed an extensive numerical study of coalescing black-hole binaries to understand the gravitational-wave spectrum of quasi-normal modes excited in the merged black hole. Remarkably, we find that the masses and spins of the progenitor are clearly encoded in the mode spectrum of the ringdown signal. Some of the mode amplitudes carry the signature of the binary's mass ratio, while others depend critically on the spins. Simulations of precessing binaries suggest that our results carry over to *generic* systems. Using Bayesian inference, we demonstrate that it is possible to accurately measure the mass ratio and a proper combination of spins even when the binary is itself invisible to a detector. Using a mapping of the binary masses and spins to the final black hole spin, allows us to further extract the spin components of the progenitor. Our results could have tremendous implications for gravitational astronomy by facilitating novel tests of general relativity using merging black holes.

4.1 Introduction

A black-hole-binary merger produces a single black hole that quickly "rings down" to the Kerr solution, fully characterised by its mass and angular momentum. It is well known that the frequencies and damping times of the ringdown gravitational waves (GWs) are described by the same two parameters (see, e.g., Ref. [39] and references therein). However, the mode distribution of the ringdown *amplitudes* depends on the progenitor. Recently Kamaretsos *et.al.* [244] suggested that we could exploit this fact to measure properties of the progenitor from the ringdown signal. This was demonstrated by using a set of numerical-relativity simulations

of non-spinning binaries parametrized by the mass ratio and constructing a signal model reflecting the clear mass-ratio dependence of the ringdown mode amplitudes.

It follows that in general the ringdown amplitudes will depend on all eight binary parameters (the two masses, plus the vector components of each black hole's spin). In this Letter we report two remarkable results. First, that at least some of the mode amplitudes depend *only* on the mass ratio of the progenitor binary, *largely independent of the spins.* Therefore, we should be able to use the ringdown to measure the individual masses of a binary even when we cannot observe the binary itself! Second, one other mode amplitude carries a clear signature of the *spins* of the progenitor black holes and depends on an effective spin parameter related to the difference in the spin magnitudes. In the case of aligned spins (*i.e.*, non-precessing binaries), this fact, along with a mapping of the progenitor configuration to the final black hole spin [245] allows us to determine the individual spin components from the ringdown phase alone.

We show that progenitor parameters *can* be measured with good accuracy with the Einstein Telescope (ET) [246]. If mode amplitudes can be extracted from GW observations, they could be used to test strong-field general relativity, study the nature of the merged object, especially if it is a naked singularity, and as the only means to observe the formation of black holes when the inspiral phase of the signal is outside a detector's sensitivity band.

The physical origin of the mode-amplitude relations is unclear; but we note a relation to post-Newtonian inspiral results, raising questions for future research.

4.2 Background

For a black hole of mass M, located at a distance D, the plus and cross polarizations, h_+ and $h_\times$, of GWs emitted due to quasi-normal mode oscillations can be written to a good approximation as

$$h_+(t) = +\frac{M}{D}\sum_{\ell,m} A_{\ell m}\, Y_+^{\ell m}\, e^{-t/\tau_{\ell m}} \cos(\omega_{\ell m} t - m\phi + \varphi_{\ell m}),$$
$$h_\times(t) = -\frac{M}{D}\sum_{\ell,m} A_{\ell m}\, Y_\times^{\ell m}\, e^{-t/\tau_{\ell m}} \sin(\omega_{\ell m} t - m\phi + \varphi_{\ell m}),$$

for $t \geq 0$, where only the first (least damped) overtone is kept and the rest are omitted. Here $A_{\ell m}$, $\omega_{\ell m}$, $\tau_{\ell m}$ are the mode amplitudes, frequencies and damping times, respectively, $Y_{+,\times}^{\ell m}(\iota)$ are related to -2 spin-weighted spherical harmonics

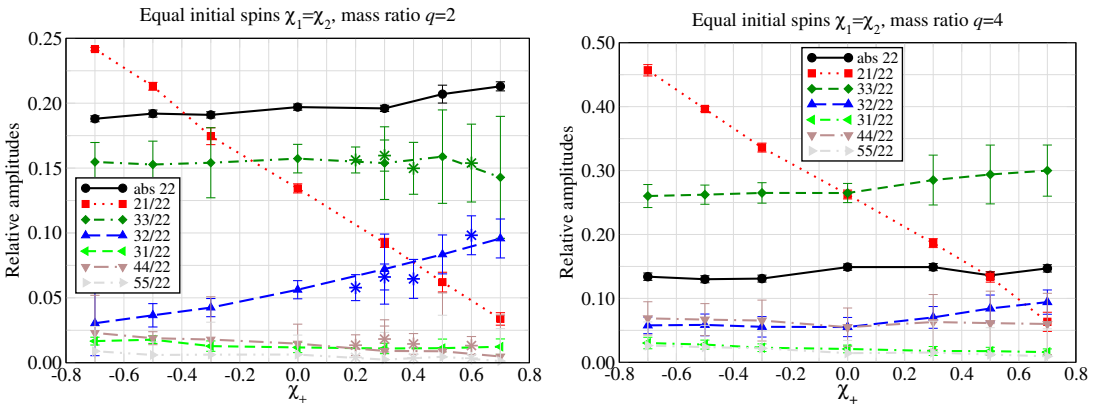

Figure 4.1: Quasi-normal mode amplitudes of binaries with aligned spins and mass ratio $q = 2$ (or $\nu = 2/9$, left panel) and $q = 4$ (or $\nu = 4/25$, right panel). The values from the non-spinning binary simulations are at $\chi_+ = 0$. Also shown in the left panel, with asterisks, are the results from the $q = 2$ equal initial χ_i precessing simulations. Note that for the 22 mode, the absolute amplitudes are always shown, scaled according to the final black hole mass, that is $(r/M)h_{22}$.

that depend only on the inclination ι of the black hole's spin axis to the observer's line-of-sight [186], ϕ is the azimuth angle at which the black hole is observed with respect to a suitably chosen frame and $\varphi_{\ell m}$ the initial phase angles of the modes.

Black hole perturbation theory can be used to compute the mode frequencies and damping times [49], but *not* the mode amplitudes $A_{\ell m}$, which depend on the nature of the perturbation—in our case, a highly distorted black hole that results from the merger. Instead, we must use numerical simulations to calculate the mode spectrum and its dependence on the progenitor parameters [198, 3, 244].

4.3 Numerical results

We explored the effect of spins with a large number of numerical binary simulations that consisted of 2-4 inspiral orbits before merger. There were three sets of simulations: (1) binaries with non-precessing equal spins $\chi_i = S_i/m_i^2 = \{0, \pm 0.3, \pm 0.5, \pm 0.7\}$ and mass ratios $q = m_1/m_2 = \{2, 4\}$, (2) systems with anti-aligned non-precessing spins such that the final black-hole spin was the same as that for the corresponding non-spinning binary for (q, $\chi_{\rm fin}$) = (2, 0.62), (3, 0.54), and (4, 0.47), using the final-spin fits in [245, 247] and (3) four $q = 2$ precessing binaries having equal initial spins with (x, y, z) components equal to $(0.2, 0, 0), (0, 0.4, 0), (0.6, 0, 0)$ and $(0.2, 0.2, 0.1)$, where the orbital plane lies on xy. There were a total of 40 configurations, not including additional tests to verify that the results were robust against changes in the number of inspiral orbits.

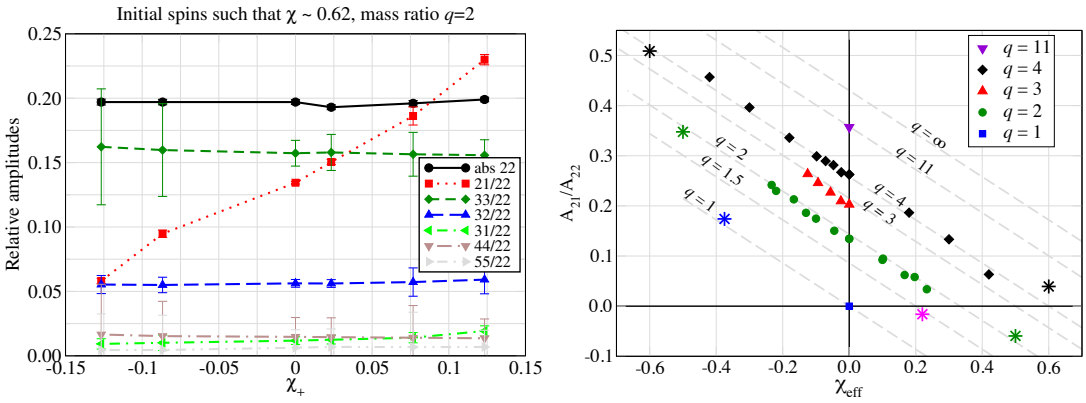

Figure 4.2: *Left* panel plots the amplitude of the various modes as a function of the total spin parameter χ_+ for the $q = 2$ simulations that end in a black hole of $\chi \simeq 0.62$. Modes 22, 33 are again rather insensitive to progenitor spins, while 21 varies by nearly a factor of 5. *Right* panel plots the 21 amplitudes from *all simulation sets* as a function of an effective spin term $\chi_{\rm eff}$ allowing us to estimate this parameter from a measurement. We verified our predictions with additional simulations marked with asterisks.

All simulations were performed with the BAM code [66]. As is standard, the error bars in the amplitudes were estimated by varying the numerical resolution and GW extraction radius. The highest resolution near the black holes was $\sim m/35$, where m is the mass of the smallest black hole, and the GW signal was typically calculated at $140\,M_{in}$ from the source. The ringdown amplitudes $A_{\ell m}$ were computed by fitting an exponential decay function to the data from $t = 10\,M$ after the peak of the $(2,2)$ luminosity, until the point where the signal was dominated by numerical noise. A_{22} and A_{21} are typically accurate to within 2%, and A_{33} and A_{32} to within 10%. The weaker modes are too noisy to be measured accurately, and are shown only for qualitative comparison.

Figure 4.1 shows the results for the first set of simulations, of equal-spin binaries. The amplitudes of the seven strongest modes ($A_{\ell m} = A_{\ell -m}$ for non-precessing binaries) are plotted as a function of a total spin parameter $\chi_+ = (m_1\,\chi_1 + m_2\,\chi_2)/M_{in}$, where $M_{in} = m_1 + m_2$ and $\chi_+ = \chi_i$ for these cases. This is the same spin parameter that has been used in recent phenomenological models of binary waveforms [248, 249]. The amplitudes are all relative to the 22 mode, for which we show the absolute amplitude.

We see immediately that A_{22} and A_{33} change with mass ratio, but vary only weakly with respect to spin. In contrast, A_{21} varies strongly with spin. Figure 4.1, therefore, suggests that the 22 and 33 modes carry information about the progenitor mass ratio, and the 21 mode carries information about the effective total spin.

The second series of simulations tests this hypothesis. For each mass ratio, this set generates approximately the same final black-hole with different progenitor spin configurations. The goal was to show that the mode amplitudes carried a signature of the progenitor spins independently of the final black hole spin. The mode amplitudes for the $q = 2$ case are shown in the left panel of Fig. 4.2, as a function of χ_+. As before, 22 and 33 show little variation, but the 21 mode changes by nearly a factor of five. This is strong evidence that the final black holes in this set are *not* really degenerate: although their mode frequencies and damping times will be identical, they will differ from one another in the 21 mode amplitude. This is consistent with studies of black-hole recoil: the recoil is mostly due to the interplay of the $(2, \pm 2)$ and $(2, \pm 1)$ modes [250], and both the recoil and $(2, \pm 1)$ mode amplitudes depend strongly on the progenitor spins.

Unfortunately, the trend of 21 is now the opposite of that in Fig. 4.1 with respect to χ_+, implying that the 21 mode amplitude is not determined by χ_+. Consider instead the effective spin parameter

$$\chi_{\rm eff} = \frac{1}{2}(\sqrt{1-4\,\nu}\,\chi_1 + \chi_-), \quad \chi_- = \frac{m_1\,\chi_1 - m_2\,\chi_2}{M_{in}},$$

The right panel of Fig. 4.2 shows the amplitude of 21 as a function of $\chi_{\rm eff}$ for all the simulations discussed so far. In *all* cases they are well approximated by

$$\hat{A}_{21} \equiv A_{21}/A_{22} = 0.43\left[\sqrt{1-4\,\nu} - \chi_{\rm eff}\right], \tag{4.1}$$

which is shown by dashed lines in Fig. 4.2 for different values of q. The above equation is consistent with the expectation that A_{21} will be excited in the case of equal mass binaries when $\chi_1 \neq \chi_2$, and also predicts that in general it will be zero when $\chi_{\rm eff} = \sqrt{1-4\,\nu} = |m_1 - m_2|/M_{in}$. We tested these predictions with six additional simulations, shown in Tab. 4.1. The predicted amplitudes $\hat{A}^{\rm P}_{21}$ agree with the computed amplitudes $\hat{A}^{\rm M}_{21}$ within the error bars shown in Figs. 4.1, 4.2. Negative values indicate that the 21 phase is offset by 180° with respect to the 22 phase; in the equal-mass cases this is equivalent to swapping χ_1 and χ_2, or rotating the initial data by half an orbit.

Table 4.1: Additional simulations to test Eq. (4.1).

q	1	1.5	2	2	4	4
$\chi_{\rm eff}$	-0.375	0.220	-0.500	0.500	-0.600	0.600
$\hat{A}^{\rm P}_{21}$	0.161	-0.005	0.358	-0.070	0.516	0.000
$\hat{A}^{\rm M}_{21}$	0.174	-0.016	0.348	-0.059	0.509	0.039

All of these results apply to non-precessing binaries: the progenitor spins and final spin were all parallel or anti-parallel to the binary's orbital angular momentum. This will not be true in general; the spins and orbital plane will precess during the inspiral, and the final black hole's spin will be mis-aligned with respect to the pre-merger orbital plane. Even if the ringdown modes were rotated into an optimal frame by a procedure like that introduced in [251], there would be an asymmetry between the $+m$ and $-m$ modes, since this is a signature of the out-of-plane recoil (see Sec. III.A in [252]). However, it is possible that if the ringdown modes were described in the optimal frame, then their *average* would satisfy the relations we have observed. To test this, we simulated four precessing binaries. In each case the final spin was mis-aligned with the initial orbital plane, but only slightly, so that to a first approximation we could still consider the average of the $(2, \pm 2)$ and $(3, \pm 3)$ modes. The results for these cases are shown in Fig. 4.1, and, remarkably, satisfy the same relations we have observed for non-precessing binaries. This provides strong evidence that our results carry over to *generic* binaries.

4.4 Interpretation

Post-Newtonian (PN) theory provides some clue to the behavior of the amplitudes of the various modes. It is quite possible that the various modes excited during the inspiral phase retain the memory of their structure through to the ringdown phase. (There are signs that this will be true from, e.g., Fig. 11 in [215] for non-spinning binaries.) It is, therefore, instructive to look at the inspiral mode amplitudes. In particular, the 21 mode reads [253]

$$h_{21} \propto \frac{\nu M_{in} v^3}{D} \left(\sqrt{1 - 4\,\nu} - \frac{3}{2}\, v\, \chi_- \right). \tag{4.2}$$

Here v is the PN expansion parameter, namely the orbital speed. There are three points to note: Firstly, for non-spinning systems, the 21 amplitude has *identical* dependence on the mass ratio during the inspiral and ringdown phases. Secondly, the spin terms in the 22 and 33 modes (indeed, all modes for which $l+m$ is even) appear at 1.5 PN order beyond the leading order and so spins have a negligible effect. For $v = 1/\sqrt{3}$, 22 and 33 vary by about $\sim 20\%$ when χ_1 and χ_2 change from -0.8 to $+0.8$. However, for 21 (and all odd $l + m$ modes) the spin effect occurs at 0.5 PN beyond the leading order; spins affect odd $l+m$ modes far more strongly than they do even $l + m$ modes. For $v = 1/\sqrt{3}$, the 21 mode varies by

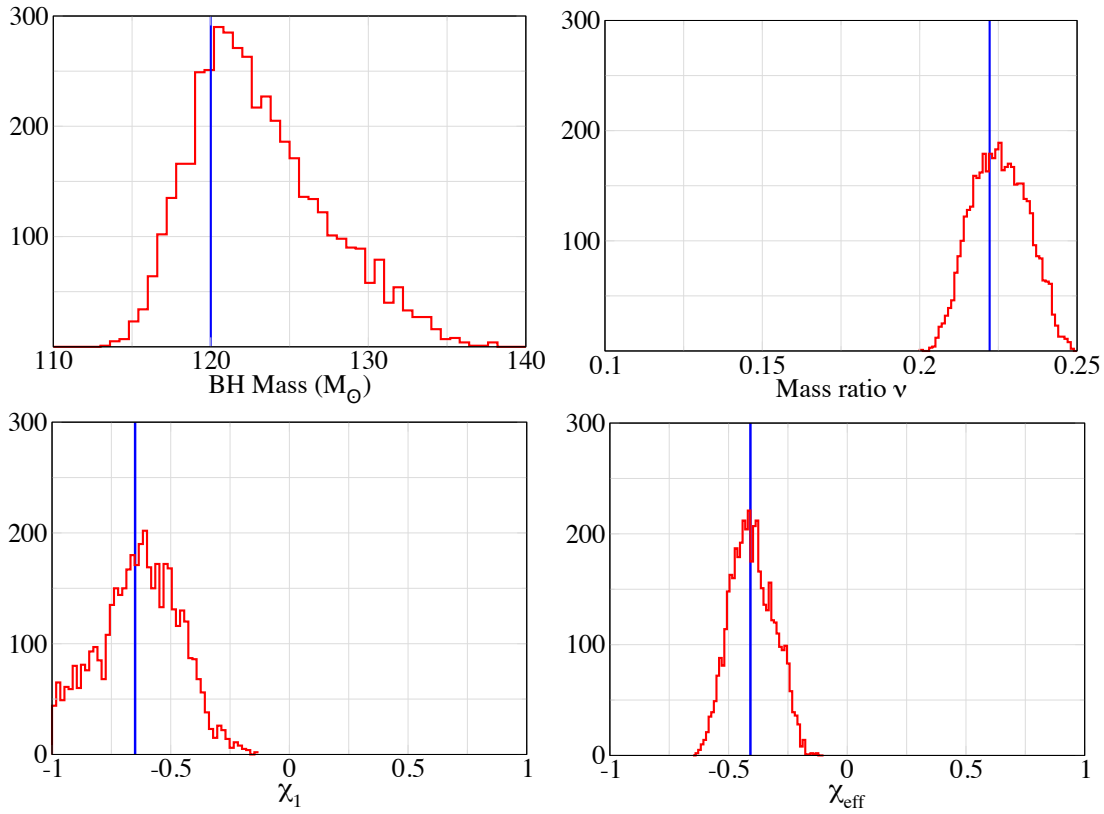

Figure 4.3: Posterior distributions are plotted for a ringdown signal detected with ET. The vertical lines correspond to the parameters of the signal injected into the ET mock data stream. The source is 1 Gpc from the detector; the SNR is ~ 27.

a factor of 4.5, and the 32 mode by 72%, when spins vary from -0.8 to $+0.8$. Finally, the dominant spin effect in the 21 mode amplitude is determined by the quantity χ_-. It is really *not* the total spin that determines the amplitude, but the difference of spins, as in the ringdown phase.

4.5 Measurement

To estimate how well the progenitor spins and mass ratio can be measured we injected a ringdown signal in background noise with power spectral density as expected in Einstein Telescope, ET-B [254], and used Bayesian inference with nested sampling [255, 256] to detect and measure its parameters. Our signal consists of the first three dominant modes, 22, 21 and 33, with the 21 mode amplitude given by Eq. (4.1) and for the 22 and 33 modes we took $A_{22} = 0.864\,\nu$, $\hat{A}_{33} = 0.44\,(1-4\nu)^{\,0.45}$. The signal and the template are both is characterized by six parameters, $(M,\, \nu,\, \chi_1,\, \chi_2,\, D,\, t_0)$, where t_0 is the time-of-arrival of the signal at the detector. The angles describing the location of the source on the sky $(\theta,\, \varphi)$,

the inclination ι of the binary and polarization angle ψ, are all assumed to be known. The azimuth angle ϕ and the initial phases of the various modes $\varphi_{\ell m}$ are all also assumed to be zero. These angles have strong correlations with the distance to the binary but not the intrinsic parameters. Thus, relaxing the above assumptions is not likely to have a big impact in the measurement of the intrinsic parameters of the source.

The posterior distributions for four of the parameters from one of our runs are plotted in Fig. 4.3, which show that the parameters of the progenitor can be quite accurately measured by using just the ringdown signal. A more detailed study is needed to fully characterize the measurement accuracies over the full parameter space, by incorporating other parameters such as the sky position of the source and its inclination, assumed to be known in this work.

4.6 Discussion

In this Letter we have addressed a question implied in Ref. [244]: *can we measure the mass ratio of a generic binary from the ringdown signal alone?* We have found two remarkable results. First, we *can* measure the mass ratio from the ringdown signal, and second, we may also be able to measure the individual black-hole spins. In other words, both the masses and spins of the two component black holes could be measured purely from the rapidly decaying perturbation that they leave on the final merged black hole.

The first result is demonstrated with a large numerical study of non-precessing binaries to show that the ratio of the amplitudes of the $(\ell = 3, |m| = 3)$ and $(\ell = 2, |m| = 2)$ ringdown modes carry a clear signature of the mass ratio. Furthermore, we have evidence from a small set of precessing-binary configurations that this signature is retained in generic binaries. And finally, we have shown that this signature could be accurately measured in observations with the Einstein Telescope.

The second result is restricted to non-precessing binaries. We found that the ratio of the $(\ell = 2, |m| = 1)$ and $(\ell = 2, |m| = 2)$ mode amplitudes depends on a certain difference between the individual black-hole spins. We produced a model of this spin dependence in terms of an effective spin parameter $\chi_{\rm eff}$, which is accurate across a wide sampling of the non-precessing-binary parameter space. In a parameter-estimation exercise, where this model is injected into simulated Einstein Telescope noise, measurements of the final mass and spin, and of $\chi_{\rm eff}$, can be used in conjunction with a final-spin fit [245, 247] to determine the individual

black-hole spins.

Many questions remain open for future research. What is the physical origin of the observed ringdown spectrum? How do we fully model the ringdown signal from generic binaries? And, of most significance, what additional astrophysics will these results allow us to learn in third generation GW detectors, and how precisely will we be able to test general relativity?

Chapter 5

Search for gravitational-wave bursts from core-collapse Supernovae with X-Pipeline

Core-collapse Supernovae (ccSN) are among the sources that will produce gravitational waves (GWs) detectable by large-scale, broad-band GW interferometers around the globe. In particular, during the initial LIGO science runs, a galactic Supernova event would likely produce a signal across a broad range of frequencies and well within the detectors' sensitivity bandwidths. In the advanced LIGO era, the horizon will increase by an order of magnitude, thus encompassing a large part of the local group of galaxies for some models of GW generation. Gravitational waves from Supernovae carry the signature of a variety of multidimensional, multi-physics source processes taking place during the violent gravitational collapse of a massive star.

Specifically, a core-collapse Supernova is believed to result from the gravitationally induced collapse of the electron-degenerate iron core of a massive star, which had a zero-age main sequence mass of at least $8\,M_{\odot}$, see [24] and references therein. A surprising discovery more than a decade ago indicated the connection between two seemingly different phenomena: long-duration gamma-ray bursts (LGRBs) and ccSNs of massive stars [257]. This connection has now been firmly established mainly with the use of spectroscopy [258]. Gravitational-wave emission from such events has been studied with some success for four decades, by performing numerical investigations [127, 6]. Several of the models predict that GWs from various phenomena associated with gravitational collapse could be detectable with ground-based and space-based interferometric observatories. Despite the long-term investigation and modelling it is yet undecided which mechanisms

would be the dominant ones and how exactly they depend on initial data, therefore having a high uncertainty about the GW signal.

Constraining the ccSN mechanism via electromagnetic (EM) observations is difficult, as the information on the core pre-explosion dynamics lies deep inside the supergiant pre-Supernova star. While some theoretical models of the ccSN mechanism can be constrained via EM observables such as nucleosynthesis products, total explosion energy, ejecta morphology and proper motion, GWs and neutrinos are the only means of delivering direct and intrinsic information of the immediate pre-explosion and explosion phases. A subject of future research, which is not addressed in this Chapter, would be the unveiling of details on the ccSN mechanism and exclusion of several models via the detection and estimation of the general properties of a GW signal, such as the initial core bounce.

A ccSN that will yield a detectable GW signature will be close enough to be an easily identifiable optical trigger. Searching for gravitational-wave bursts triggered by astronomical observations of electromagnetic transients has several benefits: prior information about the source location enhances detection efficiency, and the use of time coincidence implies analysis of only a small stretch of data which allows sophisticated analysis without high computational costs. During postprocessing, knowledge about the source enables reconstruction of the source parameters, leading to an astrophysical interpretation.

5.1 Outline of X-Pipeline

X-Pipeline is a software suite for autonomous gravitational-wave burst (GWB) searches [8]. It is a coherent search pipeline, earlier versions of which have been used for GWB searches from gamma-ray bursts (GRBs) during the LIGO S5/Virgo VSR1 [259, 260] and LIGO S6/Virgo VSR2/VSR3 Science Runs [261]. Coherent methods [262, 263, 264, 265, 266] combine data from multiple detectors before processing, creating a list of candidate events for the whole detector network.

In a coherent analysis, the contributions of the detectors in the network are naturally taken into account, eliminating the need for separate tuning in each detector. Due to that, the sensitivity of coherent searches is not limited by the least sensitive detector in the network, while it also makes coherent searches generally simpler. One last advantage of coherent searches is increased efficiency in rejecting background noise [262].

The search is astrophysically triggered, in the sense that optical transients are used as possible sources of GWBs. Initially the user has to supply the most

probable sky location and GPS trigger time of the transient, as is provided by a transient alert service, such as "The Astronomer's Telegram" or the Central Bureau of Astronomical Telegrams. Having this kind of information, constrains the amount of the detectors' datastreams to be analysed, to a few hours in the best cases. The sky localisation of the GWB associated with the optical trigger is what allows for some distinction between the so-called on- and off-source data, which denote the parts of the datastream where a GWB from the trigger is present and non-present respectively. In standard GRB searches, they refer to distinct portions of the data. However, in the current search, where the datastream under consideration can reach up to a week, the on- and off- source regions have the same time span. It is assumed that no GW signals from the specific source sky location are to be found in the off-source region. The off-source data is used to estimate the background rate and statistical significance of potential gravitational wave events in the on-source window.

5.2 Detector network formulation

Consider a gravitational wave $h_+(t,\vec{x}), h_\times(t,\vec{x})$ in the TT gauge, from a direction $\hat{\Omega} = (\theta,\phi)$ propagating through the area of the detector. It will yield a signal $h(t)$, equivalent to the detector response $\delta L/L$, that is a linear combination of the two source polarizations,

$$h(t) \equiv \frac{\delta L(t)}{L} = F_+(\theta,\phi,\psi)\, h_+(t,\vec{x}) + F_\times(\theta,\phi,\psi)\, h_\times(t,\vec{x})\,. \tag{5.1}$$

with,

$$F_+(\theta,\phi,\psi) = \frac{1}{2}(1+\cos^2\theta)\cos 2\phi\cos 2\psi - \cos\theta\sin 2\phi\sin 2\psi\,, \tag{5.2a}$$

$$F_\times(\theta,\phi,\psi) = \frac{1}{2}(1+\cos^2\theta)\cos 2\phi\sin 2\psi + \cos\theta\sin 2\phi\cos 2\psi \tag{5.2b}$$

Gravitational interferometric detectors are low-gain receiver antennas, that is, the antenna pattern functions have same order of magnitude values over the extent of the (θ,ϕ) angles. This results in a detector response $h(t)$ from practically any source position in the sky. The root mean square response function of such a detector is

$$F_{\rm rms} = \left(\int F_+^2 + F_\times^2 \;\; \mathrm{d}\psi\right)^{1/2}. \tag{5.3}$$

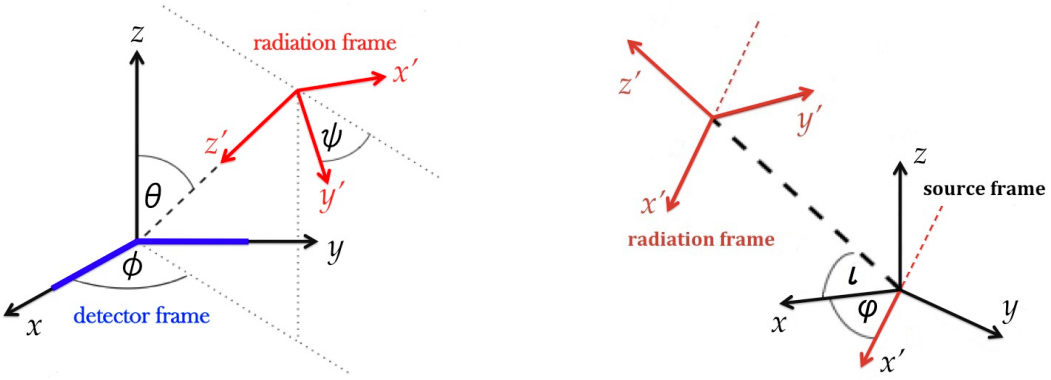

Figure 5.1: — From left to right, detector frame, radiation frame and source frame, illustrating the various angles that are mentioned in the text. In our case, the z-axis of the source frame is coincident with the collapsed core's direction of angular momentum.

As explained in Chapter 1 the true output of the detector will contain instrumental and environmental noise which is essentially superposed with the response to the GW signal, hence the true output of the detector is

$$h(t) = F_+(\theta, \phi, \psi)\, h_+(t, \vec{x}) + F_\times(\theta, \phi, \psi)\, h_\times(t, \vec{x}) + n(t)\,. \tag{5.4}$$

The power of coherent searches lies in correlating the data streams from a set of detectors that were coincidentally acquiring science-worthy data. We therefore need to expand our formulation to describe a network of detectors. As a first step I consider Eq. 5.4 as a vector containing all detectors in the network, each denoted by index d,

$$h_d(t + t_d) = F_{+d}(\theta, \phi, \psi)\, h_{+d}(t, \vec{x}) + F_{\times d}(\theta, \phi, \psi)\, h_{\times d}(t, \vec{x}) + n_d(t)\,, \tag{5.5}$$

where $(t, \vec{x})$ can be the coordinates of an Earth-corotating frame placed at its center, and t_d is the time delay between the position of detector d and an arbitrary reference position, e.g. the center of the Earth. The above equation can be written in a more compact form, using matrix notation, in the D-dimensional space of detectors,

$$\vec{d} = \boldsymbol{F}\, \vec{h} + \vec{n}\,, \tag{5.6}$$

where

$$\boldsymbol{F} \equiv [\ \vec{F_+} \quad \vec{F_\times}\ ] \equiv \begin{bmatrix} F_{+1} & F_{\times 1} \\ F_{+2} & F_{\times 1} \\ \vdots & \vdots \\ F_{+D} & F_{\times D} \end{bmatrix}, \tag{5.7}$$

while the rest of the terms are simply

$$\vec{d} \equiv \begin{bmatrix} d_1 \\ d_2 \\ \vdots \\ d_D \end{bmatrix}, \quad \vec{h} \equiv \begin{bmatrix} h_+ \\ h_\times \end{bmatrix}, \quad \vec{n} \equiv \begin{bmatrix} n_1 \\ n_1 \\ \vdots \\ n_D \end{bmatrix}. \tag{5.8}$$

In X-Pipeline, the noise, signal and detector outputs are treated in the frequency domain. Initially represented as time arrays, with a sampling rate of 16384 Hz a discrete Fourier transform is applied. In the equations below, k denotes the frequency bin. During the analysis all these terms are weighted by the noise amplitude spectral densities of the detectors, making it convenient to treat only noise-weighted quantities [8],

$$\tilde{d}_d^{\,\mathrm{nw}}(k) = \frac{\tilde{d}_k(k)}{\sqrt{\frac{N}{2}S_d(k)}}, \quad \tilde{n}_d^{\,\mathrm{nw}}(k) = \frac{\tilde{n}_k(k)}{\sqrt{\frac{N}{2}S_d(k)}}, \quad F_d^{+,\times\,\mathrm{nw}}(\hat{\Omega},k) = \frac{F_{+,\times\,d}(\hat{\Omega})}{\sqrt{\frac{N}{2}S_d(k)}}, \tag{5.9}$$

where N is the number of data points in the time domain while,

$$\tilde{d}(k) = \sum_{j=0}^{N-1} d(j)\, e^{-i2\pi jk/N}, \text{ and } \tilde{n}(k) = \sum_{j=0}^{N-1} n(j)\, e^{-i2\pi jk/N}.$$

The noise power spectral densities are defined and normalised by computing the following inner product over an ensemble of *stationary* noise instantiations, which in continuous notation is,

$$\langle \tilde{n}_d^*(f)\tilde{n}_d(f')\rangle^{(n)} = \frac{1}{2}\, S_d^{(n)}(|f|)\, \delta(f-f'). \tag{5.10}$$

Coherent combinations are thus recomputed for every frequency bin as well as for every sky position. Note also that because of the noise-spectrum weighting, the "whitened noise" Eq. 5.10 is isotropically distributed in the space of detectors 5.10. Consequently, all information on the sensitivity of the network both as a function

of frequency and sky position can be contained in the noise-weighted expression of $\boldsymbol{F}$, Eq. 5.9.

5.3 Event generation via time-frequency analysis

After loading the data in the specified time window around the SN trigger, it is divided into segments, Fourier-transformed and whitened, Eqs. 5.9, after they have been time-shifted for each sky position along the path of the SN source on the sky. Candidate events are distinguished by yielding an excess energy. By computing the summed energy in the reconstructed h_+ and $h_\times$ in each time-frequency pixel, see Section 5.4 or [8], X-Pipeline then groups those pixels that exceed a certain threshold. Each of the resulting clusters is considered a candidate detection event and assigned an energy measure which is the sum of the energy values of its constituent pixels. It can of course be the case that the higher-energy pixels do not form connected groups. X-Pipeline can handle those cases as well, but I have applied the standard clustering procedure of grouping nearest and next-nearest neighbors, which is more appropriate for a GWB with a connected shape in the time-frequency plane. These candidate events will be subject to glitch rejection coherent veto tests, as described in detail in [8].

5.4 Handling elliptically polarized waveforms

The standard likelihood

The candidate events are ranked in significance by a certain energy measure, which is some form of likelihood-ratio quantity. One of the most commonly used is the standard likelihood [263], which is the natural logarithm of the ratio of the probability obtaining the observed data from a particular GWB signal - including stationary Gaussian background noise - over the probability of obtaining it from stationary Gaussian background noise only. In X-Pipeline, where multiple sky positions are tested, the likelihood at each time-frequency pixel, k, in the returned map is the likelihood measured for that pixel for the sky position (and any other parameters) that gave the largest total likelihood for that time, summed over all

frequency bins (or smallest for null energy) [8],

$$L \equiv \ln \frac{P(\{\tilde{\boldsymbol{d}}\}|\{\tilde{\boldsymbol{h}}\})}{P(\{\tilde{\boldsymbol{d}}\}|\{0\})} = \frac{1}{2}\sum_k \left[\left| \tilde{\boldsymbol{d}} \right|^2 - \left| \tilde{\boldsymbol{d}} - \boldsymbol{F}\tilde{\boldsymbol{h}} \right|^2 \right] . \tag{5.11}$$

In a real search for GWBs the signal waveform h is unmodelled, therefore it is not clear how to compute the likelihood ratio (5.11). The usual approach has been to treat the waveform values $\tilde{h}_+$ and $\tilde{h}_\times$ in each time-frequency pixel as independent parameters to be fitted to the data. A signal present in the data should maximize the likelihood ratio,

$$0 = \left. \frac{\partial L}{\partial h} \right|_{\boldsymbol{h}_{+,\times}=\boldsymbol{h}_{+,\times}^{max}} . \tag{5.12}$$

That is, the likelihood at each time-frequency pixel k in the map is the likelihood obtained for the given sky position after maximising over all possible signal values $h_+[k]$, $h_x[k]$.

Likelihood for elliptical polarization signal model

The methodology mentioned above is standard in GRB searches [8], but refers to either circularly polarized, or linearly polarized waveforms and is not applicable to some of the numerical waveforms that are included in this search, which have an immensely variable energy content in each polarization, Section 5.6. Therefore, a more specific method has been developed for use in the Supernova searches, which does not make the circular or linear assumption and was found to raise the efficiency of the sensitivity analysis of X-Pipeline, see Section 5.8. The two polarizations can take any angle of polarization, but they are not treated independently, that is, the polarization angle takes values that maximize the following likelihood-like quantity, which is also described in [267],

$$L = \frac{\left| (\boldsymbol{F}_+ \, cos(2\psi) + \boldsymbol{F}_\times \, sin(2\psi)) \cdot \vec{d} \, \right|^2}{(\boldsymbol{F}_+ cos(2\psi))^2 + (\boldsymbol{F}_\times sin(2\psi))^2 + 1/\delta^2} . \tag{5.13}$$

This quantity is then used for sorting the candidate events, as described in Section 5.3.

5.4.1 Background noise rejection

Thus far the use of various likelihood measures has assumed a signal superposition with stationary and gaussian noise. Such a formalism would have been

very efficient in detecting true signals if it had not been that these assumptions are unrealistic. Real noise contains an abundance of random strain transients called glitches. Almost every transient event above the average noise realisation would yield an excess likelihood value, thus registering as a candidate event, in the same way a GWB signal would do. For that reason a set of additional tests need to be performed, which target the elimination of glitches and provide additional confidence in the existence of a GWB. I provide a concise description of these techniques as were implemented in the ccSN search with X-Pipeline. For a more rigorous treatment see [267, 8].

The null stream

One key technique is that of the *null stream* construction, as was devised in [268] and specialised for GWB searches in [262]. It relies on the observation that a GWB present in the data of two or more detectors can satisfy a closure condition, such that the GWB can be effectively cancelled by a particular linear combination of the data streams. This is made possible as two or more detectors can provide pleonastic measurements of the two polarization components h_+, $h_\times$ of the GWB. Such a network is called *redundant*. Hence, given the direction to the source, the strain induced by a GW signal in one or more of the detectors can be fully expressed in terms of the strain induced in others in the network. Note that the detectors need not be non-collocated, for instance, the two aligned LIGO interferometers at Hanford are redundant, as a possible signal strain would differ essentially by a factor of two in amplitude. Other examples of redundant networks are: a three-armed configuration space interferometer, the LIGO detector at Livingston is nearly redundant with either of the Hanford detectors, while almost any combination of three or more detectors involving the above with Virgo, GEO or KAGRA is redundant.

In [268], they studied a two-parameter family of linear combinations of three data streams, where the two parameters correspond to the two angular sky location coordinates, θ and ϕ of the source. They showed that when these two parameters coincide with the true location of the source, the gravitational-wave component is canceled in their linear data stream combination, leaving only the noise component.

The form of Eq. 5.6 makes it clear that, regardless of the actual polarization content of the signal, it can only contribute to the network output along the directions F_+ and $F_\times$; unlike the noise component that is not confined to the $\{F_+, F_\times\}$ subspace. Constructing the null stream therefore involves projecting

the data orthogonally to these directions [8].

5.5 Supernovae triggers

Optimistic estimates of the core-collapse SN rate in the Milky Way and the Small and Large Magellanic Clouds, predict one core-collapse event every 30-50 years and of about every 20 years for the entire local group of galaxies, including M31 at 0.8 Mpc [269]. This rate stays roughly constant until a distance of about 3-4 Mpc, where various neighboring groups with high star-formation rates, such as the Maffei and M81 groups of galaxies, increase the SN rate to an optimistic one event in every 2 years [270]. The next significant increase in the SN rate occurs towards the outskirts of the Virgo cluster, at 7-10 Mpc, where the rate is approaching one event per year [270].

Since LIGO and GEO600 began receiving science data in 2002, six type II and type Ib/c core-collapse SNe have been discovered optically within 5 Mpc from Earth, which is approximately the horizon distance in iLIGO for the most optimistic GW generation models in ccSNe. Unfortunately, all of the events, except Supernova SN 2008bk, occurred when LIGO, GEO600 and VIRGO were not taking data concurrently [271, 272, 273]. Let me note here that a small fraction of type Ia Supernovae exhibit differentiated spectrums and light curve properties from 'normal' Type Ia and do not conform to the standard model of white-dwarf thermonuclear explosions. These might be produced by a white-dwarf thermonuclear explosion under different conditions, or could even be the core collapse of massive stars [274], in which case they may be sources of GWBs. In the current search I have not included type Ia triggers, but considered only the standard type II and type Ib/c.

SN 2011dh

SN 2011dh was observed in the Whirlpool galaxy (M51) on May 31st 2011, thus placing it at a distance of 7.1 Mpc. Although it was discovered by amateur astronomer Amédée Riou, many observers have reported the non-presence and presence of the optical transient, allowing for a determination of the explosion time with an error of only a few hours [275] making it an ideal candidate for this type of search. A candidate progenitor has been detected in Hubble Space Telescope images and refers to a highly luminous yellow supergiant of initial mass between 18-24 $M_{\odot}$ [276]. Further information is given in Table 5.1.

Name	SN 2011dh	SN 2007gr	SN 2006iw
Type	IIb	Ic	IIp
Distance	8 Mpc	9.3 Mpc	125 Mpc
Discovery date	31 May 2011	15 Aug 2007	3 Oct 2006
Window start (UTC)	May 31 2011 07:46:00	Aug 10 2007 08:09:36	Oct 1 2006 00:00:00
Window end (UTC)	May 31 2011 20:10:00	Aug 15 2007 12:14:24	Oct 4 2006 00:00:00
R.A. (deg)	202.5214	40.8666	350.3312
Dec. (deg)	+47.1698	+37.3458	+0.2597
Science Run	A6	S5	S5
Widest network	G1V1	H1H2L1V1	H1H2L1
Network livetime (%)	24.0	68.4	48.7

Table 5.1: List of Supernovae used as optical triggers in searching for gravitational wave bursts. The explosion could have taken place at any time inside the given time window.

SN 2007gr

SN 2007gr was discovered on 2007 August 15.51 UT in the spiral Seyfert galaxy NGC 1058, but was not detected in an image taken from the Katzmann Automatic Imaging Telescope (KAIT) on August 10.44 UT [277]. This constrains the explosion epoch to less than five days before discovery, which along with the relatively close distance of 8.3 Mpc, makes of SN 2007gr an interesting event. Based on a spectrum obtained the following night, SN 2007gr was classified as a generic SN Ib/c since it was not clear whether the line near 6350 Å was really a Helium line. The later spectral evolution did not confirm the presence of He, therefore SN 2007gr is now classified as Type Ic. Various data on SN 2007gr are summarised in Table 5.1.

SN 2006iw

SN 2006iw was first reported on images taken by the Sloan Digital Sky Survey (SDSS) observing team on October 3rd 2006. SN 2006iw was not detected in an image taken on October 1, with a 5-sigma upper g-magnitude limit of approximately 22.6. Prior SDSS spectrum had been obtained of the apparent host galaxy indicating a redshift of $\simeq 0.03$, Table 5.1. Its distance of $\simeq 125$ Mpc eradicates the possibility of detection of a GW counterpart. However, the constrained time of explosion of the Supernova, along with a satisfactory coverage from the L1H1H2 network makes it a good candidate for demonstrating our search method.

5.6 Gravitational waveforms for sensitivity analysis

In X-Pipeline we estimate the sensitivity of the search by injecting in the data the anticipated GWBs with a time delay in the detector network that corresponds to the sky location in question [262, 8].

Stellar core-collapse is infamous for being difficult to model, as it requires three-dimensional simulations and complex statistical physics in full generality. For our purposes, what is further needed is the modelling of the gravitational-wave emission processes, so that to use the anticipated gravitational waveforms as software injected signals. Despite the impressive recent progress in the understanding of core collapse, this remains a very challenging and active field [6].

Iron core collapse of a massive star is one of the most energetic process in the nearby universe, liberating some 10^{53} erg of gravitational energy. About 99% of this energy is emitted in neutrinos as the proto-neutron star contracts and cools over a timescale of around 100 s. The rest of the energy goes into the asymptotic energy of the SN explosion and it is what is visible as an electromagnetic transient. One of the fundamental questions that core-collapse SN theory has been facing is how exactly the necessary fraction of gravitational energy is transferred to revive the shock and ultimately unbind the stellar envelope.

GWs as well as neutrinos are the only messengers with the potential of delivering first-hand information on the physical processes leading to explosion: Both are emitted deep inside the SN core and after exiting the iron core, travel to observers on Earth with minimum interaction with the interstellar and integalactic matter. In iron core collapse, the emission of GWs is expected primarily from the rotating collapse and bounce [278, 279], nonaxisymmetric rotational instabilities, postbounce convective overturn [280] and protoneutron star pulsations [281, 282, 283]. In addition, anisotropic neutrino emission, global precollapse asymmetries in the iron core and the late-time formation and settling down of a black hole may contribute to the overall GW signature [280, 127].

Anticipated GWBs as simulated signals

Even with the implementation of coherent energies, the use of accurate models for GWB waveforms is needed, as without them it would have been much harder to determine with confidence whether certain candidate detections are real GWBs or false alarms, due to some noise fluctuations occurring in coincidence in the detectors of the network. A confident detection of GWBs requires the ability

to distinguish them from such noise transients. To assess the efficiency of X-Pipeline in this task, I implement the standard procedure of performing software injections, that is, inject simulated GWB signals of a variety of types, amplitudes, orientations and polarizations into the datastream with the purpose of retrieving them. The procedure follows closely that of [8], with the additional complexity that the injection log files of another pipeline are used in producing the injections. See Sections 5.7.3 and 5.8.

For SN 2011dh and SN 2007gr we used injected waveforms from seven waveform families: four classes of numerical waveforms; Dimmelmeier, Yakunin, Ott and Mueller waveforms and three types of analytical waveforms; rotating bar waveforms, Piro waveforms and sine-Gaussian waveforms. For the SN 2006iw trigger I have used four recent numerical waveforms corresponding to different mechanisms and assumptions, as well as two sine-Gaussian waveforms. The large number of waveform families ensures a variety of GWB generating mechanisms, promotes competition among the ccSN numerical research groups and motivates them to produce more accurate waveforms. In the sections that follow, I provide details on each waveform family and the issues I have encountered in implementing them in X-Pipeline.

5.6.1 GWs from bar modes

One of the simplest sets of waveforms that can be applicable in this search are the rotating bar modes. Assuming that the collapsing massive star passes through a phase of a highly deformed, rapidly rotating core, these waveforms should to first order approximate the gravitational waves emitted in this process. Following [284, 87], the dominant component of the gravitational wave output can be expressed in terms of the reduced quadrupole moment of the source, therefore using this formalism we can analytically compute the waveform.

The reduced mass quadrupole moment of a spatial mass distribution with density $\rho(x_i)$ is generally defined as

$$\text{ɪ}_{ij} = \int dx^3 \rho(x_i) \left[x_i x_j - \frac{1}{3}\delta_{ij}\delta_{kl}x^k x^l \right] \ . \tag{5.14}$$

Taking the bar to have length L, radius R, and mean density ρ we eventually get [284]

$$h_{ij}^{TT} = \frac{2}{D}\frac{G}{c^4} P_{ik} P_{jl} \ddot{\text{ɪ}}_{kl} \ , \tag{5.15}$$

where P_{ik} is the projection operator, $P_{ik} = \delta_{ik} - n_i n_k$, that projects the traceless

reduced quadrupole moment to the transverse plane of the direction of the wave propagation, $n_i = k_i/k^j k_j$, and D is the distance to the bar. The explicit form of $\ddot{I}_{ij}$ is

$$\ddot{I}_{ij} = \frac{1}{6} M(L^2 - 3R^2)\Omega^2 \begin{pmatrix} -\cos 2\Omega t & \sin 2\Omega t & 0 \\ \sin 2\Omega t & \cos 2\Omega t & 0 \\ 0 & 0 & 0 \end{pmatrix} , \tag{5.16}$$

where we have set $M = \bar{\rho}\pi R^2 L$.

The sum $h_+ - ih_\times$ can be decomposed into modes using spin weighted spherical harmonics ${}^{-s}Y_{lm}$ of weight -2:

$$h_+ - ih_\times = \frac{1}{D} \sum_{\ell=2}^{\infty} \sum_{m=-\ell}^{\ell} H_{\ell m}(t)\, {}^{-2}Y_{\ell m}(\theta, \phi) . \tag{5.17}$$

The expansion parameters H_{lm} ($\ell = 2$ denotes the quadrupole) are complex functions of the retarded source time t.

In order to express H_{2m} in terms of $\ddot{I}_{ij}$, one first expresses $h_+(\theta, \phi)$ and $h_\times(\theta, \phi)$ in terms of $\ddot{I}_{kl}$, then convolves these with ${}^{-2}Y^*_{lm}$. The result is [87],

$$\begin{aligned} H^{\rm quad}_{20} &= \sqrt{\frac{32\pi}{15}} \frac{G}{c^4} \left(\ddot{I}_{zz} - \frac{1}{2}(\ddot{I}_{xx} + \ddot{I}_{yy}) \right) , \\ H^{\rm quad}_{2\pm1} &= \sqrt{\frac{16\pi}{5}} \frac{G}{c^4} \left(\mp \ddot{I}_{xz} + i\ddot{I}_{yz} \right) , \\ H^{\rm quad}_{2\pm2} &= \sqrt{\frac{4\pi}{5}} \frac{G}{c^4} \left(\ddot{I}_{xx} - \ddot{I}_{yy} \mp 2i\ddot{I}_{xy} \right) . \end{aligned} \tag{5.18}$$

For example, assuming the detector lies in the direction of the rotation axis of the bar ($\theta = 0$) we get:

$$h_+ = \frac{1}{D} \frac{G}{c^4} (\ddot{I}_{xx} - \ddot{I}_{yy}) \tag{5.19}$$

$$h_\times = \frac{2}{D} \frac{G}{c^4} \ddot{I}_{xy} . \tag{5.20}$$

We are now in a position to encode the above equations and compute the waveform. We first have to pick astrophysically meaningful bar parameters. For the mass we choose the expected mass of a canonical proto-neutron star (PNS), which ranges from $0.15\, M_\odot$ to $1.5\, M_\odot$. An appropriate length range is $L = 20\,\text{km} - 60\,\text{km}$, while the radius, $R = 5\,\text{km} - 20\,\text{km}$. As for the rotational frequency, $f = \Omega/2\pi$ we consider the range of values f above 200 Hz, and below 1000 Hz. Note that the duration of this process can be from $\sim 1\,\text{ms}$ to $\sim 1\,\text{s}$, during which f will decrease

noticeably, as rotational kinetic energy is lost to GWs. For simplicity we neglect this effect and consider the frequency to be a constant.

Realistic choice of waveform parameters

Spin frequencies below 200 Hz choice are not realistic, since it will be unlikely to obtain a deformed bar in this case. We therefore consider various representative frequencies starting from 400 Hz, which will give GWs at 800 Hz, broadly consistent with results in Scheidegger et al. 2010 [285], Ott et al. [286] and Dimmelmeier et al. 2007 [287, 288].

A reasonable value for the proto-neutron star radius is 15 km, since we expect that these instabilities are likely to occur relatively early in the evolution of the collapsing core. A 100 ms duration should be typical, but including the extreme case of 1 s duration would be interesting and remove any doubts of not covering a large part of the possible parameter space. An extreme choice for the mass of the bar is 1.5 $M_{\odot}$, while a conservative would be 0.2 $M_{\odot}$. Concerning the length of the bar an appropriate value would be three to four times the radius of the proto-neutron star. We have chosen L=60 km, thus giving axis ratios of one to three. The value of the bar length has a large effect on the amplitude of the signal, which is also controlled by the mass involved. We keep this parameter fixed for various values of the rest of the parameters. We therefore have the following six arrangements; all combinations of $M_{bar} = 0.2,\ 1.5\,M_{\odot}$, frequency of f = 400, 1000 Hz and a duration of t = 100, 1000 msec. See also Fig. 5.2.

5.6.2 Piro waveforms

These waveforms are produced from the inspiral of parts of a fragmented disk that is being formed at the time of the collapse, as proposed by Piro and Pfahl [289]. More specifically, parts of an outer accretion torus around a BH formed in the collapse of a massive star, become gravitationally unstable which leads to its fragmentation. The fragments condense to dense clumps of neutronized matter that then inspiral due to viscosity and/or GW emission. The inner part of the disk may be geometrically thin due to efficient neutrino cooling, but the outer regions are thick and subject to gravitational instabilities and fragmentation.

We assume a central BH of mass $M_{\rm BH}$ surrounded by a Keplerian accretion disk with orbital frequency $\Omega = (GM_{\rm BH}/r^3)^{1/2}$ and vertical scale height H. The accretion rate is $\dot{M} = 3\pi\nu\Sigma$, where Σ is the disk's surface density, $\nu = \alpha c_S H$ the usual viscosity prescription and c_S the isothermal sound speed. We assume that

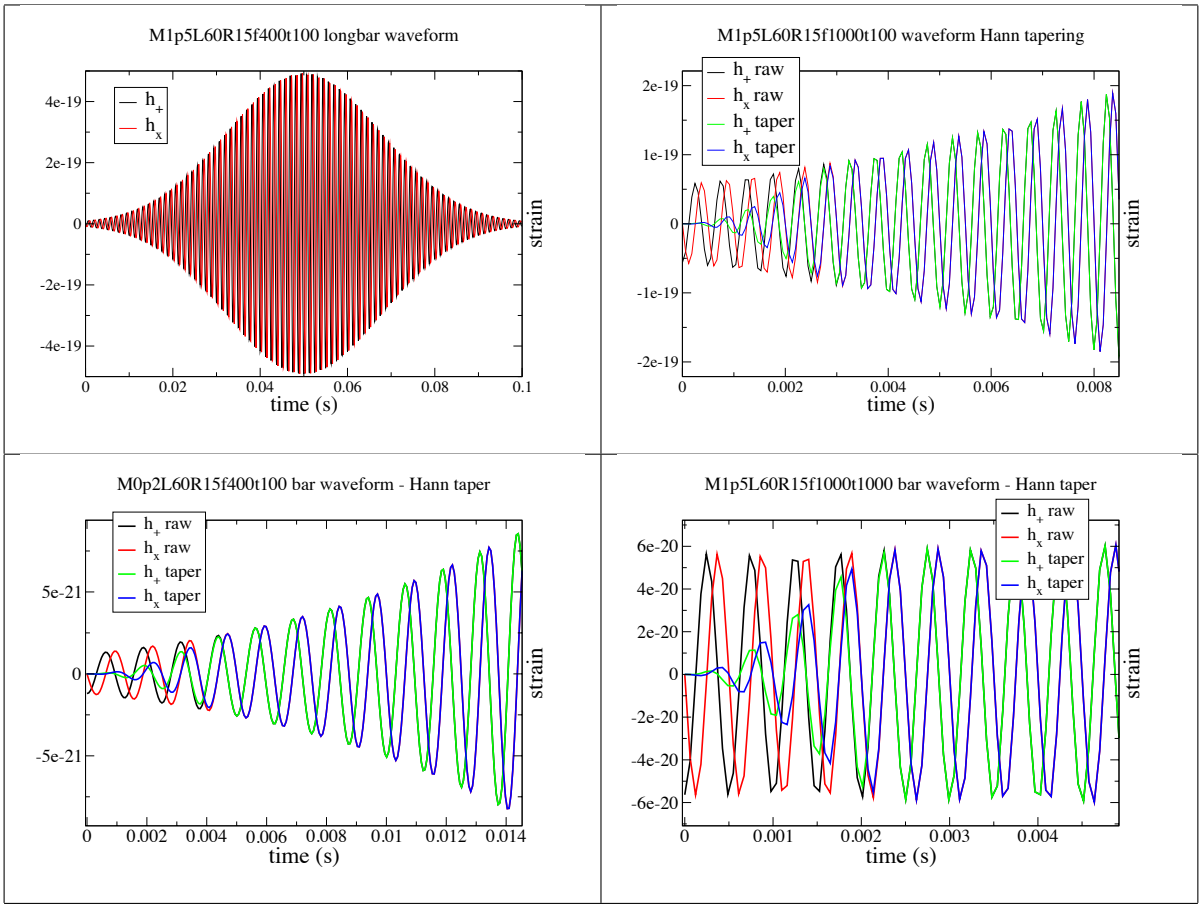

Figure 5.2: Representative rotating bar waveforms in the time domain. *Left* panel depicts the two polarizations of an optimally oriented, 400 Hz, 0.1 s long long-bar waveform. All waveforms of this type are enveloped by multiplying with a proper gaussian function. However, the use of gaussian envelopes makes them inappropriate for the current search, since for finite duration windows it creates a discontinuity in the beginning and end of the waveform, inducing non-zero strain values. *Right* panel contrasts the first cycles of the initial waveform against its conditioned, where 5-6 cycle-duration Hann half-windows are applied in the beginning and end of the waveform. The ending part is exactly the same.

$H/r = \mu$ is a fixed parameter.

It may well be that several matter aggregations will be formed inside the disk and that many of them will be massive enough to displace material, therefore losing angular momentum and migrating inwards, towards the BH. To simplify the calculation, we assume that a single, dense, massive clump is formed. In this process, the emission of energy and angular momentum via gravitational waves becomes increasingly dominant, thus leading quickly to an inspiral. The timescale of this phase can be estimated to first order via the quadrupole formula

$$t_{\rm GW} = \frac{5}{64\Omega}\left(\frac{G\mathcal{M}\Omega}{c^3}\right)^{-5/3}, \tag{5.21}$$

where $\mathcal{M}$ is the chirp mass of the system comprised of the central BH and the fragmented clump. We estimate the chirp-like gravitational signal from their inspiral phase, by essentially computing the quadrupole contribution, that is summing over Eqs. 5.18. The calculation of the evolving second moment of mass tensor is done by integrating the orbit via the ordinary differential equation

$$\frac{dr}{dt} = -r\left(\frac{1}{t_{\rm GW}} + \frac{1}{t_\nu}\right), \tag{5.22}$$

where the right-hand term describes the timescale of inward migration of the orbiting fragment due to the net torque which is the result of dissipation within the disk and emission of gravitational waves. In integrating Eq. 5.22, I implemented a fourth-order Runge-Kutta matlab integrator. Note that all initial distances are set to $100 \times GM_{\rm BH}/c^2$ and the final to the last stable orbit, hence different configurations yield different waveform durations, ranging from approximately 0.5 s to 3.5 s. Following generation, they were subsequently appended with zeros to reach the next integer second in duration, as well as tapered, see also Fig. 5.3. A realistic choice of configurations for use as injections are of a $M_{\rm BH} = 5$ and $10\,M_\odot$ with $M_{blob} \simeq 0.07,\ 0.55,\ 0.14,\ 0.11\,M_\odot$.

5.6.3 Sine-gaussian waveforms

Also included in the search is a set of two pairs of linearly and elliptically polarized sine-Gaussian waveforms, mainly because of their simplicity and to compare the sensitivity of the present search to the all-sky GWB search [290]. Linear waveforms include h_+ as in Eq. 5.23 and $h_\times = 0$, while elliptical contain both polarizations, which differ in phase by $\pi/2$, Eqs. 5.23-5.24. The two polarizations

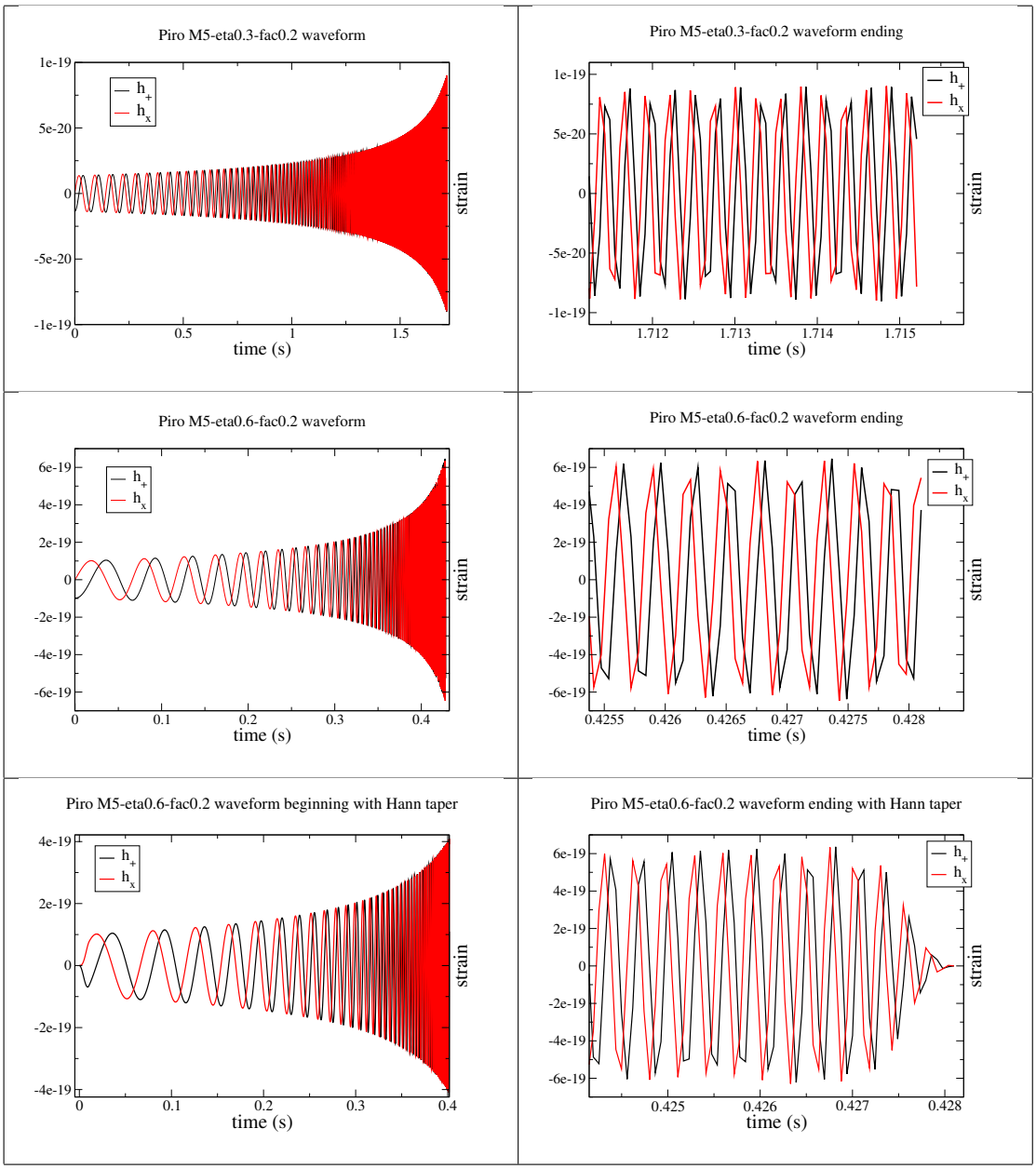

Figure 5.3: — Piro inspiral waveforms. Top panels show the full and end part of a waveform with central black hole mass of $M_{\rm BH} = 5\,M_\odot$ and $M_{blob} \simeq 0.07\,M_\odot$. Middle panels depict an inspiral of lower mass ratio, where $M_{\rm BH} = 5\,M_\odot$ and $M_{blob} \simeq 0.55\,M_\odot$; the lower chirping frequency is clearly visible. These raw waveforms start from non-zero strain values and are integrated up to the last stable orbit, hence they end in non-zero strain values. This renders them unsuitable for use in a closed-box analysis and needs to be dealt with detrending or simple tapering. Bottom panels show parts of the conditioned waveform of the middle panels, where half-Hann window tapers have been administered at the beginning and ending part. A more natural, yet more complicated, approach would have been to attach an appropriate merger-ringdown waveform.

are also multiplied by proper functions of the inclination angle,

$$h_+ = \frac{1+\cos^2(\iota)}{2}\, h_{peak}\, \sin(2\,\pi\,(t-T_o)\,f_o)\, e^{-(t-T_o)^2/\tau^2}\,, \tag{5.23}$$

$$h_\times = \cos(\iota)\, h_{peak}\, \cos(2\,\pi\,(t-T_o)\,f_o)\, e^{-(t-T_o)^2/\tau^2}\,, \tag{5.24}$$

$$h_{peak} = A\sqrt{\frac{4\,\sqrt{\pi}\,f_o}{Q\,(1+e^{-Q^2})}}\,,\;\; \tau = \frac{Q}{\sqrt{2}\,\pi\,f_o}\,, \tag{5.25}$$

where A and ι are the amplitude factor and viewing (inclination) angle. The first was fixed at 10^{-21}, while the latter was randomised for every injection in the on-source region. The selected waveforms are all combinations of : $f_o = 235\,\mathrm{Hz}$ and $1304\,\mathrm{Hz}$, with $Q = 8.9$ and either linear or elliptical polarization.

5.6.4 Dimmelmeier waveforms

In [291] are presented results of general relativistic simulations of a collapsing rotating iron core to a proto-neutron star. An extensive parameter study was undertaken to understand the dependence of the signal characteristics on variables such as the progenitor star mass, the precollapse rotation profile and the nuclear equation of state.

The authors employ the Newtonian quadrupole formula for the wave extraction, in the first-moment of momentum density formulation as discussed, e.g., in [292] to extract the gravitational waves generated by nonspherical accelerated fluid motions. It yields the quadrupole wave amplitude as the lowest order term in a multipole expansion of the radiation field into pure-spin tensor harmonics.

The authors point out that although the quadrupole formula is not gauge invariant and is only valid in the Newtonian slow-motion limit, for gravitational waves emitted in astrophysical situations of collapsing stellar cores it yields results that agree very well in amplitude and phase with more advanced methods. Three linearly polarized waveforms of a 15 $M_\odot$ progenitor core were selected, whose waveforms are depicted in Fig. 5.4.

5.6.5 Yakunin matter-generated waveforms

The Yakunin waveforms we are considering are associated with matter motion and were generated in axisymmetric two-dimensional simulations assuming 12, 15, and 25 $M_\odot$ non-rotating core progenitors [293]. The waveforms are characterised by various stages: An initial weak signal that starts at bounce and ends in between 50 and 75 ms after the bounce, followed by a quiescent phase, which is then followed

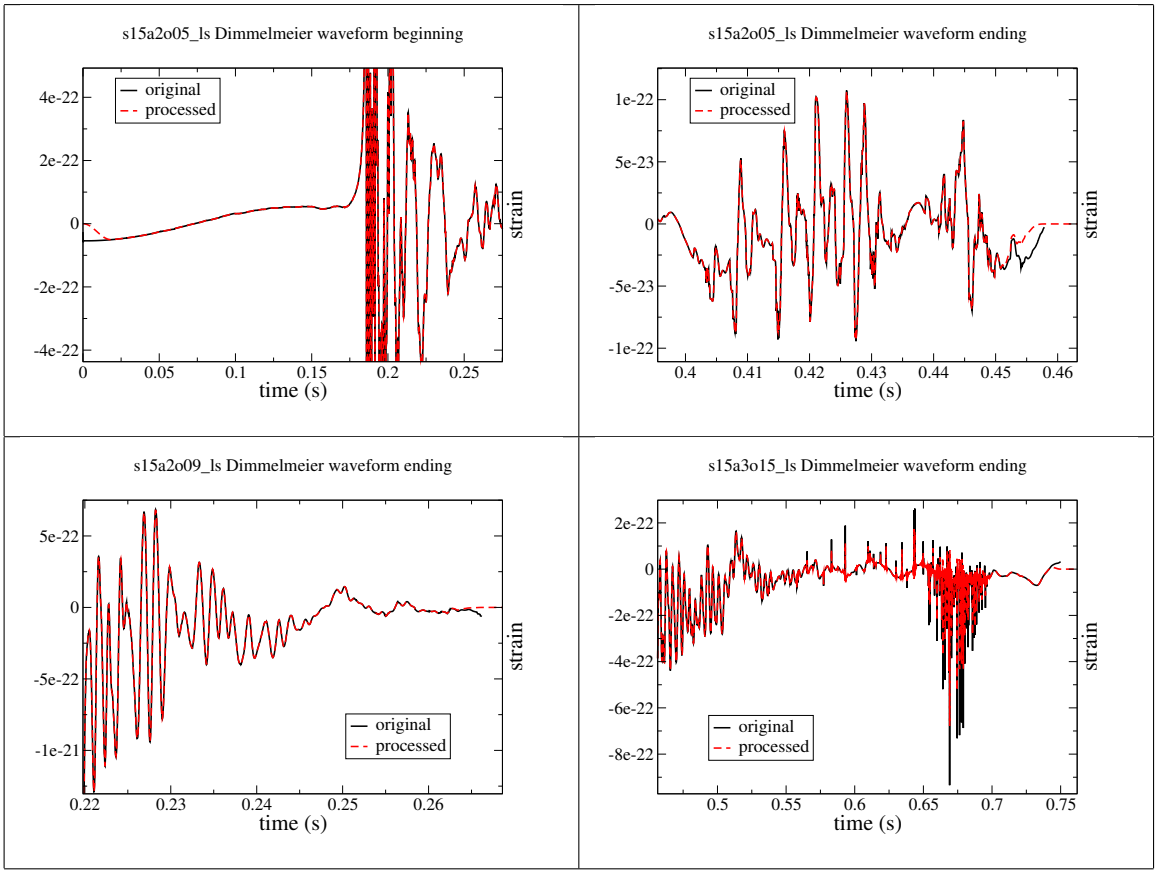

Figure 5.4: – Dimmelmeier waveforms. The general outline of the above three waveforms is very similar, especially in the beginning. The original waveforms suffer from non-zero strain values as shown in the plots with black solid lines. All waveforms except the bottom right one were simply processed by applying Hann windows and appending with zeros. Concerning the last one, s15a3o15, the presence of high frequency features near the ending required low-pass filtering, which was applied in precedence of the Hann tapering.

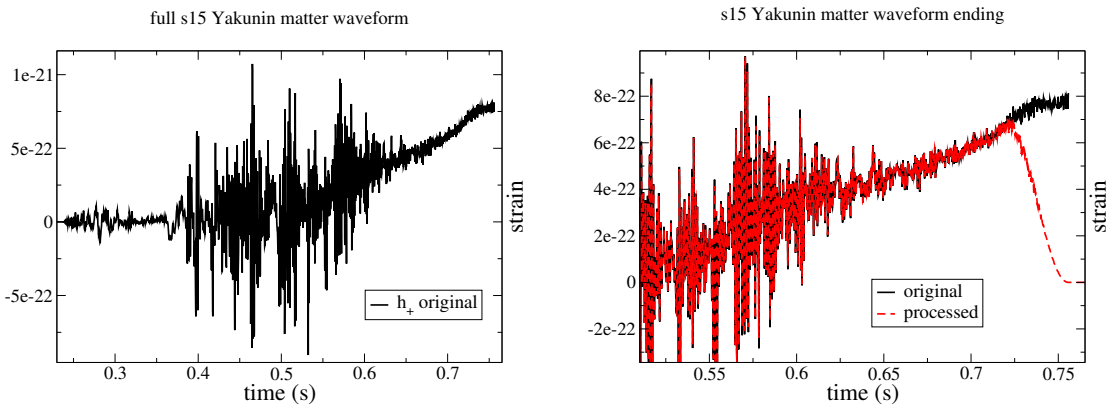

Figure 5.5: — A representative Yakunin matter generated waveform. As always, the strain values refer to a characteristic distance of 10 kpc. The mass of the progenitor core has the plausible value of 15 $M_{\odot}$. The waveform requires an upsampling to match the detectors' datastream sampling rate of 16384 Hz, as during the generation it was sampled at 3454 Hz. In addition, Hann tapering was applied at the ending stage, as shown in the *right* panel.

by the most energetic part of the GW signal. This stage ends approximately 350 ms to 450 ms post-bounce. Finally, there is a tail, which commences just before the end of the previous phase and consists of a steady increase in the strain. This tail continues to rise at the end of the simulations, reflecting the fact that the explosion and the associated matter motion is still ongoing and developing. Unfortunately, the resulting sharp cut-off in the strain makes it unphysical and thus inappropriate for use as an injected signal in GWB search pipelines. A proper tapering function is applied, which brings smoothly the strain value to zero, Fig. 5.5.

5.6.6 Burrows-Ott acoustic mechanism waveforms

These waveforms are generated via the acoustic mechanism. This was first proposed as a potentially very powerful proceess for generation of GWs in Burrows et al. [283, 294, 282] and involves the excitation of large-amplitude PNS g-modes. Turbulence and accretion downstream is what excites the $l = 1$ and $l = 2$ PNS g-modes. This mechanism is quite efficient in leading to an explosion of the star. However, its energy release is almost an order of magnitude lower than what is observed, while it takes place about one second after the bounce. If the neutrino mechanism is effective, it will probably explode the star long before the PNS pulsations grow to large amplitudes. Also, this mechanism has not been confirmed by different numerical Supernova groups. In fact, an important caveat has been noted by another group, involving the coupling of the $l = 1$ mode with higher

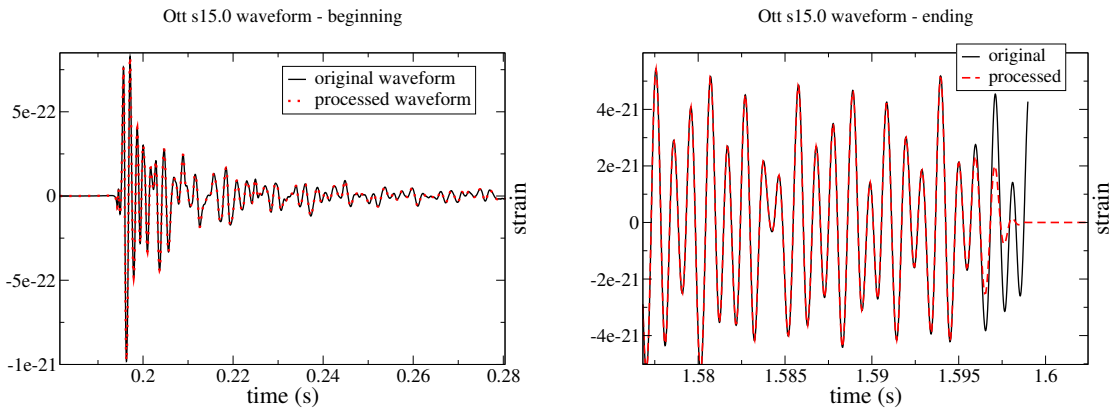

Figure 5.6: Details from the Ott numerical waveform. *Left* panel shows the beginning, while the *right* panel the ending of the waveform. For the analysis the waveform was resampled to 16384 Hz, followed by administering Hann windows in the first and last few cycles.

order modes, leading to its significant damping [295]. It is concluded in this latter work, that acoustic power is unlikely to be energetically significant in ccSN explosions. The waveform that was included in this search is of a 15 $M_{\odot}$ progenitor star and is shown in Fig. 5.6, along with the actual conditioned waveform injection.

5.6.7 Müller three-dimensional waveforms

This consists of a set of five gravitational waveforms produced in three-dimensional neutrino-driven Supernova explosions of non-rotating 15 and 20 $M_{\odot}$ stars [296]. These models do exhibit explosions, while the GW emission reaches a maximum earlier than the onset of the explosion. The generation of GWs is mostly due to anisotropic neutrino emission as well as non-radial mass motions in the accretion layer and their interaction with the outer layers of the PNS. The frequency range of the GWB is usually between 100-500 Hz. Once the explosion sets in, the GW signal exhibits a low-frequency modulation, in some cases describing a roughly monotonic growth, associated with the non-spherical expansion of the explosion shock wave and the large-scale anisotropy of the escaping neutrinos. The GW signals exhibit strong variability between the two polarizations, different explosion simulations and different observer directions. For this reason we have employed 100 different orientations for each Müller type as injected waveforms in the on-source region. A representative injected Müller waveform is shown in Fig. 5.7.

5.6.8 Numerical waveforms set for SN 2006iw

2D SASI Müller waveform

The waveform is the product of two-dimensional neutrino-driven simulations of a 15 $M_{\odot}$ slowly rotating progenitor star, where the dominant mechanisms responsible for the development of the GWB are standing accretion shock instability (SASI) and convection motion instabilities. The first refers to the standing wave that expands in an aspherical manner just outside the PNS, while the latter to convection motion in the layers surrounding the PNS [297]. See also top left panel of Fig. 5.8.

2D Takiwaki-Kotake waveform

The GW signature of two-dimensional (axisymmetric) magneto-hydrodynamically driven core-collapse Supernova explosions of a 25 $M_{\odot}$ star, with a strong precollapse magnetic field of 10^{12} G and rapid rotation [298]. See also the right panel in the middle row of Fig. 5.8.

3D SASI Kotake waveform

These are neutrino-driven waveforms from three-dimensional simulations that lead to explosions aided by the neutrinos as well as the asymmetrical expansion of the SASI [299]. The two main components are anisotropies in neutrino emission and matter motions in the layers surrounding the PNS. I have utilised the 'model A' GWB, which has a spectrum peak near $\sim 100\,\mathrm{Hz}$ and a duration of approximately 500 msec [299]. See also bottom left panel of Fig. 5.8.

3D Scheidegger waveform

The three-dimensional analog of Takiwaki-Kotake waveforms, but from a different numerical group. It concerns a 15 $M_{\odot}$ progenitor star with significant rotation and strong magnetic fields of the order of 10^{12} G [285] and viewed from the polar direction. See also bottom right panel of Fig. 5.8.

5.7 X-Pipeline and coherent WaveBurst joint search

5.7.1 Conditioning the waveforms

A few of the raw numerical waveforms were not generated at sufficient time resolution and have sampling rates as low as $\simeq 4000$ Hz. As a result, certain high-

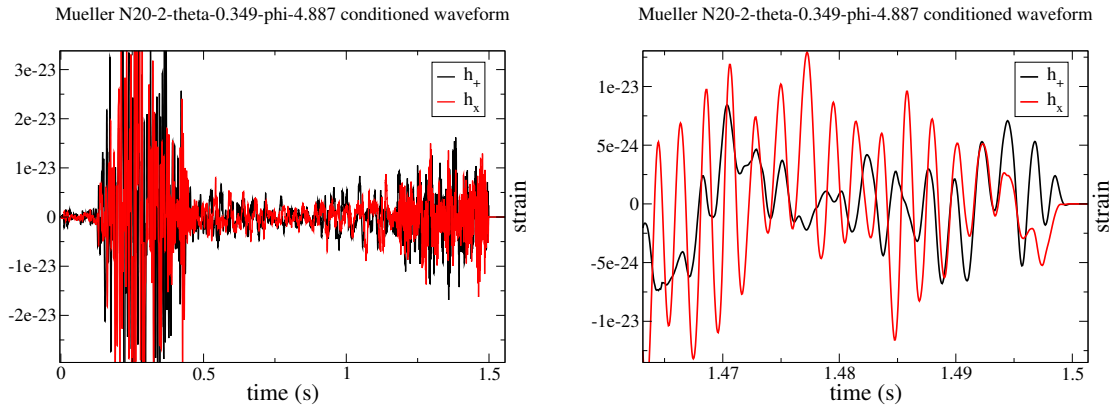

Figure 5.7: – A representative Müller numerical waveform. *Left* panel shows the full waveform, while *right* depicts the ending stage with the Hann tapering. As always, the strain data is resampled to 16384 Hz and refers to 10 kpc.

frequency features appear as 'single-point' spikes, which constitute fiducial high frequency features, ($> \sim$ 4 kHz). The interferometric detectors that are used in this search have reduced sensitivity above 2-3 kHz which means that high frequency features would not contribute to the total signal-to-noise ratio of the signal. In contrast, some numerical waveforms have extremely high sampling rates, reaching up to 10^7 Hz and do not show annoying high frequency features. In any case, applying a low-pass filter is appropriate. Apart from that, the data sampling rate of the LIGO and GEO detectors is 16384 Hz, therefore resampling to 16384 Hz is needed. Another important issue, which was mentioned in Section 5.6, is that most of the numerical waveforms were generated by numerical core-collapse simulations that did not involve the full process of core-collapse to post-bounce, therefore the waveforms have non-zero strain values in the beginning and ending part, which is dealt with Hann tapering, Figs. 5.4 - 5.8. The guideline of my conditioning procedure varies slightly between waveform families, but in general is:

1. Filter high-frequency features by applying a 9th order polynomial low-pass filter.

2. The filtering in some cases induces discontinuities at the two ends of the waveform, which are truncated.

3. Resample to 16384 Hz, to match the data acquisition sampling rate of the detectors.

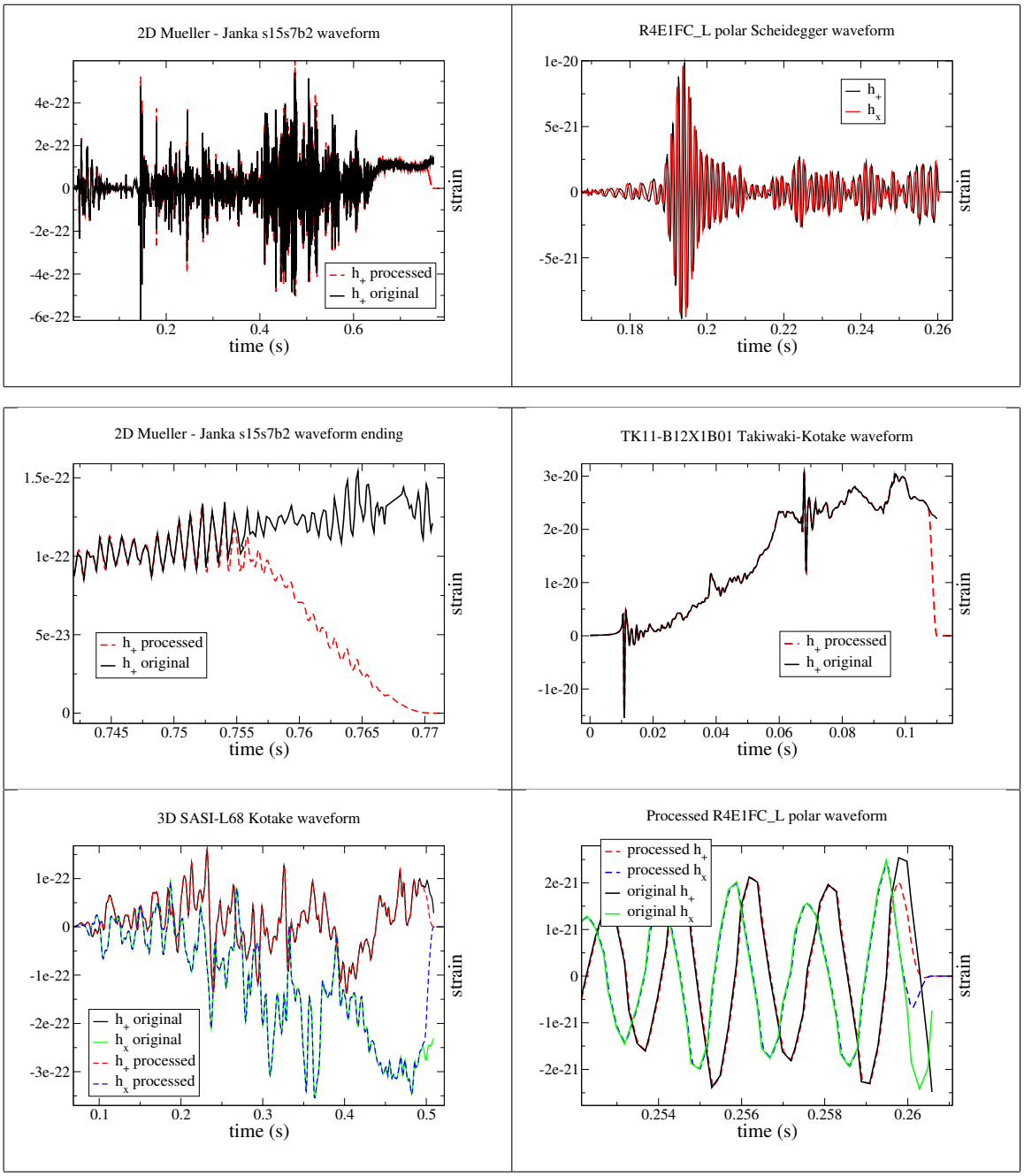

Figure 5.8: – Raw and processed numerical waveform injections that are used in the analysis of SN 2006iw. All waveforms were resampled to 16384 Hz and Hann-tapered in the beginning/end with appropriate length windows. Top row panels show the *full* waveforms from the Mueller et al. and Scheidegger et al. simulations. Middle row includes the 2D waveforms; left panel shows a detail from the end section of the Mueller waveform, while right panel shows the Takiwaki et al. waveform, 5.6.8. Bottom row shows the 3D waveforms; left panel: Kotake et al., and right panel: Scheidegger et al., 5.6.8. All strain values refer to a distance of 10 kpc to the progenitor. The arrangement of waveform types in the middle and bottom rows, follows the classification of mechanisms in Table 3 of the review [6].

4. Administer appropriate Hann half-windows at the two ends of the waveforms to account for their abrupt rise and ending.

5. Append the conditioned waveforms with zero strain values so that they reach the next integer number of seconds in duration.

5.7.2 Joint X-Pipeline and coherent WaveBurst search

In a forthcoming publication on ccSN search, X-Pipeline's sensitivity analysis results will be presented against those of the coherent WaveBurst (cWB) pipeline. Similarly to X-Pipeline, cWB combines all data streams into one coherent statistic constructed in the framework of the constrained maximum likelihood analysis [264, 266]. In cWB, the detection is based on the maximum likelihood ratio statistic which represents the total signal to noise ratio (SNR) of the GW signal detected in the network. Additional coherent statistics, such as the null stream and the network correlation coefficient can be constructed to distinguish genuine GW bursts from instrumental artifacts or environmental disturbances. More details can be found in [264, 266] and references therein.

5.7.3 Translating the burst MDC injection procedure to X-Pipeline

In order for the presentation of the results to be fair between two pipelines, it is useful to have the exact same injections. This may also allow for an explanation of why certain waveform families are retrieved more efficiently in one pipeline than the other. The goal is to have identical injected waveforms being applied at the exact same times in the on-source region. The injection procedure in each pipeline is quite differentiated, creating the need to translate the injections that one pipeline has performed for use into the other. Receiving as input the timeseries of the conditioned waveforms, Section 5.6, the GravEn engine [300, 301] in Burst MDC is producing simulated GWB injections, which are then read by cWB. I took the initiative to translate the burst MDC sets of injections into injection log files that X-Pipeline can interpret. I briefly state the main points of this procedure:

- Generate and catalogue the injections in Burst MDC [300, 301].

- Read in the Burst MDC log files and translate them to X-Pipeline log files. In general, the following metadata are translated:

    1. waveform name of the injection

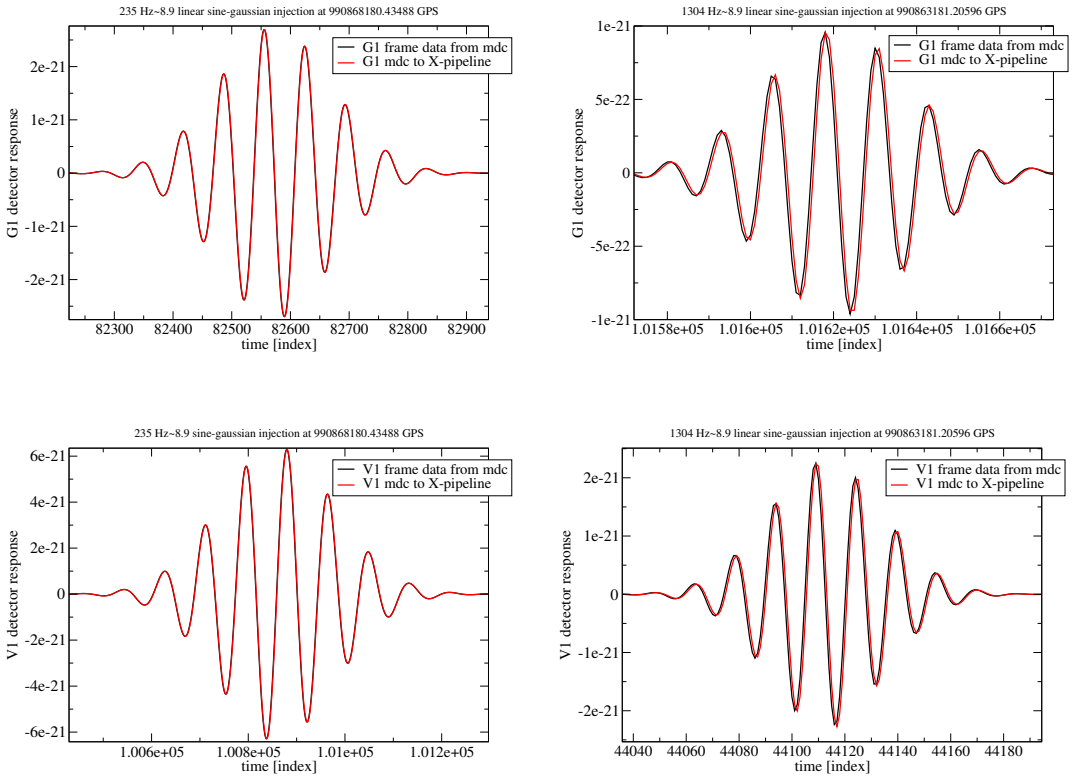

Figure 5.9: — G1 (top panels) and V1 (bottom panels) simulated detector responses to injections of 235 Hz and 1304 Hz linear sine-Gaussian waveforms for the SN 2011dh Supernova trigger. X-Pipeline is denoted with the red curve, while cWB with the black. The two responses almost overlap and the time discrepancies (maximum of ∼0.2 msec for the 1304 Hz waveform in Virgo) are considered insignificant for a comparison of the efficiencies of the two pipelines.

2. time of the injection in Earth-centered coordinates
3. sky position (θ, ϕ) of injection and polarization Ψ
4. orientation angle ι of the source and distance
5. internal parameters, dependent on the type of waveform and mechanism, such as mass, symmetric mass ratio, rotational frequency, damping time etc.

- Substitute the proper injection files in X-Pipeline with the translated injection files to actually run the cWB injections.

As a first test, the simulated response of the detectors to the software injections are computed in both pipelines and compared against. The response of detector k to an injection with specified starting time t_{inj}, sky location $\theta(t_{inj})$, $\phi(t_{inj})$ and

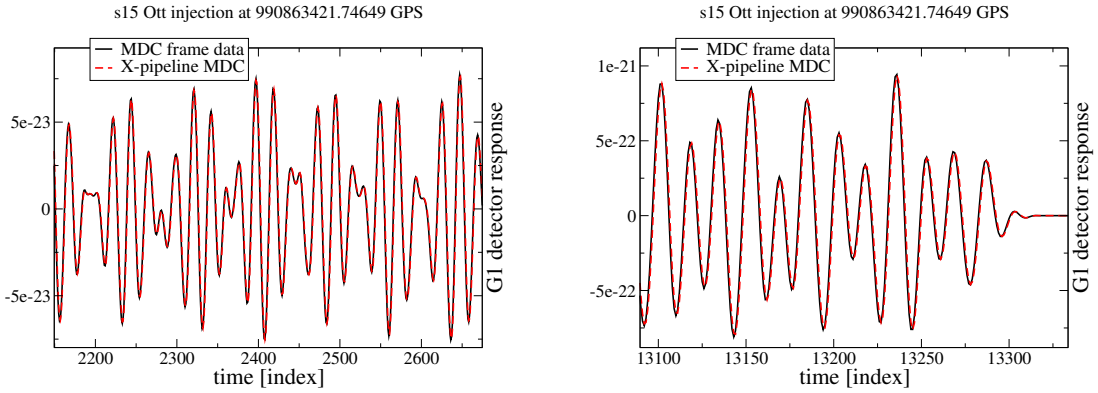

Figure 5.10: – The simulated detector network responses to an injected Ott s15 numerical waveform at the stated time for SN 2011dh, from the MDC frames and as computed in X-Pipeline. There is small time discrepancy of about one sample, which translates to approximately 0.06 msec.

polarization angle $\Psi(t_{inj})$:

$$F_{+}^{(k)}(\theta(t_{inj}),\phi(t_{inj}),\Psi(t_{inj}))\,h_{+}(t-t_{inj}) + F_{\times}^{(k)}(\theta(t_{inj}),\phi(t_{inj}),\Psi(t_{inj}))\,h_{\times}(t-t_{inj})\,.$$

The simple case of linear sine-Gaussian waveforms is plotted for Virgo and GEO in Fig. 5.9, where it can be seen that the simulated GEO response is consistent in the two pipelines. However, in the Virgo channel and particularly for the higher 1304 Hz frequency value, there is a noticeable discrepancy, whereas the responses appear to be offset in phase, which is equivalent to a time discrepancy of $\simeq 0.2$ msec. This might be due to the fact that the data sampling rate of Virgo is 20 kHz, which is subsequently downsampled to 16384 Hz, by using heterogeneous interpolation routines. For a representative simulated response to a numerical waveform injection see Fig. 5.10.

5.8 Sensitivity performance of X-Pipeline

I provide a concise description of the sensitivity analysis results of X-Pipeline in detecting GWBs associated with the optical triggers in Table 5.1. I adopt the standard measure of signal strength, which is the root-sum-squared amplitude [8], defined by

$$h_{\rm rss} = \sqrt{\int_{-\infty}^{\infty} dt\,[h_{+}^{2}(t)+h_{\times}^{2}(t)]} \;=\; \sqrt{2\int_{0}^{\infty} df\,\left[|\tilde{h}_{+}|^{2}(f)+|\tilde{h}_{\times}|^{2}(f)\right]}\,. \qquad (5.26)$$

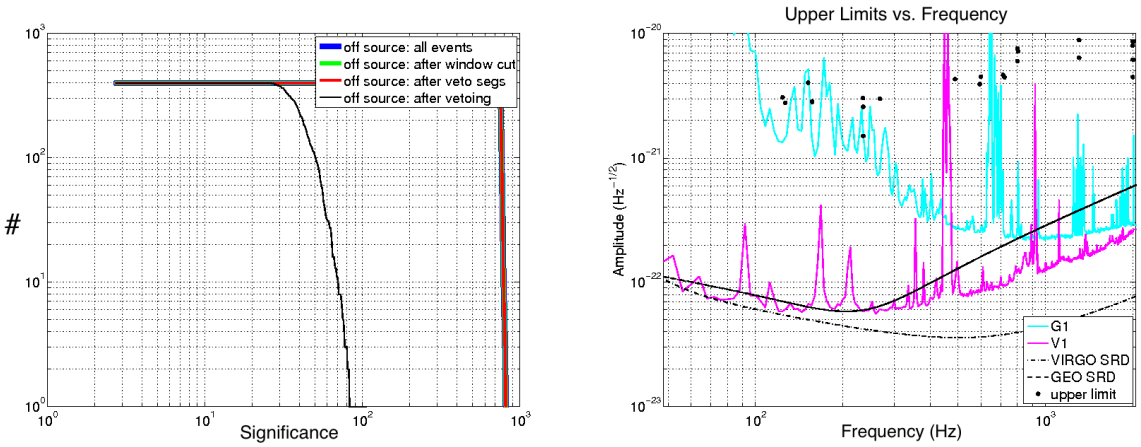

Figure 5.11: — SN 2011dh. *Left* panel depicts the rate of off-source events versus their significance before (red line) and after the coherent veto cuts (black line). *Right* panel compares the 50% upper limit amplitudes of all injections, with the G1 and V1 detector sensitivities, in terms of the central waveform frequency.

Closed-box analysis and tuning

The sensitivity performance depends largely on the relative significance of the clusters produced by actual GWB signals to those produced by background noise transients. For each given GWB injection type inside the on-source region, the 50%/90% confidence level upper limit on the signal amplitude is the minimum amplitude for which there is an equal or larger than 50%/90% possibility that such a signal would produce a cluster with significance larger than the largest measured significance in the on-source region. In what is termed a 'closed-box' or 'blind' analysis, all the on-source data is ignored, thereby using the significance of the loudest off-source events, along with the injected clusters. This procedure is identical to the one in a standard GRB search [8].

Results

For background estimation, all Supernova triggers were run on all data available in their corresponding on-source regions, Table 5.1. At the end of the analysis a web page is generated, detailing the closed-box analysis, such as optimized glitch rejection threshold values, predicted upper limits and background noise rejection [8].

The closed-box analysis discussed earlier in this Section was used to tune the coherent veto test and estimate the expected upper limit strain values in X-Pipeline. For SN 2011dh, the predicted 50/90% strain amplitude results, as well as the central frequency for each waveform type are summarised in Table 5.2. The right panel

Injected waveform type	**SN 2011dh** h_{rss} 50/90	**Central frequency(Hz)**
	Numerical waveforms	
Dim s15A2O05	4.32e-21 / -	487.4
Dim s15A2O09	- / -	620.5
Dim s15A3O15	3.07e-21 / -	123.9
Yakunin s15	- / -	673.5
Ott 2009 s15.0	- / -	803.9
Mueller W15-2	3.00e-21 / -	267.9
Mueller W15-4	3.04e-21 / -	234.3
Mueller L15-2	2.77e-21 / -	126.5
Mueller L15-3	4.03e-21 / -	151.7
Mueller N20-2	2.82e-21 / -	156.5
	Analytical waveforms	
M0p2 f400 t100	7.59e-21 / 1.31e-20	800.0
M1p5 f400 t100	6.00e-21 / 1.11e-20	800.0
M0p2 f1000 t100	8.05e-21 / 1.56e-20	1994.9
M1p5 f1000 t100	1.38e-21 / 7.55e-21	1994.9
M0p2 f1000 t1000	6.16e-21 / 1.11e-20	1999.5
M1p5 f1000 t1000	8.64e-21 / 1.56e-20	1999.5
piroM5 eta0.3	4.58e-21 / 6.21e-21	722.0
piroM5 eta0.6	4.48e-21 / 6.14e-21	714.4
piroM10 eta0.3	4.43e-21 / 5.81e-21	593.1
piroM10 eta0.6	3.35e-21 / 5.17e-21	598.1
SG 235 Hz linear	- / -	235.0
SG 1304 Hz linear	- / -	1304.0
SG 235 Hz elliptical	2.12e-21 / 7.83e-21	235.0
SG 1304 Hz elliptical	2.74e-21 / 5.35e-21	1304.0

Table 5.2: Closed-box efficiency results for Supernova 2011dh. Amplitude strain values at which 50% and 90% of all injections of the given type pass the 'alphaL-inCutCirc' coherent veto tests [8], while "-" denotes efficiency values where less than 50% and 90% respectively, of total injections were retrieved.

of Fig. 5.11 puts those values into perspective by depicting the 50% strain values onto the sensitivity curves of the detectors in the network. Excluding the Mueller family of waveforms, all waveform types are detectable with 98% confidence at the 50% strain amplitude limits shown in Table 5.2 if the supernova is located within a distance of 10 kpc, with the corresponding SNR values ranging in Virgo from $\sim$5 to $\sim$40. Considering the Mueller waveform family and the Dimmelmeier 's15A3O15' waveform model, their main power contribution is below 250-300 Hz, yielding very low SNR values in the GEO detector Fig. 5.11. This eradicates the effectiveness of the coherent veto tests, making ambiguous the discrimination between a genuine GWB and a noise transient. An additional note is that the current analysis has the best performance on waveforms containing both polarisations. Therefore, for those waveforms that either exhibit a very differentiated polarisation content between the two '+' and '$\times$' polarisations (Dimmelemeier, Yakunin and Ott in Table 5.2), or have only one polarisation component (SG linear) they fail to pass the veto tests for the range of injection amplitudes considered, thus never reaching 90% efficiency.

Upper limit results for Supernova 2006iw are pending due to a MATLAB memory issue on the cluster where the analysis is performed, but is in the final stages of processing. Results for the SN 2007gr trigger are also pending. Initial test runs on a set of waveforms have been performed, but the official X-Pipeline results will have to be produced by making use of the output of the Burst MDC injection engine. The generation of injections with GravEn is ongoing, by other members of the LVC-Supernova working group.

Chapter 6

Discussion

No gravitational-wave events have been detected thus far. However, performing Science with gravitational-waves should begin after 2016, giving life to the field of gravitational-wave Astronomy, see Chapter 1. To this point, upper limits to the gravitational-wave flux emitted from various types of sources have been established, while indirect evidence exists that supports the existence of gravitational waves being emitted by binary neutron stars, Chapter 1. I have presented part of the science potential of measuring the gravitational-wave signature of two general types of sources; merging binary BHs and core-collapse Supernovae.

The late-time radiation emitted by a highly deformed BH that has ensued from the merger of a BH binary is a phenomenon taking place in the strong field regime. Probing this type of radiation, will not only reveal information about the BH and its progenitor binary, but constitutes a stringent test of general relativity. We argued that in non-spinning and spinning binaries with aligned/anti-aligned spins, the ratio of component masses can be extracted by measuring the relative excitation of the most dominant modes in the BH quasi-normal mode spectrum. A fractional error in the mass ratio of better than 10% for 500 $M_{\odot}$ (intermediate-mass) BHs at a distance of 1 Gpc is typical in ET and aLIGO, while similar accuracies can be achieved out to cosmological distances for a supermassive BH with a space-based detector such as NGO and LISA, Chapters 2, 3 and 4. The mass ratio constitutes a key astrophysical parameter of the binary. In the stellar mass range, observations will shed light on their population and mass distribution inside dense clusters, as well as the distribution of their spin magnitudes. Evidence from electromagnetic observations on the existence of BHs more massive than 200 $M_{\odot}$ is ambiguous. Gravitational observations of the ringdown part will confirm their existence and aid in discriminating among the various models of formation of intermediate and supermassive black holes. BHs of the latter category may play a

key role in the formation of galaxies, Chapter 3. An important relevant question is whether supermassive BHs acted as proto-nuclei in the formation of galaxies, or if they gradually formed within the galaxy, for instance via mass segragation processes. Perhaps the most important limitation of our study is that it refers to non-precesing, or mildly precessing binaries, in quasi-circular orbits, addressing the need to produce a multimodal signal model referring to a generic binary.

Core-collapse Supernovae should constitute an important GW source. Despite the fact that the detection horizon is of the order of a few tens of kpc for the majority of GW generation models during S5 and S6, a small number of detections in the aLIGO era may suffice to constrain the dominant underlying mechanisms that take place in the explosion phase of massive stars, Chapter 5. This last chapter illustrates the limited detection horizon of the current search with iLIGO and provides the methodology which will be applied in triggered GWB searches from Supernovae in the aLIGO era.

Bibliography

[1] 'Dying tones of black holes', School of Physics and Astronomy, Cardiff University Press Release. October 1st 2012.

[2] Ioannis Kamaretsos. 'Explaining black holes', YouTube, Cardiff University Channel. September 2012.

[3] Yi Pan, Alessandra Buonanno, Michael Boyle, Luisa T. Buchman, Lawrence E. Kidder, et al. Inspiral-merger-ringdown multipolar waveforms of nonspinning black-hole binaries using the effective-one-body formalism. *Phys.Rev.*, D84:124052, 2011.

[4] Gijs Nelemans, L.R. Yungelson, and S.F. Portegies Zwart. Short- period AM CVn systems as optical, x-ray and gravitational wave sources. *Mon.Not.Roy.Astron.Soc.*, 349:181, 2004.

[5] Chris Van Den Broeck, M. Trias, B.S. Sathyaprakash, and A.M. Sintes. Weak lensing effects in the measurement of the dark energy equation of state with LISA. *Phys.Rev.*, D81:124031, 2010.

[6] Kei Kotake. Multiple physical elements to determine the gravitational-wave signatures of core-collapse supernovae. 2011.

[7] J. Abadie et al. Predictions for the Rates of Compact Binary Coalescences Observable by Ground-based Gravitational-wave Detectors. 2010.

[8] Patrick J Sutton, Gareth Jones, Shourov Chatterji, Peter Kalmus, Isabel Leonor, Stephen Poprocki, Jameson Rollins, Antony Searle, Leo Stein, Massimo Tinto, and Michal Was. X-pipeline: an analysis package for autonomous gravitational-wave burst searches. *New Journal of Physics*, 12(5):053034, 2010.

[9] S.M. Carroll. *Spacetime and Geometry: An Introduction to General Relativity*. Addison Wesley, 2004.

[10] W. L. Ames and K. S. Thorne. The Optical Appearance of a Star that is Collapsing Through its Gravitational Radius. *Astrophysical Journal*, 151:659, feb 1968.

[11] S.W. Hawking and G.F.R. Ellis. *The Large Scale Structure of Space-Time*. Cambridge Monographs on Mathematical Physics. Cambridge University Press, 1975.

[12] S. Chandrasekhar. *The Mathematical Theory of Black Holes*. Oxford Classic Texts in the Physical Sciences. Oxford University Press, 1998. First published in 1983.

[13] R. Ruffini and J. A. Wheeler. Introducing the black hole, 1971. Physics Today 24, 30.

[14] Ya. B. Zel'dovich Doroshkevich A. G. and I. D. Novikov. *Zh. Eksp. Teor. Fiz.*, 49:170, 1965.

[15] I. D. Novikov. *Zh. Eksp. Teor. Fiz.*, 57:949, 1969.

[16] V. L. Ginzburg. *Dokl. Akad. Nauk USSR*, 156:43, 1964.

[17] V. L. Ginzburg and L. M. Ozernoi. *Zh. Eksp. Teor. Fiz.*, 47:1030, 1964.

[18] B. Carter. *Phys. Rev. Lett.*, 26:331, 1971.

[19] R.M. Wald. *General relativity*. Physics/Astrophysics. University of Chicago Press, 1984.

[20] Ramesh Narayan, Jeffrey E. McClintock, and Rebecca Shafee. Estimating the Spins of Stellar-Mass Black Holes by Fitting Their Continuum Spectra. *AIP Conf.Proc.*, 968:265–272, 2008.

[21] Marek A. Abramowicz, Wlodek Kluzniak, Zdenek Stuchlik, and Gabriel Torok. The Orbital resonance model for twin peak kHz QPOs: Measuring the black hole spins in microquasars. *Astron.Astrophys.*, 2004.

[22] Jon M. Miller, A.C. Fabian, M.A. Nowak, and W.H.G. Lewin. Relativistic iron lines in Galactic black holes: Recent results and lines in the ASCA archive. pages 1296–1300, 2004.

[23] Ruth A. Daly. Estimates of Black Hole Spin Properties of 55 Sources. 2011.

[24] Evan O'Connor and Christian D. Ott. Black Hole Formation in Failing Core-Collapse Supernovae. *Astrophys.J.*, 730:70, 2011.

[25] S. W. Hawking. Gravitational radiation from colliding black holes. *Phys. Rev. Lett.*, 26:1344–1346, May 1971.

[26] Demetrios Christodoulou. Reversible and irreversible transformations in black-hole physics. *Phys. Rev. Lett.*, 25:1596–1597, Nov 1970.

[27] Demetrios Christodoulou and Remo Ruffini. Reversible transformations of a charged black hole. *Phys. Rev. D*, 4:3552–3555, Dec 1971.

[28] Charles W. Misner, Kip S. Thorne, and John Archibald Wheeler. *Gravitation*. W. H. Freeman, San Francisco, 1973.

[29] Ivan Booth and Stephen Fairhurst. The first law for slowly evolving horizons. *Phys. Rev. Lett.*, 92:011102, Jan 2004.

[30] T.W. Baumgarte and S.L. Shapiro. *Numerical Relativity: Solving Einstein's Equations on the Computer*. Cambridge University Press, 2010.

[31] Abhay Ashtekar, Christopher Beetle, Olaf Dreyer, Stephen Fairhurst, Badri Krishnan, Jerzy Lewandowski, and Jacek Wiśniewski. Generic isolated horizons and their applications. *Phys. Rev. Lett.*, 85:3564–3567, Oct 2000.

[32] Abhay Ashtekar, Christopher Beetle, and Stephen Fairhurst. Mechanics of isolated horizons. *Classical and Quantum Gravity*, 17(2):253, 2000.

[33] Abhay Ashtekar, Jonathan Engle, Tomasz Pawlowski, and Chris Van Den Broeck. Multipole moments of isolated horizons. *Class.Quant.Grav.*, 21:2549–2570, 2004.

[34] Emanuele Berti and Vitor Cardoso. Quasinormal ringing of Kerr black holes. I. The Excitation factors. *Phys.Rev.*, D74:104020, 2006.

[35] Emanuele Berti, Vitor Cardoso, and Andrei O. Starinets. Quasinormal modes of black holes and black branes. *Class. Quant. Grav.*, 26:163001, 2009.

[36] T. Regge and J.A. Wheeler. Stability of a schwarzschild singularity. *Phys. Rev.*, 108:1063, 1957.

[37] F J Zerilli. *Phys. Rev. D*, 2:2141, 1970.

[38] C.V. Vishveshwara. Scattering of gravitational radiation by a schwarzschild black hole. *Nature*, 227:936, 1970.

[39] S. Detweiler. Black holes and gravitational waves. III - The resonant frequencies of rotating holes. *apj*, 239:292–295, July 1980.

[40] B R Iyer, S Iyer, and C V Vishveshwara. Scalar waves in the boulware-deser black-hole background. *Classical and Quantum Gravity*, 6(11):1627, 1989.

[41] Paul D. Lasky and Daniela D. Doneva. Stability and quasinormal modes of black holes in tensor-vector-scalar theory: Scalar field perturbations. *Phys. Rev. D*, 82:124068, Dec 2010.

[42] Nils Andersson. Excitation of schwarzschild black-hole quasinormal modes. *Phys. Rev. D*, 51:353–363, Jan 1995.

[43] Edward W. Leaver. Quasinormal modes of reissner-nordström black holes. *Phys. Rev. D*, 41:2986–2997, May 1990.

[44] N. Andersson, M. E. Araújo, and B. F. Schutz. Quasinormal modes of reissner-nordström black holes: Phase-integral approach. *Phys. Rev. D*, 49:2703–2709, Mar 1994.

[45] Hans-Peter Nollert and Bernd G. Schmidt. Quasinormal modes of schwarzschild black holes: Defined and calculated via laplace transformation. *Phys. Rev. D*, 45:2617–2627, Apr 1992.

[46] Edward W. Leaver. Spectral decomposition of the perturbation response of the schwarzschild geometry. *Phys. Rev. D*, 34:384–408, Jul 1986.

[47] G. Pöschl and E. Teller. *Z. Phys.*, 83:143, 1933.

[48] Valeria Ferrari and Bahram Mashhoon. New approach to the quasinormal modes of a black hole. *Phys. Rev. D*, 30:295–304, Jul 1984.

[49] E. Berti, V. Cardoso, and C. M. Will. Gravitational-wave spectroscopy of massive black holes with the space interferometer lisa. *Phys. Rev. D*, 73(6):064030–+, March 2006.

[50] Aaron Zimmerman and Yanbei Chen. New Generic Ringdown Frequencies at the Birth of a Kerr Black Hole. *Phys.Rev.*, D84:084012, 2011.

[51] Kunihito Ioka and Hiroyuki Nakano. Second and higher-order quasi-normal modes in binary black hole mergers. *Phys.Rev.*, D76:061503, 2007.

[52] Hiroyuki Nakano and Kunihito Ioka. Second Order Quasi-Normal Mode of the Schwarzschild Black Hole. *Phys.Rev.*, D76:084007, 2007.

[53] H. Stephani. *Exact Solutions of Einstein's Field Equations*. Cambridge Monographs on Mathematical Physics. Cambridge University Press, 2003.

[54] Frans Pretorius. Evolution of binary black hole spacetimes. *Phys. Rev. Lett.*, 95:121101, 2005.

[55] Manuela Campanelli, C. O. Lousto, P. Marronetti, and Y. Zlochower. Accurate Evolutions of Orbiting Black-Hole Binaries Without Excision. *Phys. Rev. Lett.*, 96:111101, 2006.

[56] John G. Baker, Joan Centrella, Dae-Il Choi, Michael Koppitz, and James van Meter. Gravitational wave extraction from an inspiraling configuration of merging black holes. *Phys. Rev. Lett.*, 96:111102, 2006.

[57] T.G.F. Li, W. Del Pozzo, S. Vitale, C. Van Den Broeck, M. Agathos, et al. Towards a generic test of the strong field dynamics of general relativity using compact binary coalescence. *Phys.Rev.*, D85:082003, 2012.

[58] Ioannis Kamaretsos, Mark Hannam, Sascha Husa, and B. S. Sathyaprakash. Black-hole hair loss: Learning about binary progenitors from ringdown signals. *Phys. Rev. D*, 85:024018, Jan 2012.

[59] Ioannis Kamaretsos, Mark Hannam, and B. Sathyaprakash. Is black-hole ringdown a memory of its progenitor? *Phys. Rev. Lett.*, 109:141102, 2012.

[60] S. Gossan, J. Veitch, and B.S. Sathyaprakash. Bayesian model selection for testing the no-hair theorem with black hole ringdowns. *Phys.Rev.*, D85:124056, 2012.

[61] A. Lichnerowicz. L'intégration des équations de la gravitation relativiste et la probléme des n corps. 1944. J. Math. Pure Appl 23, 37-63.

[62] L.L. Smarr and Battelle Seattle Research Center. *Sources of Gravitational Radiation: Proceedings of the Battelle Seattle Workshop, July 24-August 4, 1978*. Cambridge University Press, 1979. Kinematics and dynamics of general relativity, pp. 83-126 (York, Jr., J. W.).

[63] Richard L. Arnowitt, Stanley Deser, and Charles W. Misner. The Dynamics of general relativity. 1962. Gravitation: an introduction to current research, Louis Witten ed. (Wilew 1962), chapter 7, pp 227-265.

[64] Thomas W. Baumgarte and Stuart L. Shapiro. On the numerical integration of Einstein's field equations. *Phys. Rev.*, D59:024007, 1999.

[65] Bernd Brügmann. Adaptive mesh and geodesically sliced schwarzschild spacetime in 3+1 dimensions. *Phys. Rev. D*, 54:7361–7372, Dec 1996.

[66] Bernd Brügmann et al. Calibration of Moving Puncture Simulations. *Phys. Rev.*, D77:024027, 2008.

[67] Matthew W. Choptuik. Universality and scaling in gravitational collapse of a massless scalar field. *Phys. Rev. Lett.*, 70:9–12, Jan 1993.

[68] Wolfgang Tichy and Bernd Brügmann. Quasiequilibrium binary black hole sequences for puncture data derived from helical killing vector conditions. *Phys. Rev. D*, 69:024006, Jan 2004.

[69] E. Poisson. *A Relativist's Toolkit: The Mathematics of Black-Hole Mechanics*. Cambridge University Press, 2004.

[70] Arthur Komar. Covariant conservation laws in general relativity. *Phys. Rev.*, 113:934–936, Feb 1959.

[71] Marcus Ansorg, Bernd Brügmann, and Wolfgang Tichy. A single-domain spectral method for black hole puncture data. *Phys. Rev.*, D70:064011, 2004.

[72] Steven Brandt and Bernd Brügmann. A Simple construction of initial data for multiple black holes. *Phys. Rev. Lett.*, 78:3606–3609, 1997.

[73] P.C. Peters. Gravitational radiation and the motion of two point masses. *Phys. Rev.*, 136:B1224–B1232, 1964.

[74] Luc Blanchet, Thibault Damour, and Bala R. Iyer. Gravitational waves from inspiralling compact binaries: Energy loss and waveform to second-post-newtonian order. *Phys. Rev. D*, 51:5360–5386, May 1995.

[75] Luc Blanchet, Guillaume Faye, and Bénédicte Ponsot. Gravitational field and equations of motion of compact binaries to 5/2 post-newtonian order. *Phys. Rev. D*, 58:124002, Oct 1998.

[76] Luc Blanchet, Thibault Damour, Gilles Esposito-Farèse, and Bala R. Iyer. Gravitational radiation from inspiralling compact binaries completed at the third post-newtonian order. *Phys. Rev. Lett.*, 93:091101, Aug 2004.

[77] Luc Blanchet, Thibault Damour, Bala R. Iyer, Clifford M. Will, and Alan G. Wiseman. Gravitational-radiation damping of compact binary systems to second post-newtonian order. *Phys. Rev. Lett.*, 74:3515–3518, May 1995.

[78] A. Buonanno and T. Damour. Effective one-body approach to general relativistic two- body dynamics. *Phys. Rev. D*, 59:084006, 1999.

[79] Yi Pan et al. Effective-one-body waveforms calibrated to numerical relativity simulations: coalescence of non-precessing, spinning, equal-mass black holes. 2009.

[80] Sascha Husa, Mark Hannam, Jose A. González, Ulrich Sperhake, and Bernd Brügmann. Reducing eccentricity in black-hole binary evolutions with initial parameters from post-Newtonian inspiral. *Phys. Rev.*, D77:044037, 2008.

[81] Mark Hannam, Sascha Husa, Frank Ohme, Doreen Muller, and Bernd Bruegmann. Simulations of black-hole binaries with unequal masses or non-precessing spins: Accuracy, physical properties, and comparison with post-Newtonian results. *Phys.Rev.*, D82:124008, 2010.

[82] Michael Purrer, Sascha Husa, and Mark Hannam. An Efficient iterative method to reduce eccentricity in numerical-relativity simulations of compact binary inspiral. *Phys.Rev.*, D85:124051, 2012.

[83] B.F. Schutz. *A First Course in General Relativity.* Series in physics. Cambridge University Press, 1985.

[84] Vincent Moncrief. Gravitational perturbations of spherically symmetric systems. i. the exterior problem. *Annals of Physics*, 88(2):323 – 342, 1974.

[85] Alessandro Nagar and Luciano Rezzolla. Gauge-invariant non-spherical metric perturbations of schwarzschild black-hole spacetimes. *Classical and Quantum Gravity*, 22(16):R167, 2005.

[86] Thomas W. Baumgarte and Stuart L. Shapiro. Numerical relativity and compact binaries. *Phys.Rept.*, 376:41–131, 2003.

[87] D. Brown, S. Fairhurst, B. Krishnan, R.A. Mercer, R.K. Kopparapu, et al. Data formats for numerical relativity waves. 2007.

[88] Ezra Newman and Roger Penrose. An Approach to gravitational radiation by a method of spin coefficients. *J.Math.Phys.*, 3:566–578, 1962.

[89] Manuela Campanelli and Carlos O. Lousto. Second order gauge invariant gravitational perturbations of a kerr black hole. *Phys. Rev. D*, 59:124022, May 1999.

[90] Carsten Gundlach. Pseudo-spectral apparent horizon finders: An efficient new algorithm. *Phys. Rev.*, D57:863–875, 1998.

[91] M Alcubierre, S Brandt, B Brgmann, C Gundlach, J Mass, E Seidel, and P Walker. Test-beds and applications for apparent horizon finders in numerical relativity. *Classical and Quantum Gravity*, 17(11):2159, 2000.

[92] S.T. McWilliams and College Park. Physics University of Maryland. *Applying Numerical Relativity to Gravitational Wave Astronomy*. University of Maryland, College Park, 2008.

[93] Monica Valluri, Laura Ferrarese, David Merritt, and Charles L. Joseph. The Low End of the Supermassive Black Hole Mass Function: Constraining the Mass of a Nuclear Black Hole in NGC 205 via Stellar Kinematics. *Astrophys. J.*, 628:137–152, 2005.

[94] Margarita Safonova and Prajval Shastri. Extrapolating SMBH correlations down the mass scale: the case for IMBHs in globular clusters. *Astrophys. Space Sci.*, 325:47–58, 2010.

[95] A. Beifiori, S. Courteau, E. M. Corsini, and Y. Zhu. On the Correlations between Galaxy Properties and Supermassive Black Hole Mass. 2011.

[96] Yan-Rong Li, Luis C. Ho, and Jian-Min Wang. Cosmological evolution of supermassive black holes. I. mass function at 0¡2. *Astrophys. J.*, 742:33, 2011.

[97] Alireza Rafiee and Patrick B. Hall. Supermassive Black Hole Mass Estimates Using Sloan Digital Sky Survey Quasar Spectra at 0.7 ¡ z ¡ 2. *Astrophys. J. Suppl.*, 194:42, 2011.

[98] Andreas Burkert and Scott Tremaine. A correlation between central supermassive black holes and the globular cluster systems of early-type galaxies. *Astrophys. J.*, 720:516–521, 2010.

[99] Gretchen L. H. Harris and William E. Harris. The Globular Cluster/Central Black Hole Connection in Galaxies. 2010.

[100] A. Cattaneo, S.M. Faber, J. Binney, A. Dekel, J. Kormendy, et al. The role of black holes in galaxy formation and evolution. *Nature*, 460:213–219, 2009.

[101] Ch. Filloux, J. A. de Freitas Pacheco, F. Durier, and J. C. N. de Araujo. Coalescence Rate of Supermassive Black Hole Binaries Derived from Cosmological Simulations: Detection Rates for LISA and ET. 2011.

[102] Emanuele Berti. Lisa observations of massive black hole mergers: event rates and issues in waveform modelling. *Classical Quantum Gravity*, 23:S785, 2006.

[103] Martin G Haehnelt. Hierarchical build-up of galactic bulges and the merging rate of supermassive binary black holes. *Classical and Quantum Gravity*, 20(10):S31, 2003.

[104] Kirsty J. Rhook and J. Stuart B. Wyithe. Realistic Event Rates for Detection of Supermassive Black Hole Coalescence by LISA. *Mon. Not. Roy. Astron. Soc.*, 361:1145–1152, 2005.

[105] Adrienne L. Erickcek, Marc Kamionkowski, and Andrew J. Benson. Supermassive Black Hole Merger Rates: Uncertainties from Halo Merger Theory. *Mon. Not. Roy. Astron. Soc.*, 371:1992–2000, 2006.

[106] Miroslav Micic, Kelly Holley-Bockelmann, Steinn Sigurdsson, and Tom Abel. Supermassive Black Hole Growth and Merger Rates from Cosmological N-body Simulations. *Mon. Not. Roy. Astron. Soc.*, 380:1533, 2007.

[107] Z. L. Wen, F. A. Jenet, D. Yardley, G. B. Hobbs, and R. N. Manchester. Constraining the coalescence rate of supermassive black- hole binaries using pulsar timing. *Astrophys. J.*, 730:29, 2011.

[108] Jose Antonio de Freitas Pacheco, Charline Filloux, and Tania Regimbau. Capture Rates of Compact Objects by Supermassive Black Holes. *Phys. Rev.*, D74:023001, 2006.

[109] Pau Amaro-Seoane and Marc Freitag. Intermediate-mass black holes in colliding clusters: Implications for lower-frequency gravitational-wave astronomy. *Astrophys. J.*, 653:L53–L56, 2006.

[110] Pau Amaro-Seoane and Lucia Santamaria. Detection of IMBHs with ground-based gravitational wave observatories: A biography of a binary of black holes, from birth to death. *Astrophys.J.*, 722:1197–1206, 2010.

[111] John M. Fregeau, Shane L. Larson, M. Coleman Miller, Richard W. O'Shaughnessy, and Frederic A. Rasio. Observing IMBH-IMBH Binary Coalescences via Gravitational Radiation. *Astrophys. J.*, 646:L135–L138, 2006.

[112] Ilya Mandel, Jonathan R. Gair, and M. Coleman Miller. Detecting coalescences of intermediate-mass black holes in globular clusters with the Einstein Telescope. 2009.

[113] Darren J. White, E.J. Daw, and V.S. Dhillon. A List of Galaxies for Gravitational Wave Searches. *Class.Quant.Grav.*, 28:085016, 2011. * Temporary entry *.

[114] Jay Strader, Laura Chomiuk, Thomas Maccarone, James Miller-Jones, and Anil Seth. Two stellar-mass black holes in the globular cluster M22. *Nature*, 490:71–73, October 2012.

[115] Vassiliki Kalogera, K. Belczynski, C. Kim, Richard W. O'Shaughnessy, and B. Willems. Formation of Double Compact Objects. *Phys.Rept.*, 442:75–108, 2007.

[116] R. M. O'Leary, B. Kocsis, and A. Loeb. Gravitational waves from scattering of stellar-mass black holes in galactic nuclei. July 2008.

[117] V. Kalogera, A. R. King, and F. A. Rasio. Could black hole x-ray binaries be detected in globular clusters? *The Astrophysical Journal Letters*, 601(2):L171, 2004.

[118] Thomas J. Maccarone, G. Bergond, Arunav Kundu, Katherine L. Rhode, John J. Salzer, et al. An X-ray emitting black hole in a globular cluster. *IAU Symp.*, 2007.

[119] S. Sigurdsson. Estimating the detectable rate of capture of stellar mass black holes by massive central black holes in normal galaxies. *Class. Quantum Grav.*, 14:1425–1429, 1997.

[120] Duncan A. Brown, Hua Fang, Jonathan R. Gair, Chao Li, Geoffrey Lovelace, et al. Prospects for detection of gravitational waves from intermediate-mass-ratio inspirals. *Phys.Rev.Lett.*, 99:201102, 2007.

[121] Steve Drasco and Scott A. Hughes. Gravitational wave snapshots of generic extreme mass ratio inspirals. *Phys.Rev.*, D73:024027, 2006.

[122] Clovis Hopman. Astrophysics of extreme mass ratio inspiral sources. *AIP Conf.Proc.*, 873:241–249, 2006.

[123] Chunglee Kim, Vicky Kalogera, and Duncan R. Lorimer. Effect of PSR J0737-3039 on the DNS Merger Rate and Implications for GW Detection. *New Astron.Rev.*, 2006.

[124] Philip Nutzman, Vassiliki Kalogera, Lee Samuel Finn, Cy Hendrickson, and Krzysztof Belczynski. Gravitational waves from extragalactic inspiraling binaries: Selection effects and expected detection rates. *Astrophys.J.*, 612:364–374, 2004.

[125] S Marka, for the LIGO Scientific Collaboration, and the Virgo Collaboration. Transient multimessenger astronomy with gravitational waves. *Classical and Quantum Gravity*, 28(11):114013, 2011.

[126] V. Predoi, J. Clark, T. Creighton, E. Daw, S. Fairhurst, et al. Prospects for joint radio telescope and gravitational wave searches for astrophysical transients. *Class.Quant.Grav.*, 27:084018, 2010.

[127] Christian D. Ott. The Gravitational Wave Signature of Core-Collapse Supernovae. *Class.Quant.Grav.*, 26:063001, 2009.

[128] Ehud Nakar. Short-hard gamma-ray bursts. *Phys. Rept.*, 442:166–236, 2007.

[129] Elena Pian, P.A. Mazzali, N. Masetti, P. Ferrero, S. Klose, et al. An optical supernova associated with the X-ray flash XRF 060218. *Nature*, 442:1011–1013, 2006.

[130] V. Predoi and Kevin Hurley. Search for gravitational waves associated with the InterPlanetary Network short gamma ray bursts. *J.Phys.Conf.Ser.*, 363:012034, 2012.

[131] Alicia M. Soderberg, S.R. Kulkarni, E. Nakar, E. Berger, Derek B. Fox, et al. Relativistic ejecta from X-ray flash XRF 060218 and the rate of cosmic explosions. *Nature*, 442:1014–1017, 2006.

[132] Anna Watts, Badri Krishnan, Lars Bildsten, and Bernard F. Schutz. Detecting gravitational wave emission from the known accreting neutron stars. *Mon.Not.Roy.Astron.Soc.*, 389:839–868, 2008.

[133] Bence Kocsis, Merse E. Gaspar, and Szabolcs Marka. Detection rate estimates of gravity-waves emitted during parabolic encounters of stellar black holes in globular clusters. *Astrophys.J.*, 648:411–429, 2006.

[134] Clovis Hopman, Marc Freitag, and Shane L. Larson. Gravitational wave bursts from the Galactic massive black hole. *Mon.Not.Roy.Astron.Soc.*, 378:129–136, 2007.

[135] Thibault Damour and Alexander Vilenkin. Gravitational wave bursts from cusps and kinks on cosmic strings. *Phys.Rev.*, D64:064008, 2001.

[136] Louis Leblond, Benjamin Shlaer, and Xavier Siemens. Gravitational waves from broken cosmic strings: The bursts and the beads. *Phys. Rev. D*, 79:123519, Jun 2009.

[137] T. Regimbau and V. Mandic. Astrophysical Sources of Stochastic Gravitational-Wave Background. *Class.Quant.Grav.*, 25:184018, 2008.

[138] J.H. Taylor and J.M. Weisberg. A new test of general relativity: Gravitational radiation and the binary pulsar psr 1913+16. *Astrophys. J.*, 253:908–920, 1982.

[139] J. M. Weisberg and J. H. Taylor. The relativistic binary pulsar b1913+16: Thirty years of observations and analysis. In F. A. Rasio and I. H. Stairs, editors, *ASP Conf. Ser. 328: Binary Radio Pulsars*, page 25, January 2005.

[140] Paulo C.C. Freire, Norbert Wex, Gilles Esposito-Farese, Joris P.W. Verbiest, Matthew Bailes, et al. The relativistic pulsar-white dwarf binary PSR J1738+0333 II. The most stringent test of scalar-tensor gravity. *Mon.Not.Roy.Astron.Soc.*, 423:3328, 2012.

[141] J.J. Hermes, Mukremin Kilic, Warren R. Brown, D.E. Winget, Carlos Allende Prieto, et al. Rapid Orbital Decay in the 12.75-minute WD+WD Binary J0651+2844. 2012.

[142] Directional limits on persistent gravitational waves using ligo s5 science data. *Phys. Rev. Lett.*, 107:271102, Dec 2011.

[143] B. Abbott et al. Limits on gravitational wave emission from selected pulsars using ligo data. *Phys. Rev. Lett.*, 94:181103, 2005.

[144] B. Abbott et al. Upper limits on a stochastic background of gravitational waves. *Phys. Rev. Lett.*, 95:221101, 2005.

[145] J. Abadie et al. Upper limits on a stochastic gravitational-wave background using LIGO and Virgo interferometers at 600-1000 Hz. 2011.

[146] Search for Gravitational Waves from Binary Black Hole Inspiral, Merger and Ringdown in LIGO-Virgo Data from 2009-2010. 2012.

[147] A Gravitational wave observatory operating beyond the quantum shot-noise limit: Squeezed light in application. *Nature Phys.*, 7:962–965, 2011.

[148] M. et al. Ando. Stable operation of a 300-m laser interferometer with sufficient sensitivity to detect gravitational-wave events within our galaxy. *Phys. Rev. Lett.*, 86:3950–3954, 2001.

[149] Kentaro Somiya. Detector configuration of kagra - the japanese cryogenic gravitational-wave detector. *Classical and Quantum Gravity*, 29(12):124007, 2012.

[150] Einstein telescope. `http://www.et-gw.eu/`, 2008.

[151] B. Sathyaprakash, M. Abernathy, F. Acernese, P. Ajith, B. Allen, et al. Scientific Objectives of Einstein Telescope. *Class.Quant.Grav.*, 29:124013, 2012.

[152] B.S. Sathyaprakash, B.F. Schutz, and C. Van Den Broeck. Cosmography with the Einstein Telescope. *Class.Quant.Grav.*, 27:215006, 2010.

[153] Tania Regimbau, Thomas Dent, Walter Del Pozzo, Stefanos Giampanis, Tjonnie G.F. Li, et al. A Mock Data Challenge for the Einstein Gravitational-Wave Telescope. 2012.

[154] Et sensitivities page. `http://www.et-gw.eu/etsensitivities`.

[155] A Freise, S Chelkowski, S Hild, W Del Pozzo, A Perreca, and A Vecchio. Triple michelson interferometer for a third-generation gravitational wave detector. *Classical and Quantum Gravity*, 26(8):085012, 2009.

[156] Ligo-india. `http://www.gw-indigo.org/tiki-index.php?page=LIGO-India`, 2011.

[157] Stephen Fairhurst. Improved source localization with ligo india. *ICGC2011 Conference Proceedings*, 2012.

[158] Scientific benefits of moving one of ligo hanford detectors to india. `https://dcc.ligo.org/cgi-bin/DocDB/ShowDocument?docid=91470`, 2012.

[159] Jonathan R. Gair, Christopher Tang, and Marta Volonteri. LISA extreme-mass-ratio inspiral events as probes of the black hole mass function. *Phys.Rev.*, D81:104014, 2010.

[160] Alexander Stroeer, Matthew Benacquista, and Frank Ceballos. Detecting Double Degenerate Progenitors of SNe Ia with LISA. *Proceedings of IAU Symp. 281, Binary Paths to Type Ia Supernovae Explosions*, 2011.

[161] Pau Amaro-Seoane, Sofiane Aoudia, Stanislav Babak, Pierre Binetruy, Emanuele Berti, et al. eLISA: Astrophysics and cosmology in the millihertz regime. 2012.

[162] J. Weber. Gravitational-wave-detector events. *Phys. Rev. Lett.*, 20:1307–1308, Jun 1968.

[163] J. Weber. Evidence for discovery of gravitational radiation. *Phys. Rev. Lett.*, 22:1320–1324, 1969.

[164] L Ju, D G Blair, and C Zhao. Detection of gravitational waves. *Reports on Progress in Physics*, 63(9):1317, 2000.

[165] E. Coccia, V. Fafone, G. Frossati, J.A. Lobo, and J.A. Ortega. A Hollow sphere as a detector of gravitational radiation. *Phys.Rev.*, D57:2051–2060, 1998.

[166] C. A. K. Robinson, B. S. Sathyaprakash, and Anand S. Sengupta. A geometric algorithm for efficient coincident detection of gravitational waves. *Phys. Rev.*, D78:062002, 2008.

[167] B. S. Sathyaprakash and B. F. Schutz. Physics, Astrophysics and Cosmology with Gravitational Waves. *Living Rev. Rel.*, 12:2, 2009.

[168] L. P. Grishchuk, V. M. Lipunov, K. A. Postnov, M. E. Prokhorov, and B. S. Sathyaprakash. Gravitational wave astronomy: in anticipation of first sources to be detected. *Usp. Fiz. Nauk*, 171:3, 2001.

[169] Michele Vallisneri. Use and abuse of the fisher information matrix in the assessment of gravitational-wave parameter-estimation prospects. *Phys. Rev. D*, 77:042001, 2008.

[170] L. S. Finn. Detection, measurement, and gravitational radiation. *Phys. Rev. D*, 46:5236, 1992.

[171] D.S. Sivia and J. Skilling. *Data Analysis: A Bayesian Tutorial*. Oxford Science Publications. Oxford University Press, 2006.

[172] John Veitch and Alberto Vecchio. A Bayesian approach to the follow-up of candidate gravitational wave signals. *Phys.Rev.*, D78:022001, 2008.

[173] R.P. Kerr. *Phys. Rev. Lett.*, 11:237, 1963.

[174] E.T. Newman, K. Couch, K. Chinnapared, A. Exton, A. Parakash, and Torrence. *J. Math. Phys.*, 6:918, 1965.

[175] W. Israel. *Phys. Rev.*, 164:1776, 1967.

[176] W. Israel. *Commun. Math. Phys.*, 8:245, 1968.

[177] S.W. Hawking. *Commun. Math. Phys.*, 25:152, 1972.

[178] D.C. Robinson. *Phys. Rev. Lett.*, 34:905, 1975.

[179] C.V. Vishveshwara. Stability of the schwarzschild metric. *Phys. Rev. D*, 1:2870, 1970.

[180] W.H. Press. Long wave trains of gravitational waves from a vibrating black hole. *Astrophys. J. Lett.*, 170:L105, 1971.

[181] S. A. Teukolsky. Rotating black holes - separable wave equations for gravitational and electromagnetic perturbations. *Phys. Rev. Lett.*, 29:1114–1118, 1972.

[182] S.A. Teukolsky. Perturbations of a rotating black hole. 1. Fundamental equations for gravitational electromagnetic and neutrino field perturbations. *Astrophys. J.*, 185:635–647, 1973.

[183] W.H. Press and S.A. Teukolsky. Perturbations of a Rotating Black Hole. II. Dynamical Stability of the Kerr Metric. *Astrophys. J.*, 185:649–674, 1973.

[184] B. F. Whiting. Mode stability of the Kerr black hole. *Journal of Mathematical Physics*, 30:1301–1305, June 1989.

[185] Olaf Dreyer, Bernard Kelly, Badri Krishnan, Lee Samuel Finn, David Garrison, and Ramon Lopez-Aleman. Black hole spectroscopy: Testing general relativity through gravitational wave observations. *Class. Quantum Grav.*, 21:787, 2004.

[186] E. Berti, J. Cardoso, V. Cardoso, and M. Cavagliá. Matched filtering and parameter estimation of ringdown waveforms. *Phys. Rev.*, D76:104044, 2007.

[187] K Danzmann. LISA - an ESA cornerstone mission for a gravitational wave observatory. *Class. Quantum Grav.*, 14:1399, 1997.

[188] M. Punturo, M. Abernathy, F. Acernese, B. Allen, N. Andersson, et al. The Einstein Telescope: A third-generation gravitational wave observatory. *Class.Quant.Grav.*, 27:194002, 2010.

[189] David Shoemaker. Advanced LIGO Anticipated Sensitivity Curves. Technical report, 2009.

[190] J. Smith (for the LIGO Scientific Collaboration). The path to the enhanced and advanced ligo gravitational-wave detectors. *Classical and Quantum Gravity*, 26(11):114013, June 2009.

[191] Gregory M Harry and the LIGO Scientific Collaboration. Advanced ligo: the next generation of gravitational wave detectors. *Classical and Quantum Gravity*, 27(8):084006, 2010.

[192] B Abbott et al. Advanced ligo reference design. Technical Report LIGO-M060056-08-M, LIGO Project, 2007.

[193] K. G. Arun. Parameter estimation of coalescing supermassive black hole binaries with LISA. *Phys. Rev. D*, 74(2):024025–+, July 2006.

[194] Sascha Husa, Jose A. González, Mark Hannam, Bernd Brügmann, and Ulrich Sperhake. Reducing phase error in long numerical binary black hole evolutions with sixth order finite differencing. *Class. Quant. Grav.*, 25:105006, 2008.

[195] Jeffrey M. Bowen and James W. York, Jr. Time asymmetric initial data for black holes and black hole collisions. *Phys. Rev.*, D21:2047–2056, 1980.

[196] Mark Hannam, Sascha Husa, Denis Pollney, Bernd Brügmann, and Niall Ó Murchadha. Geometry and Regularity of Moving Punctures. *Phys. Rev. Lett.*, 99:241102, 2007.

[197] M. Shibata and T. Nakamura. Evolution of three-dimensional gravitational waves: Harmonic slicing case. *Phys. Rev.*, D52:5428–5444, 1995.

[198] E. Berti, V. Cardoso, J. Gonzalez, U. Sperhake, M. Hannam, S. Husa, and B. Brugmann. Inspiral, merger and ringdown of unequal mass black hole binaries: A multipolar analysis. *Phys. Rev.*, D76:064034, 2007.

[199] Thibault Damour, Alessandro Nagar, Mark Hannam, Sascha Husa, and Bernd Bruegmann. Accurate Effective-One-Body waveforms of inspiralling and coalescing black-hole binaries. *Phys.Rev.*, D78:044039, 2008.

[200] Christian Reisswig and Denis Pollney. Notes on the integration of numerical relativity waveforms. *Class.Quant.Grav.*, 28:195015, 2011.

[201] Mark Hannam, Sascha Husa, Ulrich Sperhake, Bernd Bruegmann, and Jose A. Gonzalez. Where post-Newtonian and numerical-relativity waveforms meet. *Phys.Rev.*, D77:044020, 2008.

[202] Stanislav Babak, Mark Hannam, Sascha Husa, and Bernard F. Schutz. Resolving Super Massive Black Holes with LISA. 2008.

[203] Jose A. Gonzalez, Ulrich Sperhake, and Bernd Bruegmann. Black-hole binary simulations: The Mass ratio 10:1. *Phys.Rev.*, D79:124006, 2009.

[204] Carlos O. Lousto, Hiroyuki Nakano, Yosef Zlochower, and Manuela Campanelli. Intermediate Mass Ratio Black Hole Binaries: Numerical Relativity meets Perturbation Theory. *Phys.Rev.Lett.*, 104:211101, 2010.

[205] Carlos O. Lousto, Hiroyuki Nakano, Yosef Zlochower, and Manuela Campanelli. Intermediate-mass-ratio black hole binaries: Intertwining numerical and perturbative techniques. *Phys.Rev.*, D82:104057, 2010.

[206] L.E. Kidder. Using full information when computing modes of post-newtonian waveforms from inspiralling compact binaries in circular orbit. *Phys. Rev. D*, 77:044016, 2008.

[207] Luc Blanchet. Second-post-newtonian generation of gravitational radiation. *Phys. Rev. D*, 51:2559–2583, Mar 1995.

[208] K G Arun, Luc Blanchet, Bala R Iyer, and Moh'd S S Qusailah. The 2.5pn gravitational wave polarizations from inspiralling compact binaries in circular orbits. *Classical and Quantum Gravity*, 21(15):3771, 2004.

[209] Luc Blanchet, Guillaume Faye, and Samaya Nissanke. Structure of the post-newtonian expansion in general relativity. *Phys. Rev. D*, 72:044024, Aug 2005.

[210] Luc Blanchet and Thibault Damour. Tail-transported temporal correlations in the dynamics of a gravitating system. *Phys. Rev. D*, 37:1410–1435, Mar 1988.

[211] Luc Blanchet and Thibault Damour. Hereditary effects in gravitational radiation. *Phys. Rev. D*, 46:4304–4319, Nov 1992.

[212] Luc Blanchet, Bala R. Iyer, and Benoit Joguet. Gravitational waves from inspiraling compact binaries: Energy flux to third post-newtonian order. *Phys. Rev. D*, 65:064005, Feb 2002.

[213] Denis Pollney and Christian Reisswig. Gravitational memory in binary black hole mergers. 2010.

[214] J. Baker, A. Abrahams, P. Anninos, S. Brandt, R. Price, J. Pullin, and E. Seidel. Collision of boosted black holes. *Phys.Rev.D*, 55:829–834, January 1997.

[215] John G. Baker, William D. Boggs, Joan Centrella, Bernard J. Kelly, Sean T. McWilliams, and James R. van Meter. Mergers of nonspinning black-hole binaries: Gravitational radiation characteristics. *Phys.Rev.*, D78:044046, 2008.

[216] John G. Baker, Sean T. McWilliams, James R. van Meter, Joan Centrella, Dae-Il Choi, et al. Binary black hole late inspiral: Simulations for gravitational wave observations. *Phys.Rev.*, D75:124024, 2007.

[217] Alessandra Buonanno, Lawrence E. Kidder, and Luis Lehner. Estimating the final spin of a binary black hole coalescence. *Phys.Rev.*, D77:026004, 2008.

[218] L. Rezzolla, E. Barausse, E.N. Dorband, D. Pollney, C. Reisswig, J. Seiler, and S. Husa. On the final spin from the coalescence of two black holes. *Phys. Rev. D*, 78, 2007.

[219] L. Rezzolla, E.N. Dorband, C. Reisswig, P. Diener, D. Pollney, E. Schnetter, and B. Szilágyi. Spin diagrams for equal-mass black-hole binaries with aligned spins. *Astrophys. J.*, 679:1422–1426, 2007.

[220] L. Rezzolla, P. Diener, E.N. Dorband, D. Pollney, C. Reisswig, E. Schnetter, and J. Seiler. The final spin from the coalescence of aligned-spin black hole binaries. *Astrophys. J. Lett.*, 674:L29–L32, 2008.

[221] E. Berti, V. Cardoso, J.A. Gonzalez, U. Sperhake, and Bernd Bruegmann. Multipolar analysis of spinning binaries. *Class.Quant.Grav.*, 25:114035, 2008.

[222] Kip S. Thorne. Gravitational radiation. In S.W. Hawking and W. Israel, editors, *Three hundred years of gravitation*, pages 330–458. Cambridge University Press, 1987.

[223] Stefan Hild, Simon Chelkowski, Andreas Freise, Janyce Franc, Nazario Morgado, et al. A Xylophone Configuration for a third Generation Gravitational Wave Detector. *Class.Quant.Grav.*, 27:015003, 2010.

[224] K.G. Arun, Stas Babak, Emanuele Berti, Neil Cornish, Curt Cutler, et al. Massive Black Hole Binary Inspirals: Results from the LISA Parameter Estimation Taskforce. *Class.Quant.Grav.*, 26:094027, 2009.

[225] K.A. Arnaud, S. Babak, J. Baker, M.J. Benacquista, N.J. Cornish, et al. An Overview of the second round of the Mock LISA Data Challenges. *Class.Quant.Grav.*, 24:S551–S564, 2007.

[226] Stanislav Babak et al. Report on the second Mock LISA Data Challenge. *Class.Quant.Grav.*, 25:114037, 2008.

[227] L A Wainstein and V D Zubakov. *Extraction of Signals from Noise*. Prentice-Hall, Englewood Cliffs, 1962.

[228] R Balasubramanian, B S Sathyaprakash, and S V Dhurandhar. Gravitational waves from coalescing binaries: detection strategies and monte carlo estimation of parameters. *Phys. Rev. D*, 53:3033, 1996. Erratum-ibid. D **54**, 1860 (1996).

[229] C Cutler. Angular resolution of the lisa gravitational wave detector. *Phys. Rev. D*, 57:7089, 1998.

[230] K G Arun, Bala R Iyer, B S Sathyaprakash, Siddhartha Sinha, and Chris Van Den Broeck. Higher signal harmonics, lisa's angular resolution and dark energy. *Phys. Rev. D*, 76:104016, 2007.

[231] Samaya Nissanke, Daniel E. Holz, Scott A. Hughes, Neal Dalal, and Jonathan L. Sievers. Exploring short gamma-ray bursts as gravitational-wave standard sirens. *Astrophys.J.*, 725:496–514, 2010.

[232] C. Van Den Broeck and A. S. Sengupta. Binary black hole spectroscopy. *Class. Quantum Grav.*, 24:1089–1113, March 2007.

[233] Alberto Vecchio. Lisa observations of rapidly spinning massive black hole binary systems. *Phys. Rev. D*, 70:042001, 2004.

[234] Ryan N. Lang and Scott A. Hughes. Measuring coalescing massive binary black holes with gravitational waves: The impact of spin-induced precession. *Phys. Rev. D*, 74:122001, 2006. Erratum-ibid. **D** 75, 089902 (2007).

[235] D. Merritt and R.D. Ekers. Tracing black hole mergers through radio lobe morphology. *Science*, 297:1310–1313, 2002.

[236] K. Nandra, J.A. Aird, D.M. Alexander, D.R. Ballantyne, X. Barcons, et al. The Growth of Supermassive Black Holes Across Cosmic Time. 2009. * Brief entry *.

[237] Rachel S. Somerville. The Co-evolution of Galaxies, Black Holes, and AGN in a Hierarchical Universe. 2008. * Brief entry *.

[238] Kostas D. Kokkotas and Bernd G. Schmidt. Quasinormal modes of stars and black holes. *Living Rev.Rel.*, 2:2, 1999.

[239] M. Coleman Miller. Intermediate-Mass Black Holes as LISA Sources. *Class. Quant. Grav.*, 26:094031, 2009.

[240] Eva Noyola and Holger Baumgardt. Testing Photometric Diagnostics for the Dynamical State and Possible IMBH presence in Globular Clusters. 2011.

[241] F. N. Bash, K. Gebhardt, W. M. Goss, and P. A. Vanden Bout. Very large array limits for intermediate-mass black holes in three globular clusters. *The Astronomical Journal*, 135(1):182, 2008.

[242] Marta Volonteri, Piero Madau, Eliot Quataert, and Martin J. Rees. The distribution and cosmic evolution of massive black hole spins. *Astrophys. J.*, 620:69–77, 2005.

[243] Kristen Menou, Zoltan Haiman, and Vijay K. Narayanan. The Merger history of supermassive black holes in galaxies. *Astrophys.J.*, 558:535–542, 2001.

[244] Ioannis Kamaretsos, Mark Hannam, Sascha Husa, and B. S. Sathyaprakash. Black-hole hair loss: learning about binary progenitors from ringdown signals. 2011.

[245] Enrico Barausse and Luciano Rezzolla. Predicting the direction of the final spin from the coalescence of two black holes. *Astrophys.J.*, 704:L40–L44, 2009.

[246] M Abernathy et al. *Einstein Telescope: Conceptual Design Study*. European Gravitational Observatory, document `ET-0106A-10`, 2011.

[247] Wolfgang Tichy and Pedro Marronetti. Final mass and spin of black-hole mergers. *Phys. Rev. D*, 78:081501, Oct 2008.

[248] P. Ajith, M. Hannam, S. Husa, Y. Chen, B. Bruegmann, et al. Inspiral-merger-ringdown waveforms for black-hole binaries with non-precessing spins. *Phys.Rev.Lett.*, 106:241101, 2011.

[249] L. Santamaria, F. Ohme, P. Ajith, B. Bruegmann, N. Dorband, et al. Matching post-Newtonian and numerical relativity waveforms: systematic errors and a new phenomenological model for non-precessing black hole binaries. *Phys.Rev.*, D82:064016, 2010.

[250] Frank Herrmann, Ian Hinder, Deirdre Shoemaker, Pablo Laguna, and Richard A. Matzner. Gravitational recoil from spinning binary black hole mergers. *Astrophys.J.*, 661:430–436, 2007.

[251] Patricia Schmidt, Mark Hannam, Sascha Husa, and P. Ajith. Tracking the precession of compact binaries from their gravitational-wave signal. *Phys.Rev.*, D84:024046, 2011.

[252] Bernd Bruegmann, Jose A. Gonzalez, Mark Hannam, Sascha Husa, and Ulrich Sperhake. Exploring black hole superkicks. *Phys.Rev.*, D77:124047, 2008.

[253] Yi Pan, Alessandra Buonanno, Ryuichi Fujita, Etienne Racine, and Hideyuki Tagoshi. Post-Newtonian factorized multipolar waveforms for spinning, non-precessing black-hole binaries. *Phys.Rev.*, D83:064003, 2011.

[254] Stefan Hild, Simon Chelkowski, and Andreas Freise. Pushing towards the ET sensitivity using 'conventional' technology. 2008.

[255] J. Skilling. Nested Sampling for General Bayesian Computation. *Bayesian Analysis*, 1(4):833–860, 2006.

[256] F. Feroz and M. P. Hobson. Multimodal nested sampling: an efficient and robust alternative to Markov Chain Monte Carlo methods for astronomical data analyses. *MNRAS*, 384:449–463, February 2008.

[257] T. J. Galama et al. Discovery of the peculiar supernova 1998bw in the error box of GRB980425. *Nature*, 395:670, 1998.

[258] Li-Xin Li. The GRB-Supernova Connection. 2008.

[259] B. P. Abbott, The LIGO Scientific Collaboration, and the Virgo Collaboration. Search for gravitational-wave bursts associated with gamma-ray bursts using data from ligo science run 5 and virgo science run 1. *The Astrophysical Journal*, 715(2):1438, 2010.

[260] J. Abadie et al. Implications For The Origin Of GRB 051103 From LIGO Observations. 2012.

[261] M.S. Briggs et al. Search for gravitational waves associated with gamma-ray bursts during LIGO science run 6 and Virgo science runs 2 and 3. 2012.

[262] Shourov Chatterji, Albert Lazzarini, Leo Stein, Patrick J. Sutton, Antony Searle, and Massimo Tinto. Coherent network analysis technique for discriminating gravitational-wave bursts from instrumental noise. *Phys. Rev. D*, 74:082005, Oct 2006.

[263] Warren G. Anderson, Patrick R. Brady, Jolien D. E. Creighton, and Éanna É. Flanagan. Excess power statistic for detection of burst sources of gravitational radiation. *Phys. Rev. D*, 63:042003, Jan 2001.

[264] S. Klimenko, S. Mohanty, M. Rakhmanov, and G. Mitselmakher. Constraint likelihood analysis for a network of gravitational wave detectors. *Phys. Rev. D*, 72:122002, Dec 2005.

[265] Antony C Searle, Patrick J Sutton, and Massimo Tinto. Bayesian detection of unmodeled bursts of gravitational waves. *Classical and Quantum Gravity*, 26(15):155017, 2009.

[266] S. Klimenko, I. Yakushin, A. Mercer, and Guenakh Mitselmakher. Coherent method for detection of gravitational wave bursts. *Class.Quant.Grav.*, 25:114029, 2008.

[267] Michal Was, Patrick J. Sutton, Gareth Jones, and Isabel Leonor. Performance of an externally triggered gravitational-wave burst search. *Phys.Rev.*, D86:022003, 2012.

[268] Yekta Gürsel and Massimo Tinto. Near optimal solution to the inverse problem for gravitational-wave bursts. *Phys. Rev. D*, 40:3884–3938, Dec 1989.

[269] S. V. Bergh and G. A. Tammann. Galactic and extragalactic supernova rates. *Ann. Rev. Astron. Astrophys.*, 29:363–407, 1991.

[270] Shin'ichiro Ando, John F. Beacom, and Hasan Yüksel. Detection of neutrinos from supernovae in nearby galaxies. *Phys. Rev. Lett.*, 95:171101, Oct 2005.

[271] `http://www.ligo.caltech.edu`. LIGO.

[272] `http://geo600.aei.mpg.de`. GEO600.

[273] `https://wwwcascina.virgo.infn.it`. VIRGO.

[274] Wolfgang Hillebrandt and Jens C. Niemeyer. Type Ia supernova explosion models. *Ann.Rev.Astron.Astrophys.*, 38:191–230, 2000.

[275] `http://www.rochesterastronomy.org/sn2011/sn2011dh.html`. Supernova 2011dh in M51.

[276] `http://www.astronomerstelegram.org/?read=3401`. Properties of the Candidate Progenitor of SN 2011dh in M51, The Astronomer's Telegram.

[277] S. Valenti, N. Elias-Rosa, S. Taubenberger, V. Stanishev, I. Agnoletto, et al. The carbon-rich type Ic SN 2007gr: the photospheric phase. *The Astrophysical Journal*, 673, L155, 2008.

[278] E. Muller and W. Hillebrandt. The collapse of rotating stellar cores. *Astron. Astrophys.* 103, 358, 1981.

[279] E. Muller. Gravitational radiation from collapsing rotating stellar cores. *Astron. Astrophys.* 114, 53, 1982.

[280] Hans-Thomas Janka, K. Langanke, A. Marek, G. Martinez-Pinedo, and B. Mueller. Theory of Core-Collapse Supernovae. *Phys.Rept.*, 442:38–74, 2007.

[281] J. A. Wheeler. *Ann. Rev. Astron. Astroph.* 4, 393, 1966.

[282] Christian D. Ott, Adam Burrows, Luc Dessart, and Eli Livne. A New Mechanism for Gravitational Wave Emission in Core-Collapse Supernovae. *Phys.Rev.Lett.*, 96:201102, 2006.

[283] Adam Burrows, Eli Livne, Luc Dessart, Christian Ott, and Jeremiah Murphy. A new mechanism for core-collapse supernova explosions. *Astrophys.J.*, 640:878–890, 2006.

[284] Christian D. Ott. 2010. Unpublished LIGO document, https://dcc.ligo.org/cgi-bin/private/DocDB/ShowDocument?docid=21139.

[285] S. Scheidegger, R. Kaeppeli, S.C. Whitehouse, T. Fischer, and M. Liebendoerfer. The Influence of Model Parameters on the Prediction of Gravitational wave Signals from Stellar Core Collapse. 2010.

[286] C. D. Ott, H. Dimmelmeier, A. Marek, H.-T. Janka, B. Zink, I. Hawke, and E. Schnetter. Rotating collapse of stellar iron cores in general relativity. *Classical and Quantum Gravity*, 24:139, June 2007.

[287] Harald Dimmelmeier, Christian D. Ott, Hans-Thomas Janka, Andreas Marek, and Ewald Mueller. Generic Gravitational Wave Signals from the Collapse of Rotating Stellar Cores. *Phys.Rev.Lett.*, 98:251101, 2007.

[288] Harald Dimmelmeier, Christian D. Ott, Hans-Thomas Janka, Andreas Marek, and Ewald Mueller. Generic Gravitational Wave Signals from the Collapse of Rotating Stellar Cores: A Detailed Analysis. 2007.

[289] Anthony L. Piro and Eric Pfahl. Fragmentation of collapsar disks and the production of gravitational waves. *The Astrophysical Journal*, 658(2):1173, 2007.

[290] : J. Abadie et al. All-sky search for gravitational-wave bursts in the second joint LIGO-Virgo run. 2012.

[291] Harald Dimmelmeier, Christian D. Ott, Andreas Marek, and H.-Thomas Janka. The Gravitational Wave Burst Signal from Core Collapse of Rotating Stars. *Phys.Rev.*, D78:064056, 2008.

[292] Masaru Shibata and Yu-Ichirou Sekiguchi. Gravitational waves from axisymmetrically oscillating neutron stars in general relativistic simulations. *Phys.Rev.*, D68:104020, 2003.

[293] Konstantin N. Yakunin, Pedro Marronetti, Anthony Mezzacappa, Stephen W. Bruenn, Ching-Tsai Lee, et al. Gravitational Waves from Core Collapse Supernovae. *Class.Quant.Grav.*, 27:194005, 2010.

[294] Adam Burrows, Luc Dessart, Christian D. Ott, and Eli Livne. Multi-Dimensional Explorations in Supernova Theory. *Phys. Rept.*, 442:23–37, 2007.

[295] N. N. Weinberg and E. Quataert. Non-linear saturation of g-modes in proto-neutron stars: quieting the acoustic engine. *MNRAS*, 387:L64–L68, June 2008.

[296] E. Müller, H.-T. Janka, and A. Wongwathanarat. Parametrized 3D models of neutrino-driven supernova explosions. Neutrino emission asymmetries and gravitational-wave signals. *Astronomy & Astrophysics*, 537:A63, January 2012.

[297] B. Mueller, H.-Th. Janka, and A. Heger. New Two-Dimensional Models of Supernova Explosions by the Neutrino-Heating Mechanism: Evidence for Different Instability Regimes in Collapsing Stellar Cores. 2012.

[298] Tomoya Takiwaki and Kei Kotake. Gravitational Wave Signatures of Magnetohydrodynamically-Driven Core-Collapse Supernova Explosions. *Astrophys.J.*, 743:30, 2011.

[299] Kei Kotake, Wakana Iwakami, Naofumi Ohnishi, and Shoichi Yamada. Stochastic Nature of Gravitational Waves from Supernova Explosions with Standing Accretion Shock Instability. *Astrophys.J.*, 697:L133–L136, 2009.

[300] Amber Lynnell Stuver and Lee Samuel Finn. GravEn: Software for the simulation of gravitational wave detector network response. *Class.Quant.Grav.*, 23:S799–S807, 2006.

[301] Amber Stuver. GravEn Simulation Engine Primer. Technical report, 2004.